Modulation of Protein-Membrane Interactions by Lipids and Divalent Cations

By

Victor Vasquez Montes
M.S., University of Kansas Medical Center, 2014
B.S., University of Kansas, 2011

Submitted to the graduate degree program in Biochemistry and Molecular Biology and the Graduate Faculty of the University of Kansas in partial fulfillment of the requirements for the degree of Doctor of Philosophy.

_____
Committee Chair: Alexey S. Ladokhin, Ph. D.

_____
Liskin Swint-Kruse, Ph. D

_____
Aron W. Fenton, Ph. D.

_____
Russell Swerdlow, M. D.

_____
Joanna Slusky, Ph. D.

Date Defended: 05/12/2020

The dissertation committee for Victor Vasquez Montes certifies that
this is the approved version of the following dissertation:

Modulation of Protein-Membrane Interactions by Lipids and Divalent Cations

_____
Chair: Alexey S. Ladokhin, Ph. D.

_____
Graduate Director: Aron W. Fenton, Ph. D.

Date Approved: 05/19/2020

Abstract

The post-translational insertion of proteins into membranes is common in a number of biologically important processes, such as the cellular entry of bacterial toxins or regulation of apoptosis by the Bcl-2 family of proteins, as well as in targeted drug delivery. While our ability to target or manipulate these processes can be beneficial for human health, the basic knowledge of the mechanism of membrane modulation of conformational switching is lacking.

To provide a more complete picture of protein-membrane interactions in the cell, this manuscript explores the effects of lipid composition and physiological [Ca^{2+}/Mg^{2+}] on the membrane insertion and refolding of peptides and proteins. The main focus is on the peptide pHLIP (pH-Low Insertion Peptide), a promising cancer targeting system, and the apoptotic inhibitor Bcl-xL. The results presented here demonstrate that physiological concentrations of Ca^{2+} and Mg^{2+} induce the membrane insertion and refolding of both pHLIP and Bcl-xL. In both cases, the divalent cation-dependent effects are further modulated by lipid composition. These results highlight the importance of physiological conditions on the study of protein membrane interactions and shows that their omission can lead to false assumptions of unfavorable interactions.

Table of Contents

List of Figures

List of Tables

Chapter 1: Introduction

1.1 Overview

Proteins can be subdivided into two broad categories: Soluble proteins (Fig. 1.1a) and membrane proteins (Fig. 1.1b). There is, however, a third group of proteins that are capable of transitioning between solution and membranes (Fig. 1.1c-e). This group includes several disease relevant proteins such as toxins (both viral and bacterial), apoptotic regulators and others [1-14].

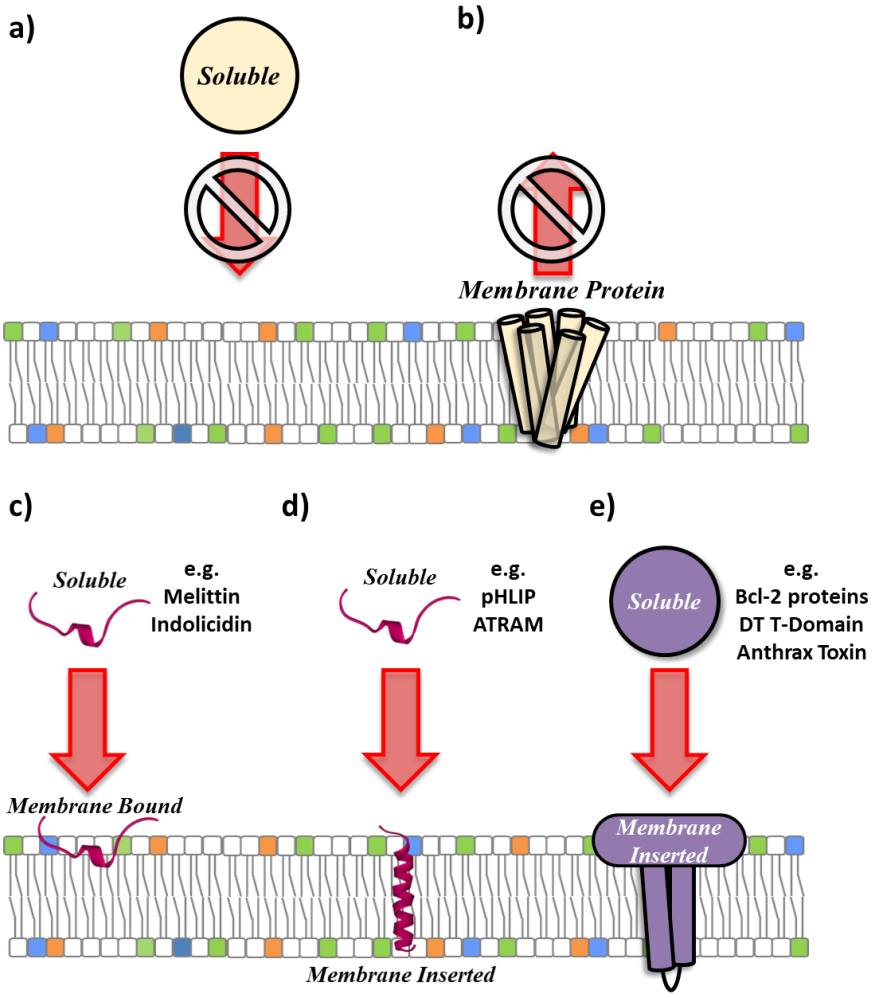

FIGURE 1.1. Soluble and membrane proteins

Proteins can be subdivided into (a) soluble or (b) membrane proteins. The former is characterized by a high hydrophilic character, which prevents its interaction with membranes. Membrane proteins, on the other hand, are highly hydrophobic, which limits them to lipid bilayers. (c-e) Membrane active peptides and proteins are a special group of proteins, that are stable in solution but also capable of interacting and in some cases inserting into membranes.

The transition of proteins from aqueous environments to the non-polar milieu of lipid bilayers is a complex process. This complexity arises from the difference in interactions of the protein in its initial and final conformation with aqueous and lipid environments, respectively. Satisfying both sets of interactions normally requires substantial structural rearrangements. This is exemplified in Fig. 1.2, which shows the extensive conformational changes that take place during the membrane binding and insertion of the diphtheria toxin translocation domain [15]. A long-standing goal of the membrane protein field has been to accurately predict the membranous conformation of these proteins based solely on their sequence. A corollary of this challenging problem is being to accurately determine which proteins present in the cytosol or extracellular fluid can redistribute to cellular membranes.

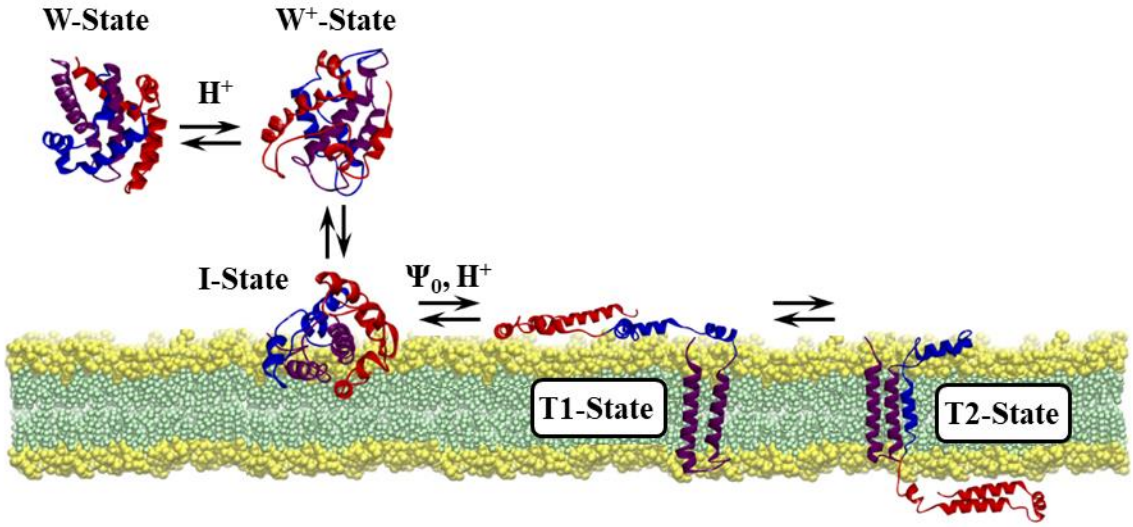

FIGURE 1.2. Membrane insertion and refolding of diphtheria toxin translocation domain

The interaction of proteins with lipid bilayers is accompanied by extensive refolding events. This is exemplified here with the pH-dependent membrane insertion pathway of the diphtheria toxin translocation domain. This protonation dependent pathway involves rearrangements between different water-soluble states (W-State and W^+-State) and extensive membrane-induced refolding to reach the interfacial form (I-State) and the inserted conformations (T1-State and T2-State). The transition to the inserted conformations is also modulated by the anionic content of the bilayer (Ψ_0). This figure was adapted from Kyrychenko et al., Reviews in Fluorescence, 2016

1.2 Fundamentals of lipid bilayer structure

A proper discussion of protein-membrane interactions is not possible without an introduction into the complexity of lipid bilayers. Cellular membranes, unlike homogeneous aqueous environments, are composed of different intermingling regions, each with distinct properties (Fig. 1.3). The presence of several different lipid components as well as exterior factors such as temperature and anionic strength add to this complexity.

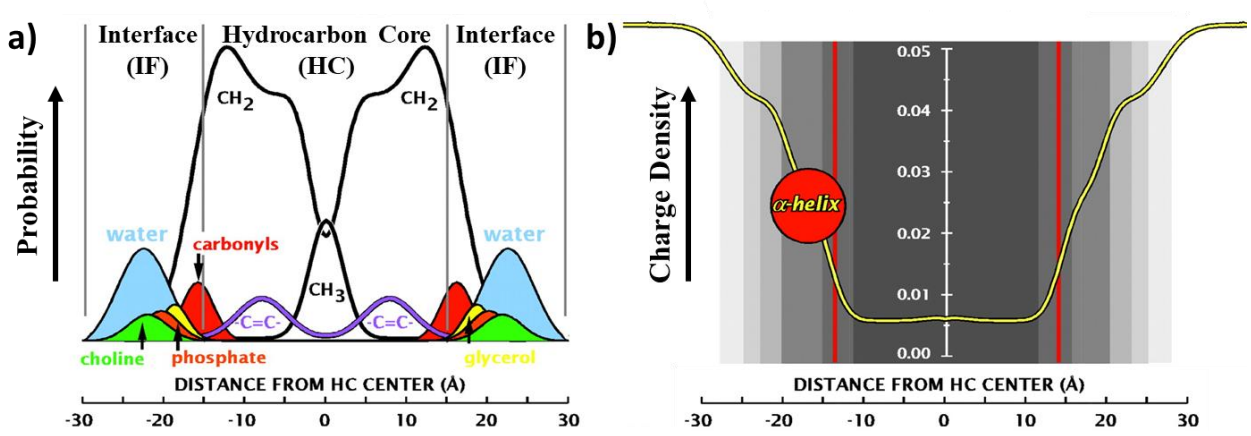

FIGURE 1.3. Structure of fluid lipid bilayers

(a) Structure of a DOPC (dioleoyl phosphatidylcholine) lipid bilayer determined by X-ray crystallography and NMR [16]. The moieties of the DOPC lipids are indicated as color coded distributions of their most likely localization in the membranes. The broad distributions are characteristic of the thermally disordered nature of lipid bilayers. The interface is defined by the penetration of water (blue) in the membrane. (b) The trace in yellow denotes the polarity profile of the bilayer, calculated from the partial charges present in each region [17]. It represents the steep depth-dependent decrease in polarity that proteins experience in the interface as they interact with membranes and approach the hydrocarbon core. Each of the interfacial regions flaking the hydrocarbon core have a depth of ~ 15 Å, which is large enough to accommodate a folded α-helix (red circle). Both panels are based on [17, 18] and adapted from Dr. Stephen White's website (http://blanco.biomol.uci.edu/Bilayer_Struc.html).

Lipid bilayers are subdivided into two regions: The interface and the hydrocarbon core. The interface constitutes the outermost layer of the membrane; its boundary within the membrane is defined as the depth to which water penetrates into the bilayer [19]. Interfacial regions are ~ 15 Å in thickness, which is large enough to accommodate a folded alpha helix oriented parallel to the bilayer plane [19]. The different chemical groups within the interface including water, lipid

phosphates, carbonyl groups, and the substantial number of lipid head group moieties give rise to very intricate physiochemical properties [19] (Fig. 1.3a). The hydrocarbon core of the bilayer is not as chemically diverse as the interface, however, varying degrees of acyl chain properties such as saturation, length, oxidation and the presence of molecules like sterols (*e.g.,* cholesterol) bring further complexity to a bilayer.

One of the most intriguing characteristics of biological membranes is the large array of lipid species present (Fig. 1.4), with some lipids being specific to particular leaflets and others present only in certain organelles [20]. Furthermore, their ratios (relative to other lipids) and abundance are modulated during specific events like cell division [21, 22], apoptosis [23-26] or cancer [27-30]. The lipid composition of a cellular membrane can therefore vary, and these changes will lead to different interfacial chemistry and hydrocarbon core properties that could affect their interaction with proteins.

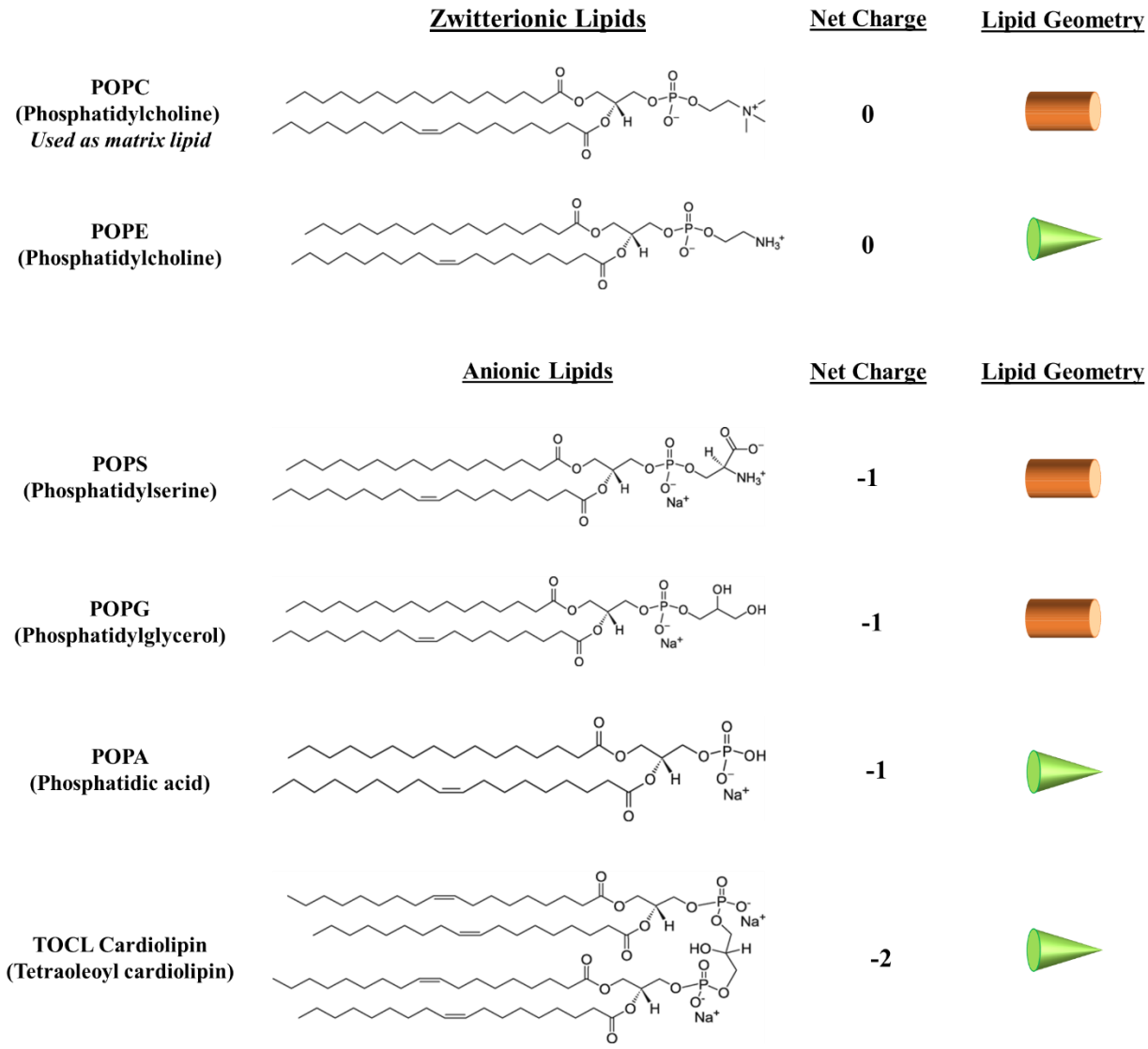

FIGURE 1.4. List of phospholipids used in this dissertation

Cellular membranes contain a large diversity of different phospholipids, each of which imposes a particular set of properties to the bilayer. For example, although structurally similar to POPC, the zwitterionic lipid POPE increases the lateral pressure of membranes [31]. Additionally, its conical geometry compared to the cylindrical shape of POPC leads promotes curvature. Anionic lipids such as POPS introduce negatively charged groups in the bilayer which introduce and electrostatic component to protein membrane interactions [32]in addition to any non-electrostatic effect they may introduce (*e.g.*, different lipid geometry).

1.3 Predicting protein-membrane interactions: Hydrophobicity scales

Research over the past decades has employed different approaches and model systems to develop "hydrophobicity" scales aimed at predicting the transition and stability of proteins in lipid bilayers

[33-37]. These scales provide experimentally derived free energies for the transition of all twenty common amino acids to hydrophobic environments that serve as a good first approximation for the propensity of these interactions.

Accurate predictions of protein-membrane partitioning were not possible until the development of the Wimley-White (WW) interfacial hydrophobicity scale [33]. What separated this approach from previous methodologies was their use of lipid bilayers instead of organic solvents (as membrane mimetics). This allowed the WW scale to account for the complexity of the membrane interface and separate the free energy of proteins partitioning to the membrane interface (ΔG_{IF}) from the estimated free energy of proteins being stable in the hydrocarbon core (ΔG_{TM}). The latter was calculated from a more traditional approach using water-to-octanol partitioning as a proxy for the hydrocarbon core of membranes [34]. It should also be noted that the WW scales were the first to determine the free energy penalty of peptide bonds residing in the interface or hydrocarbon core.

A drawback of current interfacial scales like the WW interfacial scale [33] and the Moon-Fleming Scale [35] is that they only account for the hydrophobic component involved in protein-membrane interactions. Furthermore, no current hydrophobicity scale has systematically explored the effect of non-lipid components such as soluble ions on protein-membrane interactions. The lack of thermodynamic models for more complex systems hinders accurate predictions of protein-membrane interactions in the cell. This can lead to underpredictions of transitions that require additional components such as electrostatic interactions between proteins and charged lipids. In line with these observations, this work builds on previous thermodynamic studies and explores the importance of physiological concentrations of divalent cations (Ca^{2+} and Mg^{2+}) and their coupling to membrane lipid composition on protein-membrane interactions. The model systems used in this

study are the peptide pHLIP (pH-Low Insertion peptide) in Chapters 2-4 and the apoptotic inhibitor Bcl-xL in Chapters 5-6

1.4 Cancer targeting peptide pHLIP

The pH-Low Insertion Peptide (pHLIP) has emerged as a promising system for the selective delivery of drugs to tumors [38-42]. This is due to a unique set of properties which allow pHLIP to be stable as an unstructured monomer in solution while remaining capable of inserting as a transmembrane α-helix [43, 44]. The transition between these states is controlled by environmental acidity, which leads to the protonation of several anionic residues and an increase in hydrophobicity. Coincidently, the pH required for the transmembrane insertion of pHLIP matches the mildly acidic conditions surrounding tumors [45, 46], making pHLIP an ideal cancer targeting system.

The current pHLIP insertion model postulates that the transmembrane insertion of pHLIP involves three different steps: The unstructured State I in solution (Fig. 1.5, black), the interfacially bound and structured State II (Fig. 1.5, red), and the pH-induced transmembrane State III (Fig. 1.5, red). This model was proposed based on measurements performed using simple model membranes composed of a single zwitterionic lipid species, namely POPC (palmitoyl oleoyl phosphatidylcholine) [43, 44]. The effect of physiological conditions such as complex lipid bilayers on the three-state model or the influence of soluble ions are not fully known. Understanding these effects is, however, critical for the safe use of pHLIP as a drug carrier system in humans.

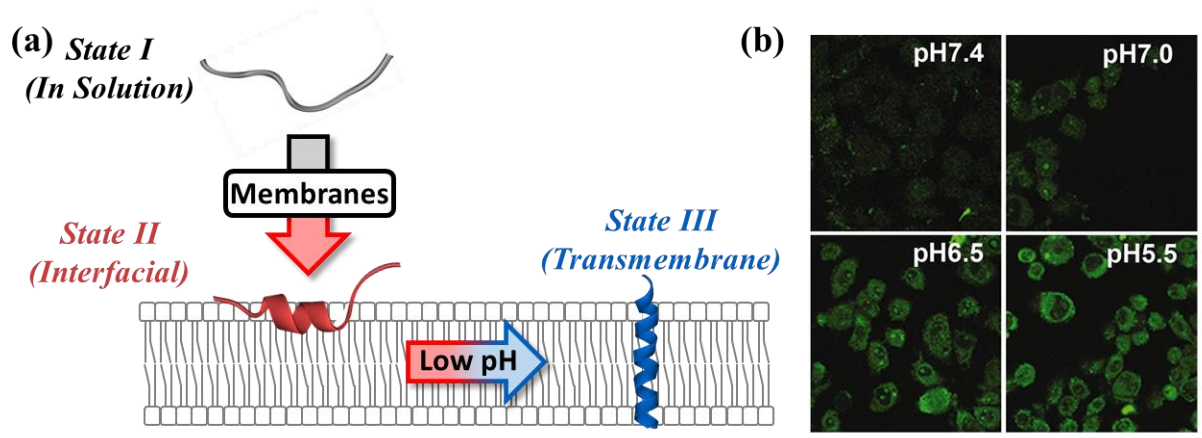

FIGURE 1.5. pHLIP (pH-Low Insertion Peptide) three-state model

(a) The three states involved in the transmembrane insertion of pHLIP are the soluble State I (black), the interfacial State II (red) and the transmembrane State III (blue). The anionic character of pHLIP (AAEQNPIYWARYADWLFTTPLLLLDLALLVDADEGG) keeps as an unstructured monomer in the absence of membranes. At neutral pH, pHLIP partitions to lipid bilayers while remaining mostly unstructured. Protonation of its anionic residues at mildly low pH (pK_{50} ~ 6 in POPC membranes) leads to its membrane insertion as a transmembrane α-helix. (b) Protonation-dependent transmembrane insertion of pHLIP visualized by its translocation of the fluorophore Alexa 488 into HeLa cells. Cells were incubated with pHLIP-A488 at the designated pH and washed with PBS buffer prior to imaging. Figures in panel b were adapted from Reshetnyak et al. PNAS, 2006.

The Ladokhin lab, for example, has shown that lipids play a crucial role on the three-state mechanism of pHLIP [47]. Their results suggest that the interfacial State II (Fig. 1.5, red) is only present in membranes composed only of choline containing lipids (the lipid composition used in the original pHLIP studies [43, 44]). More complex membrane compositions containing even 10% of a different phospholipid species or cholesterol resulted in an abolished State II (Fig. 1.5, red). This indicates that the insertion of pHLIP into plasma membranes may be more complex than the initially proposed three-state model. Furthermore, the protonation-dependent pK_{50} determined for the transition of pHLIP into its transmembrane State III (Fig. 1.5, blue) was modulated by lipid composition. Anionic lipids, in particular showed a linear response between the insertion pK_{50} and the molar content of anionic lipids in the bilayer.

The clinical use of pHLIP requires detailed understanding of its targeting and transmembrane insertion (drug delivery) in complex membrane environments. These models are not representative of the complexity of the plasma membrane or the significant changes in its lipid composition that take place during cancer development [27-30].

1.5 Apoptotic inhibitor Bcl-xL

The apoptotic inhibitor Bcl-xL (Fig. 1.6b) is a member or the vast Bcl-2 family of apoptotic regulators (Fig. 1.6) [14, 48, 49]. Bcl-xL inhibits the permeabilization of the mitochondrial outer membrane (MOMP), considered as the commitment step into the apoptotic pathway [9, 50-56].

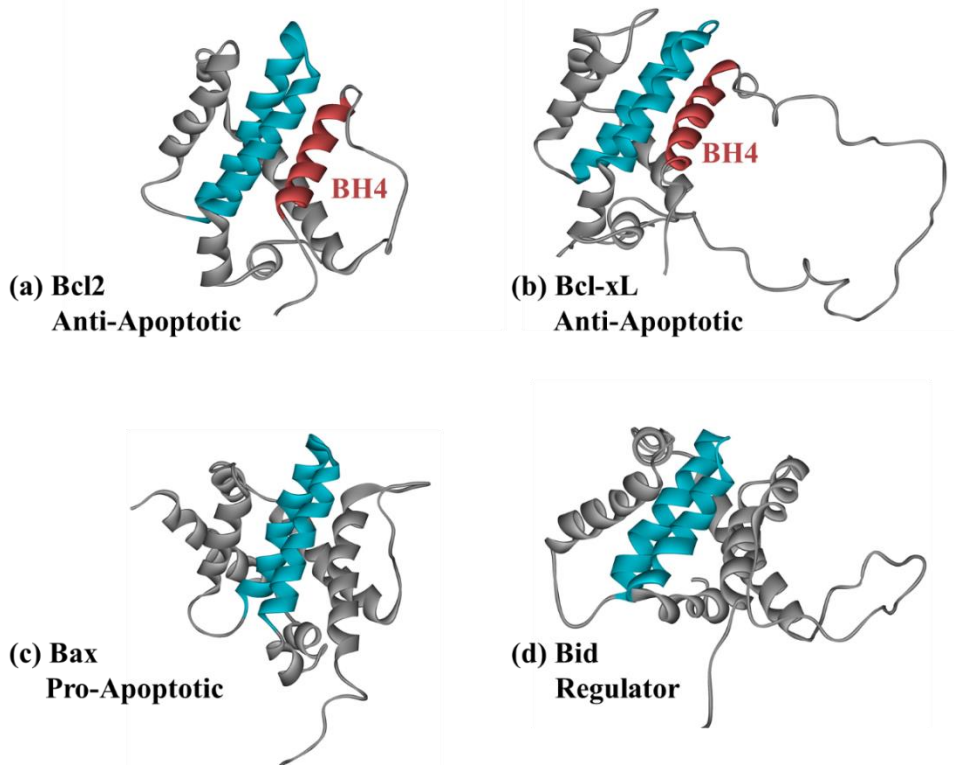

FIGURE 1.6. Bcl-2 proteins

Representative members of the Bcl-2 family of apoptotic regulators. This protein group cn be functionally divided into: (a, b) Anti-apoptotic proteins, (c) pro-apoptotic proteins and (d) apoptotic regulators. (a, b) Anti-apoptotic proteins like Bcl2 and Bcl-xL block the permeabilization of the mitochondrial outer membrane by pore formers like Bax. They are characterized by a N-terminal BH4 domain (red) linked to the rest of the protein structure through a loop. (c) Pro-apoptotic proteins like Bax permeabilize the mitochondrial outer membrane. (d) Apoptotic regulators such as Bid interact with anti- and pro-apoptotic proteins to modulate their interactions with mitochondrial membranes. The central hydrophobic hairpin of all proteins is show in cyan.

Bcl-xL is expressed in the cytosol in an inactive state and must redistribute to the mitochondrial outer membrane (MOM) to perform its anti-apoptotic activity. The transition of Bcl-xL to the MOM is currently believed to require previous activation by binding its homolog, Bid. The importance of Bcl-xL in preventing MOMP makes it an ideal anti-cancer target, however, the lack of structural and mechanistic details of its active conformation in the MOM has hindered drug development.

1.6 Methodology

The presence of fluid lipid bilayers imposes constrains on experimental design. For example, it significantly complicates the use of high-resolution techniques such as X-ray crystallography to determine the conformation of membranous states. Membranes, however, also introduce particular properties that can be taken advantage by several spectroscopic techniques, fluorescence spectroscopy, in particular.

1.6.1 Fluorescence spectroscopy: Environmentally Sensitive probes

As previously mentioned, the transition of proteins from water to lipid bilayers involves a drastic decrease in the polarity of the surrounding environment (Fig. 1.3b). This change in polarity affects the emission fluorescence of several environmentally sensitive fluorophores such as the intrinsic fluorophore tryptophan and the fluorescent probe NBD (nitrobenzoxadiazole).

The transition of either Trp or NBD to lipid bilayers from solution leads to a blue shift of their respective emission spectrum (*i.e.*, a shift of the spectrum towards lower wavelengths), accompanied by an intensity increase. These changes are exemplified in Fig. 1.7a for the interaction of NBD labeled Bcl-xL with membranes. The transition of the Trp and NBD from hydrophilic to hydrophobic environments can also be detected by lifetime fluorescence, a complimentary technique that yields the fluorescence decay of the fluorophores in the sample.

Since the fluorescence decay of environmentally sensitive probes is related to the polarity of the surrounding environment the water to membrane transition of Trp and NBD will be reflected in changes in their lifetime (Fig. 1.7b).

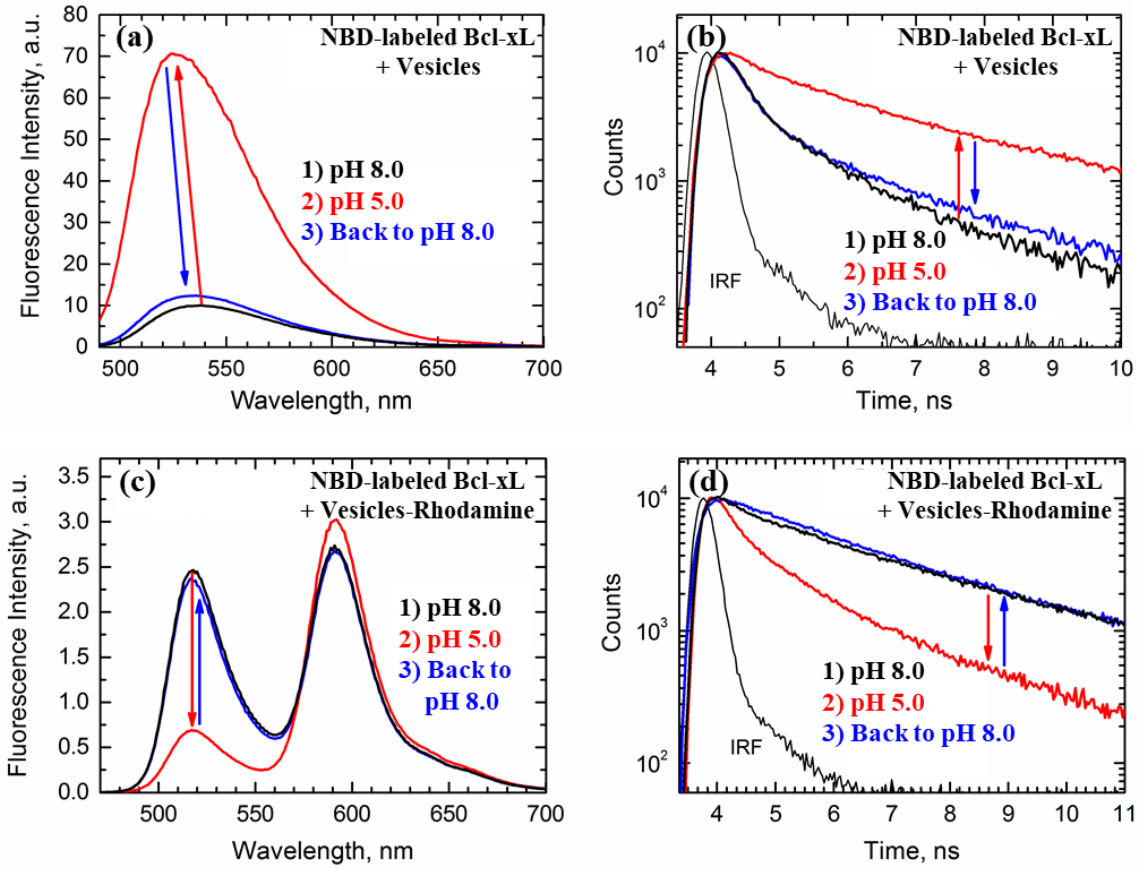

FIGURE 1.7. Examples of NBD emission fluorescence and FRET measurements

Fluorescence changes of (a, b) NBD labeled Bcl-xL or (c, d) FRET measurements using Alexa labeled Bcl-xL and rhodamine labeled vesicles. The membrane interaction of Bcl-xL was induced by a decrease in pH from 8.0 to 5.0 and reversed by raising the pH back to 8.0. (a) The transition of NBD to lipid bilayers results in an increase of the emission fluorescence intensity and a shift of its position of maximum to lower wavelengths. (b) This is accompanied by a decrease in NBD fluorescence lifetime. (c, d) FRET measurements result in a change in fluorescence intensity of the donor and acceptor fluorophores, which can also be observed by a change in fluorescence lifetime. The figure was modified from This figure was adapted from Kyrychenko et al., Reviews in Fluorescence, 2016

The use of Trp vs NBD will depend on the system studied. For example, pHLIP naturally contains two Trp (pHLIP was originally derived from the helix C of bacteriorhodpsin) [43, 44], which makes pHLIP amenable for Trp fluorescence (Chapter 2 and 3). Bcl-xL, on the other hand, has 7 Trp in its amino acid sequence, preventing its use as an indicator of membrane interactions. This

is because, the substantial number of Trp prevents the accurate interpretation of spectral changes, as deconvolving the signal to assign the contribution of each Trp would be very complicated. This can be circumvented by selectively labeling Bcl-xL NBD (Chapter 4 and 5), which has a different excitation and emission range than Trp.

The sensitivity of Trp and NBD to the polarity of the environment means that non-membrane related processes can also induce changes to its fluorescence. For example, the aggregation of proteins in solution (a common problem with membrane active proteins) creates hydrophobic environments which lead to similar effects as those induced by membrane interactions. This, however, can be prevented by using low protein concentrations and appropriate buffer conditions, which have to be empirically determined for each system.

1.6.2 Fluorescence spectroscopy: Förster resonance energy transfer (FRET)

Förster energy transfer (FRET) is a flexible technique that is used to determine the interaction between two or more complimentary fluorophores. As its name implies, it relies on the transfer of energy from one of the fluorophores, the donor, to a second fluorophore, the acceptor.

For FRET to occur the experimental setup must meet certain criteria: 1) The fluorophores used must be a FRET pair. This means that there must be an overlap between the emission spectrum of the donor and the excitation spectrum of the acceptor. 2) The spatial distance between the donor and acceptor fluorophores must be short enough for energy transfer to occur. Loss of FRET, however, can also be used as a readout to indicate an increase in distance upon a certain stimulus (*e.g.*, protein unfolding).

FRET can be measured in different ways; this dissertation employs emission spectra and lifetime measurements. Both of which are exemplified in Fig. 1.7b and 1.7c, respectively. In the case of

spectral measurements, positive FRET is identified by the presence of two bands (one for each fluorophore) when only the donor is excited. An increase in FRET indicates a shortening in the spatial distance between the donor and acceptor. This is observed by a decrease in the fluorescence intensity of the donor band and a concomitant increase in the intensity of the acceptor peak. While the opposite trend would indicate a loss of FRET caused by an increase in distance between both probes. These spectral changes can be used to study the refolding of proteins such as those seen for Bcl-xL in Chapter 4 and 5.

1.6.3 Fluorescence spectroscopy: Depth-dependent quenching

NBD/Trp measurements experiments provide an indication of the membrane interacting regions. They, however, provide limited information on the location of the fluorophore's location in the bilayer. Depth-dependent quenching solves this predicament by using membranes with quenchers at known depths in the membrane (Fig. 1.8a, b) which yield a quenching distribution profile obtained through gaussian fitting of the data. These distributions can be observed in Fig 1.8c for NBD quenching data collected by steady-state (Fig. 1.8c. blue) and lifetime fluorescence (Fig. 1.8c, green) for a residue located 13 Å (L350 in the helix 9 of diphtheria toxin translocation domain [57]) away from the center of the bilayer.

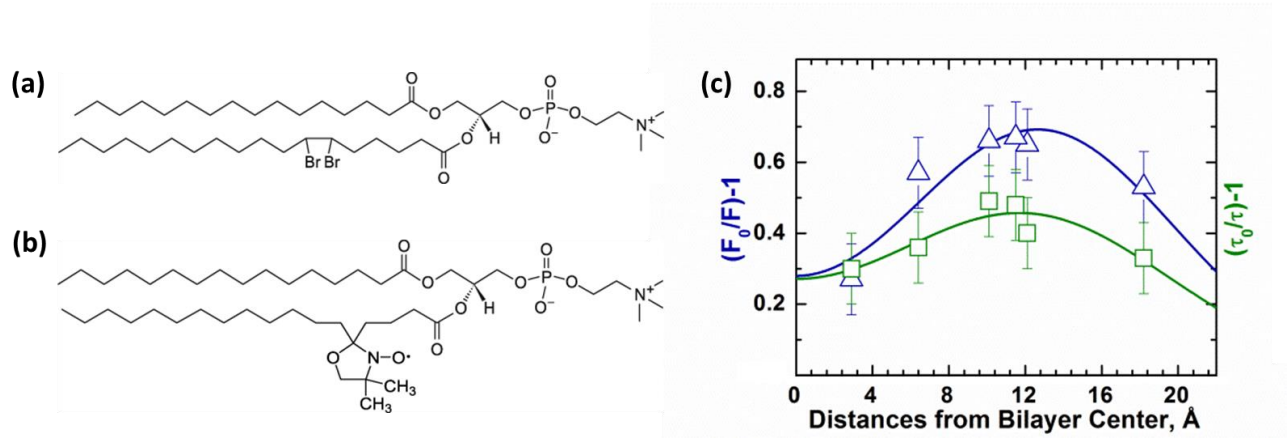

FIGURE 1.8. Quenching lipids and depth-dependent quenching profiles

(a, b) Different quenching lipids are available depending on the fluorophore used. Bromolipids are used for Trp quenching and spin-lipids (doxyl and TEMPO) for NBD quenching (a) Phosphocholine lipid labeled at carbons 6-7, other labeling sites include 9-10, and 11-12. (b) Phospholipid labeled with a doxyl quenching moiety at carbon 5, other labeling sites include 5, 7, 10, 12, 14, 16. Additionally, TEMPO labeled lipids possess a NBD quenching group at the headgroup region. (c) Quenching data of NBD labeled diphtheria toxin translocation domain L350C obtained through steady state (blue) and lifetime (green). The data is plotted as the ratio in fluorescence intensity (or lifetime) in the presence or absence of quencher), fitted to a double gaussian distribution. The data in panel c was adapted from Kyrychenko et al., J. Membr. Biol. (2018)

One of the applications of depth-dependent quenching is to determine the orientation of helices in membrane associated proteins. This is performed by labeling different neighboring residues in a putative helix and determining their quenching profile. A transmembrane helix for example, is expected to have the residues in the middle of the helix close to the center of the bilayer, while the ends remain at the interface. An interfacial helix on the other hand has all its residues away from the center of the bilayer. Depth-dependent quenching results are also complimentary with other quenching techniques such as electron paramagnetic resonance (EPR) O_2/NiEDDA quenching. This technique relies on the poor membrane accessibility of NiEDDA compared to O_2 to determine the number of water accessible residues. An interfacial helix for example, has half its residues exposed to water, while the other half is protected by the bilayer; while a transmembrane helix only has its terminal residues exposed to water. Both of these techniques are used in Chapter 5 to determine the topology of Bcl-xL helix α6.

1.6.4 Circular dichroism

Circular dichroism (CD) provides low-resolution information about the conformation of the peptide or protein under study. Two distinct patterns are important for the systems employed in this dissertation (Fig. 1.9). Unstructured sequences like the soluble and interfacial forms of pHLIP present a CD spectrum with a single minimum around 200 nm (Fig. 1.9a, black and blue), while conformations like transmembrane pHLIP present a CD spectrum with a double minimum at 209 and 222 nm (Fig. 1.9a, red).

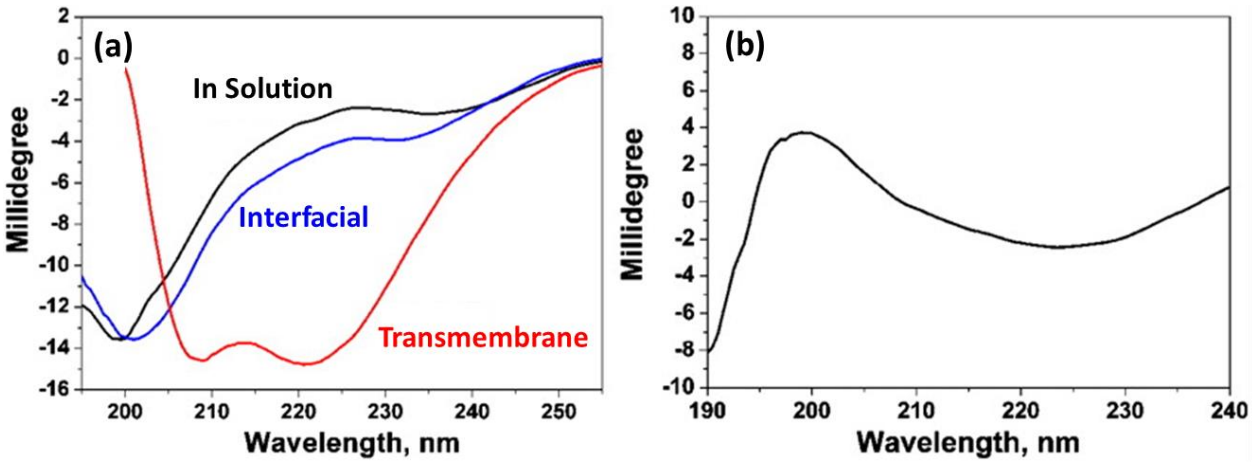

FIGURE 1.9. Circular dichroism and oriented circular dichroism spectra of pHLIP

(a) Circular dichroism provides information about a peptide or protein's secondary structure. An unstructured conformation is characterized by a single minimum at ~ 200 nm. This is shown in black and blue for the soluble and interfacial forms of pHLIP respectively. An α-helical conformation like the transmembrane form of pHLIP (red) has a double minimum at 209 and 222 nm. (b) Oriented circular dichroism is used to determine the orientation of helical peptides in membranes. Transmembrane peptides have a single minimum at ~ 228 nm, while interfacial peptides have a double minimum at ~ 205 and 222 nm. This figure was adapted from Karabadzhak et al., PNAS (2009)

The traditional CD setup measures the conformation of the peptides or proteins in the sample present in solution. A common approach in the membrane active peptide field employs a modified approach called oriented circular dichroism (OCD), which uses peptides immobilized in membranes. This technique takes advantage of the different way in which polarized light interacts with peptides aligned perpendicularly to the incident beam compared to those aligned in a

horizontal orientation. This leads to two distinct spectra for transmembrane α-helices, which are characterized by a single minimum at ~ 228 nm (Fig. 1.9b) and interfacial helices which have a double minimum at ~ 205 and 222 nm. OCD is therefore a convenient way to determine if a peptide is able to adopt an α-helical transmembrane orientation.

The main disadvantages of OCD, however, are that it is limited to helical conformations and that it can only be reliably applied to peptides. Additionally, the incident beam does not pass through enough peptides in a single bilayer to obtain a measurable signal. A stack of lipid bilayers has to therefore be created to increase the amount of peptide in the beam path. CD and OCD are employed in Chapters 2, 3, and 5 to measure the conformation of pHLIP and Bcl-xL under different conditions.

Each chapter in this dissertation also includes a methods section detailing the experimental design and techniques employed for each respective chapter.

Chapter 2: Comparison of Membrane Insertion of pHLIP and its pHLIP-P20G Variant

This chapter has been previously published as Vasquez-Montes, V., Gerhart, J., King, K. E., Thevenin, D., & Ladokhin, A. S. (2018). Comparison of lipid-dependent bilayer insertion of pHLIP and its P20G variant. Biochim Biophys Acta, 1860(2), 534-543. doi:10.1016/j.bbamem.2017.11.006. It is reprinted here with permission in whole without any adaptations since the original publication.

2.1 ABSTRACT

The ability of the pH-Low Insertion Peptide (pHLIP) to insert into lipid membranes in a transbilayer conformation makes it an important tool for targeting acidic diseased tissues. pHLIP can also serve as a model template for thermodynamic studies of membrane insertion. We use intrinsic fluorescence and circular dichroism spectroscopy to examine the effect of replacing pHLIP's central proline on the pH-triggered lipid-dependent conformational switching of the peptide. We find that the P20G variant (pHLIP-P20G) has a higher helical propensity than the native pHLIP (pHLIP-WT), in both water:organic solvent mixtures and in the presence of lipid bilayers. Spectral shifts of tryptophan fluorescence reveal that with both pHLIP-WT and pHLIP-P20G, the deeply penetrating interfacial form (traditionally called State II) is populated only in pure phosphocholine bilayers. The presence of either anionic lipids or phosphatidylethanolamine leads to a much shallower penetration of the peptide (referred to here as State II^S, for "shallow"). This novel state can be differentiated from soluble state by a reduction in accessibility of tryptophans to acrylamide and by FRET to vesicles doped with Dansyl-PE, but not by a spectral shift in fluorescence emission. FRET experiments indicate free energies for interfacial partitioning range from 6.2 to 6.8 kcal/mol and are marginally more favorable for pHLIP-P20G. The effective pKa for the insertion of both peptides depends on the lipid composition, but is always higher for pHLIP-P20G than for pHLIP-WT by approximately one pH unit, which corresponds to a difference of 1.3 kcal/mol in free energy of protonation favoring insertion of pHLIP-P20G.

2.2 INTRODUCTION

The discovery of pHLIP (pH-Low Insertion Peptide) is a compelling example of how a basic-science study can be translated into a very useful and practical biomedical tool. While originally designed from the sequence of the C-helix of bacteriorhodopsin to study membrane protein folding [44], pHLIP is currently and most often used for imaging tumors and other acidic diseased tissues [38-40, 58-62], as well as for targeted drug delivery [63-66]. The underlying mechanism of pHLIP's pH-dependent action is associated with the protonation of Asp residues, allowing for membrane insertion at acidic pH [67-69]. Many other mechanistic and thermodynamic aspects of membrane interactions of pHLIP, however, remain the subjects of active studies.

Traditionally, membrane interactions of pHLIP are described in the context of the following three states, which were originally identified for partitioning into phosphatidylcholine (PC) bilayers [70]: unfolded and soluble state in water at neutral pH (State I), unfolded interfacial state at neutral pH (State II), and a transmembrane α-helical state at low pH (State III). Each of the states has a defined spectroscopic signature associated with the amount of secondary structure (measured by circular dichroism) and membrane penetration (blue shift of Trp fluorescence spectrum relative to that of the solution State I). In our previous study we challenged this view for bilayers of mixed lipid composition by demonstrating that the spectroscopic signature of the interfacial State II is only observed in pure PC bilayers [71].

A surprising feature of pHLIP is the apparent lack of folding upon interfacial penetration, which sets it apart from numerous membrane active peptides that undergo a partitioning-folding coupling [72-74]. To examine the effects of helical propensity on membrane interactions of pHLIP, we examine here the folding and membrane interactions of the native peptide (referred to here as the wild type, pHLIP-WT) and those of the P20G variant (pHLIP-P20G), lacking the helix-breaking

proline in the middle of the hydrophobic stretch. Both pHLIP-WT and pHLIP-P20G have been previously used by Engelman and co-workers [68] to investigate the effect of acyl chain-length on membrane insertion in the context of phosphatidylcholine membranes. They have demonstrated that both membrane thickness and fluidity modulate pHLIP membrane insertion and that Pro20-to-Gly replacement resulted in a more favorable membrane insertion. By examining the pH range from 4.5 to 8, the authors concluded that the insertion pKa for pHLIP-P20G is less acidic than that of the pHLIP-WT, with the difference ranging from 0.1 to 1.0 pH units, for 22 and 14 carbon lipids, respectively. Here, we reexamine the pH-titration of both peptides into both pure POPC bilayers and bilayers containing 25% POPE or 25% POPS in POPC matrix. We find that a wider range of pH (4.5-10) is necessary to accurately characterize the insertion and that the difference for the insertion of the two peptides may be larger than reported. Our results indicate that, in all three lipid compositions, the difference is approximately 1 unit of pH and that, consistent with our previous report [71], lipid headgroups modulate the insertion of pHLIP. We introduce a revised version of the insertion scheme, which contains an alternative interfacial State II^S, to indicate a more "shallow" bilayer penetration as compared to traditional interfacial State II.

2.3 MATERIALS AND METHODS

2.3.1 Materials and Lipid Abbreviations.

N-Hydroxybenzotriazole (HOBt), o-benzotriazol-N, N, N, N', N'-tetramethyluronium hexafluorophosphate (HBTU), and all N-fluorenyl-9-methoxycarbonyl (Fmoc) protected L-amino acids were purchased from GL Biochem Ltd. H-Rink Amide-ChemMatrix solid support resin was purchased from PCAS BioMatrix Inc. Diisopropylehtylamine (DIEA), piperazine, N, N-dimethylformamide (DMF), dichloromethane (DCM) and trifluoroacetic acid (TFA) were from Thermo Fisher Scientific Inc. All lipids were purchased from Avanti Polar Lipids (Alabaster, AL). 1-palmitoyl-2-oleoyl-sn-glycero- 3-phospholcholine (POPC), 1-palmitoyl-2-oleoyl-sn-glycero-3-phosphoethanolamine (POPE), 1- palmitoyl-2-oleoyl-sn-glycero-3-phosphoserine (POPS).

2.3.2 Peptide Synthesis.

pHLIP-WT (H_2N-AAEQNPIYWARYADWLFTTPLLLLDLALLVDADEGG-$CONH_2$) and pHLIP-P20G (H_2N-AAEQNPIYWARYADWLFTTGLLLLDLALLVDADEGG-$CONH_2$) were prepared by Fmoc solid-phase synthesis as described previously [63-66], using H-Rink Amide-ChemMatrix resin affording an amidated C-terminus and purified *via* reverse-phase high performance liquid chromatography (RP-HPLC) (Phenomenex Luna prep 10 µ 250 x 21.20 mm C8; flow rate 10mL/min; phase A: water 0.1% trifluoroacetic acid (TFA); phase B: acetonitrile 0.1% TFA; gradient 60 min from 95/5 A/B to 0/pure A/B). The purity of the peptides was determined by RP-HPLC (Agilent Zorbax Eclipse 5 µm 4.6 x 50 mm XDB-C8; flow rate 1 mL/min; phase A: water 0.01% TFA; phase B: acetonitrile 0.01% TFA; gradient 45 min from 95/5 A/B to 0/pure A/B) and their identity was confirmed *via* matrix-assisted laser desorption ionization time of flight (MALDI-TOF) mass spectrometry.

2.3.3 Preparation of lipid vesicles.

Large Unilamellar Vesicles (LUV) were prepared by drying the required volume of chloroform lipid stocks under a nitrogen stream before overnight drying using high vacuum. Dried lipid films were re-suspended in 50 mM phosphate buffer (pH 8) to a final concentration of 20 mM and vortexed. For FRET measurements, 2% of Dansyl-PE (1,2-dioleoyl-***sn***-glycero-3-phosphoethanolamine-N-(5-dimethylamino-1-naphthalenesulfonyl) was incorporated into lipid mixture. LUV were formed by extrusion using a Mini-Extruder (Avanti Polar Lipids, Alabaster, AL) through nucleopore polycarbonate membranes of 0.1 μm pore size (Whatman, Philadelphia, *PA)* [75, 76]. LUV stocks were stored at -4 ^{o}C in 50mM phosphate buffer, pH 8.

2.3.4 Sample preparation.

2 μM of pHLIP were mixed and incubated with 1-2 mM LUV stock in 10 mM phosphate, pH 8 or 10 mM borate buffer, pH 10, resulting in molar lipid to peptide ratios of 500:1. pHLIP membrane binding and insertion were initiated by manual addition of the appropriate aliquots of 0.5 M acetate buffer.

2.3.5 Fluorescence Measurements.

Fluorescence emission was measured using a SPEX Fluorolog FL3-22 steady-state fluorescence spectrometer (Jobin Yvon, Edison, NJ) equipped with double-grating excitation and emission monochromators. The measurements were made in a 2×10 mm cuvette oriented perpendicular to the excitation beam and maintained at 25 °C using a Peltier device from Quantum Northwest (Spokane, WA). For tryptophan fluorescence measurements, the excitation wavelength was 285 nm and the slits were 4 and 6 nm for emission and excitation, respectively. For acrylamide quenching, 295 nm excitation was used to reduce inner filter effects and 3 nm slits. The appropriate

background spectra were subtracted in all cases. Spectral analysis was carried out using Origin 8.5 (OriginLab, MA).

2.3.6 Membrane partitioning.

Membrane partitioning was measured by fluorescence titration of peptides with LUV containing 2% Dansyl-PE as acceptors. Interfacial partitioning is indicated by a decrease in the intensity of the donor Trp peak as it associates with the interface as a function of LUV concentration (Fig. A4). Results are plotted as the relative decrease in Trp intensity, I, versus lipid concentration, [L], and fitted as described previously using the following equation [77]:

$$I = 1 + (I_{\infty} - 1)\left(\frac{K_x \cdot [L]}{[W] + (K_x \cdot [L])}\right), \text{(Eq. 2.1)}$$

where I_{∞} denotes the relative intensity at infinite lipid saturation, [W] is the concentration of water (55.3 M) and K_x represents the mole fraction partitioning coefficient [78]:

$$K_x = \frac{[P_{bil}]/[L]}{[P_{water}]/[W]}, \text{(Eq. 2.2)}$$

where $[P_{bil}]$ and $[P_{water}]$ corresponds to the bulk concentrations of peptide in the bilayer and in water respectively. The calculated partitioning constant (K_x) was used to determine the free energy of interfacial partitioning (ΔG_{IF}) using the following formula:

$$\Delta G_{IF} = -RT \cdot \ln(K_x), \text{(Eq. 2.3)}$$

Where R is the gas constant (1.985×10^{-3} kcal K^{-1} mol^{-1}) and T is the experimental temperature in Kelvin (298 K). Errors in the fits were determined by support plane analysis [79] and are indicated in brackets (Fig. A5-6).

Analysis of the pH-dependent membrane insertion. The spectral data were fitted by applying nonlinear least-square analysis with the following equation [80]:

$$\lambda = \frac{\lambda_N + \lambda_L \cdot 10^{m(pK_a - pH)}}{1 + 10^{m(pK_a - pH)}}, \text{ (Eq. 2.4)}$$

Where λ_N and λ_L are the limiting values of fluorescence maximum at neutral and low pH, respectively; pK_a is an apparent constant and *m* is a transition slope. Errors in the fits were determined by support plane analysis and are indicated in brackets. The protonation-dependent free energy of transmembrane (TM) insertion, ΔG_{TM}^{H+}, was calculated using the following formula:

$$\Delta G_{TM}^{H+} = -2.3RT \cdot pK_a, \text{ (Eq. 2.5)}$$

Where R is the gas constant (1.985×10^{-3} kcal K^{-1} mol^{-1}) and T is the experimental temperature in Kelvin (298 K).

CD experiments. CD measurements were performed using an upgraded Jasco-720 spectropolarimeter (Japan Spectroscopic Company, Tokyo). Normally 60-80 scans were recorded using a 1-mm optical path cuvette. All CD spectra were corrected for background.

Percent helical folding was calculated assuming ellipticity at 222 nm corresponds only to α-helical content following the methodology proposed by Chen et al [81]:

$$\%\ \text{helical content} = \frac{[\theta]_{222}}{[\theta]_{222}^{Max}\left(1 - \frac{k}{n}\right)}, in\ \text{deg} \cdot cm^2 \cdot dmol^{-1}, \text{ (Eq. 2.6)}$$

Where $[\theta]_{222}$ is the observed ellipticity at 222 nm, $[\theta]_{222}^{\mathrm{Max}}$ is the theoretical mean residue ellipticity for an infinitely long helical peptide (-39,500 deg cm^2 $dmol^{-1}$), n is the number of residues (36 in pHLIP), and k is a wavelength dependent constant (2.57 at 222 nm) [81].

Table 2.1. pHLIP Sequences.

Both pHLIP sequences used in this study are composed of 36 amino acids total, including six anionic residues (blue). The pHLIP-P20G variant contains a Gly substitution at position Pro20 (red); located in the middle of the transmembrane region of the peptide.

Peptide	Sequence
pHLIP-WT	AAEQNPIYWARYADWLFTTPLLLLDLALLVDADEGG
pHLIP-P20G	AAEQNPIYWARYADWLFTTGLLLLDLALLVDADEGG

2.4 RESULTS

2.4.1 Folding of pHLIP-WT and pHLIP-P20G in TFE.

In solution, pHLIP exists as a soluble and unstructured peptide; capable of inserting into lipid bilayers as a transmembrane α-helix under mildly acidic conditions. The unstructured conformation of pHLIP in solution is maintained by electrostatic repulsion between six anionic residues throughout its sequence and two proline residues (Table 2.1). Several studies have shown the importance of the anionic residues on the transmembrane transition of the peptide, but little attention has been paid to the prolines. Pro20, in particular, is in the middle of the region that transitions into a transmembrane helix. To better understand the role of Pro20 on the transition of pHLIP to a transmembrane helix, we studied the folding of both pHLIP-WT and pHLIP-P20G in 2,2,2-trifluoroethanol (TFE). This organic solvent is known to induce α-helical folding of unstructured peptides [82, 83], presumably by disrupting hydrogen bonding with water, while stabilizing intramolecular hydrogen bonding [84]. As such, TFE has been traditionally used to study the α-helical folding of disordered peptides in solution and also as a simplest mimetic for thermodynamic studies of folding of membrane-active peptides [73, 85].

TFE-induced conformational changes of both pHLIP-WT and P20G were assessed by circular dichroism spectroscopy (CD). This technique allows for a simple readout of the folding transition, as it provides characteristic spectra for both unstructured and α-helical conformations. In aqueous solution (0 M TFE), pHLIP-WT showed a characteristic spectrum for an unstructured State I peptide, with a single minimum at 200 nm (Fig. 2.1a). Meanwhile, a spectrum with a double minimum around 208 and 222 nm, characteristic of α-helices, is obtained by substituting Pro20 for Gly. The measured molar ellipticity at 222 nm can be used to estimate the helical content of peptides as described by Chen et al. [81]. Using this method, we calculated the helical content to

be 12% and 21% for pHLIP-WT and pHLIP-P20G in solution, respectively. In peptides of 36 amino acid residues in length, this amounts to only 4 and 7 folded residues in pHLIP-WT and pHLIP-P20G, respectively (Table 2.2). Maximum peptide helical content can be achieved by placing them in pure organic solvent, 14 M TFE. As expected, while both pHLIP variants showed α-helical spectra in TFE (Fig. 2.1a), pHLIP-WT is shown to remain more unstructured, with an estimated 36% helicity (13 folded residues) as opposed to 47% for pHLIP-P20G (17 folded residues).

The folding transition of both pHLIP-WT and P20G was studied in more detail by measuring their CD at increasing TFE:water ratios and plotting the ellipticity at 222 nm vs [TFE] (Fig. 2.1b). This analysis revealed a large difference in the folding behavior of both pHLIP variants. As TFE concentration increases, pHLIP-P20G folds into an α-helical structure in a single sigmoidal transition, achieving maximum ellipticity at 9 M TFE (47% helicity, 17 folded residues). In contrast, pHLIP-WT exhibits two transitions: first reaching a plateau between 5-10 M TFE (27% helicity, 10 residues in helical conformation). A second transition begins above 10 M TFE and does not reach completion even in pure TFE. These results show that Pro20 is not only important in determining the maximum helical content that pHLIP can achieve, but also modulates its folding behavior in hydrophobic environments. The sequential folding observed with pHLIP-WT upon increase in TFE concentration suggests that Pro20 is breaking the helix into two independently folding segments with different helical propensities.

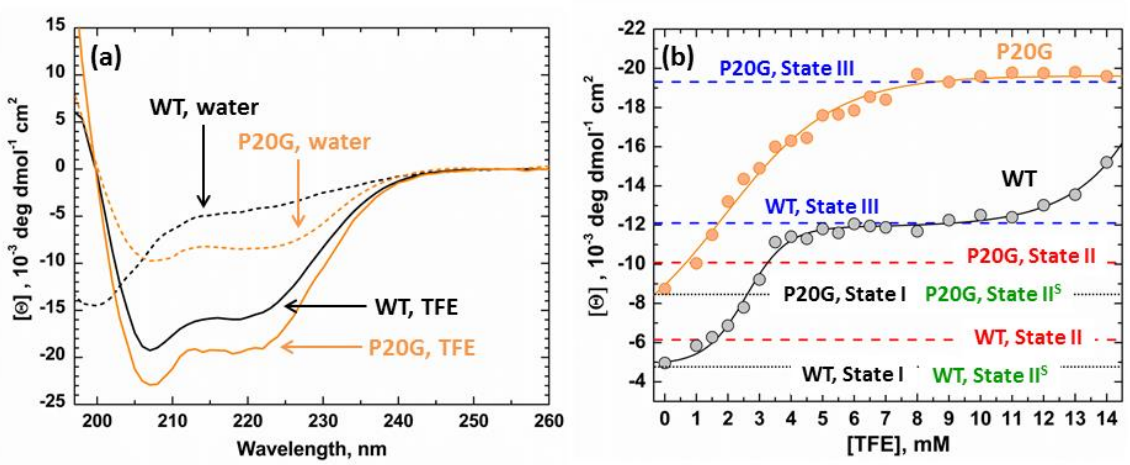

FIGURE 2.1. Folding of pHLIP in TFE.

(a) Circular Dichroism spectroscopy was used to characterize the folding of pHLIP-WT (grey) and pHLIP-P20G (orange) as a function of TFE concentration. In water, both peptides start in their relatively unstructured State I (dashed lines) and transition to α-helices in higher TFE concentration (solid lines). (b) Measured molar ellipticity at 222 nm, an indication of helical content, was plotted against experimental [TFE]. As TFE concentration increases, pHLIP-P20G achieves maximum ellipticity at 9 M TFE with a sigmoidal transition. Under the same conditions pHLIP-WT undergoes a double transition with an initial plateau between 4-9 M TFE. A second transition starts after 9 M TFE and never achieves the second plateau, indicating that maximum ellipticity is not obtained. In membranes, the average ellipticity of the inserted transmembrane State III, under acidic conditions, of both peptides matched the observed plateaus in TFE (blue lines). Only a small increase in ellipticity was observed in pure POPC for each peptide State II at pH 10 (red lines). This indicates the lack of a folded interfacial form even after the P20G substitution. No change in ellipticity was observed for either peptide in non-pure POPC membranes at pH 10 (Fig. A1-3) in their respective State II^S (green lines). The black line indicates the starting ellipticity for each peptide in aqueous environment (State I).

2.4.2 Folding of pHLIPs in lipid bilayer.

In membranes composed purely of POPC, pHLIP-WT has been shown to form an interfacial and unstructured State II [44]. This state is characterized by a blue shift in Trp emission spectra at pH 8 from 357 nm in solution to 354 nm in the membrane interface, indicative of membrane association (Fig. A1a). This spectral change is also accompanied by a slight increase in secondary structure, measured by CD (Fig. A1b; ellipticity at 222 nm) [44]. In a previous study, however, we demonstrated extensively that this interfacial State II is not identifiable by either technique in any membrane composition tested other than pure POPC [71]. Even the presence of only 10% of a different phospholipid (*i.e.*, phosphatidylserine, phosphatidylglycerol, phosphatidic acid,

phosphatidylethanolamine and others) or cholesterol eliminated these spectral differences [71], traditionally used as the hallmarks of pHLIP's interfacial State II.

Table 2.2. Helical content of pHLIP variants in LUV.

Circular Dichroism was used to measure the conformation of both pHLIP-WT and P20G in increasing TFE concentrations (Fig. A1-3). Helical fractions (f_α) were calculated using estimates of maximum helicity discussed by Chen et al. [81] and described in the methods section (Eq. 2.6). Number of folded residues (n_α) was determined using a 36-residue total for both peptides. *Number of folded residues adjusted by the fraction of peptide bound to POPC membranes, based on FRET binding data (Fig. 2.3)

Sample		State	pHLIP-WT		State	pHLIP-P20G	
			f_α	n_α		f_α	n_α
Water	pH 10	I	12	4	I	21	7
pure POPC	pH 10	II	14	5 (6)*	II	23	8
	pH 8	II	14	5	II-III	26	9
	pH 4	III	26	10	III	48	17
25POPE:75POPC	pH 10	II^S	12	4	II^S	18	7
	pH 8	II^S	12	4	II^S-III	24	9
	pH 4	III	27	10	III	48	17
25POPS:75POPC	pH 10	II^S	12	4	II^S	18	7
	pH 8	II^S	12	4	II^S-III	21	7
	pH 4	III	27	10	III	45	16

Interfacial membrane partitioning of unstructured peptides often results in gain in secondary structure due to partitioning-folding coupling, driven by a relatively high gain in per-residue folding free energy [72, 74]. Therefore, the lack of helix formation in pHLIP during its interfacial partitioning to State II is rather unusual. To better understand the contribution of Pro20 in the peptide's folding, we compared conformational changes of pHLIP-WT and pHLIP-P20G upon

membrane addition by using CD and Trp fluorescence spectroscopy. These experiments were conducted on membranes composed either purely of POPC or containing 25 molar percent POPS or POPE in POPC matrix.

We first measured conformational changes in both pHLIP variants under conditions known to induce formation of the interfacial State II in pHLIP-WT, namely the addition of LUV containing only POPC at pH 8. It resulted in characteristic blue shifts to its Trp spectra (357 nm to 354 nm; Fig. A1a) and small changes to its CD spectra, indicative of membrane interaction and a small gain of secondary structure (Fig. A1b, red vs black spectra). Under the same conditions (*i.e.*, POPC LUV at pH 8), pHLIP-P20G exhibited a more pronounced change in emission blue shift (354 nm to 348 nm) and an increase in secondary structure (Fig. A1d). The larger changes in the Trp and CD spectra observed for pHLIP-P20G in POPC at pH 8 are consistent with previous reports [68], which concluded that State II for this mutant has a very high helical content. The alternative explanation would be that the pH-dependent transition from States II-to-III in pHLIP-P20G is shifted. Our data presented in the next section confirm that this is indeed the case (Fig. 2.4 and C9). Therefore, the standard condition for State II for pHLIP-P20G is not pH 8, as it is for the WT-pHLIP, but pH 10. (Fig. A1d red vs green spectra and Fig. 2.4). For this reason, all further measurements discussed in this report involving the State II were performed at pH 10.

Under acidic conditions in the presence of membranes the CD spectra of both pHLIP-WT (blue spectra in Fig. A1b, A2b, and A3b) and pHLIP-P20G (blue spectra in Fig. A1d, A2d, and A3d) contain a double minimum, characteristic of α-helices. Both peptides show conformational differences between lipid compositions consistent with our previous report [71], however, they are more pronounced in the pHLIP-P20G variant. Under these conditions pHLIP-P20G shows a spectral disruption below 210 nm that could be attributed to different absorbance artifacts. One of

these possibilities is that the discrepancies in the CD spectra of pHLIP-P20G are a result of differences in the uniformity of its distribution in the LUV population compared to pHLIP-WT. This would result in some vesicles with very high peptide to lipid ratio, leaving others with very low peptide content and lead to absorbance flattening. Discrepancies between the CD spectra of the transmembrane State III of different pHLIP variants are a phenomenon that has been observed in different studies and the reason behind it remains unclear [62, 67].

We have followed the example of the Engelman group [62, 67] and used the ellipticity measured at 222 nm to analyze the spectra of both pHLIP variants in the presence of membranes and compared it to their folding in TFE (Fig. 2.1b). The previously mentioned artifact is only observed for the State III of pHLIP-P20G and will affect its 208 nm band. This artifact, however, is not present in any other spectra measured and will therefore not affect their analysis. As for the particular case of the State III of pHLIP-P20G, this artifact will introduce a degree of uncertainty, which will be reduced by focusing on the 222 nm band.

We mapped the observed ellipticities for the different states of both peptides in the presence of membranes to their corresponding folding in TFE (Fig 3.1b, black vs red dashed lines). Substituting Pro20 for Gly in pHLIP allowed for higher overall interfacial folding on pure POPC bilayers (23% folded helix, 8 folded residues) compared to pHLIP-WT (14% folded helix, 6 folded residues). Spectroscopic measurements in the presence of 25POPS:75POPC and 25POPE:75POPC LUV showed no change in folding or position of Trp emission as compared to the solution State I (Fig. A2a-d, A3a-d). This absence of the expected spectroscopic signature for State II in both peptides in the presence of membranes of mixed lipid compositions is consistent with our previous pHLIP-WT results [71], and suggests that it could be a general property of the entire pHLIP family. The observed lack of a measurable blue shift in the Trp emission spectra or

increase in secondary structure upon addition of LUV with mixed lipid composition at neutral to basic pH can be explained by two different possibilities: (a) pHLIP is not partitioning to these bilayers at neutral to slightly basic pH or (b) pHLIP does interact with the membrane interface but does not penetrate deep enough to cause changes in folding or to alter the environment of Trp residues. To resolve these two possibilities, we performed fluorescence quenching and Förster Resonance Energy Transfer (FRET) experiments described in subsequent sections.

The ellipticities of both peptides at 222 nm in the presence of membranes at low pH, State III, were also compared to their helical folding in TFE (Fig. 2.1b blue dashed lines). The ellipticities calculated for both pHLIP-WT and P20G matched their respective plateaus observed in TFE. In the case of pHLIP-WT this amounts to an average ellipticity of 26% (10 folded residues); while an average higher helical content of 46% percent (17 folded residues) was observed for pHLIP-P20G

2.4.3 Fluorescence quenching with acrylamide (Identification of a new interfacial state).

Acrylamide quenching measurements were performed under conditions that allow for the formation of the interfacial State II in both pHLIP-WT and P20G and compared to their quenching in solution.

In solution, the addition of the soluble quencher acrylamide interacts with the two Trp in pHLIP and reduces the observed intensity. The interaction of pHLIP with membrane interfaces, however, provides protection from acrylamide quenching, reducing its effect. Quenching constants, K_{SV}, are obtained from the slope of intensity measurements in the absence/presence of quencher versus acrylamide concentration (Fig. 2.2), with higher values indicating more effective quenching. Measurements of both peptides in solution showed very similar quenching constants. We attribute the small difference between the 15.5 ± 0.1 M^{-1} K_{SV} of pHLIP-WT and 14.4 ± 0.2 M^{-1} of pHLIP-

P20G to the slightly higher protection from the higher secondary structure content of the latter (Fig. 2.2). The addition of LUV containing only POPC at pH 10 greatly reduce the measured K_{SV} of both pHLIP-WT (K_{SV} = 3.7 ± 0.1 M^{-1}) and pHLIP-P20G (K_{SV} = 3.1 ± 0.1 M^{-1}) compared to solution (Fig. 2.2). The decrease in quenching constants observed after the addition of pure POPC LUV indicates that both pHLIP-WT and pHLIP-P20G partition to these interfaces, which is consistent with State II formation.

Acrylamide quenching measurements for both pHLIP variants in the presence of membranes containing either 25POPE:75POPC or 25POPS:75POPC at pH 10 also showed a decrease in their respective K_{SV} compared to solution (Fig. 2.2). The observed reduction in quenching under these conditions, suggest that pHLIP is in fact partitioning to the membranes, despite being spectroscopically silent. The K_{SV} measured for pHLIP-WT in LUV with mixed lipid compositions (7.2 ± 0.2 M^{-1} for 25POPE:75POPC and 6.1 ± 0.4 M^{-1} for 25POPS:75POPC) were higher than the one seen in POPC (3.7 ± 0.1 M^{-1}), indicating lower protection from the membrane consistent with a more shallower interfacial location. Similarly, quenching measurements with pHLIP-P20G showed increased K_{SV} values in 25POPE:75POPC (9.8 ± 0.3 M^{-1}) and 25POPS:75POPC (9.5 ± 0.2 M^{-1}) compared to pure POPC (3.1 ± 0.1 M^{-1}). The presence of two Trp in the pHLIP constructs used in this study, however, do not allow for precise depth determination and prevent parsing out these slight differences. Future experiments using single Trp mutants will be performed to better understand the effect of interfacial properties on the depth of transmembrane pHLIP. Together, the combination of spectroscopic and quenching results indicates that pHLIP interacts with the interfaces of membranes with mixed lipid compositions without the partial folding or deeper penetration of Trp residues, characteristic of its State II in LUV containing only phosphatidylcholine. These results confirm our previous observation that the traditionally defined

interfacial State II is observed only in pure PC bilayers [71]. In all mixed lipid bilayers both pHLIP-WT and pHLIP-P20G are populating a novel State II^S (for 'shallow' State II). This state is distinguished from State II by the lack of spectral shift of fluorescence and by lack of additional folding; and from State I by the reduction in acrylamide quenching.

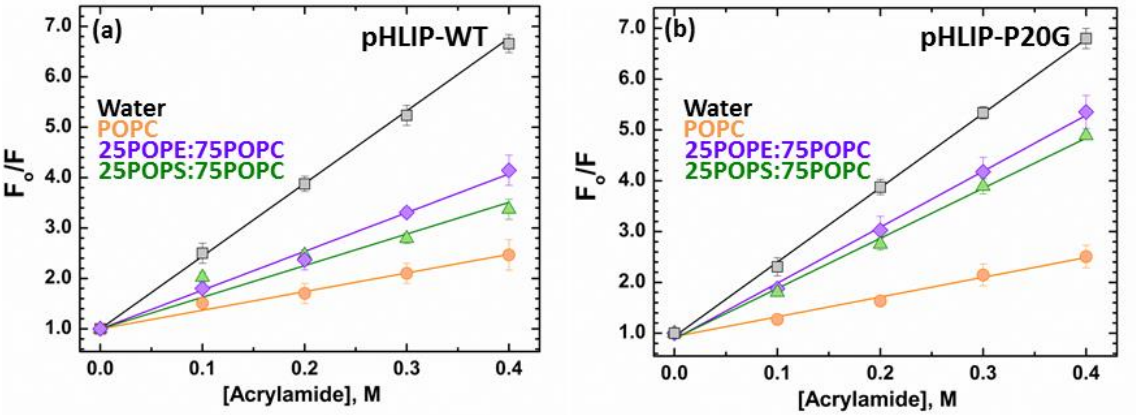

FIGURE 2.2. Stern-Volmer plots for acrylamide quenching of tryptophan fluorescence of pHLIP-WT (a) and pHLIP-P20G (b) measured at pH 10 in the absence and presence of membranes.

Stern-Volmer constants (K_{SV}) were obtained from the slope of the measured intensities in the absence of quencher divided by the intensities in the presence of acrylamide vs quencher concentration. The decrease in K_{SV} observed for both peptides in the presence of membranes compared to solution (Water K_{SV}: pHLIP-WT = 15.1 ± 0.1 M^{-1}, pHLIP-P20G = 14.4 ± 0.2 M^{-1}) indicates their interaction with the membranes. The reduction in K_{SV} is higher for either pHLIP variants in pure POPC membranes (pHLIP-WT K_{SV} = 3.7 ± 0.1 M^{-1}, pHLIP-P20G K_{SV} = 3.1 ± 0.1 M^{-1}) compared to lipids with mixed lipid compositions: 25POPE:75POPC LUV (pHLIP-WT K_{SV} = 7.2 ± 0.2 M^{-1}, pHLIP-P20G K_{SV} = 9.8 ± 0.2 M^{-1}) and 25POPS:75POPC (pHLIP-WT K_{SV} = 6.1 ± 0.4 M^{-1}, pHLIP-P20G K_{SV} = 9.5 ± 0.3 M^{-1}).

2.4.4 Measuring the free energy for interfacial partitioning, ΔG_{IF}.

To confirm the existence of the interfacial State II^S, indirectly inferred from acrylamide experiments described above, we conducted the following membrane-binding experiments. To enhance spectroscopic response to membrane partitioning, we have doped LUV with 2% Dansyl-PE, a lipid labeled at its head group with a fluorophore that can act as a FRET acceptor for Trp fluorescence. As shown in supplemental Fig. A4, addition of such vesicles to pHLIP peptide results in a decrease of tryptophan fluorescence emission, which can be used to quantitate the partitioning. The decrease in pHLIP's fluorescence intensity observed upon titration with Dansyl-PE-doped LUV is plotted in figure 2.3. The data are analyzed by fitting them to a standard

partitioning equation (Eq. 2.1) commonly used in spectroscopic titration measurements [78]. The only distinction from more familiar cases of fluorescence increase upon partitioning (*e.g.*, [77]), is that, in this case, we have fluorescence decrease and consequently the parameter corresponding to the ratio of intensities of completely bound peptide to that for the free peptide in solution is below one, I_∞ <1. In order to explore how the variation in the latter parameter affects the precision of the determination of free energy of interfacial partitioning (ΔG_{IF}), we performed a support-plane analysis [79]; which examines the variation of the goodness of fit (χ^2 in this case) as a function of the value at which I_∞ was fixed during the fit (Fig. A5). We used a cut-off of 1 standard deviation increase in χ^2 over its lowest value to estimate the variation in ΔG_{IF} that are presented in the square brackets after the most probable value of free energy below.

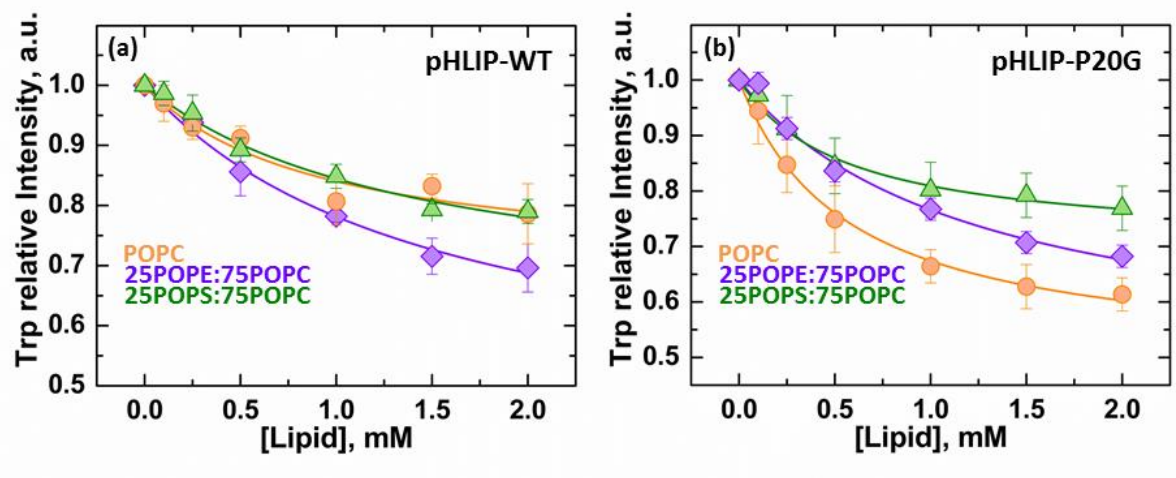

FIGURE 2.3. Membrane partitioning free energy of pHLIP-WT and P20G.

Partitioning of pHLIP to membranes was measured in duplicate by FRET between both Trp in pHLIP (donor) and 2% Dansyl-PE in LUV as acceptors (Fig. A4). The measured data was fit as explained in the methods section, and the interfacial partitioning coefficient (K_x), defined as the [Lipid] required for maximum intensity was used to calculate the partitioning free energy ΔG_{IF}. Data is shown as the relative decrease in intensity of the Trp band as a function of lipid (acceptor) concentration for both pHLIP variants; errors were calculated by support plane analysis and indicated as a range in brackets (Fig. A5-6). (a) pHLIP-WT ΔG_{IF}: POPC = -6.5 [-6.3;-6.7] kcal/mol (I_∞ = 0.7 [0.5;0.8])), 25POPE:75POPC = -6.2 [-6.1; -6.3] kcal/mol (I_∞ = 0.4 [0.1;0.6]), 25POPS:75POPC = -6.3 [-6.1;-6.4] kcal/mol (I_∞ = 0.6 [0.5;0.7]). (b) pHLIP-P20G ΔG_{IF}: POPC = -6.8 [-6.7;-6.9] kcal/mol (I_∞ = 0.5 [0.4;0.5]), 25POPE:75POPC = -6.3 [-6.2;-6.4] kcal/mol (I_∞ = 0.5 [0.4;0.5]), 25POPS:75POPC = -6.8 [-6.8;-6.9] kcal/mol (I_∞ = 0.7 [0.6;0.7]).

The free energy of interfacial partitioning into POPC (State II) was found to be ΔG_{IF} = -6.8 [-6.7;-6.9] kcal/mol for pHLIP-P20G and ΔG_{IF} = -6.5 [-6.3;-6.7] kcal/mol for pHLIP-WT (Fig. 2.3, A5). The latter corresponds well with previously reported value of -6.7 kcal/mol obtained by isothermal titration calorimetry by Reshetnyak et al. [86]. The values of ΔG_{IF} for partitioning to the shallow interfacial State II^S, populated in mixed lipid compositions, were found to be similar to those of State II for both peptides (Fig. 2.3): (a) pHLIP-WT: ΔG_{IF} = -6.3 [-6.1;-6.4] kcal/mol for 25POPS:75POPC and ΔG_{IF} = -6.2 [-6.1;-6.3] kcal/mol for 25POPE:75POPC; (b) pHLIP-P20G: ΔG_{IF} = -6.3 [-6.2;-6.4] kcal/mol for 25POPE:75POPC and ΔG_{IF} = -6.8 [-6.7;-6.9] kcal/mol for 25POPS:75POPC LUV.

2.4.5 pH-dependent insertion into bilayers of various compositions.

Under acidic conditions in the presence of membranes, pHLIP transitions into a transmembrane State III helix, regardless of membrane composition [71]. The transition to this transmembrane state is observed by increase in α-helical content (Fig. A1b and d, blue spectra) and by large blue shifts in Trp emission spectra from 357 to 341 nm, and from 354 to 343 nm, for pHLIP-WT and pHLIP-P20G, respectively (Fig. A1a and c, blue spectra). Under these conditions, CD measurements showed that the average ellipticity observed for both pHLIP variants in their transmembrane forms (Fig. A1-3, blue CD spectra) matched their respective plateaus in TFE (Fig. 2.1b, blue lines). The larger overall helical fraction of the transmembrane State III of pHLIP-P20G compared to that of pHLIP-WT (Table 2.2) indicates that the presence of Pro20 constrains the transmembrane conformation of pHLIP-WT. This difference in helicity of State III between the two peptides is about 6-7 residues and is independent of lipid composition (Table 2.2; pH 4).

The pH-dependent membrane insertion of both pHLIP-WT and pHLIP-P20G was characterized by measuring their Trp emission spectra in membranes containing purely POPC,

25POPE:75POPC or 25POPS:75POPC as a function of pH (Fig. 2.4). The pH range used in these experiments was extended to pH 10 to accommodate the formation of State II in pHLIP-P20G; which is formed under more basic conditions than pHLIP-WT (Fig. A10). The observed pH dependencies of the positions of maxima are fitted (Fig. 2.4a-c), as explained in the Methods section (Eq. 2.4), errors were calculated by support plane analysis and are shown in brackets (Fig. A7-8). Extending the pH range of the titration had no effect on the calculated insertion pK_a of pHLIP-WT in pure POPC, remaining constant at 6.1 [6.0;6.3]. Meanwhile, the protonation-dependent insertion pK_a of pHLIP-P20G increased to 7.2 [7.0;7.4] compared to 6.8 obtained in previous measurements performed using a shorter pH range (pH 8-4) [68]. The previously observed pK_a of 6.8 for pHLIP-P20G in pure POPC by Barrera et al. [68] can still be calculated, if only the pH 4-8 range is considered (Fig. A10). Insertion of pHLIP into LUV containing mixed lipid compositions, which start their transition from the shallower interfacial State II^S, also show more favorable insertion for pHLIP-P20G. This can be appreciated in the 1.1 pH unit difference between the protonation-dependent insertion pK_a of pHLIP-P20G into 25POPE:75POPC (pK_a = 6.7 [6.6;6.9]) compared to pHLIP-WT (pK_a = 5.6 [5.5;5.7]). A similar difference was observed between the insertion pKa of both peptides into 25POPS:75POPC membranes (pHLIP-WT: 5.4 [5.4;5.5], pHLIP-P20G: 6.4 [6.2;6.5]. Our titration measurements clearly show that interfacial properties affect the interaction and insertion of both pHLIP-WT and P20G into membranes. Not only by affecting its starting position (*i.e.*, interfacial state), but also the protonation-dependent pK_a of insertion. Under all membrane compositions tested, pHLIP-P20G showed an average insertion pK_a 1 pH unit higher than those seen for pHLIP-WT (Fig. 2.4a-c).

2.4.6 Confirmation of the spectroscopically silent State II^S by reversed fluorescence shift.

In the absence of membranes, the protonation of anionic residues in acidic environments leads to the aggregation of pHLIP. This process creates a hydrophobic environment around both Trp in the interior of the aggregate. As with membrane insertion, these changes in environment can be detected spectroscopically by measuring the resulting blue shifts in the emission spectra of Trp. In solution, pHLIP-WT and pHLIP-P20G have a pK_a of aggregation of 5.9 [5.9;6.0] (Fig.2.5a) and 6.4 (Fig. A9), respectively. In the case of pHLIP-WT, its pH-dependent aggregation in solution can be compared to its protonation-driven insertion into membranes containing 25POPS:75POPC. In the presence of these LUV, pHLIP-WT has a pK_a of 5.4 [5.4;5.5]; 0.5 pH units lower than the pK_a for its aggregation in solution (Fig. 2.5a).

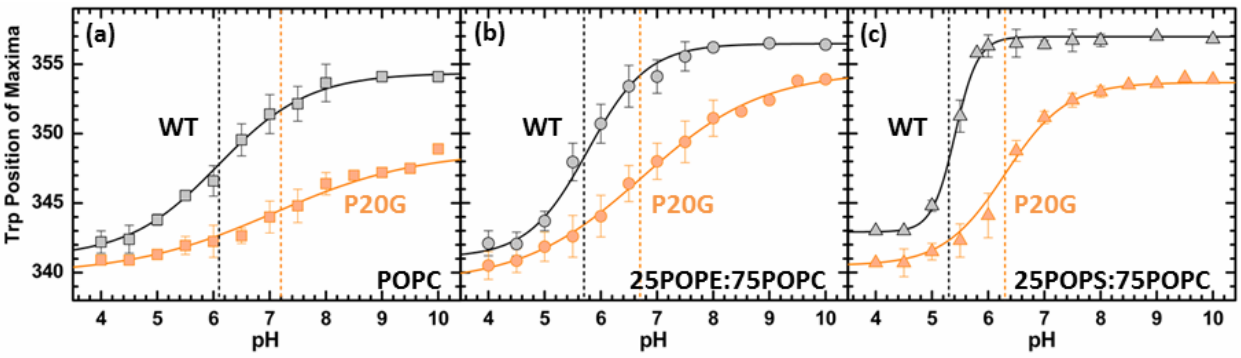

FIGURE 2.4. pH-Dependent membrane insertion of pHLIP-WT (black) and pHLIP-P20G (orange) in pure POPC (a), 25POPE:75POPC (b) and 25POPS:75POPC (c), monitored by Trp fluorescence emission maximum.

Insertion into membranes is indicated by progressive blue shifts, decreases in position of maxima, in the measured Trp emission spectra. Dashed lines indicate the pH-dependent membrane insertion pK_a color coded for each pHLIP variant. The following pK_a values were obtained by fitting the data to Eq. 2.4: (a) In POPC: WT = 6.1 [6.0;6.3] (m = 0.6 [0.5;0.7]) and P20G = 7.2 [7.0;7.4] (m = 0.4 [0.3;0.6]), (b) in 25POPE:75POPC: WT = 5.6 [5.5;5.7] (m = 0.9 [0.7;1.1]) and P20G = 6.7 [6.6;6.9] (m = 0.4 [0.3;0.5]), (c) in 25POPS:75POPC: WT = 5.4 [5.4;5.5] (m = 1.7 [1.5;2.0]) and P20G = 6.4 [6.2;6.5] (m = 0.8 [0.6;1.1]). Decrease Trp position of maxima from State I in solution, WT: 357 nm and P20G: 354 nm, in pure POPC indicates formation of State II. No changes in starting positions of maxima were observed in the pH-titrations of either 25POPE:75POPC or 25POPS:75POPC. All data points in the titrations contain error bars and are represented as the average of 3 measurements. Regardless of membrane composition, the protonation-dependent insertion of pHLIP-P20G is more favorable than that of the pHLIP-WT by 1.3 kcal/mol (equivalent of the 1 pH unit difference in pK_a). Errors in the fit were calculated by support plane analysis for the protonation-dependent insertion pK_a (Fig. A7) and the slope (Fig. A8).

Close to its aggregation pK_a, at pH 5.8, pHLIP-WT is in a partially aggregated state in solution with a 10-nm blue shifted Trp position of maxima of 348 nm compared to 358 nm for its soluble State I (Fig. 2.5b, grey vs black spectra). At the same pH, pHLIP-WT in presence of 25POPS:75POPC LUV shows little to no change in Trp emission spectra from its State I in solution, with a position of maxima of 357 nm (Fig. 2.5a, green line), consistent with our previous report [71]. However, when 25POPS:75POPC LUV are added to partially aggregated pHLIP-WT at pH 5.8, an immediate redshift is observed in the Trp spectra to 356 nm (Fig. 2.5b, red spectra). For the recovery of Trp position of maxima to occur, pHLIP must be interacting with the membrane interface, which in turn causes the dissipation of the aggregates and formation of the interfacially bound state. This redshift of fluorescence provides additional confirmation of the presence of the State II^S identified by fluorescence quenching and FRET measurements.

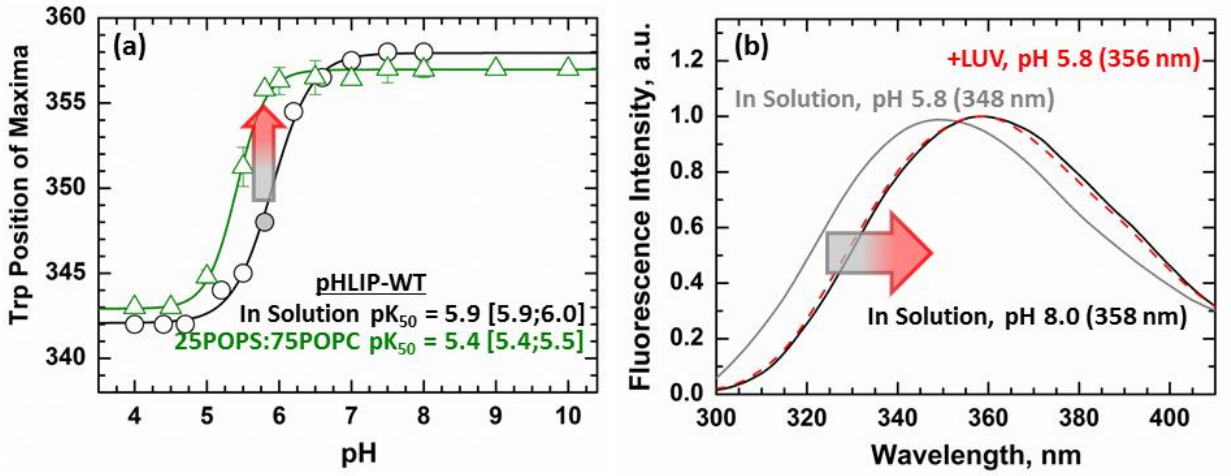

FIGURE 2.5. Interaction with membranes in mixed membrane composition.

(a) Trp emission was used to measure the pH-dependent aggregation of pHLIP-WT in solution (black) and compared to the insertion of pHLIP in 25POPS:75POPC membranes (green). At pH 5.8 pHLIP-WT is in a partially aggregated form (348 nm, grey circle). At that same pH, little to no change is observed for the sample containing a peptide and 25POPS:75POPC LUV mixture (green) (b) The Trp spectra of the partial aggregate shows a large 10 nm blue shift with a position of maxima of 348 nm (grey) compared to 358 nm for the soluble peptide at pH 8 (black). Addition of membranes to this partially aggregated form results in an immediate red shift of the spectra from 348 nm (grey) to 356 nm (red).

The existence of the fluorescence red shift upon peptide binding to membranes is rather exotic and is observed for pHLIP only in a narrow pH window where solution aggregation already occurs, but full membrane insertion into State III has not yet happened. Because this window depends on a fortuitous combination of peptide properties in solution and in the membrane, this phenomenon is most pronounced for pHLIP-P20G in 25POPS:75POPC LUV. When similar measurements were made with pHLIP-WT, the difference between both spectra was found to be too small to be resolved (Fig. A9).

The tendency of pHLIP to aggregate even at moderate ionic strength (*e.g.*, in a 50 mM phosphate buffer) is one of the challenges of using it as a targeted drug carrier [69]. Consequently, the available concentration of active/functioning pHLIP (*i.e.*, available for binding and inserting in membranes) has always been in question. Our results indicate that, despite its tendency to aggregate in solution, pHLIP can disaggregate after binding to bilayer interfaces and become available for productive pH-mediated insertion.

2.5 DISCUSSION

The association and insertion of peptides into membranes is a complex process governed by an intricate interplay of hydrophobic and electrostatic interactions [78]. While substantial progress has been made in understanding the thermodynamics of interfacial partitioning to neutral [33] and charged bilayers [32], and interfacial folding [72, 74], the thermodynamics of transmembrane insertion present a formidable challenge due to solution aggregation of TM sequences [85, 87]. The pHLIP system bypasses this restriction by ensuring that the peptide is a monomer at (a) high pH in solution and (b) in a transmembrane state at acidic pH [70], thus making it into a useful model to study thermodynamics of membrane insertion.

Traditionally, the membrane insertion of this peptide has been described as a 3-state process [44]. In solution at neutral pH, pHLIP exists as a stable and unstructured State I peptide that can partition as a State II unstructured peptide to membrane interfaces. Under acidic conditions protonation of anionic residues allows its insertion into bilayers as a transmembrane State III α-helix. These properties make pHLIP amenable to thermodynamic membrane partitioning and insertion studies. Additionally, this peptide is of particular importance as its pH-dependent insertion into membranes is capable of directionally translocating various compounds into mildly acidic tissues. As such, it has been proposed as a targeted drug carrier into these environments, found in most solid-state tumors, inflamed tissues, and other disease conditions [38-40, 58-66].

To simplify these complex systems, many thermodynamic studies involving protein-membrane interactions have been performed with membranes composed solely of phosphatidylcholine [44, 72, 87, 88]. As shown by Ladokhin and White [32], the presence of anionic lipids leads to non-additivity of free energy components and significantly complicates thermodynamic analysis. Similarly, pHLIP's 3-state model has been confirmed only with this membrane composition [44].

The interaction of pHLIP with biological membranes, however, involves complex lipid compositions that could affect the traditional model. In our previous publication, we demonstrated that lipid headgroups can modulate the pH-dependent insertion of pHLIP and challenged the universality of the traditional 3-state model [71].

Using a combination of various fluorescence techniques, we show here that the lack of an interfacially unstructured State II observed in our previous report in lipid compositions other than pure POPC, was due to the formation of a shallower State (State II^S). Unlike the traditionally described interfacial State II in pure POPC membranes, the formation of this novel state does not result in Trp emission spectra blue shifts or measurable changes to its conformation. Instead, it is spectroscopically indistinguishable from its unstructured and soluble State I despite its association to the membrane interface. Here, we detected this new state in LUV containing mixed lipid compositions through acrylamide quenching measurements (Fig. 2.2), FRET between pHLIP and the acceptor-doped bilayers (Fig. 2.3). The identification of State II^S shows that the pH-dependent insertion of pHLIP is lipid-dependent and more complex than previously thought. In membranes composed of pure POPC, pHLIP follows the traditional 3-state pathway, passing through a deeply penetrating and relatively unstructured State II. In other lipid compositions, however, pHLIP transitions through a shallower State II^S, which is indistinguishable from its soluble State I by CD and position of Trp emission. They can be distinguished, however, by the presence of an unusual Trp red shift phenomenon that occurs when a partial pHLIP aggregate interacts and dissolves in membrane interfaces (Fig. 2.5). Observed under conditions where pHLIP appears to remain soluble in the presence of LUV, the measured Trp red shift shows that pHLIP-membrane interactions take place even if they are otherwise spectroscopically unresolved.

Taken together with our previous results on pHLIP-WT, we show that properties of the membrane interface have a large effect on the pH-dependent insertion of pHLIP; not only in modulating its insertion pK_a, but also affecting the pathway towards insertion. Properties of the peptide itself can also affect this process. Most studies have focused on the role of the anionic Asp and Glu residues on the protonation-dependent insertion mechanism. Here, however, we inspected the role of Pro20, located in the middle of the transmembrane helix, and its role on pHLIP folding and insertion. This was done by comparing the folding of both pHLIP-WT and pHLIP-P20G variants using CD and tracking their interaction/insertion into membranes by Trp emission spectra and acrylamide quenching experiments. Substituting Pro20 for Gly had been previously observed to increase the insertion propensity of pHLIP in pure POPC membranes. We expanded this observation to membranes with different interfacial properties, previously shown to modulate pHLIP membrane insertion. Regardless of lipid composition, however, pHLIP-P20G maintained a higher insertion pK_a of about 1 pH unit compared to pHLIP-WT.

Our CD measurements indicate that replacement of P20 has a profound effect on folding of pHLIP in solution and on the membrane. In water:TFE mixtures, pHLIP-WT folds in two-stage transition (Fig. 2.1), which is likely due to Pro20 inducing a kink and splitting the sequence into two segments with different folding propensities. Meanwhile, pHLIP-P20G folds with only a single sigmoidal transition and reaches higher helical content (Fig. 2.1) Similar results were observed in membranes, where pHLIP-P20G always achieved higher helical fraction than its pHLIP-WT counterpart. Interestingly, while the replacement of P20 leads to a gain in helical content (at pH 10.0: P20G $f\alpha \sim 20\%$ and WT $f\alpha \sim 14\%$, Table 2.2); it does not result in a folded interfacial state in any lipid composition. Because interfacial partitioning of unstructured peptides is thermodynamically coupled with their folding [72], the existence of unstructured States II and II^S

is an unusual feature of pHLIP peptides and is possibly due to the lack of substantial hydrophobic moment.

For interfacial partitioning into vesicles of all lipid compositions, we consistently observe a marginally more favorable free energy ΔG_{IF} for pHLIP-P20G, than that for pHLIP-WT (Fig. 2.3). In case of POPC (State II), this can be explained by taking in account two crucial but opposing factors: side chain hydrophobicity and free energy gain due to difference in partitioning folding coupling. For POPC, interfacial hydrophobicity scale favors the partitioning of pHLIP-WT ($\Delta\Delta G_{Pro \rightarrow Gly}$ = -0.44 kcal/mol) [88]. In contrast, the difference in helix formation on the interface favors partitioning of the pHLIP-P20G by $\Delta G_{Folding}$ ~ 0.4 kcal/mol per residue [72]. Thus, the difference in helical gain upon interfacial binding to vesicles between the two peptides (Fig. 2.3) is expected to make the partition of pHLIP-P20G slightly more favorable than that of pHLIP-WT. This explanation, however, cannot be automatically extended to mixed lipid compositions (State II^S), due to the lack of folding upon transfer from State I to State II^S for either peptide. It is also worth noting that interfacial hydrophobicity scale is applicable only to pure POPC and breaks down for mixed lipid compositions due to nonadditivity of various free energy components [32].

The exact reason to why the deep interfacial State II is only formed in pure PC bilayers remains puzzling, especially when considering that the presence of rather small fractions (as low as 10% [71]) of other lipids result in the formation of the shallower State II^S. One can assume that for anionic lipids such as POPS, electrostatic repulsion between charged headgroups and peptide's anionic side chains play a role in disfavoring deeper penetration. In the case of POPE, however, this explanation is insufficient as this lipid caries no total charge. One can speculate that the reason POPE eliminated State II and converts it into State II^S might be related to ability of ethanolamine to form a network of hydrogen bonds in the interfacial region of the bilayer [89]. The exact

mechanism of how this would affect the partitioning of pHLIP is not clear, however, the evidence exists that PE can engage proteins into hydrogen bonding [90]. The latter can be important in the case of unstructured peptides like pHLIP that have to satisfy their hydrogen bonds to be stable at the interface. One would expect interfacial interactions of pHLIP to become even more complex when the possibility of hydrogen bonding by headgroups in anionic phospholipids (*e.g.*, phosphatidylserine [91, 92], phosphatidic acid [91]) is considered. The ability of pHLIP to form two different states on the interface in a lipid-dependent fashion shows the importance of membrane composition on protein-membrane interactions.

The pH-dependent insertion of pHLIP into bilayers can be coupled with the translocation of different compounds across plasma membranes. For this reason, pHLIP has been proposed as a potential targeted drug delivery system to mildly acidic tissues, such as tumors [38-40, 58-63, 65]. Most of our knowledge of pHLIP-membrane interactions is derived from simple membrane models containing only phosphatidylcholine [70]; however, cellular membranes are composed of several different lipid species. Our measurements using binary lipid compositions show that the protonation-dependent insertion of pHLIP into membranes, responsible of drug delivery, is affected by interfacial properties. Membrane composition must, therefore, be taken into account for the rational design and optimization of pHLIP or pHLIP-derived protonation-dependent drug delivery systems.

Our overall results showcase the importance of lipid composition on the insertion mechanism of pHLIP. Lipids headgroups were found to modulate not only the membrane partitioning, folding and insertion propensities of pHLIP peptides, but also peptide protonation in the interfacial state and the pathway (*i.e.*, State II vs State IIS) towards insertion (Fig. 2.6). Thermodynamics of the transmembrane insertion of pHLIP peptides can be quantitated using the free energy of protonation

associated with the transfer to State III: $\Delta G_{TM}^{H+} = -2.3RT(pK_a)$. Our results indicate that in each lipid composition the pKa of insertion is shifted toward neutral pH by approximately one pH unit upon P-to-G substitution (Fig. 2.4). This is equivalent to -1.3 kcal/mol difference in free energy in favor of pHLIP-P20G. Neither the Wimley-White octanol scale [34], nor the scale of Moon and Fleming [35] provide accurate prediction, as both suggest a more favorable insertion of the pHLIP-WT, by +1.0 and +3.2 kcal/mol, respectively. In contrast, the so-called "biological" scale [36], based on transmembrane incorporation of helical segments by a Sec61 translocon machinery, gives a rather accurate prediction of -1.5 kcal/mol for more favorable insertion of the pHLIP-P20G compared to pHLIP-WT. This somewhat surprising result (obviously pHLIP is not inserted by the translocon) may be related to the fact that the translocon sorts the hydrophobicity in the context of helical segments, for which both side-chain hydrophobicity and backbone conformation are the contributing factors. Because Pro-to-Gly replacement can affect both components, having the same helical conformational motif for both translocon-based insertion and pH-dependent insertion of pHLIP appears to be important (note that Wimley-White scale [34] and the scale of Moon and Fleming [35], utilize unfolded peptides and β-barrel proteins, respectively). The changes in sidechain protonation are among the most prominent physicochemical signals capable of triggering functionally relevant structural rearrangements, especially those involved with protein-membrane interactions. For example, pH-dependent conversion of a protein structure from a water-soluble to a membrane-inserted form is a key step in many crucial processes such as cellular entry of bacterial toxins [1-6], colicins [93, 94], and viruses [7, 8], as well as membrane-mediated regulation of apoptosis by the Bcl-2 (B-cell lymphoma-2) family of proteins [9-14]. pHLIP peptides can thus

serve as a relatively simple and controlled system for deciphering the physicochemical rules underlying membrane-modulated conformational switching in other systems.

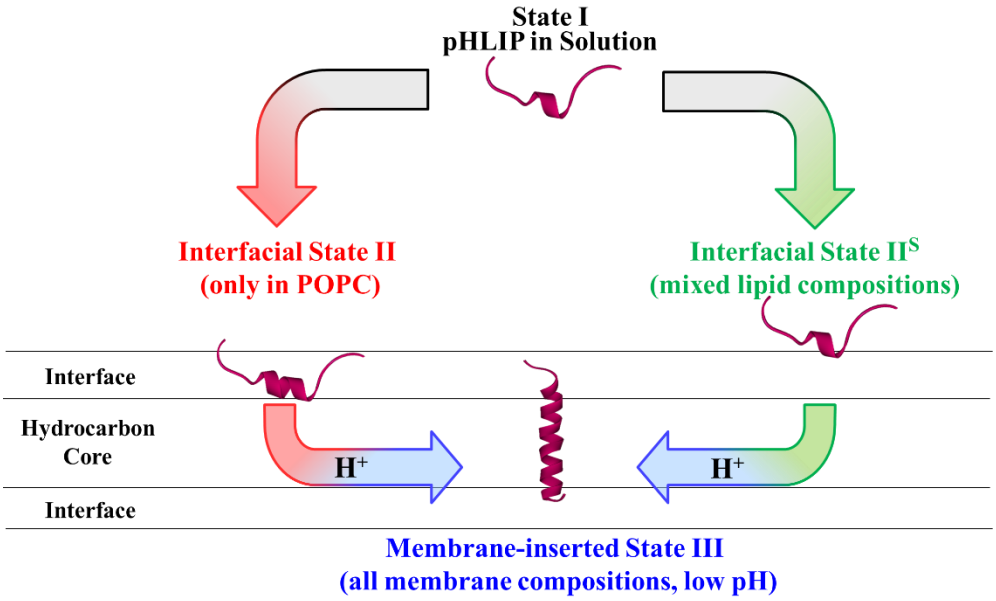

FIGURE 2.6. Revised scheme of membrane interaction of pHLIP.

In addition to traditional Stats I, II and III [44], the scheme introduces a shallow interfacial State II^S (right). The traditionally observed State II was only observed to form on pure POPC membranes with both pHLIP-WT and pHLIP-P20G. In all other membrane compositions, pHLIP forms the newly identified State II^S. Both peptide variants transitioned to the transmembrane State III regardless of membrane composition as a function of pH. Our results presented in Fig. 2.3 indicate that P20-to-G replacement doesn't affect the thermodynamics of interfacial partitioning for either State II or II^S (ΔG_{IF} ≈-6.2÷-6.8 kcal/mol). In contrast, proline replacement led to a more favorable transmembrane insertion of pHLIP-P20G in all lipid compositions by ΔG_{TM}^{H+}=1.3 Kcal/mol (equivalent of 1 pH unit, Fig. 2.4).

2.6 CONTRIBUTIONS

Vasquez Montes V. designed, performed and analyzed all experiments and wrote the manuscript.

Gerhart. J. (Thevenin lab at Lehigh University) synthesized the peptide.

Chapter 3: Modulation of pHLIP Membrane Interactions by Divalent Cations

This chapter has been previously published as Vasquez-Montes, V., J. Gerhart, D. Thevenin, and A.S. Ladokhin, Divalent Cations and Lipid Composition Modulate Membrane Insertion and Cancer-Targeting Action of pHLIP. J Mol Biol, 2019. 431(24): p. 5004-5018 doi: 10.1016/j.jmb.2019.10.016. It is reprinted here with permission in whole without any adaptations since the original publication.

3.1 ABSTRACT

The pH-Low Insertion Peptide (pHLIP) has emerged as an important tool for targeting cancer cells; it has been assumed that its targeting mechanism depends solely on the mild acidic environment surrounding tumors. Here, we examine the role of Ca^{2+} and Mg^{2+} on pHLIP's insertion, cellular targeting and drug delivery. We demonstrate that physiologically relevant concentrations of either cation can shift the protonation-dependent transition by up to several pH units towards basic pH and induce substantial protonation-independent transmembrane insertion of pHLIP at pH as high as 10. Consistent with these results, the ability of pHLIP to deliver the cytotoxic compound monomethyl-auristatin-F to HeLa cells is increased several-fold in presence of Ca^{2+}. Complementary measurements with model membranes confirmed this Ca^{2+}/Mg^{2+}-dependent membrane-insertion mechanism. The magnitude of this alternative Ca^{2+}/Mg^{2+}-dependent effect is also modulated by lipid composition—specifically by the presence of phosphatidylserine—providing new clues to pHLIP's unique tumor targeting ability in vivo. These results exemplify the complex coupling between protonation of anionic residues and lipid-selective targeting by divalent cations, which is relevant to the general signaling on membrane interfaces.

3.2 INTRODUCTION

The selective targeting of tumors is an important aspect of developing and optimizing anti-cancer therapies. In the past decade, the pH-Low Insertion Peptide (pHLIP) has emerged as a promising tool in tumor imaging and targeted drug delivery [38-42]. pHLIP remains stable in solution, yet it can also insert into membranes under mildly acidic (pH ~ 6) conditions and translocate cargo molecules (including anti-cancer drugs) conjugated to its C-terminus across the lipid bilayer [42, 95-97]. Model *in vitro* studies suggest that the interaction of pHLIP with lipid membranes involves an initial interfacial binding of unfolded peptide at neutral pH, with subsequent insertion as a transmembrane helix upon acidification [43, 44]. The latter is believed to be the molecular mechanism responsible for pHLIP's selective targeting of tumors, which are known to produce a slightly more acidic extracellular microenvironment (pH ~ 7) than healthy tissues (pH 7.4) [45, 46]. The advent of pHLIP has led to the development of other promising protonation-driven cancer targeting peptides like ATRAM [98] and TYPE7 [99], with a supposedly similar mode of action. Whether such a small difference in pH can solely explain the selectivity of pHLIP towards tumors *in vivo*, or whether other mechanisms are involved remains unknown.

One of the biggest challenges in deciphering the molecular mechanisms driving pHLIP tumor targeting arises from the often-overlooked discrepancy in experimental conditions between the studies aimed at delivering compounds into cancer cells and studies with model lipid vesicles. While delivery studies into cells are normally performed in the presence of physiological concentrations of divalent ions (present in growth media or extracellular fluid) [95, 100, 101], experiments with vesicles have been, so far, been conducted in the absence of Ca^{2+} or Mg^{2+} [44, 47, 62, 67, 102, 103]. Furthermore, most mechanistic studies have been performed on vesicles containing only phosphatidylcholine, thus neglecting the complex nature of the plasma membrane.

For instance, we have previously demonstrated that variation in lipid composition leads to a significant variation in the apparent pK_a of the insertion of pHLIP [47, 103]. Here, we examine the role of lipid composition and divalent cations in the pHLIP targeting of both model membranes and cancer cells. Using a combination of spectroscopic and cellular techniques, we show that the membrane insertion of pHLIP is strongly promoted by physiological concentrations of Ca^{2+} and Mg^{2+}. Our results also suggest a strong regulatory link between membrane lipid composition and extracellular concentrations of Ca^{2+}/Mg^{2+} on the membrane insertion of pHLIP, which may have general implications for signaling on membrane interfaces.

3.3 MATERIALS AND METHODS

3.3.1. pHLIP solid-phase synthesis

pHLIP with a cysteine residue at its N-terminus, (H_2N-GCEQNPIYWARYADWLF-TTPLLLLDLALLVDADEGTG-CONH$_2$) or its C-terminus (H_2N-GGEQNPIYWARYADWLF-TTPLLLLDLALLVDADEGTCG-CONH$_2$) were prepared by Fmoc solid-phase synthesis on an automated microwave peptide synthesizer (CEM Liberty Blue) using rink amide resin (CEM, 0.19 mmol/g loading capacity). The peptides were purified *via* RP-HPLC (Phenomenex Luna prep 5 µm Omega Polar C18 250 x 21.20 mm; flow rate 5 mL/min; phase A: water 0.1% TFA; phase B: acetonitrile 0.1% TFA; gradient 60 min from 95/5 A/B to 0/100 A/B. The purity of the peptides was determined by RP-HPLC (Phenomenex Luna 5 µm Omega Polar C18 250 x 100 mm; flow rate 5 mL/min; phase A: water 0.01% TFA; phase B: acetonitrile 0.01% TFA; gradient 60 minutes from 95/5 A/B to 0/100 A/B), and their identity was confirmed *via* MALDI-TOF MS (Shimadzu 8020).

3.3.2. Preparation of conjugates

Conjugating Alexa488 C5 maleimide (Invitrogen #A10254) to the N-terminus cysteine of pHLIP was achieved by dissolving pHLIP in DMF with 50 mM HEPES, pH 7.2, followed by the addition of 1 molar equivalent of Alexa488 C5 maleimide. The solution was flushed with nitrogen and mixed at room temperature for 4 hours. pHLIP-MMAF was prepared by conjugating Py-ds-Prp-MMAF (Levena Biopharma) to pHLIP with a C-terminus cysteine residue utilizing the same procedure. The desired pHLIP conjugates were isolated using the same techniques described for the pHLIP peptides. The purity of the pHLIP conjugates were determined by RP-HPLC, and their identity was confirmed by MALDI-TOF MS. Alexa488-pHLIP: purity >99%; calculated (M+H+) = 4874, found (M+H+) = 4874. pHLIP-MMAF: purity >98%; calculated (M+H+) = 5030, found (M+H+) = 5030. The Alexa488-pHLIP conjugate was quantified at 493 nm by UV/Vis absorbance

spectroscopy using the molar absorption coefficient of Alexa488 C5 maleimide (72,000 $M^{-1} \cdot cm^{-1}$). The pHLIP-MMAF conjugate was quantified at 280 nm using the molar absorption coefficient of pHLIP (13940 $M^{-1} \cdot cm^{-1}$). The conjugates were then lyophilized in 10^{-8} mole aliquots.

3.3.3. Cell culture

Human cervical adenocarcinoma HeLa and human breast adenocarcinoma MDA-MB-231 cells were cultured in Dulbecco's modified Eagle's medium (DMEM) high glucose supplemented with 10% fetal bovine serum (FBS), 100 units/mL penicillin, and 0.1 mg/ mL of streptomycin. The cells were cultured in a humidified atmosphere of 5% CO2 at 37 °C.

3.3.4. Cell viability assay

HeLa cells were plated in 96-well plates at a cell density of 5,000 cells/well and incubated overnight. pHLIP-MMAF was solubilized in an appropriate volume of Dulbecco's phosphate buffered saline (DPBS) containing 1.2 mM calcium (Sigma #D8662) or lacking calcium (Sigma #D8537) pH 7.4, so that upon pH adjustment the desired treatment concentration (10 μM) was obtained. The samples were then gently sonicated for 30−60 s using a bath sonicator (Branson Ultrasonics). After removal of cell media, the cells were washed twice with phosphate buffered saline (PBS), and then pHLIP-MMAF was added to the appropriate wells and incubated for 5 minutes at 37 °C. Then, the media was adjusted to the desired pH (final volume = 50 μL) using a pre-established volume of DPBS buffered with acetic acid, pH 4.0, and incubated for 2 hours. Acetic acid was used for sample acidification due to the high affinity and/or chelating properties of other acids (*i.e.,* citric acid) towards Ca^{2+}. Following the treatment, the plate was washed once with 100 μL of complete DMEM and then recovered for 72 hours at 37 °C in 100 μL of complete DMEM. Cell viability was assessed with the MTT colorimetric assay. Briefly, MTT was solubilized in PBS (10 mg/mL) with brief sonication, and 10 μL was added to each well. After

incubation for 2 hours at 37 °C, the formazan crystals were solubilized in 200 μL of dimethyl sulfoxide (DMSO), and the absorbance at 580 nm was measured using an Infinite F200 PRO microplate reader (Tecan). Cell viability was normalized to control cells treated with media at pH 7.4.

3.3.5. Cell binding experiments

MDA-MB-231 human breast cancer cells were harvested and washed twice with PBS, pH 7.4. Alexa488-pHLIP was solubilized in an appropriate volume of 10 mM HEPES, 19.5 mM NaCl, pH 7.4 without calcium so that upon a 2-fold dilution, and after pH adjustment the desired treatment concentration (1 μM) was obtained. Next, 220,000 cells were incubated in suspension with Alexa488-pHLIP at two times the desired concentration without calcium for 5 minutes at 37 °C. After the incubation, an equal volume of 10 mM HEPES, 19.5 mM NaCl, pH 7.4 containing either 0, 2.4, or 3.6 mM calcium was added to bring the final calcium concentration to 0, 1.2, 1.8 mM, and incubated for an additional 5 minutes at 37 °C. Then, the pH was adjusted (final volume = 300 μL) using a pre-established volume of 10 mM HEPES, 19.5 mM NaCl, containing the appropriate calcium concentration, buffered with acetic acid, pH 4.0, and incubated for 10 minutes at 37 °C. The cells were then washed at the same pH and calcium concentration as the treatment, and fixed with 4% paraformaldehyde (PFA) for 10 minutes at 4 °C. The cells were then resuspended in PBS and analyzed by flow cytometry using a BDFacs Canto II flow cytometer equipped with a 488 nm argon laser and a 530/30 bandpass filter. The data was analyzed using FACSDiva version 6.1.1 software. The fluorescence data are expressed as mean arbitrary fluorescence units and were gated to include all healthy mammalian cells. Fluorescence was normalized to cells treated at pH 7.4 with 0 mM calcium.

For microscopy, MDA-MB-231 cells were seeded on glass coverslips pretreated with poly-lysine and allowed to reach ~70% confluency. The cells were then treated with Alexa488-pHLIP (1 µM) at pH 7.4 or 6.0 for 10 minutes at 37 °C as described above. Following the treatment, the cells were washed once at the same pH and calcium concentration as the treatment, and immediately fixed with ice cold methanol for 10 minutes. The fixed cells were then washed twice with PBS and incubated with 1 µg/mL Hoechst (Invitrogen #H3570) in PBS for 10 minutes at room temperature and washed twice again. The coverslips were mounted onto a slide with fluoromount (SouthernBiotech #0100-01) and stored at 4 °C until images were taken with a Nikon Eclipse Ti microscope with a 20x objective.

3.3.6. Vesicle preparation

The appropriate volume of lipid stocks dissolved in chloroform were dried under a nitrogen stream and dried overnight using high vacuum. The dried lipids were re-suspended in 50 mM phosphate buffer, pH 8.0 to a final concentration of 20 mM and large unilamellar vesicles (LUV) were formed by extrusion using a Mini-Extruder (Avanti Polar Lipids, Alabaster, AL). Extrusion was performed using 0.1 µm nucleopore polycarbonate membranes (Whatman, Philadelphia, PA) and the prepared stocks were stored at -4 °C. Lipids used in this study: Palmitoyl-oleoyl-phosphatidylcholine (POPC), palmitoyl-oleoyl-phosphatidylserine (POPS), and 1-palmitoyol-2-oleoyl-sn-glycero-3-phosphoethanolamine (POPE) were purchased from Avanti Polar Lipids (Alabaster, AL)

3.3.7. Trp fluorescence measurements

The steady-state Trp fluorescence emission measurements of pHLIP were performed on a SPEX Fluorolog FL3-22 steady-state fluorescence spectrometer (Jobin Yvon, Edison, NJ) equipped with double-grating excitation and emission monochromators. Experiments were carried out on 2x10

mm cuvettes oriented perpendicular to the excitation beam. Sample temperature was maintained constant at 25 °C using a Peltier device from Quantum Northwest (Spokane, WA.). Measurements were performed using 2 μM pHLIP and 1.0 mM LUV after 20 min sample equilibration. Spectra were collected between 300-450 nm with an excitation wavelength of 285 nm at 1.0 nm steps, using 3.0 and 4.0 nm slits on the excitation and emission monochromators, respectively and averaged over 3 scans. The positions of maximum of the averaged spectra were determined by fitting them to a log-normal distribution using the following formula [77]:

$$For\ \lambda > \lambda_{max} - \frac{\rho\Gamma}{\rho^2-1},$$

$$I(\lambda) = I_0 exp\left[\frac{ln2}{ln^2\rho} ln^2\left(1 + \frac{(\lambda-\lambda_{max})(\rho^2-1)}{\rho\Gamma}\right)\right], \text{(Eq. 3.1a)}$$

$$While\ for\ \lambda < \lambda_{max} - \frac{\rho\Gamma}{\rho^2-1}, I(\lambda) = 0, \text{(Eq. 3.1b)}$$

Where I_0 is the maximal intensity of the analyzed spectrum at the fluorescence maximum λ_{max}, Γ is the width of the spectrum at the half maximum intensity, and ρ represents the asymmetry of the distribution.

Experiments performed between pH 8.0 and 4.0 in the absence of Ca^{2+} or Mg^{2+} were carried out in 10 mM phosphate buffer. The high binding propensity of phosphates for divalent cations which then precipitate as a salt makes this buffer unsuitable for measurements in the presence of Ca^{2+} or Mg^2. For this reason, we substituted 10 mM phosphate buffer for either 10 mM HEPES + 19.5 mM NaCl (experiments between pH 8.0-6.0) or 10 mM borate buffer + 19.5 mM NaCl (experiments at pH > 8.0) due to their lack of affinity for Ca^{2+} or Mg^{2+}. The shorter buffering range of HEPES buffer, however, limited the experimental pH range to pH ≥ 6.0. Sample acidification was achieved by the addition of small aliquots of acetic/acetate buffer. As in the case of several buffers, many acids commonly used to induce acidification (*i.e.*, citrate) chelate Ca^{2+} and Mg^{2+},

eliminating any divalent cation-mediated effect. Acetate, however, is compatible with assays performed in the presence of Ca^{2+} or Mg^{2+}. Divalent cation titrations were performed at pH 10.0 to minimize possible contribution form protonation events in our measurements.

The pK_a of the protonation-dependent insertion of pHLIP into LUV was calculated by fitting the data to the following equation using nonlinear least-square analysis [47, 104]:

$$\lambda = \frac{\lambda_N + \lambda_L\,(10^{m(pK_a - pH)})}{1 + 10^{\mathrm{m(pK}_a - \mathrm{pH})}}\text{, (Eq. 3.2)}$$

where λ is the Trp position of maximum measured as a function of pH, the λ_N and λ_L parameters correspond to the saturating Trp positions of maximum at high and low pH, m is the slope of the transition, and pK_a denotes the negative logarithm of the dissociation constant.

3.3.8. Membrane insertion calculations

The protonation-dependent membrane insertion free energy (ΔG_{TM}^{H+}) was calculated using the following equation:

$$\Delta G_{TM}^{H+} = -2.3RT \cdot pK_a \text{ , (Eq. 3.3)}$$

Where R is the gas constant (1.985×10^{-3} kcal K^{-1} mol^{-1}) and T is the experimental temperature in Kelvin (298 K). The effect of Ca^{2+} on this process is given by the term $\Delta G_{TM}^{H+,\,Ca2+} - \Delta G_{TM}^{H+}$ which is calculated by subtracting the protonation-dependent membrane insertion free energy in the presence of Ca^{2+} ($\Delta G_{TM}^{H+,\,Ca2+}$) from the one obtained in the absence of Ca^{2+} (ΔG_{TM}^{H+}). This term is by definition equal to zero in the absence of divalent cations and is lower in more favorable interactions.

The Ca^{2+}-induced protonation-independent membrane insertion free energy ($\Delta G_{TM}^{[Ca2+]}$) was estimated using the decreases in Trp fluorescence maximum at pH 10.0 as proxies for the transmembrane populations of pHLIP at each [Ca^{2+}] using the following formula [105]:

$$\Delta G_{TM}^{[Ca2+]} = -RTln\left(\frac{f_{TM}}{f_{IF}}\right), \text{(Eq. 3.4)}$$

Where $\Delta G_{TM}^{[Ca2+]}$ represents the free energy of the Ca^{2+}-induced insertion of pHLIP measured at pH 10.0 for a particular [Ca^{2+}], R and T denote the gas constant (1.985 x 10^{-3} kcal K^{-1} mol^{-1}) and experimental temperature (298 K) respectively and f_{TM} and f_{IF} correspond to the fractional transmembrane and interfacial populations. For reference, a $\Delta G_{TM}^{[Ca2+]}$ = 0 kcal/mol represents a f_{TM} = 0.5, a $\Delta G_{TM}^{[Ca2+]}$ < 0 kcal/mol represents a f_{TM} > 0.5, and a $\Delta G_{TM}^{[Ca2+]}$ > 0 kcal/mol represents a f_{TM} < 0.5.

3.3.9. Circular dichroism and oriented circular dichroism

Circular dichroism (CD) and oriented CD (OCD) measurements were performed using an upgraded JASCO-720 spectropolarimeter (JASCO, Easton, MD). CD spectra were collected using 15.0 μM pHLIP and 1.0 mM POPC LUV on a 1.0 mm optical path cuvette and corrected to their appropriate backgrounds. At least 30 scans were collected for each spectrum and averaged for each sample. As for fluorescence, measurements in the presence of divalent cations were performed using 10 mM HEPES buffer + 19.5 NaCl, while 10 mM phosphate buffer was employed for experiments in the absence of divalent cations and acidification induced by acetic/acetate buffer.

OCD spectra were obtained by creating a stack of oriented multilayers on a quartz disc as previously described [106]. This technique allows the differentiation of interfacial α-helices, which present with a double minimum at ~ 205 and 222 nm, from transmembrane α-helices, which have a single minimum at ~ 228 nm [106, 107]. Briefly, pHLIP and POPC lipids were codissolved at a

1:100 ratio in methanol (10 mM lipids and approximately 0.1 mM pHLIP) and 2.5 μL of the mixture was layered carefully on a ~ 1.0 cm circle at the center of a 2.5 cm disc. The solvent was then air dried and hydrated using warm air at ~ 100% relative humidity. The prepared disc was mounted on a sealed tube with the sample side pointing inwards. Samples were kept hydrated by placing a drop of water in the tube before closing. At least 50 scans were collected at four different orientations increasing by 90^{o}-angles along the central axis and averaged. For measurements in the presence of divalent cations a 2 μL drop of 2.0 mM Ca^{2+} or Mg^{2+} dissolved in 5.0 mM HEPES buffer was added in-between each bilayer of the multilayer stack. Similarly, a drop of buffer at pH 4.0 was added in-between each layer for the collected spectrum at low pH. Buffer drops were completely dried before continuing with the multilayer stack protocol. The background signal was determined by collecting the spectra of a multilayer stack in the absence of pHLIP. The data is presented normalized to the ellipticity of their minima due to difficulties calculating the peptide concentration present.

3.3.10. LUV aggregation measurements

The aggregation of LUV containing POPC, 25POPS:75POPC, 25POPE:75POPC, and 75POPS:25POPC (as a control) in the presence of increasing concentrations of Ca^{2+} or Mg^{2+} were determined by measuring light scattering changes at 400 nm as previously described [108, 109]. Samples were performed on a 4x10 mm quartz cuvette containing 0.1% LUV in 10 mM HEPES buffer + 19.5 mM NaCl. Cuvette orientation did not affect the results obtained. Similar measurements have been previously performed to characterize the aggregation of 100POPS vesicles and shown to reproduce results obtained by small-angle-scattering and dynamic light scattering [108, 109].

3.4 RESULTS

3.4.1 Ca^{2+} promotes the cellular interaction of pHLIP

The cellular interaction between pHLIP, labeled at its N-terminus with the fluorophore Alexa488 (A488-pHLIP), and human MDA-MB-231 breast cancer cells was inspected by fluorescence microscopy under two different conditions: (1) in the absence of divalent cations to reflect conditions most commonly used to characterize pHLIP interactions with vesicles, and (2) in the presence of 1.8 mM Ca^{2+}, as a simplified mimetic of extracellular divalent cation concentration. In both cases, cells are incubated with A488-pHLIP at the appropriate pH, washed and imaged. No significant fluorescence was observed at pH 7.4 in the absence of divalent cations (Fig. 3.1b), pointing to a weak cellular interaction of pHLIP-A488 under these conditions. It should be noted that the formation of the interfacial form of the peptide is still expected, but likely removed by the washes performed before microscopy imaging. As expected, acidification of the solution to pH 5.0 resulted in a large increase in A488 fluorescence intensity (Fig. 3.1a), attributed to the pH-dependent membrane insertion character of pHLIP. At a pH of 7.4, the addition of 1.8 mM Ca^{2+} also resulted in a significant increase in A488 fluorescence intensity (Fig. 3.1c), suggesting that the presence of Ca^{2+} induces the interaction of A488-pHLIP with cellular membranes without the need for acidification.

The effect of Ca^{2+} on pHLIP cellular interactions was quantified by flow cytometry. At pH 7.4, the presence of Ca^{2+} led to a concentration-dependent increase in A488 fluorescence, with a 1.8 and 2.8-fold increase at 1.2 and 1.8 mM Ca^{2+}, respectively (Fig. 3.1g). These results are consistent with the fluorescence increase observed by microscopy (Fig. 3.1a-f) and confirm the ability of Ca^{2+} to promote the interaction of pHLIP with cells. A similar trend was observed when cells were incubated with A488-pHLIP at pH 6.0, albeit with higher A488 intensity, likely due to the pH-

dependent insertion of pHLIP. Representative microscopy images of the conditions used in the flowcytometry measurements are shown in Fig. B1. These results indicate that acidic conditions and Ca^{2+} work in tandem to induce the interaction of pHLIP with cells and its possible membrane insertion. Understanding the role of divalent cations as possible regulators of pHLIP membrane interaction is, therefore, critical to establishing the molecular mechanism of pHLIP under physiological conditions.

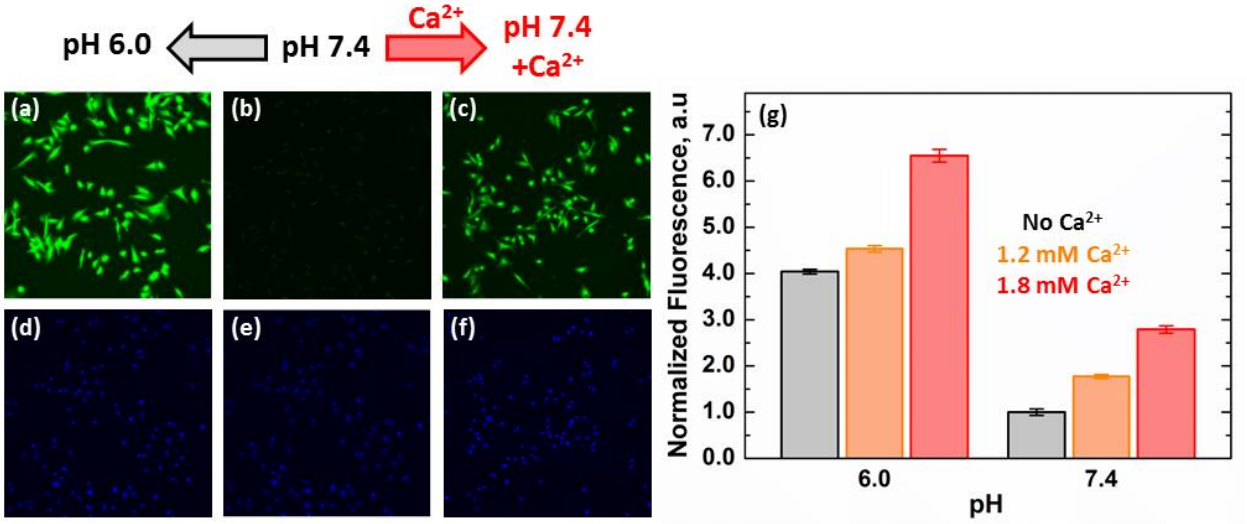

FIGURE 3.1. Comparison of pH-dependent and Ca^{2+}-dependent cellular targeting by pHLIP.

The cellular interaction of pHLIP N-terminally conjugated to an Alexa488 fluorophore (A488-pHLIP) was determined by fluorescence microscopy (a-f) and flowcytometry (g) using MDA-MB-231 cells. (a-c) An increase in A488 intensity (green), indicative of pHLIP cellular interaction, was observed either by acidification (a) or the addition of 1.8 mM Ca^{2+} at pH 7.4 (c) to a sample at pH 7.4 lacking Ca^{2+} (b). (d, f) Hoechst staining of MDA-MB-231 cells used in microscopy images. (g) Flow-cytometry was used to quantify the effects of [Ca^{2+}] on the interaction of A488-pHLIP with MDA-MB-231 cells at pH 7.4 to mimic the extracellular pH of healthy cells or at mildly acidic pH 6.0. At both pH the presence of Ca^{2+} led to higher fluorescence, due to larger populations of membrane bound pHLIP. Normalized fluorescence represents the fold increase over cells incubated without Ca^{2+} at pH 7.4. Data are represented as mean values from which the error bars represent the standard error of the mean (n = 3). Representative microscopy images of conditions used in flowcytometry measurements are shown in Fig. B1. Cellular measurements were performed in collaboration with the Damien Thevenin Lab

3.4.2 Ca^{2+} promotes pHLIP-mediated translocation of cargo molecules and cytotoxicity

We evaluated the effect that Ca^{2+} may have on the ability of membrane-inserted pHLIP to translocate cargo molecules into cancer cells using a construct, in which the cytotoxic agent MMAF (monomethyl auristatin F) is conjugated to the C-terminus of pHLIP *via* a disulfide bond

(pHLIP-MMAF). We know from our previous reports, that pHLIP can translocate, release MMAF into the cytoplasm, and induce cancer cell death in a pH-dependent manner [63, 66]. The presence of 1.2 mM Ca^{2+} greatly increased cytotoxicity at pH 7.4, indicated by an at least 10-fold decrease in the IC_{50} from ≥ 8.5 μM in the absence of Ca^{2+} (Fig. 3.2a, black) to 0.9 ± 0.1 μM (Fig. 3.2a, red). The decrease in cellular viability observed in absence of Ca^{2+} is attributed to non-specific killing due to background levels of endocytosis upon association of pHLIP-MMAF to cell membranes, as we previously reported [63, 66]. Nevertheless, these results are consistent with the increase in A488 intensity observed by microscopy and flow cytometry (Fig. 3.1) and indicates that Ca^{2+} promotes the interaction of pHLIP with cells, and possibly its transmembrane insertion.

Treating cells with pHLIP-MMAF at pH 6.0 in the absence Ca^{2+} led to a 5-fold decrease in IC_{50} (1.6 ± 0.1 μM; Fig. 3.2b, black) as compared to pH 7.4 (≥ 8.5 μM; Fig. 3.2a, black). Inclusion of Ca^{2+} in the treatment solution, resulted in another 5-fold decrease in IC_{50} (0.3 ± 0.1 μM; Fig. 3.2b, red). The addition of Ca^{2+} not only resulted in lower IC_{50} values, but also in a steeper cytotoxicity response. We attribute this change to a more favorable transmembrane insertion of pHLIP and subsequent drug delivery in the presence of Ca^{2+}. The increased cooperativity led to a 10-fold difference in the concentration of pHLIP-MMAF required to kill 80% of cells between both conditions tested. Where 0.53 μM pHLIP-MMAF was sufficient to kill 80% of cells in the presence of Ca^{2+}, while an equimolar concertation of pHLIP-MMAF only resulted in 23% cytotoxicity in the absence of Ca^{2+}.

Our cytotoxicity results, together with the fluorescence microscopy (Fig. 3.1a-c) and flow cytometry measurements (Fig. 3.1g), show that the presence of physiological Ca^{2+} concentrations promote the ability of pHLIP to translocate compounds across cellular membranes. Physiological conditions must therefore be considered when characterizing and optimizing the interaction and mechanism of pHLIP-like cancer targeting systems.

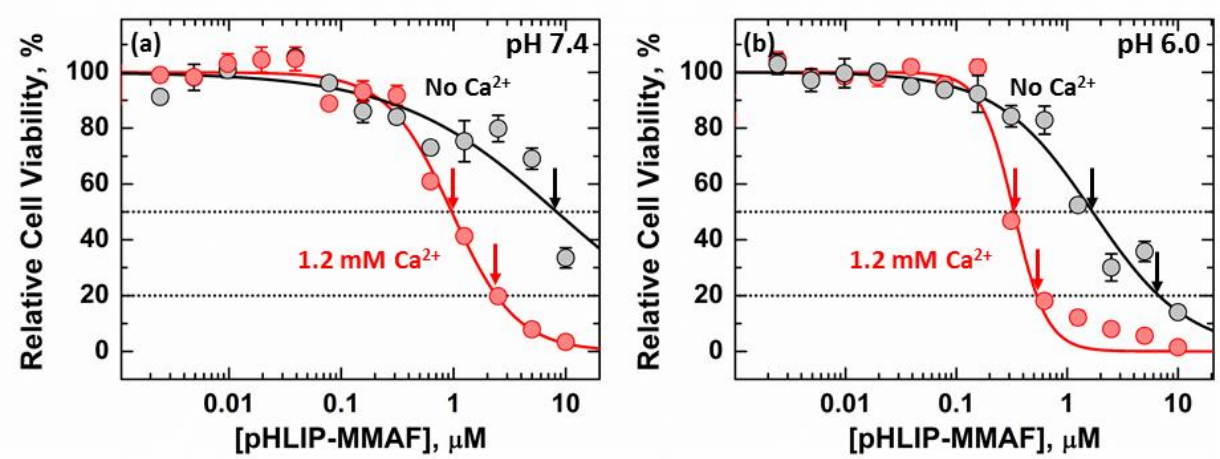

FIGURE 3.2. Comparison of pH-dependent and Ca^{2+}-dependent cellular targeting by pHLIP.

The cellular interaction of pHLIP N-terminally conjugated to an Alexa488 fluorophore (A488-pHLIP) was determined by fluorescence microscopy (a-f) and flowcytometry (g) using MDA-MB-231 cells. (a-c) An increase in A488 intensity (green), indicative of pHLIP cellular interaction, was observed either by acidification (a) or the addition of 1.8 mM Ca^{2+} at pH 7.4 (c) to a sample at pH 7.4 lacking Ca^{2+} (b). (d, f) Hoechst staining of MDA-MB-231 cells used in microscopy images. (g) Flow-cytometry was used to quantify the effects of [Ca^{2+}] on the interaction of A488-pHLIP with MDA-MB-231 cells at pH 7.4 to mimic the extracellular pH of healthy cells or at mildly acidic pH 6.0. At both pH the presence of Ca^{2+} led to higher fluorescence, due to larger populations of membrane bound pHLIP. Normalized fluorescence represents the fold increase over cells incubated without Ca^{2+} at pH 7.4. Data are represented as mean values from which the error bars represent the standard error of the mean (n = 3). Representative microscopy images of conditions used in flowcytometry measurements are shown in Fig. B1. Cellular measurements were performed in collaboration with the Damien Thevenin Lab

3.4.3 Ca^{2+}-dependent transmembrane insertion into model POPC membranes

The common way of characterizing pH-dependent membrane interactions of pHLIP is through a combination of changes in its tryptophan (Trp) emission maximum and circular dichroism (CD) spectrum [44, 47, 62, 67, 102, 103]. Here, we used these techniques to compare the spectral

responses of pHLIP observed at neutral pH in the presence of Ca^{2+} to those observed upon transmembrane insertion at acidic pH.

The spectral hallmarks of the interfacial (State II) and transmembrane (State III) states of pHLIP and have been firmly established by previous studies [44, 47, 70]. Our data collected in the absence of Ca^{2+} are consistent with these hallmarks (Fig. 3.3). Specifically, Trp fluorescence maximum of the interfacial State II of pHLIP (populated in the presence of large unilamellar vesicles (LUV) composed of POPC at pH 8.0) is 354 nm (Fig. 3.3a, black), indicating that the Trps are in a relatively polar environment. In State III (populated at pH 4), the maximum is blue-shifted to 342 nm (Fig. 3.3a, blue), consistent with a more nonpolar environment. Our data collected at pH 8, but in the presence of 2.0 mM Ca^{2+} (Fig. 3.3a, red), clearly indicate that, under these conditions, pHLIP exhibits fluorescence hallmarks of the transmembrane State III.

A similar pattern is observed with conformational changes measured by CD spectroscopy for solution samples containing LUV (Fig. 3.3b) or samples in oriented multilayers (Fig. 3.3c). In the absence of Ca^{2+} at pH 8.0, the CD spectrum of pHLIP showed a single minimum ~ 200 nm, typical of unstructured peptides and consistent with the largely unfolded interfacial State II (Fig. 3b, black) [44]. In contrast, the CD spectra of pHLIP collected at pH 4.0 in the absence of Ca^{2+} (transmembrane State III) and at pH 8.0 in the presence of Ca^{2+} were equivalent (Fig. 3b, blue and red), with both spectra presenting a double minimum at ~ 209 and 222 nm, characteristic of α-helices.

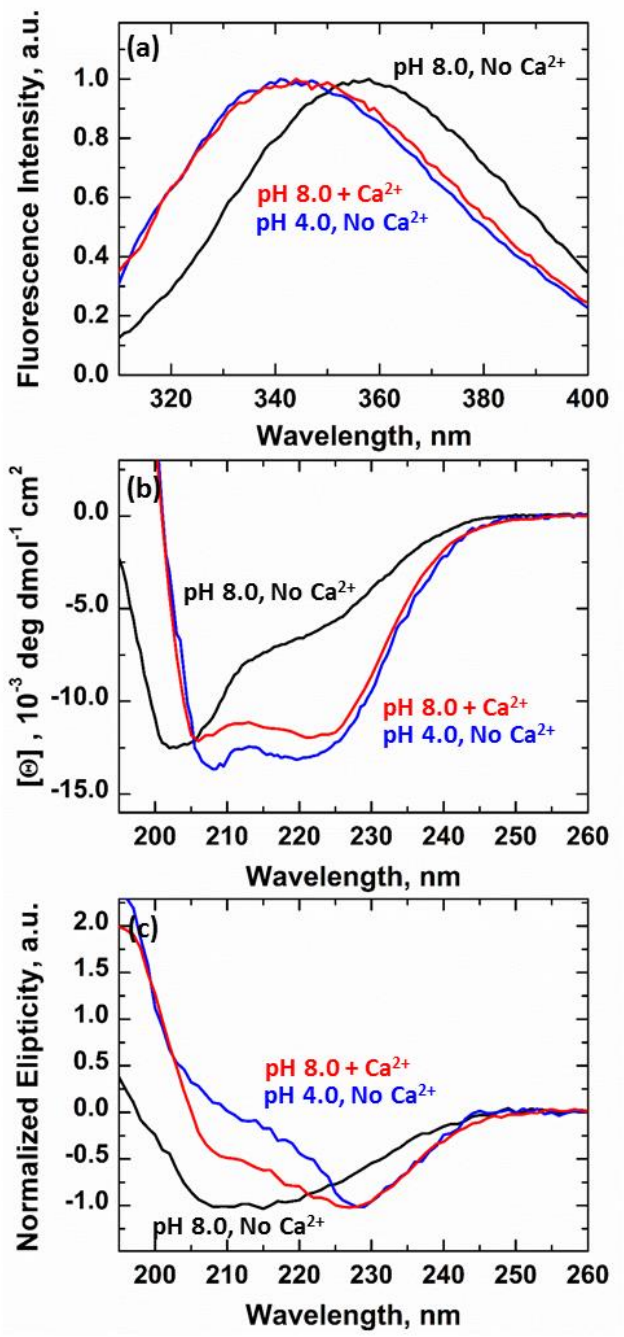

FIGURE 3.3. Comparison of pH-dependent and Ca^{2+}-dependent insertion of pHLIP into model POPC membranes.

The transmembrane insertion of pHLIP was characterized by (a) Trp fluorescence and (b) circular dichroism (CD) in LUV and by oriented circular dichroism (OCD) in flat multilayers. (a) At pH 8.0, the interfacial form pHLIP presents a Trp position of maximum of 354 nm (black). Acidification of the sample to pH 4.0 leads to a 12 nm blue shift to 342 nm, characteristic of pHLIP's transmembrane State III (blue) [44]. Introducing 2.0 mM Ca^{2+} (a proxy for extracellular divalent cation concentration) while maintaining the pH constant at 8.0 results in a similar 9 nm blue shift to 345 nm (red). (b) CD measurements in the absence of Ca^{2+} at pH 8.0 (black) and 4.0 (blue) show characteristic signals for unstructured peptides and α-helices respectively, consistent with its previously reported pH-dependent transmembrane insertion [44]. The addition of 1.0 mM Ca^{2+} at pH 8.0 resulted in a typical α-helical spectrum (red)

with a similar ellipticity as the one observed at pH 4.0 in the absence of Ca^{2+}. (c) OCD measurements were performed in the presence of Ca^{2+} at pH 8.0 (red); and in the absence of Ca^{2+} at pH 4.0 (blue) and 8.0 (black). The latter two conditions correspond to those of the transmembrane State III and interfacial State II of pHLIP respectively. The Ca^{2+}-inserted and pH-inserted samples exhibited similar spectra with a single minimum ~ 228 nm, characteristic of the OCD spectra of transmembrane α-helices [110].

The pH- and Ca^{2+}-induced helices also have similar orientations with respect to membrane plane, as revealed by the oriented circular dichroism (OCD) measurements performed in lipid multilayers (Fig. 3.3c). Both OCD spectra (red and blue curves) have a single sharp minimum at 228 nm, characteristic of transmembrane α-helices [28,29][110]. The spectra are also consistent with the previously reported OCD spectrum of the transmembrane State III of pHLIP [111, 112]. As expected, these spectra are quite different from that measured at pH 8.0 in the absence of Ca^{2+} (black line), *i.e.*, under conditions corresponding to the interfacial State II. Together, all fluorescence and CD measurements indicate that the Ca^{2+}-inserted state resides in the lipid bilayer in the same conformation as the conventional pH-inserted transmembrane State III of pHLIP.

3.4.4 Effects of lipid composition on Ca^{2+}-mediated insertion of pHLIP

One of the hallmarks of cancer cells, is the change in lipid composition of the outer leaflet of the plasma membrane, specifically the increase in phosphatidylethanolamine (PE) and phosphatidylserine (PS) [28-30, 113, 114]. Previously we have established that additions of many non-PC lipids, including PE and PS, have a substantial effect on the pH-dependent insertion of pHLIP [47, 103]. Here, we compared how the membrane insertion of pHLIP into pure POPC bilayers and bilayers containing 25% of either POPE or POPS, is affected by the presence of Ca^{2+}.

Trp emission spectra were collected in the presence of POPC LUV at pH 10.0 and increasing Ca^{2+} concentrations to characterize the Ca^{2+}-mediated membrane insertion of pHLIP. The positions of their maxima were then compared to the known maxima of the interfacial State II (Fig. 3.4a red dashed line) and transmembrane State III (Fig. 3.4a blue dashed line) forms of pHLIP at pH 10.0

and 4.0, respectively. Incremental addition of Ca^{2+} at pH 10.0 led to progressive decreases in pHLIP Trp maxima until they approached saturation at 343 nm in 5.0 mM Ca^{2+} (Fig. 3.4a, filled circles). The positions of maxima observed at 4.0-5.0 mM Ca^{2+} match those observed for the transmembrane State III of pHLIP. Together with the α-helical conformation determined by CD (Fig. 3.3b) and transmembrane orientation determined by OCD (Fig. 3.3c), these results confirm that Ca^{2+} induces the transition of pHLIP into its transmembrane State III. These results also imply that 2.0 mM Ca^{2+}, a proxy for extracellular divalent cation concentration, is sufficient to induce the transmembrane insertion of ~ 70% of pHLIP present in the sample at pH 10.0. The Ca^{2+}-dependent blue shifts were reversible in the presence of EDTA (Fig. 3.4a, open circles).

Control measurements in the absence of membranes were performed to confirm that the Ca^{2+}-dependent Trp blue shifts were not caused by aggregation-induced Trp burial. No significant changes in the Trp emission spectrum of pHLIP were observed after the addition of Ca^{2+} (356 nm, Fig. B2a, red) as compared to samples lacking Ca^{2+} (357 nm, Fig. B2b, black). This indicates that the results observed in the presence of LUV are membrane-dependent and not due to peptide aggregation. The small 1 nm blue shift from 357 nm after the addition of Ca^{2+} suggests, however, that Ca^{2+} likely affects the unstructured "conformation" of pHLIP in solution. Moreover, the effect of Ca^{2+} concentration on the aggregation of POPC LUV was also tested by light scattering measurements. No Ca^{2+}-dependent membrane aggregation of POPC LUV was detected under the concentrations used in this study (Fig. B3a).

We next characterized the effect of Ca^{2+} on the protonation-dependent insertion of pHLIP into POPC LUV using intrinsic Trp fluorescence as a function of pH. In the absence of Ca^{2+}, the pH-dependent insertion of pHLIP into POPC bilayers yielded a protonation-dependent membrane insertion pK_a of 6.1 ± 0.1 (Fig. 3.4b, black), consistent with previous reports [67, 69]. The presence

of 2.0 mM Ca^{2+} (Fig. 3.4b, brown) led to two prominent changes in the pH-dependent insertion of pHLIP: 1) A pronounced decrease in the Trp fluorescence maximum at pH 10.0 (Fig. 3.4b, red arrow) and 2) a significant shift of the titration curve towards basic pH (Fig. 3.4b, blue arrow). The 7 nm blue shift at pH 10.0 from 354 nm to 347 likely reflects the Ca^{2+}-mediated membrane insertion of pHLIP independent of pH. The presence of 2.0 mM Ca^{2+} also led to a 1.5 pH-unit shift in the pK_a of the titration curve to 7.6 ± 0.1 (Fig. 3.4b, brown) compared to 6.1 ± 0.1 in the absence of Ca^{2+} (Fig. 3.4b, black). These results, together with our measurements at constant pH 10.0 (Fig. 3.4a), indicate a dual effect for Ca^{2+} on the interaction of pHLIP with POPC membranes: 1) Ca^{2+} induces the transmembrane insertion of a significant fraction of the pHLIP population without need of acidification. 2) Ca^{2+} promotes the pH-dependent transmembrane insertion of the remaining interfacial population.

Measurements were replicated with LUV containing 25% of the zwitterionic lipid POPE or the anionic lipid POPS. The addition of POPE or POPS-containing LUV did not result in the characteristic 4 nm Trp blue shift associated with the interfacial State II of pHLIP in the absence of Ca^{2+}. This effect has been previously described and relates to the formation of the spectroscopically silent interfacial State II^S (Fig. 3.4c and 4e, black dashed line) [26]. Regardless of the starting interfacial form, the incremental addition of Ca^{2+} resulted in concentration-dependent Trp blue shifts. The observed endpoint between the different LUV used were similar with a 12 nm decrease from 356 nm in the absence of Ca^{2+} to 344 nm at 5.0 mM Ca^{2+} observed for 25POPE:75POPC (Fig. 3.4c). While a 14 nm decrease from 356 nm to 342 nm was observed in the case of 25POPS:75POPC LUV under the same conditions (Fig. 3.4e). Compared to zwitterionic POPC and POPE membranes, the Ca^{2+}-dependent transition of pHLIP into its transmembrane State III was significantly steeper in the presence of the anionic POPS lipids. This

suggests that the POPS lipids exposed in the membranes of cancer cells promote the Ca^{2+}-dependent membrane insertion of pHLIP.

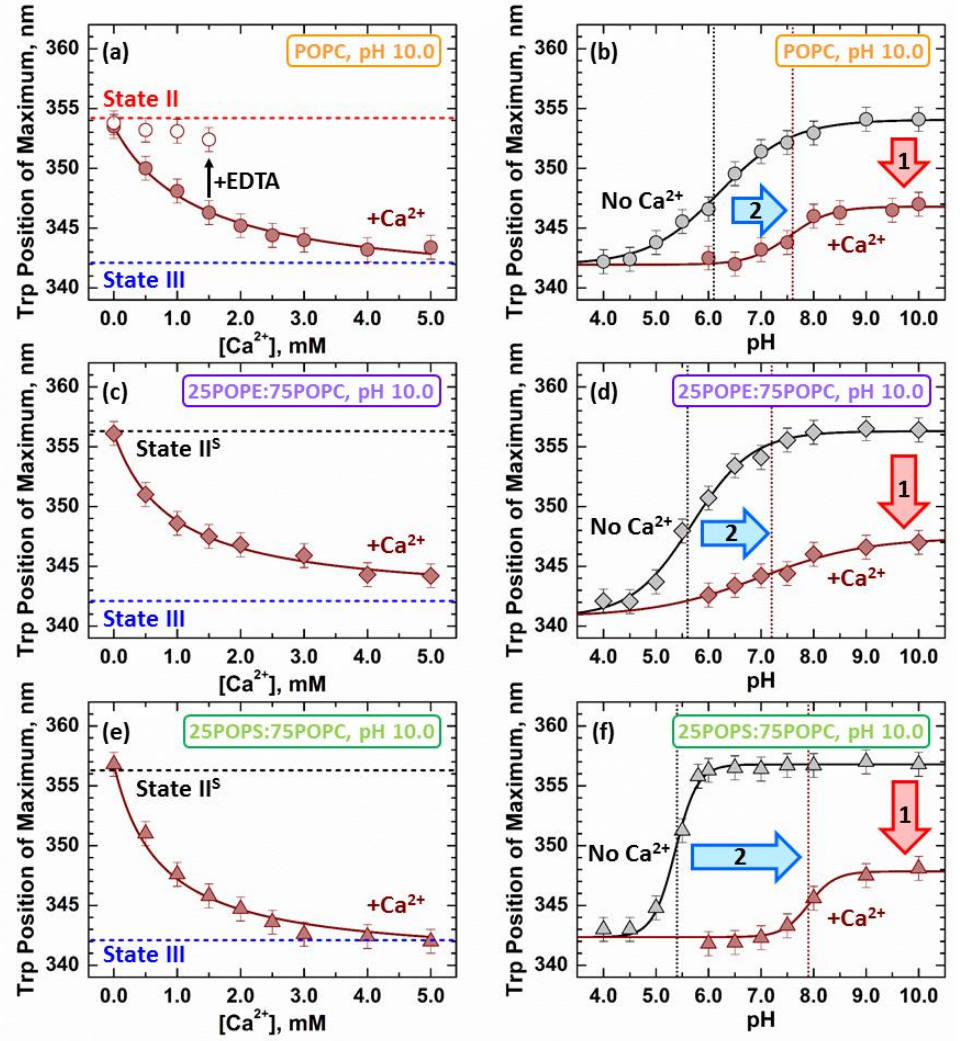

FIGURE 3.4. Lipid modulation of Ca^{2+}-dependent membrane interactions of pHLIP.

Ca^{2+} titrations at constant pH 10.0 and pH-titrations in the presence of 2.0 mM Ca^{2+} were performed in the presence of POPC (a, b), 25POPE:75POPC (c, d), or 25POPS:75POPC (e, f) LUV. (a, c, and e) The intrinsic fluorescence of pHLIP was measured at pH 10.0 and increasing [Ca^{2+}]. Positions maximum for the two known interfacial forms of pHLIP (State II in POPC and II^S in non-POPC LUV) and transmembrane State III are indicated by the horizontal dashed lines [103]. Incremental addition of Ca^{2+} at pH 10.0 resulted in large concentration dependent blue shifts regardless of lipid composition (filled circles). In all cases saturation was achieved at the Trp positions of maxima expected for the transmembrane State III of pHLIP. The large spectral changes observed show that Ca^{2+} induces the transmembrane insertion of pHLIP without any acidification, even at pH 10.0 (red arrows). Addition of EDTA reversed the Ca^{2+}-dependent spectral changes (open circles). (b, d, and f) The presence of 2.0 mM Ca^{2+} promoted the pH-dependent insertion of pHLIP into all LUV compositions tested, indicated as an increase in its transition pK_a (blue arrows). A 1.5 pH unit increase was observed POPC from 6.1 ± 0.1 to 7.6 ± 0.1 and a 1.5 pH shift from 5.7 ± 0.1 to 7.2 ± 0.1 was calculated for the 25POPE:75POPC LUV. While a larger 2.4 pH unit shift from 5.4 ± 0.1 to 7.8 ± 0.1 was detected in 25POPS:75POPC LUV. The transition pK_a of each curve is graphically indicated by color-coded vertical dotted lines.

The insertion of pHLIP was also measured for 25POPE:75POPC (Fig. 3.4 c, d) and 25POPS:75POPC LUV (Fig. 3.4 e, f). Overall the effects of Ca^{2+} in these lipid compositions are qualitatively similar to those in pure POPC (Fig. 3.4 a, b), and are characterized by the induction of insertion at neutral and basic pH (arrow 1, Figs. 3.4 b, d, f) and changes in pK_a for acid-induced insertion (arrow 2). The quantitative effects, however, are lipid dependent. In the absence of Ca^{2+}, the lipid-dependent changes in pK_a are consistent with those reported previously [47, 102, 103]. Namely, the insertion in mixed lipid compositions requires stronger acidic environment (*e.g.*, pK_a = 5.8 ± 0.1 in 25POPE:75POPC LUV and a pK_a = 5.4 ± 0.1 in 25POPS:75POPC LUV) as compared to pure POPC (pK_a = 6.1 ± 0.1 for POPC). The presence of 2.0 mM Ca^{2+} leads to a blue shift in the Trp fluorescence maxima at pH 10.0 as well as a move of the titration curves towards alkali pH, regardless of lipid composition. The magnitude of the associated changes, however, is modulated by lipid composition and were particularly prominent for the protonation-dependent insertion of pHLIP. In the case of the zwitterionic 25POPE:75POPC LUV the presence of Ca^{2+} led to a 1.5 pH unit increase in pK_a from 5.7 to 7.2 (Fig. 3.4d). Meanwhile, the anionic 25POPS:75POPC LUV showed a larger 2.4 pH unit increase from 5.4 to 7.8 between samples lacking and containing Ca^{2+}, respectively (Fig. 3.4d). Together with the Ca^{2+} titration measurements, these results reveal a strong lipid dependence for the Ca^{2+}-dependent modulation of pHLIP membrane insertion with a strong preference towards anionic POPS bilayers.

3.4.5 Effects of Ca^{2+} on the thermodynamics of pHLIP membrane insertion

Our measurements of pHLIP insertion in the presence of Ca^{2+} demonstrated the simultaneous presence of two distinct effects: (i) induction of protonation-independent membrane insertion at neutral and basic pH (Fig. 3.4 a, c, and e), and (ii) shift of the protonation-dependent insertion toward more neutral pHs (Fig. 3.4b, d, and f). To quantify the thermodynamics of both processes,

we repeated the same experiments done at 2.0 mM Ca^{2+} (presented in Fig. 3.4) at intermediate [Ca^{2+}] (Fig. B4).

The thermodynamics of the protonation-independent membrane insertion of pHLIP was characterized with the free energy term $\Delta G_{TM}^{[Ca2+]}$. This parameter was derived from the fractional insertion, f_{TM}, which was calculated using the changes in fluorescence emission maximum (Eq. 3.4) at pH 10.0 for each [Ca^{2+}] tested in our pH-titrations (Fig. B4). This thermodynamic approach is essentially identical to that used in the derivation of the so-called biological hydrophobicity scale [36] and in the quantitation of insertion by molecular dynamics simulations [105]. The results presented in Fig. 3.5a demonstrate that all lipid compositions present a similar susceptibility to this process, particularly at [Ca^{2+}] $\geq$ 1.0 mM. At lower [Ca^{2+}], however, membranes composed purely of POPC lipids show a lower susceptibility than the mixed lipid compositions. Nevertheless, at least half of the population of pHLIP is already inserted at the physiologically relevant concentrations of extracellular Ca^{2+} at neutral and acidic pH.

To examine the effects of Ca^{2+} on the thermodynamics of protonation-dependent insertion, we used the same procedure than in our previous publications on the lipid-dependent modulation of pHLIP insertion [47, 103]. Specifically, we used pH-titration plots to determine the apparent pK_a for the insertion transition (Eq. 3.2), from which the free energy was calculated using Eq. 3.3. The results presented in Fig. 3.5b show that the effect in pure POPC and 25POPE:75POPC mixtures is almost indistinguishable and saturates at about 2 kcal/mol after 1.0 mM Ca^{2+} is present. In contrast, the gain in free energy of protonation-dependent insertion in 25POPS:75POPC is more pronounced and reaches 3.0 kcal/mole at 2.0 mM Ca^{2+}.Interesting observations come from a cross-correlation analysis, in which the protonation-dependent gain in free energy is plotted against the protonation-independent (calcium-induced) free energy of insertion (Fig. 3.5c). Remarkably, the

correlations are linear, yet the slope varies dramatically with lipid composition, suggesting that the lipid composition modulates the interplay of various modes of pHLIP membrane insertion on a thermodynamic level (see discussion).

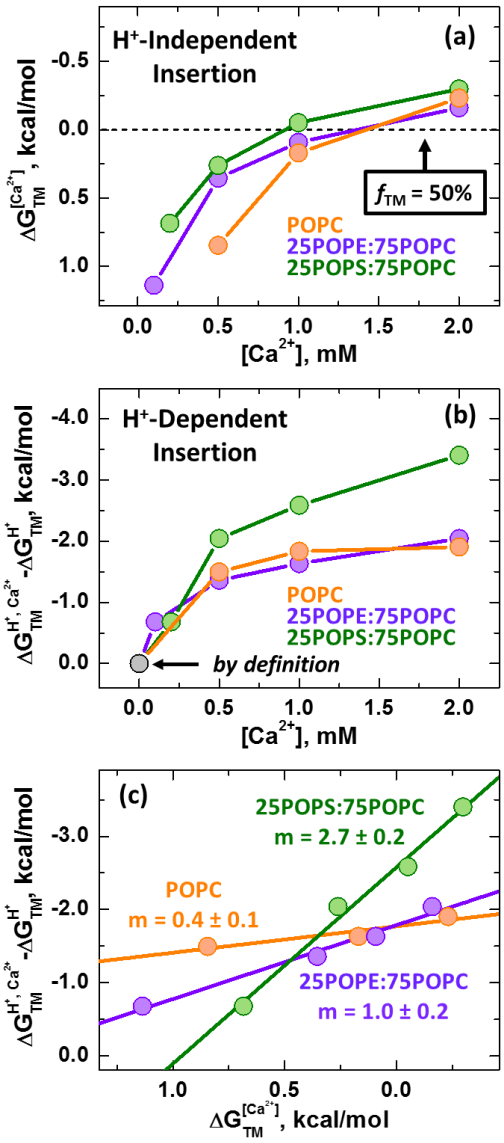

FIGURE 3.5. Effects of Ca2+ on thermodynamics of membrane insertion of pHLIP.

The membrane insertion of pHLIP into POPC (orange), 25POPE:75POPC (purple), and 25POPS:75POPC (green) LUV was measured as a function of pH at [Ca^{2+}] ranging from 0 – 2.0 mM (for complete set of raw data see Fig. B5). (a) The effect of Ca^{2+} on the free energy of pH-independent insertion of pHLIP $\Delta G_{TM}^{[Ca2+]}$, which were calculated using Eq. 3.4. This free energy is based on the fractional insertion f_{TM} measured at pH 10.0 and equals $\Delta G_{TM}^{[Ca2+]} = 0$ kcal/mol when half of pHLIP molecules are inserted (dashed line). (b) The effect of Ca^{2+} on the free energy of protonation-dependent insertion of pHLIP, calculated from the pK_a's according to Eq. 3.3. For each lipid composition,

the data are plotted as a difference between the free energy in the presence of Ca^{2+} ($\Delta G_{TM}^{H+, Ca2+}$) and the corresponding free energy in the absence of Ca^{2+} (ΔG_{TM}^{H+}). By definition, all curves originate from the common origin point (*i.e.*, $\Delta G_{TM}^{H+, Ca2+}$ - ΔG_{TM}^{H+} = 0 kcal/mol at 0 mM Ca^{2+} for each lipid composition). (c) The cross-correlation of the free energies determined for the protonation-dependent and protonation-independent insertion of pHLIP. For each concentration of Ca^{2+}, the pH-independent mode (obtained from panel a) is plotted against the free energy difference for pH-dependent mode (obtained from panel b). The lines represent the linear approximations for each lipid composition with the following parameters: Slopes: POPC = 0.4 ± 0.1, 25POPE:75POPC = 1.0 ± 0.2, and 25POPS:75POPC = 2.7 ± 0.2. Intercepts (Y value at X = 0): POPC = -1.8 kcal/mol, 25POPE:75POPC = -1.8 kcal/mol, and 25POPS:75POPC = -2.6 kcal/mol.

3.4.6 Comparison of Ca^{2+} and Mg^{2+} dependent effects

To determine whether other divalent cations exhibited an effect similar to that of Ca^{2+}, we repeated our experiments with LUV in the presence of 2.0 mM Mg^{2+}. Similar to Ca^{2+}, incremental increases in [Mg^{2+}] at constant pH 10.0 in the presence of POPC LUV showed concentration-dependent Trp blue shifts (Fig. B5a). The endpoint at saturating Mg^{2+} concentrations, however, did not reach the expected Trp fluorescence maximum for the transmembrane State III. Instead, the signal saturated at ~ 348 nm, 6 nm higher than the 342 nm expected when the entire population is present in its transmembrane conformation (Fig. 3.4a). Similarly, Mg^{2+} titrations in the presence of zwitterionic 25POPE:75POPC LUV showed a reduced effect for Mg^{2+} compared to Ca^{2+}, resulting in a 9 nm blue shift to 347 nm from 356 nm (Fig. B5c), compared to the 12 nm blue shift in the presence of Ca^{2+} (Fig. 3.4c). Measurements with 25POPS:75POPC also showed a reduced effect when compared to Ca^{2+}. In the case of these anionic bilayers, the presence of Mg^{2+} only resulted in a 4 nm maximal blue shift to 352 nm from 356 nm in the absence of divalent cations (Fig. B5e). The inability of Mg^{2+} to yield the same blue shifts as equimolar concentrations of Ca^{2+} indicates that Mg^{2+} is less efficient in promoting the transition of pHLIP into its transmembrane state. Despite these weaker effects, the ability of Mg^{2+} to induce the transmembrane insertion of pHLIP without lowering the pH was confirmed by OCD measurements (Fig. B6). The intermediate Trp fluorescence maxima were therefore interpreted as a combination of transmembrane and interfacial pHLIP populations.

We also performed pH-titrations in the presence of 2.0 mM Mg^{2+} and vesicles with different composition (POPC, 25POPE:75POPC, and 25POPS:75POPC). As in the case of Ca^{2+}, the presence of Mg^{2+} led to a decrease in the Trp fluorescence maximum at pH 10.0 compared to measurements in the absence of divalent cations (Fig. B5b, d, and f). This is consistent with the Mg^{2+}-dependent insertion of pHLIP into membranes without the need for protonation. This effect appears to be more moderate with Mg^{2+} than with Ca^{2+} (Fig. 3.4b, d, and f). The decrease in Trp position of maximum at pH 10.0 was accompanied by a shift of the curves towards alkali pH (Fig. B5, blue arrows). The magnitude of this shift, however, was reduced compared to equimolar concentrations of Ca^{2+}. In the case of POPC, the presence of 2.0 mM Mg^{2+} led to a 1.0 pH unit increase in its pK_a from 6.1 ± 0.1 to 7.1 ± 0.1 (Fig. B5b), compared to the 1.5 pH units gain in the case of Ca^{2+} (Fig. 3.4b). Similarly, the presence of 2.0 mM Mg^{2+} increased the pK_a of the pH-dependent insertion of pHLIP into 25POPE:75POPC LUV by 0.3 pH unit shift from 5.7 ± 0.1 to 6.1 ± 0.1 (Fig. B5d), compared to 1.0 pH unit in the presence of Ca^{2+} (Fig. 3.4d). A shift of the pH-titration curve towards a more basic pH range was also observed for 25POPS:75POPC bilayers when 2.0 mM Mg^{2+} was present (Fig. B6f). The shorter buffering range of HEPES buffer compared to the traditional phosphate buffer (see methods for details), however, limited our measurements to pH ≥ 6.0. This prevented us from accurately determining the pK_a under these conditions, but it was estimated to be ≤ 6.0 compared to 5.4 in the absence of Mg^{2+}.

Our measurements with Mg^{2+} show that the modulation of pHLIP membrane insertion is not specific to Ca^{2+}, suggesting a more general role of divalent cations in this process. Nevertheless, in all lipid compositions, the addition of Ca^{2+} had a more prominent effect compared to that of Mg^{2+}. Preferential effects of specific divalent cations, particularly for calcium, on protein membrane interactions have been previously observed for other systems such as α-synuclein [115],

highlighting the importance of proper cation conditions when characterizing membrane active proteins.

3.5 DISCUSSION

The results presented here provide new insights into our understanding of the physicochemical mechanisms underlying the ability of pHLIP to target tumors and other disease tissues. The standard pH-dependent targeting mechanism involves protonation of key acidic residues (*e.g.*, D14 and D25) [67, 69, 116] and subsequent membrane insertion. At mildly acidic pH (pH < 6.0), pHLIP adopts a transmembrane conformation, with characteristic spectroscopic signatures that have been well-established for model membrane systems [44, 70, 111]. Here, we demonstrated that addition of either Ca^{2+} or Mg^{2+} at neutral or even basic pH, results in the same fluorescence and CD changes as those usually observed at low pH (Fig. 3.3). The addition of divalent cations produces two independent effects: (1) pH-independent insertion at neutral and basic pH (arrows 1 in Fig. 3.4b, d, f and Fig. B6b, d, and f), and (2) modulation of pKa for the acid-driven insertion (arrows 2 in Fig. 3.4b, d, f and Fig. B6b, d, and f). These effects are depicted by a red and blue arrows respectively in Fig. 4.6. Both effects have been found to be modulated by the lipid composition (Figs. 4.4, 4.5), which might be a contributing factor in tumor targeting [28-30, 113, 114].

We illustrate the effects of divalent cations on the bilayer insertion of pHLIP using the schemes in Fig. 3.6a. The top panel contains a standard pH-dependent insertion scheme [47, 70, 103], which depicts the conversion of the interfacial unfolded state, populated at high and neutral pH, and the transmembrane helical state, populated al low pH. Insertion is characterized by the transition pK_a, which is influenced by both mutations of pHLIP [47, 62, 103, 104] and variations in lipid composition [47, 68, 102, 103, 112]. The free energy for this protonation-dependent transition, ΔG_{TM}^{H+}, is calculated from the pK_a's using Eq. 3.3. The presence of divalent cations investigated here requires revising this standard pH-dependent insertion scheme (Figure 3.6a, lower panel).

The pH-dependent transition is characterized by a free energy $\Delta G_{TM}^{[Ca2+]}$, calculated using Eq. 3.4; and the results are presented in Fig. 3.5a. The pH-independent transition is best described by the difference in free energies of protonation in the presence and absence of Ca^{2+} $\Delta G_{TM}^{H+,\ Ca2+}$ - ΔG_{TM}^{H+}, calculated separately for each lipid composition (Fig. 3.5b). The cross-correlation analysis of the free energies of pH-dependent and pH-independent effects of Ca^{2+} is shown in Fig. 3.5c and discussed below.

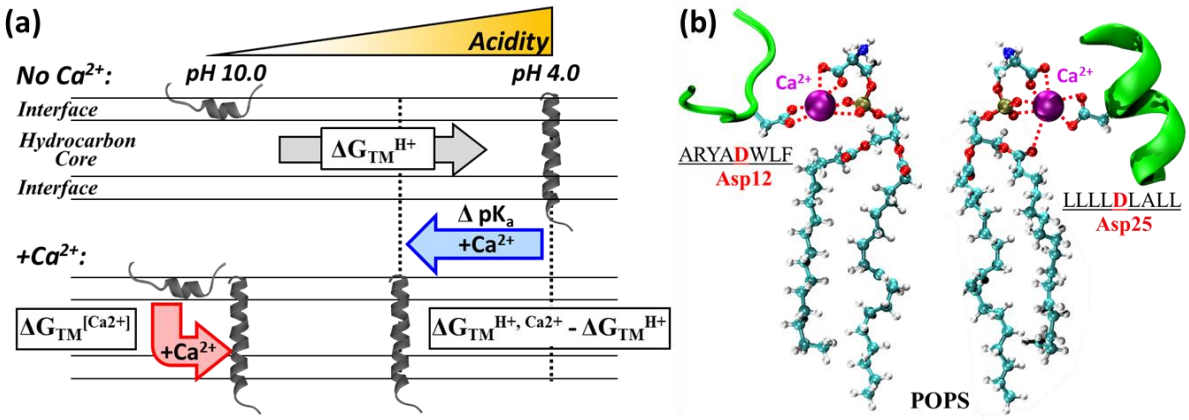

FIGURE 3.6. Thermodynamic scheme of pHLIP membrane interactions.

(a) Thermodynamic scheme of pHLIP membrane insertion in the presence and absence of Ca^{2+}. In the absence of divalent cations, the only factor driving the membrane insertion of pHLIP is its protonation-dependent insertion with a ΔG_{TM}^{H+}. The presence of Ca^{2+} leads to a more favorable protonation-dependent insertion (lower acidity levels required for insertion) with a free energy of $\Delta G_{TM}^{H+,\ Ca2+}$ - ΔG_{TM}^{H+}. Additionally, Ca^{2+} introduces a new pH-independent membrane insertion free energy with a $\Delta G_{TM}^{[Ca2+]}$. While the scheme only shows the free energies in the presence of Ca^{2+}, other divalent cations (*e.g.*, Mg^{2+}) with corresponding free energies are also expected to modulate pHLIP insertion (see Supplementary Fig. B5). (b) Schematic representation of pHLIP fragments in a putative unstructured and helical conformation (green) bound to POPS lipids in the presence of Ca^{2+} (purple). The coordination of Ca^{2+} by Asp 12 or Asp 25 in pHLIP and the known possible coordination sites of divalent cations [117-119] in POPS lipids is indicated by dashed red lines. In case of POPC, the interactions coordinating to serine group on the lipid will be absent (*e.g.*, top two dashed lines), resulting in weaker coupling of lipid-Ca^{2+}-protein interactions.

The interplay between lipid composition and calcium concentrations on pHLIP membrane insertion is best illustrated by the plots of the corresponding free energies for pH-dependent and calcium-induced insertion (Fig. 3.5c). For pure POPC, the dependence is rather shallow, suggesting a limited ability of pH-dependent modulation by Ca^{2+} on the insertion of pHLIP. For a

25POPE:75POPC lipid composition, the slope equals one, suggesting that both effects are equally important. The presence of 25% POPS results in a dramatic increase of the slope, indicating that POPS when coupled with Ca^{2+} strongly promotes pH-dependent insertion. We speculate that the reasons for this lipid-dependent modulation of insertion thermodynamics may be related to the ability of different lipids to co-coordinate divalent cations with the acidic sidechains of pHLIP (Fig. 3.6b).

It has been long established that interactions of cations with lipid bilayers depend on the nature of the cation and the lipid headgroups [120]. However, the complex nature of these interactions is still an active area of experimental and computational research. For example, Melcrova and co-authors recently demonstrated that lipid membranes have substantial calcium-binding capacity, with several types of binding sites present [117]. It is worth noting that the mechanism of action of Ca^{2+} and Mg^{2+} on the insertion of pHLIP is not likely to involve changes in surface potential. This is evident from the fact that the effects of divalent cations led to pK_a shifts in the opposite direction as those caused by the decrease in surface potential due to the additions of high concentrations of monovalent cations [121] or the decrease of anionic lipid content [47, 103]. While the exact nature of the coupling between lipid headgroups and divalent cations in the insertion of pHLIP requires further investigation, it is reasonable to assume that the ability of Ca^{2+} and Mg^{2+} to coordinate bonding with lipid headgroups and acidic residues, plays an important role. This effect has been illustrated in Fig. 3.6b, which shows the putative interaction between POPS lipids and the unstructured and helical conformations of pHLIP (Fig. 3.6b, green) in the presence of Ca^{2+}. We hypothesize that divalent cations (Fig. 3.6, purple spheres) mediate this interaction through anionic residues in pHLIP (*e.g.*, D14 and D25, indicated in red), which are involved in its protonation-mediated folding and insertion [43, 67, 69, 116]. It should be noted that in the case of

POPS we expect Ca^{2+} and Mg^{2+} to be coordinated not just by the phosphates present in the lipids and anionic groups in pHLIP (dashed lines), but also by the POPS anionic head group or possibly its ester oxygens [117-119]. Zwitterionic lipids on the other hand lack a coordination group in their head group, which would lead to lower binding of divalent cations and a lessening of the Ca^{2+}/Mg^{2+} -mediated effects on pHLIP insertion. Similar interactions have been suggested for other membrane-binding proteins in the literature [115, 122-124].

How does this new knowledge on the role of Ca^{2+} and Mg^{2+} change our understanding of the mechanism of selective targeting of tumor cells by pHLIP? The conventional explanation relies on the mild acidification produced by tumors, which lowers the outside pH to ~7.0, supposedly providing the necessary selectivity [100]. While plausible for zwitterionic lipids, this explanation does not hold in the presence of anionic POPS. As demonstrated in Fig. 3.4f (black) and in our previous publications [47, 103], no pHLIP insertion into 25POPS:75POPC bilayer is observed at pH >5.8. Since the transfer of phosphatidylserine to the outer leaflet of the plasma membrane is known to occur in cancerous cells, other mechanisms besides acidification are expected to contribute to targeting selectivity. Here, we demonstrate that divalent cations constitute an important factor, modulating interactions of pHLIP with model membranes and cells alike. The presence of physiological concentrations of Ca^{2+} improves both cellular labeling (Fig. 3.1) and drug delivery by pHLIP (Fig. 3.2). This has important implications for the optimization of cancer imaging and targeted drug delivery strategies that rely on pHLIP variants and similar membrane-active peptides. Future strategies should account for both pH-dependent and divalent cation-dependent mechanisms as well as lipid variations in targeted cells. Moreover, the modulation of the protonation-dependent insertion pathways with Ca^{2+} and Mg^{2+} may be important for

conformational switching in other physiological processes (*e.g.*, entry of bacterial toxins [4, 6] and insertion of apoptotic regulators [125, 126]).

3.6 CONTRIBUTIONS

Vasquez Montes V. designed, performed and analyzed all biophysical assays and wrote the manuscript. Gerhart. J. (Thevenin lab at Lehigh University) synthesized the peptide and designed and performed all cellular assays.

Chapter 4: Modulation of Bcl-xL Membrane Insertion and Refolding by Lipid Headgroups

This chapter has been previously published as Vasquez-Montes, V., M. Vargas-Uribe, N.K. Pandey, M.V. Rodnin, R. Langen, and A.S. Ladokhin, Lipid-modulation of membrane insertion and refolding of the apoptotic inhibitor Bcl-xL. Biochim Biophys Acta Proteins Proteom, 2019. 1867(7-8): p. 691-700 doi: 10.1016/j.bbapap.2019.04.006. It is reprinted here with permission in whole without any adaptations since the original publication.

4.1 ABSTRACT

Bcl-xL is a member of the Bcl-2 family of apoptotic regulators, responsible for inhibiting the permeabilization of the mitochondrial outer membrane, and a promising anti-cancer target. Bcl-xL exists in the following conformations, each believed to play a role in the inhibition of apoptosis: (a) a soluble folded conformation, (b) a membrane-anchored (by its C-terminal α8 helix) form, which retains the same fold as in solution and (c) refolded membrane-inserted conformations, for which no structural data are available. Previous studies established that in the cell Bcl-xL exists in a dynamic equilibrium between soluble and membranous states, however, no direct evidence exists in support of either anchored or inserted conformation of the membranous state in vivo. In this in vitro study, we employed a combination of fluorescence and EPR spectroscopy to characterize structural features of the bilayer-inserted conformation of Bcl-xL and the lipid modulation of its membrane insertion transition. Our results indicate that the core hydrophobic helix α6 inserts into the bilayer without adopting a transmembrane orientation. This insertion disrupts the packing of Bcl-xL and releases the regulatory N-terminal BH4 domain (□1) from the rest of the protein structure. Our data demonstrate that both insertion and refolding of Bcl-xL are modulated by lipid composition. We hypothesize that conformational rearrangements associated with the bilayer insertion of Bcl-xL result in its switching to a so-called non-canonical mode of apoptotic inhibition. Presented results suggest that the alteration in lipid composition before and during apoptosis can serve as an additional factor regulating the permeabilization of the mitochondrial outer membrane.

4.2 INTRODUCTION

The critical step in triggering apoptosis is the permeabilization of the mitochondrial outer membrane (MOM), which releases apoptotic factors into the cytosol ultimately leading to cell death [24, 127]. MOM permeabilization (MOMP) is controlled and executed by the numerous proteins of the Bcl-2 family [14, 48, 49], which include three types: pro-apoptotic pore formers (*e.g.*, Bax, Bak), anti-apoptotic pore inhibitors (*e.g.*, Bcl-xL, BCL2), and BH3-only regulators (*e.g.*, Bid, Bim) [13, 128]. According with the prevailing "Embedded Together" model, many functional interactions between Bcl-2 family proteins occur in membranes [12-14], however, the mechanisms by which the membrane induces conformational changes and modulates protein–protein interactions remain largely unknown [49, 129]. The main role of Bcl-xL in the cell is to prevent MOMP by interacting with and blocking pro-apoptotic pore forming proteins like Bax [9, 50-54]. The molecular details of this process, are not known, and multiple modes of inhibition have been suggested [14, 49, 52, 53, 56]. Consistent with the postulated multiple modes of action, Bcl-xL exists in several conformations, both soluble and membranous (Fig. 4.1).

The structure of Bcl-xL in solution is derived from high-resolution structures of the soluble construct Bcl-xL ΔTM, lacking its hydrophobic C-terminal α8 helix (Fig. 4.1a). The structure consists of a globular arrangement of α-helices with helices α5-α6 forming the hydrophobic core (Fig. 4.1, cyan) [130-132]. The structural and functional features of Bcl-xL bound to the membrane, however, are less clear. The only available structure of a lipid-associated form is the NMR structure of the bilayer anchored form of Bcl-xL Δ45-82 (Fig. 4.1b), a construct with a deleted long loop between helices α1 and α2 [133]. The anchoring was achieved not by insertion into a membrane mimetic, but by forming nanodiscs around the hydrophobic α8 helix, and the resulting fold was found to be the same as in the soluble form of Bcl-xL ΔTM [133]. Previous

studies established that in the cell Bcl-xL exists in a dynamic equilibrium between soluble and membranous states [9, 52-54, 56], and the anchored conformation is often assumed for the latter. Nevertheless, no direct evidence exists in support of either anchored or inserted conformation of the membranous state *in vivo*.

Very little is known about the structure of the membrane-inserted conformation of Bcl-xL (Fig. 4.1c), other than it does not require the presence of its C-terminal α8 helix, and is likely to involve substantial refolding and membrane insertion of the α5-α6 helical hairpin [125, 134-137]. The proposed model of membrane-inserted Bcl-xL, in which α5-α6 adopts a transmembrane (TM) conformation [5, 6, 138, 139], is based on the topology of the bilayer-inserted translocation domain in diphtheria toxin, which shares the solution fold with many Bcl-2 proteins, including Bcl-xL [10, 130]. This model has not been verified experimentally.

Previously, we compared the protonation-triggered membrane insertion pathway of Bcl-xL to that of diphtheria toxin and found that lipids can play a far more prominent role in the insertion of Bcl-xL [137]. Here we follow up with direct testing of the putative insertion model of Bcl-xL using EPR and fluorescence spectroscopy. We also use FRET to examine the insertion-related refolding of Bcl-xL, specifically the release of the N-terminal BH4 (α1) regulatory domain from the folded structure. The latter is relevant to the so-called non-canonical mode of apoptotic inhibition, suggested for the close functional homologue of Bcl-xL, BCL2 [140]. Our results demonstrate that alteration in lipid composition can serve as a regulatory factor for preparing Bcl-xL for the switching between the canonical and non-canonical forms of inhibition.

4.3 MATERIALS AND METHODS

4.3.1 Materials

All lipids used in this study: Palmitoyl-oleoyl-phosphatidylcholine (POPC), palmitoyl-oleoyl-phosphatidylglycerol (POPG), palmitoyl-oleoyl-phosphatidylserine (POPS), palmitoyl-oleoyl-phosphatidic acid (POPA), 1,1,2,2-tetraoleoyl-cardiolipin (TOCL), 1-palmitoyl-2-stearoyl-(5-doxyl)-sn-glycero-3-phosphocholine (5-Doxyl PC), 1-palmitoyl-2-stearoyl-(10-doxyl)-sn-glycero-3-phosphocholine (10-Doxyl PC), 1-palmitoyl-2-stearoyl-(12-doxyl)-sn-glycero-3-phosphocholine (12-Doxyl PC), 1-palmitoyl-2-stearoyl-(14-doxyl)-sn-glycero-3-phosphocholine (14-Doxyl PC), 1,2-dipalmitoyl-sn-glycero-3-phospho(tempo)choline (TEMPO-PC) were purchased from Avanti Polar Lipids (Alabaster, AL). Fluorescent dyes: IANBD-ester and AlexaFluor488-maleimide were obtained from Invitrogen (Carlsbad, CA)

4.3.2 Cloning, expression and labeling

mCherry2-C1 plasmid containing the mCherry encoding gene was purchased from Adgene (Cambridge, MA). The mCherry insert was PCR amplified using the following forward and reverse primers: GCGTATGCGGCCGGTGAGCAAGGGCGA-GGAGGATAAC and CGCATACCGGCCGGGTCCGCCGTTGTACAGCTCGTCCAT, both containing EagI sites. Both the insert and pET28b plasmid containing the Bcl-xL gene [137] were cleaved by EagI and ligated overnight at 4 ^{o}C. The presence of the insert was determined by the red coloring from expressed mCherry in colonies grown on 1.0 mM IPTG containing plates and confirmed by sequencing. The resulting construct contained a N-terminal 6His-tag followed by mCherry at the N-terminus of Bcl-xL connected through a flexible 6 amino acid linker (GGPGRH) in-between mCherry and Bcl-xL. The desired mutations were introduced using QuickChange Site-Directed Mutagenesis Kit (Stratagene, La Jolla, CA). BL23DE3pLysS cells were transformed with the prepared plasmid for the recombinant expression of the construct. Single colonies were grown

overnight in 5.0 mL of LB media supplied with 50 mg/mL of kanamycin. Overnight cultures were inoculated in 500 mL flasks with LB + 50 mg/mL kanamycin and grown to an OD_{600} = 0.6 at 37 ^{o}C. At this point the temperature was decreased to 24 ^{o}C and the synthesis of recombinant protein was induced by the addition of 0.8 mM IPTG. After 18 hours the cells were centrifuged at 4000 rpm for 15 min and frozen overnight at -80^{o}C. Cells were thawed and resuspended in binding buffer containing 50 mM Tris-HCl, pH 8.0, 300 mM NaCl, and 5.0 mM imidazole and lysed by sonication. Cell debris was removed by centrifugation (10000 rpm, 30 min) and the clarified lysate was bound overnight to Ni-agarose. After several washes the bound protein was eluted with 0.5 M imidazole in binding buffer and further purified by FPLC on a Superose6 1x30 cm column in 50 mM Na-phosphate buffer, pH 8.0. The purity of mCherry-Bcl-xL containing fractions was checked by SDS-PAGE and the concentration determined using the following molar extinction coefficients: 41000 $M^{-1}cm^{-1}$ for Bcl-xL only, 72200 $M^{-1}cm^{-1}$ for mCherry-Bcl-xL at 280 nm and 72000 $M^{-1}cm^{-1}$ at 587 nm for mCherry. Bcl-xL ΔTM was treated with 4x molar excess MTSL ((1-oxy-2,2,5,5-tetramethyl-d-pyrroline-3-methyl)-methanethiosulfonate) for EPR measurements. Excess MTSL was removed with PD10 columns. The final concentration of MTSL Bcl-xL was assessed using ε = 36440 M^{-1} cm^{-1}. Fluorescent labeling with IANBD and Alexa 488 was performed using a standard labeling protocol for thiol-reactive dyes [141]. Excess dye was removed by gel-filtration in a Superose 6 1x30 cm column.

4.3.3 LUV preparation

Large unilamellar vesicles (LUV) were prepared by drying the required volume of chloroform lipid stocks under a nitrogen stream before overnight drying using high vacuum. Dried lipid films were re-suspended in 50 mM phosphate buffer (pH 8.0 for fluorescent measurements or 7.4 for EPR experiments) to a final concentration of 20 mM and vortexed. Rehydrated lipid solutions for

EPR measurements were subjected to 7-10 freeze-thaw cycles. LUV were formed by extrusion using a Mini-Extruder (Avanti Polar Lipids, Alabaster, AL) through nucleopore polycarbonate membranes of 0.1 μm pore size (Whatman, Philadelphia, PA). LUV stocks were stored at -4°C in 50 mM phosphate buffer, pH 8.0 [75, 76]. LUV used in depth-dependent quenching experiments were prepared by including 30% molar content of the appropriate spin-lipid into the lipid mixture prior to nitrogen drying.

4.3.4 Fluorescence measurements and analysis

Steady-state fluorescence emission experiments were performed using a SPEX Fluorolog FL3-22 steady-state fluorescence spectrometer (Jobin Yvon, Edison, NJ) equipped with double-grating excitation and emission monochromators. Measurements were made using a 2x10 mm cuvette oriented perpendicular to the excitation beam and maintained at 25 °C using a Peltier device from Quantum Northwest (Spokane, WA.). All measurements were collected after the sample was equilibrated for at least 20 minutes. All spectral measurements were collected with 1.0 nm steps. FRET measurements between mCherry and A488 were collected between 480-720 nm using an excitation wavelength of 465 nm. Membrane insertion measurements using NBD labeled Bcl-xL were collected from 490 to 700 nm using an excitation wavelength of 470 nm. Depth-dependent measurements used an excitation wavelength of 465 nm. All emission measurements were collected using 5.0 nm slits on both monochromators and were averaged over 3-5 scans with at least 20 min incubation for equilibration. The samples normally contained 0.3 μM protein in 50 mM phosphate buffer at pH 8.0, unless otherwise indicated, and 1.0 mM of lipid. Sample acidification was achieved by the addition of small aliquots of acetic/acetate buffer. Fluorescence intensity of NBD measured at 510 nm was used to quantitate insertion, and fluorescence intensity

of donor (Alexa 488) measured at 520 nm was used to quantitate FRET. The pH-dependencies of both insertion and refolding were fitted to the following equation [142]:

$$I = \frac{I_N + I_L\,(10^{m(pK_a - pH)})}{1 + 10^{m(pK_a - pH)}}, \text{ (Eq. 4.1)}$$

where I is the fluorescence intensity measured as a function of pH, I_N and I_L represent the limiting intensities at high and low pH respectively, pK_a denotes the negative logarithm of the dissociation constant, and m is the transition slope.

The protonation-dependent free energies of both membrane insertion ($\Delta G_{TM}^{H^+}$) and BH4 domain release ($\Delta G_{BH4}^{H^+}$) were calculated using the determined pK_a values using Eq. 4.1 in a rearranged Gibbs free energy equation:

$$\Delta G = -2.3RT(pK_a), \text{ (Eq. 4.2)}$$

where R and T are the gas constant and absolute temperature, respectively, and the pK_a is obtained with Eq. 4.1.

4.3.5 Membrane surface potential calculations

Membrane surface potential calculations were performed using Gouy-Chapman theory [143]. This model describes the electric potential along the axial plane of the membrane, where the potential at the membrane surface Ψ_0 depends on the surface charge density σ and the concentration of counterions according to:

$$\Psi_0 = \frac{2\kappa_B T}{ze} \times \sinh^{-1}\left(\frac{\Sigma}{\sqrt{8N\varepsilon_0\varepsilon_r\kappa_B T \times c}}\right), \text{ (Eq. 4.3)}$$

Where κ_B is the Boltzmann constant (1.38 x 10^{-23} J/K), T is the absolute temperature, z is the valence of the counterion (+1 in our case), e is the elementary electric charge (-1.602 x 10^{-19} C),

N is the Avogadro number (6.022 x 10^{23} mol^{-1}), ε_0 is the permittivity in vacuum (8.854 x 10^{-12} C^2m^{-1}/J), ε_r is the dielectric constant of water (78.3). c is the concentration of counterions expressed in mol/m^3, while Σ is the surface charge density expressed in C/m^2.

The surface charge density for the different anionic LUV used was calculated according the following equation:

$$\Sigma = \frac{\chi_{AL} \times z_{AL} e}{\chi_{AL} A_{AL} + \chi_{NL} A_{NL}}, \text{ (Eq. 4.4)}$$

where z_{AL} is the net charge of the anionic lipid, χ_{AL} and χ_{NL} are the mole fractions of the anionic and neutral lipid, respectively, and A_{AL} and A_{NL} are the area per lipid of the anionic and neutral lipid, respectively, in units of m^2. For the net charges, we used values of 0 for POPC, -1 for POPG, POPS and POPA, and -2 for TOCL. For the areas per lipid, we assumed a cylindrical shape and used the cross-sectional areas described in the literature for the crystalline phase: 64 $Å^2$ for POPC [144], 66 $Å^2$ for POPG [145], 63 $Å^2$ for POPS [146], 68 $Å^2$ for POPA [147], and 130 $Å^2$ for TOCL [148]. We further assumed that the area per lipid was not affected by the mixing of different lipids, the presence of the protein, or the concentration of ions.

4.3.6 Depth-Dependent Quenching

Depth-dependent quenching profiles (QP's) were generated using measurements of NBD fluorescence quenching with a series of lipids labeled with spin probes at different depths, *h*, defined as the distance from the bilayer center. Both steady-state and time-resolved and measurements were used to determine the intensities, F(h), and lifetimes, $\tau(h)$, as a function of quencher depth and the corresponding values in the absence of quenchers, F_0 and τ_0. Because of the heterogeneity of the fluorescence decay and scattering contributions, the following procedure was employed to calculate the average time of the decay [149]: (i) Time-resolved data were

subjected to a standard deconvolution procedure that assumes three exponential components, with the shortest lifetime fixed at 0.1 ns; (ii) the amplitude-weighted average lifetime of the two longest components was used as the average τ. The two QP's were generated as follows: Steady-state (or total) QP(h) = (F_0/F(h))-1, and differential QP(h) = (F_0/F(h)) - (τ_0/τ(h)) [150]. The latter reduces the dynamic contribution from the transverse diffusion of a probe occurring during the excited-state lifetime, and has been shown to provide a more accurate position of the probe than conventional total QP, based only on steady-state measurements [150-152]. Both total and differential QP's were subjected to Distribution Analysis (DA) methodology [153, 154], which approximates the transverse quenching with a sum of two mirror-imaged Gaussian functions, G(h):

$$QP(h) = G(h) + G(-h) = \frac{S}{\sigma\sqrt{2\pi}} \exp\left[-\frac{(h-h_m)^2}{2\sigma^2}\right] + \frac{S}{\sigma\sqrt{2\pi}} \exp\left[-\frac{(h+h_m)^2}{2\sigma^2}\right], \text{(Eq. 4.5)}$$

where, h_m is the most probable depth of the probe measured from bilayer center, σ, is the dispersion of the transverse profile, and S, corresponds to the overall quenching efficiency, related to lipid exposure of a probe. A symmetrical second Gaussian distribution, G(-h), added to account for trans-leaflet quenching, is important for analyzing deeply penetrating fluorophores [155]. Both G(h) and G(-h) share the same three fitting parameters. The average positions of the spin quenchers, h, calculated from the center of the lipid bilayer have been previously determined by MD simulations of a series of spin-labeled lipids in a model membrane [156].

4.3.7 Support Plane Analysis

The robustness of the determined h_m parameters in the total quenching and differential quenching profiles obtained by DA analysis were determined by subjecting the fits to support plane analysis [79], as described previously [150]. Briefly, a series of least-square fits were generated, in which the h_m parameter was fixed at different values with 0.1-0.3 Å steps around the most optimal solution. The ratio between every X^2 value and the optimal X^2 solution (X^2_{Min}) were plotted and a

cut-off corresponding to a single standard deviation (X^2/ X^2_{Min} = 1.33) was used to identify the range of h_m values [79].

4.3.8 EPR measurements:

Power saturation experiments were performed in the range of 1.3 - 63.5 mW incident microwave power, on a Bruker EMX spectrometer equipped with a dielectric resonator. The O_2 and NiEDDA accessibilities were estimated using a previously established method [157, 158]. The O_2 accessibility (ΠO_2) was measured with samples in the presence of air and the accessibility to NiEDDA (ΠNiEDDA) was obtained by the addition of 10.0 mM NiEDDA to a sample equilibrated under a constant stream of N_2 gas. The depth parameter, Φ, was determined using the following equation:

$$\Phi = \ln\left[\frac{\pi O_2}{\pi \text{NiEDDA}}\right], \text{ (Eq. 4.6)}$$

Measurements were performed on LUV containing either 3TOCL:2POPC or 75POPG:25POPC keeping the protein:lipid ratio >1:500. Bcl-xL V161C, I166C, and A168C were measured in 3TOCL:2POPC LUV, while V161C, V163C, I166C, A167C, A168C, W169C, M170C, N175C, and H177C were measured in 75POPG:25POPC LUV.

4.4 RESULTS

4.4.1 Bcl-xL membrane insertion correlates with the release of its N-terminal BH4 domain

The insertion of Bcl-xL ΔTM into membranes from its soluble form was determined by fluorescence emission spectroscopy using the environmentally sensitive fluorophore NBD. The emission spectrum of this probe increases in intensity and the position of its maximum shifts to lower wavelengths when the probe relocates to a more hydrophobic environment (*i.e.,* lipid bilayers). These spectroscopic changes allow us to track the transition of NBD labeled Bcl-xL ΔTM from solution to membranes. NBD was introduced using the single-Cys mutant N175C located in the middle of the hydrophobic α6 helix (Fig. 4.1, cyan), expected to insert into bilayers as a function of pH [125, 134-137]. Acidification is a common way of efficiently inducing the membrane-inserted form of Bcl-xL in model systems [125, 134-137]. This is not meant to be a mimic of physiological conditions, but rather a way of extracting structural and thermodynamic information on the protonation-driven insertion transition. This methodology is similar to the use of high temperature in thermal stability studies, in which the conditions used are a tool and do not suggest that high temperatures are physiologically relevant. We have used large unilamellar vesicles (LUV) with a 1:2 ratio of cardiolipin and POPC, which approximates the cardiolipin content present at hot spots of apoptotic regulation in mitochondrial contact sites [159, 160].

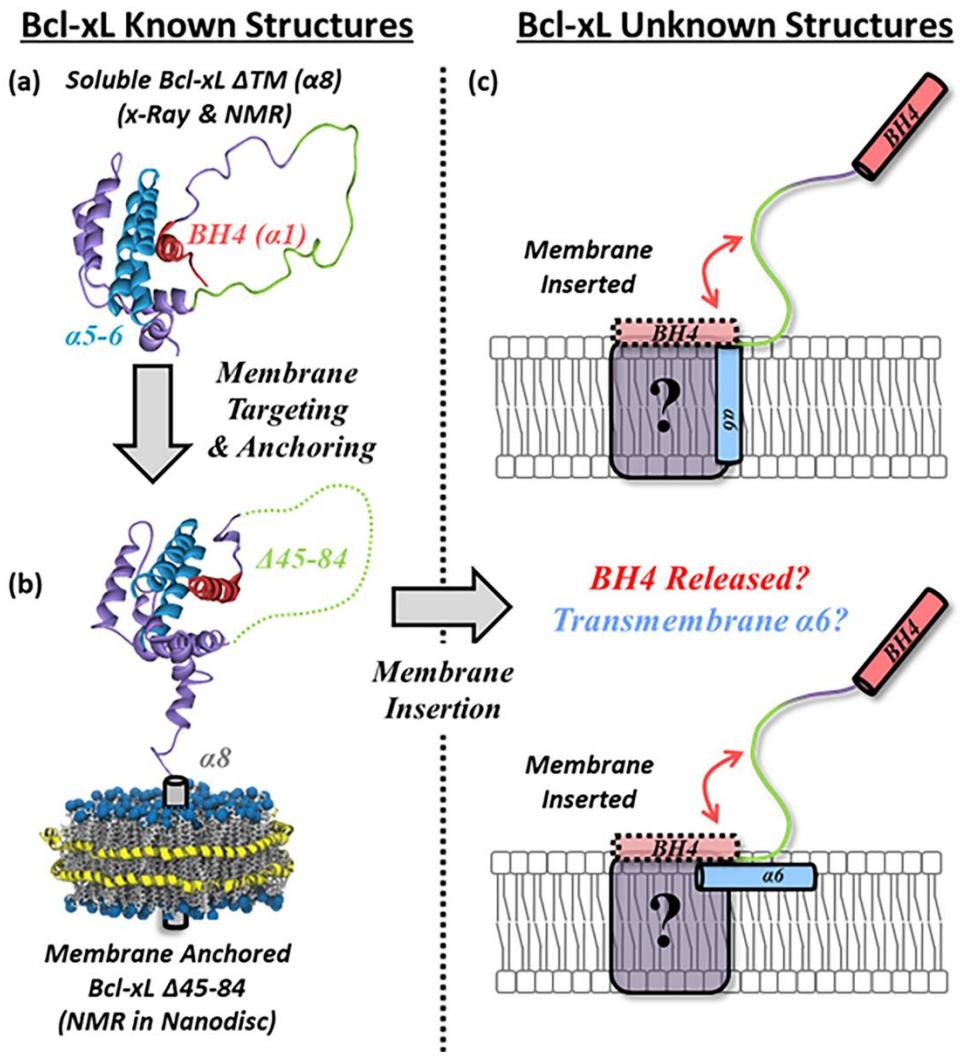

FIGURE 4.1 Bcl-xL membrane targeting/insertion and topology of membrane inserted form.

(a) The inactive form of the anti-apoptotic protein Bcl-xL exists in a soluble state that must interact with membranes to transition to its active conformation. (b) The targeting of Bcl-xL to the membrane leads to its anchoring through its C-terminal α8 helix. (c) The conformation of membrane inserted Bcl-xL, however, has not yet been determined. Here we characterize the lipid determinants that regulate the insertion of Bcl-xL into membranes. Additionally, we report the release of its N-terminal BH4 domain and its link to Bcl-xL insertion and the topology of its hydrophobic α6 helix.

Compared to Bcl-xL in solution (Fig. 4.2a, grey), the addition of 1TOCL:2POPC LUV at pH 8.0 does not result in significant spectroscopic changes (Fig. 4.2a, black). Acidification of the solution, however, leads to large pH-dependent increases in NBD intensity that saturate at pH 4.5. The intensity increase is accompanied by a blue shift of the NBD emission maxima relative to the 535.1 nm at pH 8.0 to 525.9 nm at pH 4.5. Both spectroscopic changes are associated with the transition

of NBD to hydrophobic environments and indicate the pH-dependent membrane insertion of the hydrophobic α6 helix. The transition of Bcl-xL into its inserted conformation is likely to destabilize the packing of its helices and result in its refolding in the membrane. The N-terminal BH4 helix (α1), in particular, is packed against the hydrophobic α6 helix and is connected through a long loop to the rest of the protein fold in its soluble conformation (Fig. 4.1a). Destabilization of the overall fold of Bcl-xL is likely to result in its release from the rest of the protein structure. This helix has been previously linked to apoptotic progression through a potential non-canonical anti-apoptotic mechanism [161-163], characterizing its topology on the inserted form of Bcl-xL is therefore crucial to our understanding of apoptotic repression.

The release of the N-terminal BH4 domain was characterized by conjugating the fluorescent protein mCherry to the N-terminus of Bcl-xL ΔTM. This construct was then used to perform FRET measurements between N-terminal mCherry and Alexa488 (A488) labeled Bcl-xL ΔTM. The fluorescent probe A488 was introduced using the single Cys D189C mutant, positioning the donor fluorophore in the folded structure <20 Å of the N-terminus to which the mCherry acceptor is attached. Both fluorophores form an efficient FRET pair (R_0 ~61 Å) when Bcl-xL is in solution and its BH4 domain is tucked into the main body of the protein (Fig. 4.1a). This is evident by the two bands observed in their emission spectra when only the donor A488 is excited in the presence of 1TOCL:2POPC LUV, pH 8.0 (Fig. 4.2b, blue). Acidification in the presence of membranes, however, leads to complete loss of FRET, indicated by the large increase in the intensity of the donor A488 band and the elimination of the acceptor mCherry peak at low pH (Fig. 4.2b, red). These spectroscopic changes are related to the increase in spatial distance between the donor A488 at the main body of Bcl-xL ΔTM and the N-terminal acceptor mCherry and indicate the release of the N-terminal BH4 domain. Together with the observed protonation-dependent insertion of Bcl-

xL ΔTM (Fig. 4.2a) these results suggest that the insertion of Bcl-xL into membranes leads to the release of its N-terminal BH4 domain.

To further explore the connection between the membrane insertion of Bcl-xL ΔTM and the release of its N-terminal BH4 domain we compared the relative signal changes in both events as a function of pH (Fig. 4.2c). The results are depicted as the percent change observed in the intensity signals for each respective event (NBD signal change: relative membrane insertion, % FRET loss: relative BH4 domain release). 100% release corresponds to the complete ablation of the acceptor mCherry band in FRET measurements and 100% insertion refers to the NBD intensity signal saturation observed at pH 4.5. This analysis showed that the relative changes in the insertion of Bcl-xL ΔTM into membranes completely overlapped with the release of its N-terminal BH4 domain. This overlap yielded a $pK_a = 5.8 \pm 0.1$ for both protonation-dependent transitions, indicating that both events are linked. Further kinetic studies will be required to investigate whether or not the two folding steps occur simultaneously.

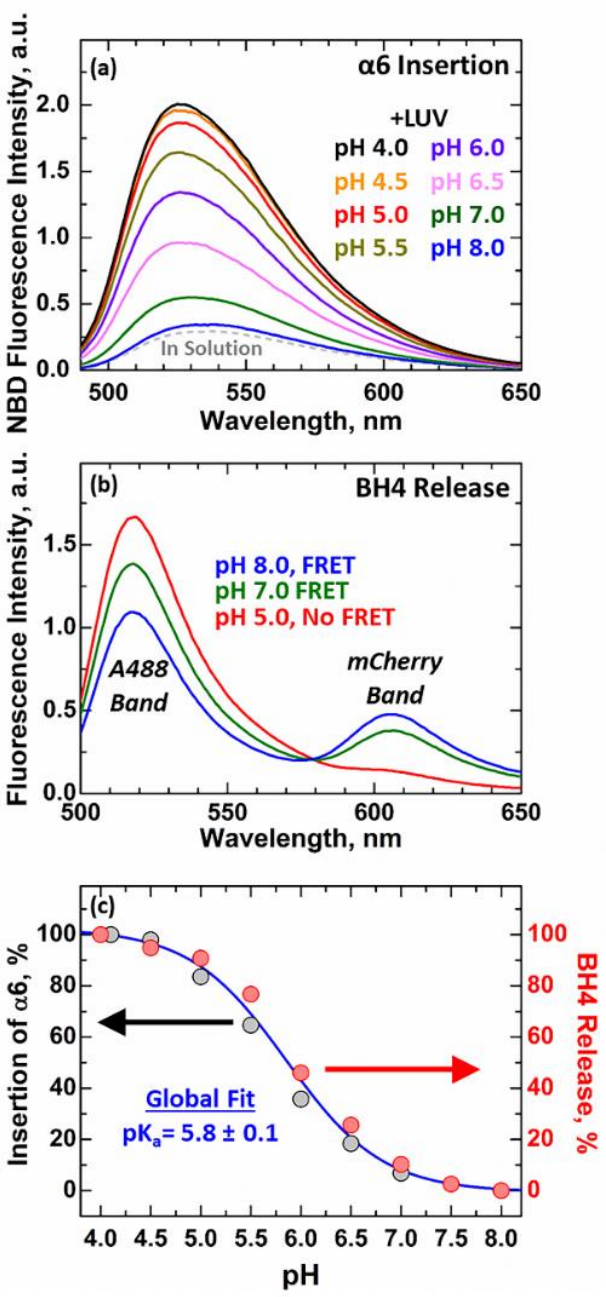

FIGURE 4.2. Protonation-dependent membrane insertion and refolding of Bcl-xL.

(a) Representative spectra of Bcl-xL ΔTM N175C-NBD inserting into cardiolipin containing LUV (1TOCL:2POPC). Increase in fluorescence intensity and blue shift in spectral position of maxima observed upon acidification in the presence of membranes are indicative of the membrane insertion of the NBD-labeled site. (b) Changes in fluorescence emission spectra of donor- and acceptor-labeled Bcl-xL ΔTM upon acidification in the presence of 1TOCL:2POPC LUV. The release of BH4 domain was determined by the loss of FRET between Alexa 488 (donor), attached to single-Cys mutant D189C, and mCherry (acceptor) fused to the N-terminus next to the BH4 domain. (c) Comparison of protonation-dependent insertion and refolding of Bcl-xL (see text for details). Both datasets can be accurately described by a single global fitting curve (blue).

4.4.2 Lipid modulation of Bcl-xL membrane insertion and BH4 domain release

The activation of the apoptotic pathway leads to changes in the molar content of several mitochondrial lipids, including cardiolipin, that have been linked to apoptotic regulation [25, 159, 160, 164-167], summarized in Fig. C1. To gain insight into the regulatory role of cardiolipin we measured the protonation-dependent insertion of Bcl-xL ΔTM into membranes containing increasing concentrations of cardiolipin (Fig. 4.3a). Our measurements show that the membrane insertion of Bcl-xL ΔTM, defined as the relative change in NBD intensity at a constant wavelength, becomes more favorable in membranes with higher cardiolipin content. This results in a 1.0 pH unit difference between the insertion pK_a of Bcl-xL ΔTM in high cardiolipin membranes containing 3TOCL:2POPC (pK_a = 6.1 ± 0.1) compared to the low cardiolipin membranes composed of 1TOCL:6POPC (pK_a = 5.1 ± 0.1). Similar measurements were performed on the full-length variant of Bcl-xL (Bcl-xL FL N175C-NBD) to determine whether the cardiolipin-dependent effect observed was affected by the absence of the α8 helix in the ΔTM construct (Fig. 4.3b). The insertion of full-length Bcl-xL into membranes containing high (3TOCL:2POPC) or low (1TOCL:6POPC) cardiolipin content did not affect the calculated insertion pK_a's compared to the ΔTM variant. The only effect of the presence of the C-terminal helix α8 is a slight increase in the apparent cooperativity of the insertion transition. As pointed out in our previous publication, thermodynamic studies with a full-length protein are extremely difficult to carry out [137], therefore we do not attribute much significance to these changes. Nevertheless, it is clear that full-length Bcl-xL undergoes a very similar insertion process.

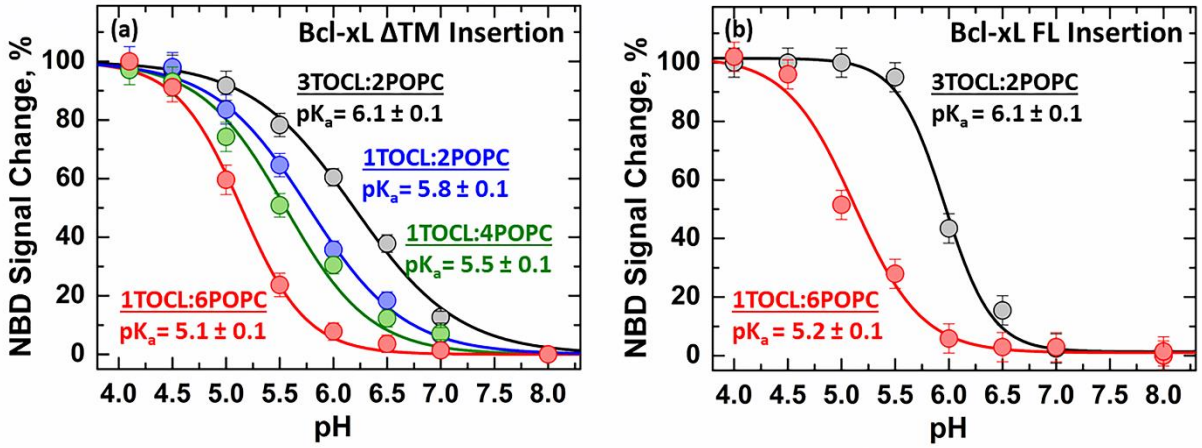

FIGURE 4.3. Membrane insertion of Bcl-xL is modulated by cardiolipin content.

The insertion of Bcl-xL was measured as a function of pH into membranes with increasing cardiolipin molar contents. Measurements were performed as in Fig. 4.2 using either Bcl-xL ΔTM (a) or full-length Bcl-xL (b). Increase in content of anionic cardiolipin shifts membrane insertion towards more neutral pH. This leads to a shift in the insertion pK_a by 1.0 pH unit between low cardiolipin (1TOCL:6POPC) and high cardiolipin (3TOCL:2POPC) membranes. The presence of the C-terminal α8 helix in the full-length protein does not affect this lipid-dependent modulation of Bcl-xL insertion.

We further explored the modulation of Bcl-xL protonation-dependent membrane insertion by anionic membrane content using four different anionic lipids present in the mitochondria: cardiolipin (TOCL), phosphatidic acid (POPA), phosphatidylserine (POPS), and phosphatidylglycerol (POPG). The structure and relative abundance of studied lipids in the mitochondria before and during apoptosis are indicated in Fig. C1. Measurements were performed by inducing the insertion of Bcl-xL ΔTM N175C-NBD as a function of pH and measuring the changes in NBD intensity at a constant wavelength. The determined pK_a's were converted into protonation-dependent membrane insertion free energies ($\Delta G_{TM}^{H^+}$) using Eq. 4.2 in the methods section. The data is depicted in Fig. 4.4 as the calculated $\Delta G_{TM}^{H^+}$ plotted against membrane surface potential, which provides a measure of the electrostatic effect at the surface of anioinic membranes (calculated using the Gouy-Chapman model as described in the methods section). Under all membrane compositions tested, the protonation-dependent free energy of transmembrane

insertion, $\Delta G_{TM}^{H^+}$, showed a linear dependence with membrane surface potential, Ψ_0 (Fig. 4.4a, solid symbols). Two different slopes arose to describe the linear releationship between Bcl-xL ΔTM membrane insertion and Ψ_0, which were dependent on the type of anionic lipid present. The mitochondrial specific lipid cardiolipin, and POPA presented the most favorable slope; meanwhile, POPG and POPS had a shallower slope. Measurements performed at the endpoints of both slopes with Bcl-xL FL show that the lipid-specific effects on Bcl-xL membrane insertion are not affected by the presence or absence of the C-terminal α8 (Fig. 4.4a, clear symbols) anchor helix. The two different slopes observed in this analysis indicate that in addition to anionic lipid content, the insertion of Bcl-xL into membranes is modulated by other factors. In particular, it correlates with differences in lipid geometry between the tested anionic lipids. In the case of cardiolipin and POPA, the lack of a moiety in their headgroup is expected to result in a shallower interface compared to POPG and POPS (Fig. C1). Additional changes to non-electrostatic membrane properties such as differences in spontaneous curvature and lateral pressure, however, cannot be disregarded.

The protonation-dependent release of Bcl-xL ΔTM N-terminal BH4 domain was also measured in membranes with different anionic lipid species to confirm its correlation to Bcl-xL ΔTM membrane insertion. BH4 domain release was measured as previously described for Fig. 4.2b by measuring the loss of FRET in the mCherry-Bcl-xL ΔTM D189C-A488 construct in cardiolipin and POPG containing bilayers. The protonation-dependent free energy of BH4 domain release ($\Delta G_{BH4}^{H^+}$) was calculated from determined pK_a's as for Fig. 4.4a and plotted against membrane surface potential, Ψ_0 (Fig. 4.4b). The calculated $\Delta G_{BH4}^{H^+}$ were compared to Bcl-xL $\Delta G_{TM}^{H^+}$ membrane insertion slopes determined in Fig. 4.4a. Our analysis shows that the calculated $\Delta G_{BH4}^{H^+}$

values overlap with $\Delta G_{TM}^{H^+}$ membrane insertion slopes regardless of lipid composition, confirming the link between BH4 domain release and Bcl-xL membrane insertion.

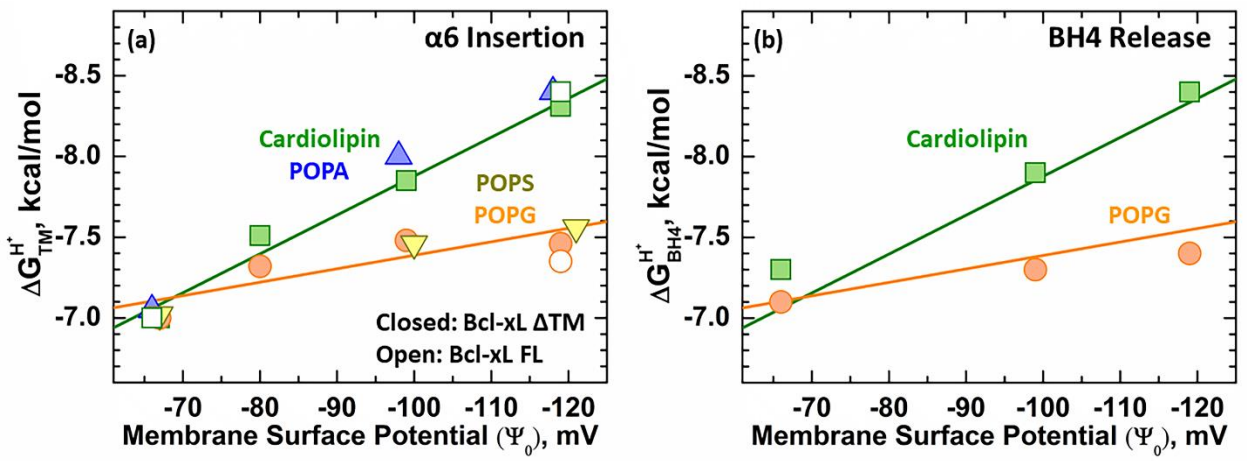

FIGURE 4.4. Effect of membrane surface potential (Ψ_0) on the insertion of α6 and release of Bcl-xL BH4 domain.

Bcl-xL membrane insertion and the release of its N-terminal BH4 domain were characterized in several anionic lipid compositions. (a) Protonation-dependent free energy of transmembrane insertion (ΔG_{TM}^{H+}) was calculated from the measured transition pK_a and plotted as a function of membrane surface potential (Ψ_0). The membrane insertion of α6 is modulated by the bilayer anionic content and lipid geometry, giving rise to two different slopes. Closed symbols represent measurements performed with the Bcl-xL ΔTM variant, while open symbols denote the results using full-length Bcl-xL. (b) Release of the N-terminal BH4 domain was modulated in the same fashion as membrane insertion. The calculated protonation-dependent free energy for the release of the BH4 domain (ΔG_{BH4}^{H+}) overlapped with the previously observed membrane insertion slopes in Fig. 4.4a. These results confirm that both, the insertion of α6 and the release of the N-terminal BH4 domain correlate in all lipid compositions.

4.4.3 Topology of hydrophobic α6 helix in membrane inserted Bcl-xL

We confirmed the membrane insertion of Bcl-xL by characterizing the topology of α6 in membrane inserted Bcl-xL. This was achieved using a combination of electron paramagnetic resonance (EPR) and fluorescence depth-dependent quenching measurements. To ensure uniformity of our membrane inserted Bcl-xL population we used 3TOCL:2POPC or 75POPG:25POPC membranes, which showed the most favorable insertion $\Delta G_{TM}^{H^+}$ (Fig. 4.4).

Measurements were performed using the Bcl-xL ΔTM variant to prevent any anchored intermediate and insertion induced by decrease in pH.

EPR experiments were first carried out to determine the membrane topology of selected residues along helix α6 in Bcl-xL ΔTM, which were replaced by spin-label R1, one amino acid at a time. (Fig. 4.5). The membrane immersion depths of spin-labeled side chains were then determined from their respective accessibilities to O_2 and NiEDDA. These measurements are based on the fact that the more hydrophobic O_2 preferentially partitions into the membrane while the more hydrophilic NiEDDA mainly remains in the aqueous environment [157, 158]. As a consequence, more deeply membrane inserted residues become progressively more accessible to O_2 and less accessible to NiEDDA. The log of the ratio of the O_2 and NiEDDA accessibilities is directly proportional to membrane immersion depth and it is typically summarized by the depth parameter Φ. As shown in Fig. 4.5, the Φ-values strongly depend on the labeling position. High values are observed for residues on the hydrophobic surface, while low (negative) values are obtained for residues on the hydrophilic helix surface. Such behavior is commonly observed for amphipathic helices that are asymmetrically solvated by the membrane on their hydrophobic side and by an aqueous environment on their hydrophilic side. The notion of an asymmetrically solvated amphipathic helix is further supported by the sinusoidal curve shown in Fig. 4.5. This curve fits the data well and has a periodicity of 3.6 amino acids, the number of amino acids required for one turn of an α-helix.

Two distinct topologies can result in asymmetric solvation of membrane helices. The first scenario is for α6 to exist in a transmembrane orientation, where it is aligned with neighboring inserted helices to form a “pore”. The second possibility is an interfacial orientation for the hydrophobic α6 helix, perpendicular to the bilayer normal. The finding that the maxima for Φ have comparable

values suggests that the immersion depth of membrane exposed residues is relatively constant. Such a behavior is typically seen for interfacial, but not transmembrane helices.

In either orientation half of the probes placed along α6 would be partially exposed to soluble quenchers, while the other half remain protected by the membrane. To distinguish between these possibilities, we performed depth-dependent fluorescent quenching using the distribution analysis (DA) methodology, which we have described recently for diphtheria toxin T-domain [150]. This technique relies on measuring the steady-state and lifetime fluorescence of NBD labeled Bcl-xL, with fluorescent probes placed along α6. Four residues were selected along the α6 helix, two in the middle: W169C and A168C and one on each end: W177C and V161C (Fig. 4.6i). Measurements were conducted on membranes with high cardiolipin 3TOCL:2POPC at pH 4.5 to ensure insertion in the presence or absence of 30 mol% spin-lipid quenchers introduced by co-extrusion (as described in the methods section). Five different spin-lipid NBD quenchers were selected with either TEMPO or Doxyl moieties attached at progressively deeper positions along the lipids [168]. Their spacing in the membrane therefore results in different quenching levels as a function of their distance to the fluorophore.

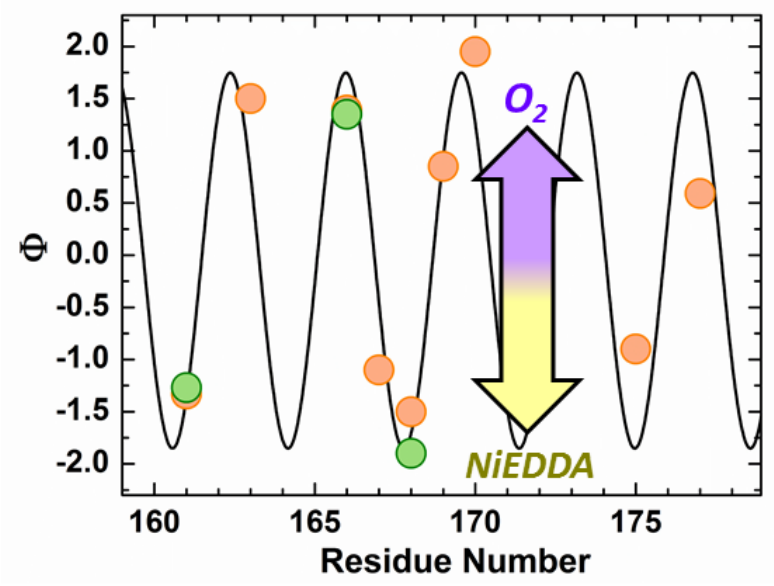

FIGURE 4.5. EPR O_2/NiEDDA accessibility of MTSL labeled helix α6 in membrane inserted Bcl-xL.

Accessibility of spin labeled Bcl-xL ΔTM single-Cys mutants inserted into 75POPG:25POPC (orange) LUV at pH 4.5. Residues that were also measured in 3TOCL:2POPC LUV at pH 4.5 are indicated in green. Results are plotted as the ratio in quenching between membrane accessible O_2 and water-soluble Ni-EDDA for each residue tested. Accessibility was determined as described in the methods section. A $\Phi > 0$ represents membrane-protected spin probes and a $\Phi < 0$ denotes a more solvent exposed probe. The black trace represents a cosine fit of the quenching data, which yielded a periodicity of 3.6 residues, consistent with an α-helix. The asymmetric protection of spin-labeled residues along α6 from O_2/NiEDDA indicates an asymmetrically solvated α-helix. EPR measurements were performed in collaboration with the Ralf Langen lab

The differential quenching profiles for the depth-dependent measurements in membranes containing 3TOCL:2POPC are shown in Fig. 4.6. They are obtained by subtracting the lifetime profile from the steady-state profile and depict the quenching distribution of the NBD fluorophore within the membrane. In the case of transmembrane helices, it is expected that residues near the center of the helix be located near the center of the bilayer at 0 Å, while the ends remain near the phosphates. All the quenching profiles of the α6 helix in membrane inserted Bcl-xL ΔTM, however, indicate that the labeled residues are far from the bilayer center. This includes residues W169C and A168C, located in the middle of the helix and indicate that the helix does not insert in a transmembrane orientation. Quantitative analysis of the depth-dependent measurements was

performed using the distribution analysis (DA) methodology. This involves fitting the quenching data to a sum of two gaussian functions (Eq. 4.5) to account for quenching from the trans-leaflet. Determined parameters include the most probable depth (h_m) and dispersion of the transverse position (σ), the colored profile depicts a data fit using a single gaussian function. Using this analysis, we determined that all tested residues were located far from the center of the bilayer at the following positions: H177C-NBD at 8.0 ± 1.2 Å, W169C-NBD at 10.6 ± 0.9 Å, A168C-NBD at 15.8 ± 0.1 Å, and V161C-NBD at 11.3 ± 1.0 Å away from the center of the bilayer (Fig. 4.6a, c, e, and g).

The robustness of the calculated depth, h_m, parameter associated with the fit was determined by subjecting both the total quenching and differential profiles to support plane analysis [79, 150] (Fig. 4.6b, d, f, and h). For this analysis the X^2 goodness of the least-square fit was determined for a series of solutions using a fixed h_m parameter around the optimal fit using 0.1-0.3 Å steps. A cutoff of 1 standard deviation (horizontal line at $X^2/X^2_{Min} = 1.33$) was used to estimate the ranges in h_m that yield an indistinguishable fit, indicated below the line. For every residue the support plane analysis shows a narrow error distribution around the optimal h_m value calculated in the differential profile using the DA analysis. The optimization of the DA analysis compared to using raw data to analyze depth dependence can be clearly shown in the case of A168C-NBD (Fig. 4.6f). The support plane analysis shows that in the case of this residue the error associated with the fit of the raw data was greater than the thickness of a monolayer (h_m= [15.0 ÷ >20 Å]). In contrast, a more defined fit is obtained by subtracting the dynamic quenching component, resulting in a more accurate error distribution. Together with our EPR measurements, these results confirm an asymmetrically solvated α6 helix in a deep interfacial orientation (Fig. 4.6i). The variance in depth between these residues was attributed to differences in the orientation of the tested labeled residues

along the interfacial helix. Primary steady-state (blue triangles) and lifetime (green squares) data collected for all tested mutants is presented in Fig. C2. The lower quenching levels observed with the lifetime data (green) compared to the total quenching (steady-state, blue) are common [150-152] and reflects the "dynamic" component of the quenching process occurring on timescales longer than 0.1 ns.

Depth-dependent quenching measurements were also carried out in membranes containing 75POPG:25POPC (equivalent Ψ_0 as 3TOCL:2POPC). Two mutants in the middle of α6 were selected for these measurements: W169C-NBD and A168C-NBD. Both residues yielded depths far from the center of the bilayer, with DA analysis placing them at $h_m = 9.9 \pm 0.5$ Å for W169C-NBD and $h_m = 11.3 \pm 0.5$ Å for A168C-NBD (Fig. C3). These results are consistent with our experiments in cardiolipin containing membranes (Fig. 4.6) and point to the interfacial orientation of the helix regardless of lipid composition.

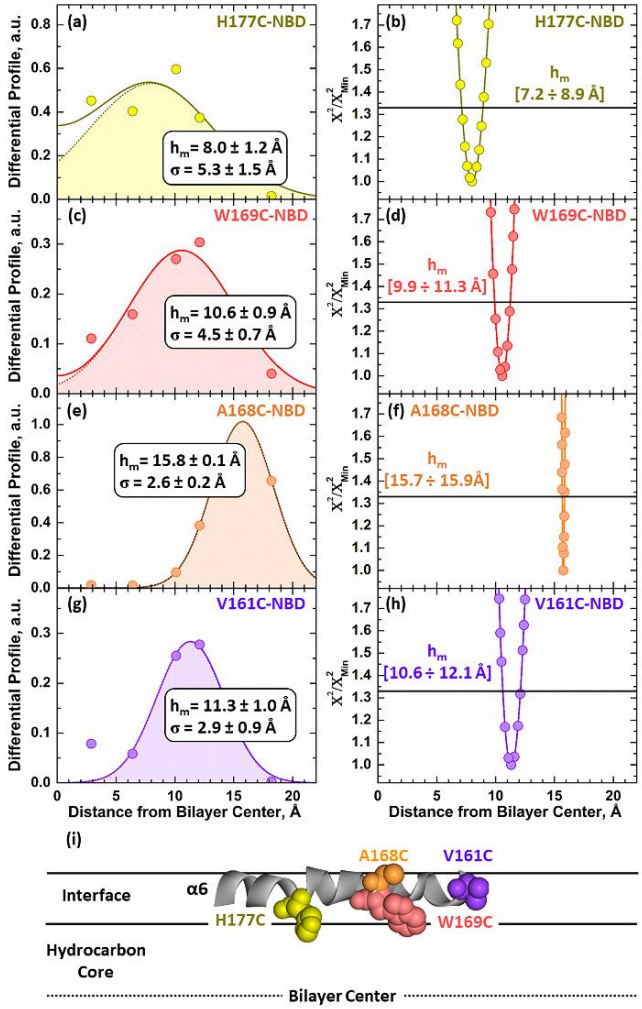

FIGURE 4.6. Depth-dependent fluorescence quenching of NBD selectively attached along the α6 helix in membrane inserted Bcl-xL.

The following positions along α6 were selectively labeled (top to bottom): 177, 169, 168 and 161. Insertion of Bcl-xL ΔTM NBD-labeled mutants was initiated by mixing the samples incubated with 3TOCL:2POPC LUV (no quencher composition) at pH 4.5. The vesicles that contained quenchers had 30% of one of the five spin-labeled lipids used substituting an equimolar concentration of POPC. Left panels: Differential Quenching Profiles for each tested mutant were obtained by subtracting the dynamic quenching component from steady-state quenching measurements (original data are presented in Fig. C2). The most probable depth (h_m) of each labeled residue and the width of the transverse distribution (σ) were obtained by fitting the data to Eq. 4.5. Panels on the right: Support-plane analysis of the robustness of the fits used in the determination of the bilayer depth (see text for details). (i) All labeling sites along α6 were 8-16 Å away from the center of the bilayer, eliminating the possibility of a transmembrane orientation. The interfacial orientation for α6 is also consistent with EPR O_2/NiEDDA accessibility measurements (Fig. 4.5).

4.5 DISCUSSION

The Bcl-2 family of proteins regulates the permeabilization of the mitochondrial outer membrane (MOMP), a key cellular process that results in cell death [11]. The well-accepted "Embedded Together" model states that critical interactions between pro- and anti-apoptotic members of the Bcl-2 family leading to MOMP occur on the mitochondrial membrane [13]. Generally, the transition between soluble and membranous conformations can follow two scenarios (both implemented by the apoptotic inhibitor Bcl-xL, studied here): anchoring of a relatively unperturbed protein to the lipid bilayer (*e.g.*, in tail-anchored proteins [169-171]) or a complete refolding and bilayer insertion of the protein (*e.g.*, in bacterial toxins). In the latter case, the properties of the lipid bilayer are expected to play an important role in modulating the structural and thermodynamic characteristics of the insertion. First, the membrane-inserted conformation will abide to general physicochemical rules that govern the organization of membrane proteins in the lipid bilayer [19]. Second, the variation in lipid composition will modulate the insertion transition *via* changes in parameters such as charge density, spontaneous curvature and physical dimensions of the hydrocarbon core and interfacial regions. Below we discuss how structural and thermodynamic properties of the bilayer insertion of Bcl-xL are modulated by lipid composition.

4.5.1 Refolding of membrane inserted Bcl-xL

The anti-apoptotic regulation of the pore former Bax by Bcl-xL has been proposed to occur by two different non-exclusive mechanisms. 1) The canonical Bcl-xL anti-apoptotic mechanism involves its binding to the BH3 domain of pro-apoptotic Bax [172]. 2) More recently Barclay et al. proposed an alternative non-canonical anti-apoptotic mechanism involving the N-terminal BH4 domain (α1 helix) of Bcl-2, an anti-apoptotic Bcl-xL homolog, binding BAX [140]. This N-terminal domain is closely linked to apoptotic progression and regulation and its deletion is lethal when expressed

in cells [161-163]. The BH4 domain of Bcl-xL is connected through a very long loop consisting of 62 a.a. (≥ 100 Å in an extended conformation) to the rest of the protein. The release of BH4 from the inserted form of the protein would greatly enhance its ability to scan the surrounding area and increase its probability of interacting with Bax (Fig. 4.1c). We have studied the release of BH4 using FRET between Alexa 488 dye selectively attached at position 189 of Bcl-xL and mCherry fluorescent protein fused at the N-terminus of the BH4 domain *via* a short flixible linker. As expected, in the folded state the FRET is readily observed by the presence of the sensitized emission peak of the acceptor, when the donor is excited (Fig. 4.2b). Our results show that the intensity of sensitized emission decreases upon insertion, and the intensity of the donor increases, indicating the loss of FRET. The complete loss of FRET observed in our measurements indicates that the separation of donor and acceptor is greater than the R_0 in the FRET pair used (~60 Å). Furthermore, the reduction in FRET appears to correlate with the insertion-associated increase in intensity of the environment-sensitive probe NBD attached at residue 175 of α6 (Fig. 4.2c). This indicates that the release of BH4 is closely associated with the refolding accompanying the membrane insertion of Bcl-xL. In addition, both BH4 release and insertion are modulated by membrane lipid composition in a similar fashion (Fig. 4.4).

The high-resolution structure of the membrane-inserted form of Bcl-xL remains unavailable, while the suggested low-resolution topology model is traditionally based on that for the diphtheria toxin translocation (T) domain [10]. The latter undergoes a dramatic refolding on the membrane interface which results in a transmembrane positioning of the hydrophobic hairpin TH8-9 [139, 150, 173-175]. Because the soluble conformations of many Bcl-2 proteins (including pro-apoptotic Bax and anti-apoptotic Bcl-xL) are similar to that of the soluble T domain, it has been assumed that upon bilayer insertion their central helical hairpin (*i.e.*, α5-6 in Bcl-xL and Bax) will be

positioned in a transmembrane orientation. Here we have tested this assumption using EPR and fluorescence spectroscopy using selective labeling of a series of single cysteine mutants along the α6 helix.

The transition of Bcl-xL into its inserted conformation was confirmed by characterizing the topology of the hydrophobic α6 helix by EPR (Fig. 4.5) and depth-dependent quenching (Fig. 4.6 and C2-3). Both techniques are in agreement and indicate that the α6 helix inserts into the bilayer as a partially solvated helix in an interfacial orientation. Our depth-dependent quenching measurements place the deepest residue tested in the helix H177C-NBD at 8 Å and the shallowest A168C-NBD at 16 Å away from the center of the bilayer in cardiolipin membranes. Essentially the same results were observed in membranes containing POPG instead of cardiolipin, with both residues tested in the middle of the helix (A168C and W169C) being located at least 10 Å away from the center of the bilayer (Fig. 4.3). This is quite different from our published results on the corresponding helix in the diphtheria toxin T domain, for which the depth of several centrally located residues was <5 Å [150, 176]. Based on these EPR and fluorescence data we conclude that the central hairpin of Bcl-xL (unlike that of the T domain) does not form a transmembrane structure. Thus, the long-standing analogy of the structural aspects of the insertion of Bcl-xL (and perhaps other Bcl-2 proteins) to the insertion of the T domain can be put to rest. Previously, we have demonstrated that such analogy does not work from a thermodynamic perspective either and suggested that lipids may play a critical role in the protonation-triggered insertion of Bcl-xL [137], which has been demonstrated here.

4.5.2 Lipid-dependent modulation of Bcl-xL membrane insertion

Several studies have suggested that mitochondrial membrane lipids play a role in the action of the Bcl-2 proteins and therefore in the regulation of apoptosis [23-26, 136, 137, 164-167, 177-181].

The most prominent example is that of cardiolipin, an anionic phospholipid specific to mitochondria [182, 183], which is strongly linked to apoptotic regulation [25, 164-167]. The exact mechanism behind the role of lipids on the modulation of apoptosis as a whole, however, remains unclear. Here we conducted a systematic study of Bcl-xL insertion and refolding into membranes containing different amounts of various anionic lipids (Figs. 5.3-4).

The free energy associated with the protonation-dependent membrane insertion of Bcl-xL has a complex dependence on lipid composition (Fig. 4.3 and 4.4a). It depends linearly on the surface membrane potential (Ψ_0), but the slope is different for different lipids, and could be subdivided into two families: (1) Strong dependence between $\Delta G_{TM}^{H^+}$ on Ψ_0 seen for cardiolipin (TOCL) and phosphatidic acid (POPA) and (2) a weaker dependence seen for membranes containing phosphatidylglycerol (POPG) and phosphatidylserine (POPS). One possibility for this differential regulation is the size of the phospholipid headgroup, as illustrated in Fig. C1. Cardiolipin and phosphatidic acid have no functional group attached to the phosphate group, and therefore the thickness of the membrane interface is expected to be relatively small. Phosphatidylglycerol and phosphatidylserine, on the other hand, have functional groups attached to the phosphate group, making the membrane interface thicker. The difference in the size of the interfacial region is also connected to the variation in the spontaneous curvature of the bilayer, which is expected to affect the insertion efficiency. Regardless of the exact interpretation, our results suggest that a combination of the surface membrane potential produced by anionic lipids and non-electrostatic membrane properties modulate the membrane insertion of Bcl-xL.

4.5.3 On the possible physiological role of the membrane-inserted conformation of Bcl-xL

The modulation of protonation states in Bcl-xL titratable residues will affect its interaction and refolding into the membrane, resulting in the release of the regulatory BH4 domain. We suggest

that this release observed upon acidification in model systems can be relevant to the switching between canonical and non-canonical forms of inhibition of MOMP in the cells. Our results indicate that changes in lipid composition can bring the transition to the threshold of cellular pH, which is arguably the best position for the regulation. For example, any additional favorable interaction that brings as little as 1.0 kcal/mole in terms of free energy (equivalent of 0.8 pH unit shift in pKa), will result in an estimated 10-fold increase in the population of the inserted form according to the titration results in Fig. 4.2.

Multiple factors can influence protonation in the cellular environment [184], including variation in pH and specific interactions that can affect the pK_a's of residues (*i.e.,* membrane binding) [185] critical for conformational switching. Our studies with other membrane-inserting proteins and peptides, such as diphtheria toxin [6, 139, 150], annexin B12 [186], gp41-derived peptide [187], pHLIP [71, 188], and Bcl-xL [137] itself, show that the membrane interface can modulate membrane insertion and refolding through membrane-driven changes in protonation propensity. The results presented here indicate that the membrane interactions of Bcl-xL depend heavily on the chemical properties of the membrane interface. Specifically, we show that negatively charged membranes shift the pK_a of both its membrane insertion and refolding towards more neutral pH values. This type of changes on the mitochondria can lead to substantial fractions of Bcl-xL refolding into the lipid bilayer, provided that the membrane surface has a sufficient anionic charge. Thus, the physiological action of Bcl-xL may not require a dramatic change in pH *in vivo*, but instead, a change in lipid composition. We hypothesize that changes in the mitochondrial lipid composition, which are known to occur during apoptosis [23-26], modulate the membrane insertion and refolding of Bcl-xL into the membrane. This association would likely occur on regions of the membrane rich in anionic lipids, such as the contact sites between the inner and

outer mitochondrial membranes, where the mole percent of the anionic lipid cardiolipin is increased [159, 160]. Indeed, several studies have found other Bcl-2 proteins localizing to these contact sites [189-191]. It is possible that such hot spots will require non-canonical inhibition modes to prevent sporadic MOMP, something that should be tested in subsequent cellular studies.

4.6 CONTRIBUTIONS

Vasquez Montes V. designed, performed and analyzed most biophysical assays and wrote the manuscript. Vargas-Uribe M. (Ladokhin Lab at the University of Kansas Medical Center) collected data in Fig. 4.3 a and contributed to data collection for Fig. 4.4a in collaboration with Vasquez Montes V. EPR measurements in Fig. 4.5 were collected by N. K. Panday (Langen Lab at the University of Southern California). M. V. Rodnin (Ladokhin lab at the University of Kansas Medical Center) designed and purified the Bcl-xL constructs.

Chapter 5: Modulation of Bcl-xL Conformational Switching

Parts of this chapter have been previously published and are reprinted here with permission alongside new, never-before published results. Vasquez-Montes, V., A. Kyrychenko, M. Vargas-Uribe, M.V. Rodnin, and A.S. Ladokhin, Conformational Switching in Bcl-xL: Enabling Non-Canonic Inhibition of Apoptosis Involves Multiple Intermediates and Lipid Interactions. Cells, 2020. 9(3). doi: 10.3390/cells9030539.

5.1 ABSTRACT

The inhibition of mitochondrial permeabilization by the anti-apoptotic protein Bcl-xL is crucial for cell survival and homeostasis. Its inhibitory role requires the partitioning of Bcl-xL to the mitochondrial outer membrane from an inactive state in the cytosol, leading to its extensive refolding. The molecular mechanisms behind these events and the resulting conformations in the bilayer are unclear and different models have been proposed to explain them. In the most recently proposed non-canonical model, the active form of Bcl-xL employs its N-terminal BH4 helix to bind and block its pro-apoptotic target. Here, we have used a combination of various spectroscopic techniques to study the release of the BH4 helix (α1) during the membrane insertion of Bcl-xL. This refolding is characterized by a gradual increase in helicity due to the lipid-dependent partitioning-coupled folding and formation of new helix αX (presumably in the originally disordered loop between helices α1 and α2). Notably, comparison of various fluorescence and circular dichroism measurements suggests the presence of multiple Bcl-xL conformations in the bilayer. This conclusion is explicitly confirmed by single molecule measurements of Förster Resonance Energy Transfer from Alexa-Fluor-488-labeled Bcl-xL D189C-to to a mCherry fluorescent protein attached at the N-terminus. These measurements clearly indicate that the refolding of Bcl-xL in the bilayer is not a two-state transition and involves multiple membranous intermediates of variable compactness.

5.2 INTRODUCTION

The anti-apoptotic protein Bcl-xL is a member of the Bcl-2 family of apoptotic regulators [13, 128]. Its role in the cell is to block the mitochondrial outer membrane permeabilization (MOMP) caused by pro-apoptotic Bcl-2 proteins (*i.e.*, BAX) (Fig. 5.1a, green) [55, 56]. The prevailing Embedded Together model of MOMP regulation postulates that membrane interactions are critical for both pro- and anti-apoptotic activities of Bcl-2 proteins [12, 49]. Bcl-xL is expressed in the cytosol in an inactive state and must redistribute to the MOM where it refolds to become active. Bcl-xL promotes cell survival by inhibiting the formation of multimeric BAX pores and forming non-productive Bcl-xL/BAX heterodimers at the MOM (Fig. 5.1a, purple) [192, 193]. Recent evidence suggests that Bcl-xL is also a target of BH3-only apoptotic triggers [194, 195].

The high-resolution structure of soluble Bcl-xL (Fig. 5.1a) has been solved by both X-ray crystallography and NMR [130], revealing a helical fold typical for many Bcl-2 proteins [129]. In addition to this soluble conformation, at least two distinct conformations have been identified in membrane environments: “anchored” (Fig. 5.1b, left) and “inserted” (Figure 5.1b, right). The structure of the anchored conformation reconstituted into nanodiscs has been solved by NMR, and it consists of a transmembrane C-terminal α8 helix, anchoring the rest of the protein, which retains its solution fold [133]. Note that in this study, the unfolded loop, connecting helices α1 and α2, was deleted from the protein construct. This anchored conformation is believed to be involved in the canonical mode of apoptotic inhibition in which Bcl-xL binds BAX through the “BH3 binding groove” [172, 192, 196, 197]. In contrast, no high-resolution structure is available for the membrane-inserted conformation of Bcl-xL. It is known, however, that the protein is refolded on the membrane interface with helix α6 penetrating deep into the bilayer, while helix α1 is released from the fold [126, 137]. This α1 helix, also known as the BH4 domain, has been proposed to play

the central part in the non-canonical mode of apoptotic inhibition by engaging the target BAX *via* an alternative protein-protein interface (Fig. 5.1b, left) [140]. We hypothesized that changes in MOM lipid composition modulate the conformational switching between the anchored and inserted conformations, allowing for the use of different modes of BAX inhibition (Fig. 5.1b).

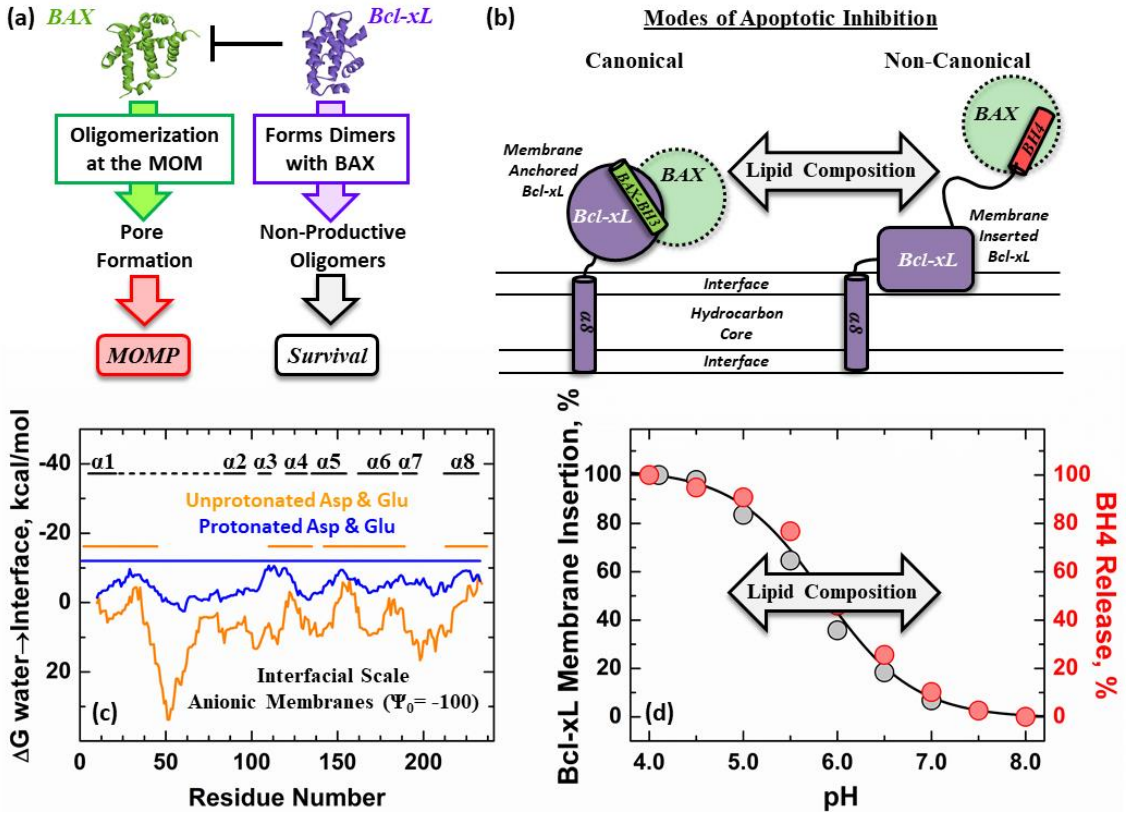

FIGURE 5.1. Conformational switching of Bcl-xL in membranes, resulting in conversion from canonical to non-canonical forms of apoptotic inhibition.

(a) The anti-apoptotic protein Bcl-xL (purple) binds to the pore former BAX (green) to block the permeabilization of the mitochondrial outer membrane (MOM) and prevent apoptosis [55, 56]. (b) Several molecular mechanisms, involving both membrane-anchored and membrane-inserted Bcl-xL, have been proposed to explain this process. The canonical mode (left) relies on the interaction of anchored Bcl-xL with the BH3 helix of BAX [192]; while in the non-canonical mode (right), BAX binds the N-terminal BH4 helix of refolded and inserted Bcl-xL. Lipid composition is hypothesized to modulate the transition between both inhibitory modes by facilitating the conformational switch between different conformations of Bcl-xL in the bilayer. (c) Bcl-xL hydropathy plot is presented for the two cases of either unprotonated (orange) or protonated (blue) titratable sidechains (D and E). This analysis was made using a modified version of the MPEx (http://blanco.biomol.uci.edu/mpex/) web tool [198], which accounts for both hydrophobic and electrostatic interfacial interactions [186]. The calculations were made assuming an approximate membrane surface potential (Ψ0) of -100 mV for a 1TOCL:2POPC bilayer, as described in Vasquez-Montes et al., 2019 [126]. Color-coded horizontal lines above the plot represent the regions of Bcl-xL predicted to interact with anionic membranes. The analysis showed a significant increase in the regions predicted to partition to the interface of anionic bilayers under protonating conditions with the largest effect observed for the unstructured α1-2 loop connecting the N-terminal BH4 (α1) helix to the rest of Bcl-xL. (d) Illustration of the lipid modulation of protonation-

dependent membrane insertion and refolding of Bcl-xL from previously published data (see Fig. 4.3 and 4.4) [126]. Relative insertion of Bcl-xL (grey symbols) is accessed by changes in fluorescence intensity of NBD (7-Nitrobenz-2-Oxa-1,3-Diazol-4-yl) attached to the N175C mutant. The refolding of Bcl-xL (red symbols) is accessed by steady-state FRET measurements of the release of its N-terminal BH4 helix. TOCL: 1,1,2,2-tetraoleoyl-cardiolipin; POPC: palmitoyl-oleoyl-phosphatidylcholine.

Deciphering the molecular mechanisms of Bcl-xL conformational switching in membrane environments is critical for understanding its role as an apoptotic gatekeeping protein. Several studies suggest that the formation of the inserted conformation of Bcl-xL is associated with the protonation of acidic residues. The role of protonation is also supported by the hydropathy analysis presented in Fig. 5.1c for the protonated (blue) and unprotonated (orange) forms of Bcl-xL. While many variables can affect the protonation in the complex milieu inside the cell, the model *in vitro* studies traditionally rely on changes in pH to trigger the insertion. Previously, we have demonstrated that the refolding and release of the Bcl-xL N-terminal BH4 helix is linked to the membrane insertion of Bcl-xL through processes that are modulated by membrane lipid composition (Fig. 5.1d). In particular, they are promoted by the presence of the mitochondrial specific lipid cardiolipin [126, 137]. In Fig. 5.1d, this is observed as a shift of the titration curves towards a more neutral pH range as a function of cardiolipin concentration. These data do not imply that *in vivo*, the pH must be very acidic for this transition to occur (in a sense, this is similar to studies of thermal stability of proteins, which utilize high temperatures to assess the propensity to refold). Under *in vitro* conditions, however, these effects are mimicked by modulating the pH of the sample, as one would use temperature to test folding stability.

In order to study conformational switching using fluorescence techniques, we designed the two Bcl-xL mutants illustrated in Fig. 5.2. The release of the BH4 domain was followed by FRET between an Alexa Fluor 488 (A488) donor dye, attached at a single Cys in the D189C mutant, and N-terminus-fused acceptor mCherry fluorescent protein (Fig. 5.2, magenta). The same construct

was used in our previously published conformational ensemble study [126], which was complemented here with lifetime measurements and single-molecule fluorescence correlation spectroscopy (FCS) measurements. Membrane interactions of the loop between helices α1 and α2 were studied using the environmentally sensitive probe NBD located at the G70C position. These measurements complement the studies of NBD membrane penetration attached along helix α6 [126]. In both constructs, the C-terminal α8 helix was removed for the following reasons. First, the proper anchoring of Bcl-xL is accomplished by complex targeting machinery *in vivo* and does not occur with high fidelity in model lipid bilayer vesicles *in vitro*. Second, the presence of the hydrophobic N-terminal tail substantially complicates the reliability of *in vitro* spectroscopic studies by promoting protein aggregation [137]. Therefore, in this study, we used a headgroup Bcl-xL construct with a 198–233 a.a. deletion, lacking the C-terminal α8 helix, which is referred from this point on in the text as Bcl-xL (in contrast, the non-truncated protein, which is referred to as full-length Bcl-xL). Note that membrane insertion of the Bcl-xL does not require the presence of the α8 helix [126].

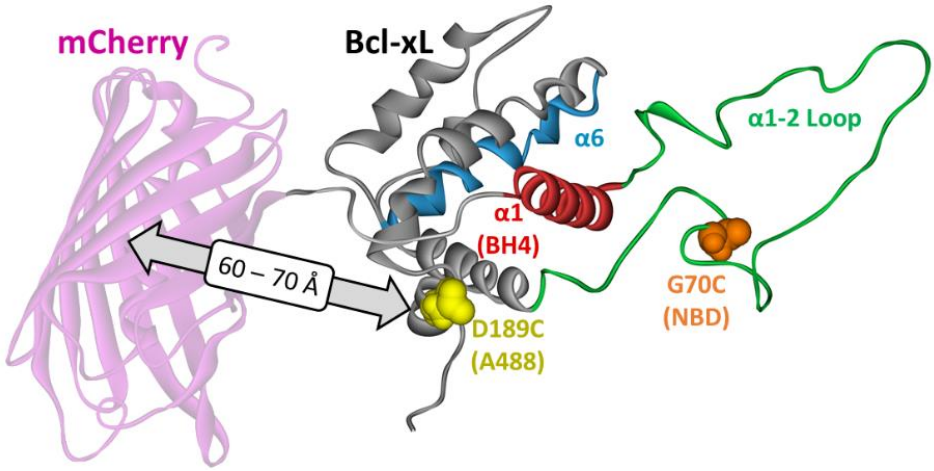

FIGURE 5.2. Bcl-xL constructs used in this study.

The structure of Bcl-xL solved by NMR [130] is presented as backbone conformation in grey with the following color highlights: hydrophobic helix α6 in blue, BH4 helix α1 (BH4 domain) in red, the loop between α1 and α2 helices in green. The NBD-labeling site in single-Cys G70C mutant is shown in orange. The FRET donor Alexa-Fluor-488-labeling site in the D189C mutant is shown in yellow. The latter construct also had an N-terminally conjugated mCherry fluorescence protein (magenta), to be used as an acceptor in FRET measurements (see text for details).

5.3 MATERIALS AND METHODS

5.3.1 Materials

The fluorescent dyes IANBD-amide (N,N'-Dimethyl-N-(Iodoacetyl)-N'-(7-Nitrobenz-2-Oxa-1,3-Diazol-4-yl)Ethylenediamine) and Alexa Fluor 488-maleimide were obtained from Invitrogen (Carlsbad, CA, USA), while the phospholipids, palmitoyl-oleoyl-phosphatidylcholine (POPC), and 1,1,2,2-tetraoleoyl-cardiolipin (TOCL) were purchased from Avanti Polar Lipids (Alabaster, AL, USA).

Preparation of large unilamellar vesicles (LUV): Chloroform lipid stocks were dried under a nitrogen stream and further dried overnight in high-vacuum. The required volume of 50 mM Na-phosphate buffer, pH 8, was added to the dried lipid films to resuspend them to a final concentration of 20 mM and vortexed. The resuspended samples were extruded using a Mini-Extruder (Avanti Polar Lipids, Alabaster, AL, USA) through 0.1 μm nucleopore polycarbonate membranes (Whatman, Philadelphia, PA, USA) to form the LUV. The vesicle stocks were stored at 4 °C in 50 mM phosphate buffer, pH 8 [75, 76].

5.3.2 Cloning, expression, and labeling

The Bcl-xL and mCherry-Bcl-xL mutants were cloned, expressed, and purified, as previously described [126]. The following mutants were employed for our fluorescent studies: 1) Bcl-xL G70C was labeled with NBD for measurements of the α1-2 loop membrane partitioning. 2) Cys-less Bcl-xL for circular dichroism measurements. 3) mCherry-Bcl-xL D189C labeled with Alexa 488 was used for FRET measurements. An additional “donor only” Bcl-xL D189C labeled with Alexa 488 was used for FRET quantification purposes. A molar extinction coefficient of 41,000 $M^{-1}cm^{-1}$ at 280 nm was used for the quantification of Bcl-xL protein concentration, while a coefficient of 72,200 $M^{-1}cm^{-1}$ at 280 nm and 72,000 $M^{-1}cm^{-1}$ at 587 nm was used for mCherry-

Bcl-xL. Fluorescent labeling with IANBD and Alexa 488 was performed using a standard labeling protocol for thiol-reactive dyes [141], and the excess dye was removed by gel-filtration in a Superose 6 1 × 30 cm column.

5.3.3 Ensemble fluorescence measurements

Ensemble steady-state fluorescence emission measurements were performed in a Fluorolog FL3-22 steady-state fluorescence spectrometer (Jobin Yvon, Edison, NJ, USA) equipped with double-grating excitation and emission monochromators. The experiments were performed using a 2 × 10 mm cuvette oriented perpendicular to the excitation beam. The sample temperature was maintained constant at 25 °C using a Peltier device from Quantum Northwest (Spokane, WA, USA). All measurements were collected after at least a 15 min equilibration period, after which all spectral measurements were collected with 1 nm steps using a 3 nm slit on the excitation monochromator and 4 nm on the emission monochromator, averaged over 3 scans. NBD fluorescence measurements were collected from 490 to 700 nm using an excitation wavelength of 465 nm. FRET measurements between Alexa Fluor 488 and mCherry dyes were collected between 490–650 nm with a 470 nm excitation wavelength.

The experiments were performed using 0.3 μM of fluorescently labeled Bcl-xL in 50 mM phosphate buffer at pH 8 and 1 mM LUV. Sample acidification was achieved by the addition of small aliquots of 2.5 M acetate. The quantification of NBD fluorescence intensity changes in Fig. 5.3b was determined at 510 nm. The pH-dependency of the α1-2 loop in the Bcl-xL G70C NBD was calculated by fitting the changes in fluorescence intensity to the following equation [142]:

$$I = \frac{I_N + I_L\,(10^{m(pK_a - pH)})}{1 + 10^{m(pK_a - pH)}}, \text{ (Eq. 5.1)}$$

where I is the fluorescence intensity measured as a function of pH, IN and IL are the limiting intensities at high and low pH, m is the transition slope, and pK_a is the negative logarithm of the dissociation constant.

The fluorescence decays of Alexa-Fluor-488/mCherry FRET samples were measured with a FluoTime 200 (PicoQuant, Berlin, Germany) time-resolved fluorescence spectrometer using a standard time-correlated single-photon counting scheme [149]. Samples were excited at 440 nm using a 10 MHz repetition rate subnanosecond pulsed diode laser, LDH 440 (PicoQuant, Berlin, Germany). Fluorescence emission was detected at 520 nm using a PMA-182 photomultiplier (PicoQuant, Berlin, Germany). The emission wavelength was selected using a Sciencetech Model 9030 monochromator. Measurements were performed using 0.3 μM of mCherry-Bcl-xL D189C-Alexa-Fluor-488 or Bcl-xL D189C-Alexa-Fluor-488 in the presence of 1 mM LUV. The fluorescence intensity decay was analyzed using the FluoFit iterative-fitting software (PicoQuant, Berlin, Germany) by subjecting the data to a standard deconvolution procedure. The fitting assumed three exponential components with the shortest lifetime fixed at 0.1 ns. The results were presented as the lifetime, τ_α, calculated as the amplitude-weighted average lifetime of the two longest components.

FRET analysis: The FRET efficiencies of ensemble steady-state and lifetimes measurements were calculated from changes in fluorescence and lifetime of the donor (Alexa-Fluor 488) in the presence of the acceptor mCherry. The following formulas were employed for the calculations [199]:

$$E = 1 - \frac{F_{DA}}{F_D}, \text{ (Eq. 5.2)}$$

$E = 1 - \frac{\tau_{DA}}{\tau_D}$, (Eq. 5.3)

where FDA and FD denote to the fluorescence intensity of the donor Alexa-Fluor-488 in the presence or absence of the acceptor mCherry. While τ_{DA} and τ_D are the corresponding lifetimes of the donor Alexa-Fluor-488 in the presence or absence of a mCherry acceptor. Donor only Bcl-xL D189C samples labeled with Alexa-Fluor-488 dye lacking mCherry were prepared for the donor only measurements.

5.3.4 Single-molecule fluorescence correlation spectroscopy (FCS)

FCS FRET measurements were performed, as previously described [200]. Single-molecule fluorescence measurements for FRET experiments were performed with a MicroTime 200 confocal microscope (PicoQuant, Berlin, Germany). The donor Alexa Fluor 488 dye was excited with a pulsed picosecond diode laser LDH-P-C-470 operated at 40 MHz. The resulting fluorescence was split through a 50/50 beam splitter cube onto two Single Photon Avalanche Diodes, SPADs (SPCM—AQR—14, Perkin Elmer Inc., Vaudreuil, Québec, Canada). The fluorescence signal was further split through a set of two filters to separate the signals from the donor (Alexa-Fluor-488) and acceptor (mCherry). An emission band filter (AHF/Chroma: HQ 520/40) was used to detect the Alexa-Fluor-488 donor signal, and a 550 nm long-pass band filter (AHF/Chroma: HQ 550LP) was used for the acceptor mCherry acceptor signal. The high numerical aperture apochromatic water immersion objective (60×, NA 1.2, Olympus), together with the 50 μm confocal pinhole, resulted in a confocal detection volume of 1 fL. The fluorescence signal was detected by applying time-correlated single-photon counting (TCSPC) with a TimeHarp 200 board, and the data was stored in the time-tagged time-resolved mode (TTTR). This allowed the recording of every detected photon with its individual timing and detection channel

information. The samples contained 0.1 µM Alexa-Fluor-488 labeled Bcl-xL D189C and 1 mM LUV in 10 mM HEPES buffer + 20 mM NaCl, pH 8. Acidification was achieved by the addition of the appropriate volumes of 0.5 M acetate, and measurements collected after 15 min incubation.

The single-molecule FRET efficiency (smFRET) was calculated from the number of photons detected in the donor (I_D) and acceptor (I_A) channels. The smFRET efficiency (E) was calculated from the following formula [201]:

$$E = \frac{I_A}{I_A + \gamma \cdot I_D}, \text{ (Eq. 5.4)}$$

where γ is a correction factor that takes into account the detection efficiency differences between the two photomultipliers used for the in donor and acceptor channels. The following γ parameters were calculated from the integral of the emission spectra of each sample: $\gamma_{pH\,8} = 3.37$, $\gamma_{pH\,7} = 3.58$, and $\gamma_{pH\,6} = 3.89$, respectively.

5.3.5 Circular Dichroism

CD measurements were performed using an upgraded Jasco-720 spectropolarimeter (Japan Spectroscopic Company, Tokyo, Japan). On average, 50 scans were recorded using a 1 mm optical path cuvette. The percent helical folding was estimated assuming the ellipticity at 222 nm corresponds only to α-helical content, following the methodology proposed by Chen et al. [81]:

$$\%\ \text{helical content} = \frac{[\theta]_{222}}{[\theta]_{222}^{Max}\left(1 - \frac{k}{n}\right)}, in\ \text{deg} \cdot cm^2 \cdot dmol^{-1}, \text{ (Eq. 5.5)}$$

where $[\theta]_{222}$ is the observed ellipticity at 222 nm, $[\theta]_{222}^{Max}$ is the theoretical mean residue ellipticity for an infinitely long helical peptide (−39,500 deg cm^2 $dmol^{-1}$), n is the number of residues (217 in Bcl-xL), and k is a wavelength-dependent constant (2.57 at 222 nm) [81].

5.4 RESULTS

5.4.1. Membrane Interactions of the Loop between α1 and α2 Helices

In our previous studies, we used the fluorescence of the environmentally sensitive probe NBD selectively attached to single-Cys residues at various positions along the Bcl-xL sequence to study its membrane partitioning and insertion [126, 137]. Here, we used the NBD-labeled G70C Bcl-xL mutant to study the partitioning of the loop between helices α1 and α2 to lipid bilayers (Fig. 5.3). In the absence of membranes, the emission spectrum of Bcl-xL G70C-NBD presented a maximum at 542 nm (Fig. 5.3a, black). The addition of large unilamellar vesicles (LUV) composed of the anionic lipid cardiolipin (TOCL) and the zwitterionic lipid phosphatidylcholine (POPC) at a 1:2 molar ratio had no effect at pH 8 (Fig. 5.3b, orange). This lipid composition represents the maximal cardiolipin content in mitochondria [159, 160]. The absence of spectroscopic changes was, therefore, attributed to the lack of Bcl-xL membrane interaction at this pH. Acidification of the sample to pH 5, however, led to a 6-fold increase in fluorescence intensity and a 14 nm blue shift of the band maximum to 528 nm (Fig. 5.3a, blue). These spectroscopic effects were characteristic of the transition of NBD to hydrophobic environments and indicated that the protonation-dependent transition of Bcl-xL to lipid bilayers led to the membrane partitioning of the α1-2 loop.

The membrane insertion of the hydrophobic α6 helix, a characteristic feature of the inserted form of Bcl-xL, is promoted by the mitochondrial specific lipid cardiolipin [126]. For this reason, we tested the effect of cardiolipin on the membrane partitioning of the α1-2 loop by performing pH-titrations in LUV with increasing cardiolipin content. No changes in NBD intensity were observed in zwitterionic bilayers composed solely of POPC lipids (Fig. 5.3b, black). This was consistent with the previously observed requirement of anionic lipids on the membrane insertion and refolding of Bcl-xL [126, 137]. Measurements in the presence of cardiolipin containing LUV

presented sigmoidal transitions with increasingly more favorable membrane interactions observed in the presence of the higher cardiolipin content. This led to a 1 pH unit difference in the calculated pK_a between membranes with the lowest (1TOCL:6POPC, pK_a = 5.4 ± 0.1) and highest (3TOCL:2POPC, pK_a = 6.4 ± 0.1) cardiolipin content.

Our results showed that the α1-2 loop interacted with cardiolipin-containing bilayers under conditions expected for the inserted form of Bcl-xL. Similar to the effects observed for α6 [126], the interaction of the α1-2 loop was modulated by lipid composition and accentuated in membranes with higher anionic content.

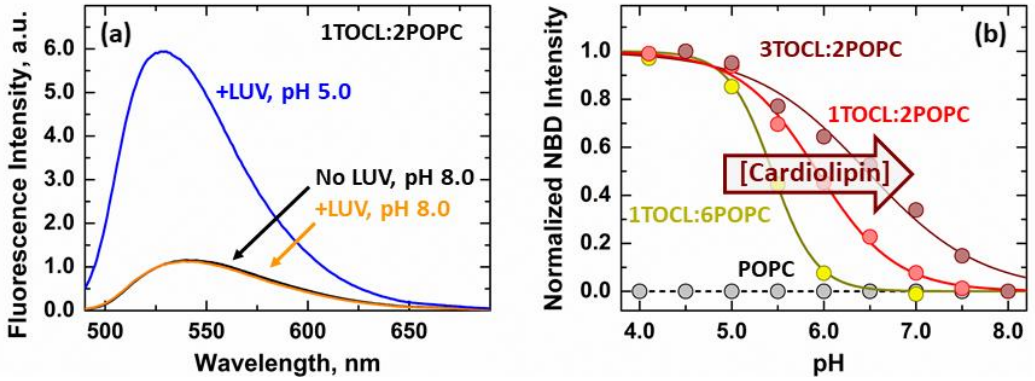

FIGURE 5.3. Fluorescence measurements of membrane interaction of the α1-2 loop.

(a) Acidification of Bcl-xL G70C-NBD in the presence of anionic large unilamellar vesicles (LUV) containing 1TOCL (cardiolipin):2POPC led to a 6-fold increase in fluorescence intensity (blue) compared to measurements at pH 8 (orange), accompanied by a 14 nm blue shift of the NBD emission spectrum from 542 to 528 nm. Both effects are characteristic of the transition of NBD to hydrophobic environments and indicate the protonation-induced membrane association of the α1-2 loop. (b) The bilayer interaction of the α1-2 loop was measured as a function of pH in membranes with increasing cardiolipin content. The presence of higher molar ratios of cardiolipin led to more neutral pK_a values, indicative of more favorable membrane interactions. The data is presented as the increase in fluorescence intensity associated with the membrane partitioning of G70-NBD measured at 510 nm.

5.4.2. Secondary Structure Changes of Membrane-inserted Bcl-xL

Circular dichroism (CD) spectroscopy was used to measure the changes in Bcl-xL secondary structure in the presence of membranes under conditions conducive for its insertion. In the presence of 1TOCL:2POPC LUV at pH 8, the CD spectrum of Bcl-xL showed a double minimum

at 209 and 222 nm, indicating an α-helical conformation (Fig. 5.4a, yellow), consistent with the X-ray and NMR structures of Bcl-xL in solution [130]. This spectrum was unchanged from the one collected in the absence of membranes. The lack of spectroscopic changes after the addition of LUV was attributed to the previously reported lack of Bcl-xL membrane interactions at this pH [126, 137].

The pH-dependent membrane insertion of Bcl-xL (Fig. 5.1d) and the partitioning of its α1-2 loop (Fig. 5.3b) were induced by the progressive acidification of the sample in the presence of LUV. This led to significant increases in ellipticity at 209 and 222 nm (Fig. 5.4a), indicating a larger α-helical content. A total helicity of 40% was calculated in the presence of LUV at pH 8 (Eq. 5.5) using the determined ellipticity at 222 nm (an α-helical content indicator) of 15,225 × 10^{-3} deg $dmol^{-1}$ cm^2. This was consistent with the overall helical value of 42% for the NMR structure of Bcl-xL in solution (PDB ID: 1LXL) [130]. A maximal gain in helical content of 4%, corresponding to ~ 10 a.a., was measured at pH 5 (using a total ellipticity of 16,260 × 10^{-3} deg $dmol^{-1}$ cm^2 at 222 nm). The relative changes in ellipticity at 222 nm are presented in Fig. 5.4b, color-coded to their respective CD spectra in Fig. 5.4a. This data was compared to the relative membrane insertion of Bcl-xL (Fig. 5.4b, black) from Fig. 5.1d, and black and partitioning of the α1-2 loop (Fig. 5.4b, blue) from Fig. 5.3a, red. The discrepancy between these data sets indicated different propensities for each of the respective transitions and a complex multi-step refolding process. Furthermore, it suggested the possibility of multiple stable intermediates in the bilayer.

These measurements showed that protonation in the presence of membranes induced the helical folding of Bcl-xL unstructured loops. Since protonation also induced the membrane insertion of Bcl-xL (Fig. 5.1d), the gain in the secondary structure was likely caused by the partitioning-

coupled folding of the α1-2 loop (hereby called helix αX in its folded state) during Bcl-xL membrane insertion.

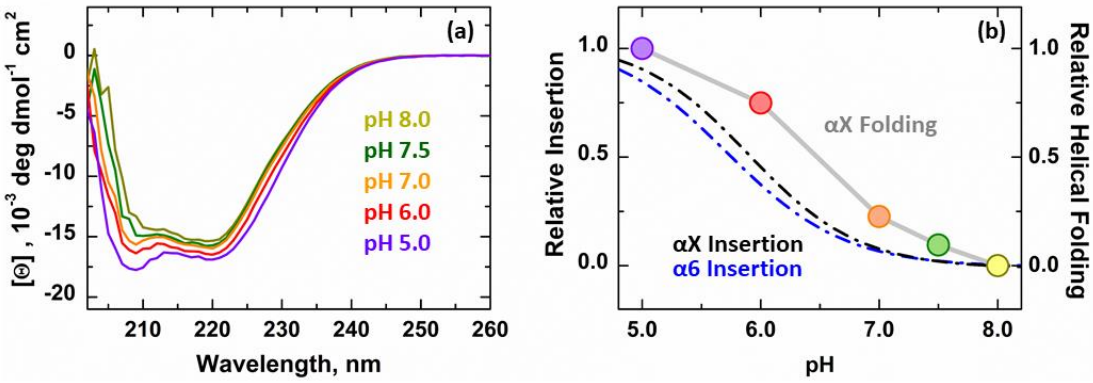

FIGURE 5.4. CD measurements of secondary structure changes of Bcl-xL in cardiolipin-containing bilayers.

(a) The secondary structure of Bcl-xL was measured by circular dichroism in the presence of anionic 1TOCL:2POPC LUV. Under all conditions, the CD spectrum of Bcl-xL presented a double minimum at ~ 209 and 222 nm, characteristic of α-helical conformations. This was consistent with its high X-ray and NMR structures, showing an all α-helical conformation [130]. Inducing the membrane insertion of Bcl-xL through protonation led to a progressive increase in ellipticity at 209 and 222 nm, indicative of a larger α-helical content. (b) The relative change in ellipticity at 222 nm, an indicator of α-helical content, at each condition was compared to the protonation-dependent insertion of the α6 helix in blue (Fig. 5.1d, black) and partitioning of the α1-2 loop in black (Fig. 5.3b, red). The helical form of the α1-2 loop in the bilayer is hereby referred to as helix αX. The difference in pH dependence between the insertion and folding data suggested that the bilayer interactions of Bcl-xL did not follow a simple two-state pathway (see also Fig. 5.6).

5.4.3. Ensemble and Single-Molecule FRET Measurements of the BH4 Domain Release in Membrane-Inserted Bcl-xL

Recently, we have demonstrated that the membrane insertion of Bcl-xL leads to the release of its N-terminal BH4 helix [126]. The refolding of membranous Bcl-xL was monitored by measuring the loss of FRET in a chimeric protein, where the fluorescent protein mCherry was conjugated at the N-terminus of a Bcl-xL construct labeled with an Alexa-Fluor-488 (A488) dye at position D189C (Fig. 5.2). This event was characterized by a protonation-dependent increase in donor (A488) fluorescence (Fig. 5.5a) at 518 nm and a concomitant decrease in acceptor mCherry intensity at 605 nm (Fig. 5.5a, inset), consistent with previous results [126]. Here, we expanded

on this work by performing complimentary lifetime measurements and characterizing this process at the single-molecule level by fluorescence correlation spectroscopy (FCS).

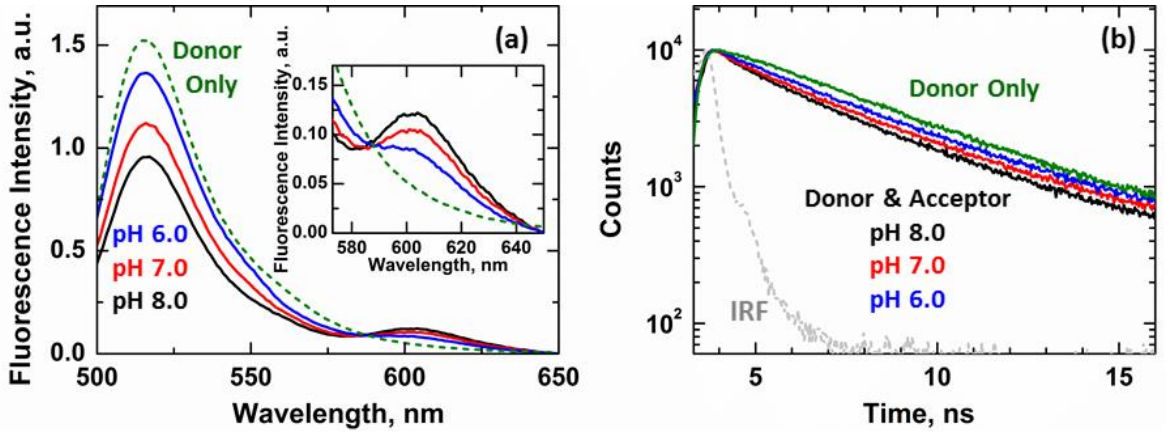

FIGURE 5.5. Ensemble FRET measurements of the release of the N-terminal BH4 domain (α1 helix).

The release of the BH4 helix was measured by loss of FRET between an N-terminally conjugated mCherry fluorescent protein and the fluorophore Alexa-Fluor-488 (A488) introduced at position D189C in Bcl-xL (Fig. 5.2). (a) Steady-state measurements in the presence of 1TOCL:2POPC LUV showed a progressive increase in donor A488 intensity at 518 nm as a function of pH. This was accompanied by a decrease in the acceptor mCherry intensity at 605 nm (insert). These spectral changes were indicative of a loss of FRET between both fluorophores and indicated the increase in distance between donor and acceptor, attributed to the release of the N-terminal BH4 helix. Insert shows a re-scale of the acceptor band. (b) Lifetime measurements showed an increase in the fluorescence lifetime of the donor-acceptor samples at increasingly acidic conditions. This was indicative of lower FRET due to a decrease in the interactions between the donor-acceptor pair, consistent with the increase in distance between both fluorophores due to the release of the BH4 helix. The following amplitude average lifetimes were calculated for the donor-acceptor pair in the presence of 1TOCL:2POPC LUV: pH 8 τ_α = 2.15 ns (black), pH 7 τ_α = 2.76 ns (red), pH 6 τ_α = 3.03 ns (blue). The lifetime τ_α = 3.42 ns was determined for a donor-only sample in the presence of LUV (green). The internal response function (IRF) of the instrument is indicated in grey.

The fluorescence lifetime of a donor-acceptor sample in the presence of 1TOCL:2POPC LUV at pH 8 (non-inserted Bcl-xL) presented an amplitude-averaged lifetime τ_α = 2.15 ns (Fig. 5.5b, black). The protonation-induced membrane insertion of Bcl-xL led to the progressively longer lifetimes until they approached the lifetime of a donor-only sample (Fig. 5.5b, green τ_α = 3.42 ns). This increase in an averaged lifetime was consistent with our steady-state measurements and caused by the loss of FRET between the donor and acceptor dyes due to the release of the N-terminal BH4 helix.

Single-molecule FCS measurements were performed on these samples to identify the underlying mechanism behind the release of the BH4 helix. Representative traces measured at pH 8, 7, and 6 are shown in Fig. 5.6a–c. A positive FRET event in these measurements was indicated by the simultaneous detection of photons in both the donor (green) and acceptor (magenta) channels while only exciting the donor A488 band. The number of these simultaneous signal spikes was reduced with increasingly acidic conditions due to the loss of FRET, consistent with our steady-state (Fig. 5.5a) and lifetime (Fig. 5.5b) measurements.

The distribution of FRET efficiencies in each single-molecule experiment was calculated using Eq. 5.4 and analyzed with a Gaussian distribution. The observed release of the BH4 helix was not a two-state transition between a globular and a refolded Bcl-xL conformation. Instead, each condition measured produced a distinctive distribution, characterized by a different average FRET efficiency (Fig. 5.6d). This indicated a gradual refolding process with multiple stable intermediates.

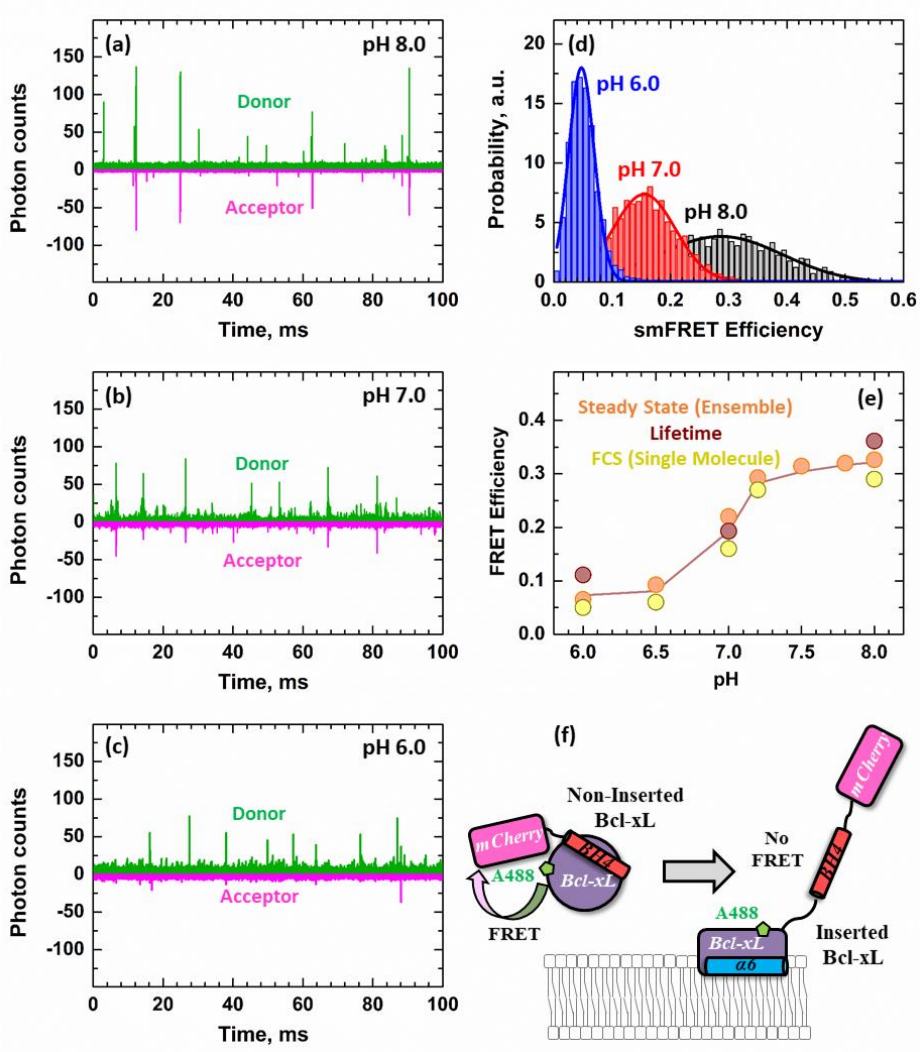

FIGURE 5.6. Single-molecule FRET measurements of Bcl-xL refolding.

The release of the N-terminal BH4 (α1) helix was inspected at the single-molecule level by fluorescence correlation spectroscopy (FCS) in the presence of 1TOCL:2POPC LUV. Measurements were performed using the same Bcl-xL construct used in Fig. 5.5 between an N-terminally conjugated mCherry fluorescent protein (donor) and acceptor Alexa-Fluor-488 fluorophore introduced at D189C (Fig. 5.2). (**a**–**c**) Representative snapshots of FCS measurements showed individual fluorescence signals detected for each A488 donor (green) or mCherry acceptor (magenta) fluorophore detected. The presence of a spike appearing simultaneously in both acceptor and donor channels indicated positive FRET events between both fluorophores. The number of FRET events decreased proportionally with the pH of the sample. (**d**) The single-molecule FRET efficiency (smFRET) in the sample was calculated using Eq. 5.4 from the number of FRET events detected and fitted to a Gaussian distribution. The loss of FRET was characterized by a progressive shift of the distributions to lower FRET efficiencies as a function of pH. This suggested the presence of multiple stable intermediate conformations during the refolding/membrane insertion of Bcl-xL, each with characteristic FRET distances between the BH4 helix and the rest of Bcl-xL. (**e**) The FRET efficiencies determined by steady-state (Fig. 5.5a), lifetime (Fig. 5.5b), and FCS (Fig. 5.6d) were plotted against experimental pH. (**f**) Schematic of the experimental set-up, indicating the presence of FRET when the acceptor mCherry was close to the donor A488 and the lack of FRET in the refolded/inserted form of Bcl-xL due to the increase in distance between the

donor-acceptor pair. The smFRET data indicated that the release of the BH4 helix was not a two-state transition and involved several Bcl-xL intermediates of various compactness.

The FRET efficiencies calculated from the FCS single-molecule measurements were compared to those determined from steady-state (Eq. 5.2) and lifetime (Eq. 5.3) experiments. All FRET measurements agreed with each other. The starting average FRET efficiency of 0.33 at pH 8 (Fig. 5.6e) was consistent with the expected distance between the donor and acceptor fluorophores in the folded construct (Fig. 5.2). All calculated FRET efficiencies decreased as a function of pH and saturated at 0.05 FRET regardless of the technique employed, indicating the unfolding of Bcl-xL and release of BH4.

5.4.4. Mg^{2+} and Ca^{2+} induce Bcl-xL membrane insertion

The presence of divalent cations has been previously shown to promote protein-membrane interactions [115, 202]. To determine if Bcl-xL was similarly affected, we measured the membrane insertion of the α6 helix in the presence of Mg^{2+} and Ca^{2+}. All measurements were performed at pH 7.5 to replicate cytosolic conditions using the Bcl-xL W169C-NBD mutant.

The addition of Mg^{2+} in the presence of 1TOCL:2POPC at pH 7.5 led to a blue shift in the emission spectrum of NBD from 528 nm (Fig. 5.7a, black) to ~ 525 nm (Fig. 5.7a, red). The spectral changes observed replicate the ones measured upon protonation in the absence of Mg^{2+} (Fig. 5.7a, blue). Control measurements in the absence of LUV showed no significant spectroscopic changes after the addition of Mg^{2+} (Fig. D1a), ruling out aggregation in solution. Control LUV scattering measurements also showed no LUV aggregation under the [divalent cation] used in this study (Fig.

D2). This suggests that Mg^{2+} at physiological pH 7.5 induces the same spectroscopic state as the one obtained by protonation, caused by the membrane insertion of the α6 helix in Bcl-xL.

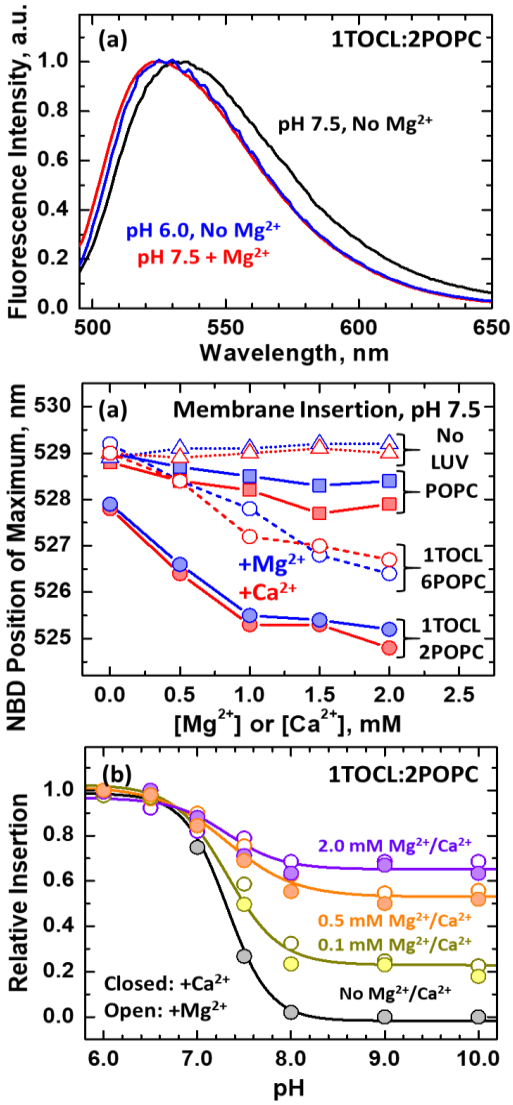

FIGURE 5.7. Mg^{2+} and Ca^{2+}-induced Bcl-xL membrane insertion.

The membrane insertion of Bcl-xL in the presence of divalent cations was measured using the Bcl-xL W169C-NBD variant, previously used to characterize the protonation-dependent insertion of Bcl-xL [126]. (a) Acidification of the sample to pH 6.0 (blue) in the presence of 1TOCL:2POPC LUV leads to a blue shift of the NBD spectrum from 528 to ~ 526 nm. This spectral change is replicated at pH 7.5 by the addition of 2.0 mM Mg^{2+} (red). (b) Mg^{2+} and Ca^{2+} titrations at pH 7.5 showed concentration-dependent decreases in NBD maximum in all lipid compositions tested. The largest effect was observed in 1TOCL:2POPC LUV (filled circles), which contained the largest cardiolipin fraction tested. No spectral changes were observed in the absence of LUV (triangles and Fig. D1). (c) The presence of Mg^{2+} or Ca^{2+} led to more favorable protonation-independent increases in Bcl-xL membrane insertion.

The Mg^{2+} -induced insertion of helix α6 was further characterized by performing Mg^{2+} and Ca^{2+} titrations in membranes with increasing cardiolipin content at pH 7.5. In all lipid compositions tested, the presence of divalent cations led to a steady decrease in NBD fluorescence maximum (Fig. 5.7b). The magnitude of this effect was modulated by lipid composition and more favorable in LUV with higher contents of cardiolipin, consistent with our previous characterization of the protonation-dependent membrane insertion of Bcl-xL [126, 137]. This suggests that increases in the amount of cardiolipin in membranes at cytosolic [Mg^{2+}] and pH 7.5 promote the transition of Bcl-xL from solution to its membrane inserted state.

The interplay between protonation and divalent cations was measured by performing pH-titrations at different [Mg^{2+}/Ca^{2+}] (Fig. 5.7c). The relative insertion of Bcl-xL at each condition was quantified by measuring the increases in NBD intensity at 510 nm. The presence of divalent cations promoted the insertion of Bcl-xL even at pH 10.0, resulting in a concentration-dependent upwards shift of the pH-titration curve. Unlike previously described systems [126], however, the higher membrane insertion propensity did not lead to more favorable membrane insertion pK_a. These discrepancies highlight the complexity of the modulation of protein membrane insertion by divalent cations. Nonetheless, to our knowledge they are the first results to provide a mechanism for the membrane interaction of Bcl-xL under cellular conditions in the absence of an activator protein.

It should be noted that all our measurements show an equivalent effect for both Mg^{2+} and Ca^{2+} on the membrane insertion of Bcl-xL. Due to the overwhelming concentration of Mg^{2+} (~ 1.0 mM) compared to Ca^{2+} (nm range), however, we speculate that Mg^{2+} is the main modulator of this process in the cell.

5.4.5. Release of Bcl-xL BH4 domain in the presence of Mg^{2+} or Ca^{2+}

The main feature of the membrane inserted form of Bcl-xL is the release of its N-terminal BH4 helix (Fig. 5.5). As in the case of Bcl-xL membrane insertion we compared the protonation-dependent release of BH4 (Fig. 5.8a, blue) to measurements performed at pH 7.5 in the presence of Mg^{2+} (Fig. 5.8a, red) in the presence of 1TOCL:2POPC LUV. Measurements were performed using the same FRET construct introduced in Fig 6.2 following the procedure presented for Fig. 5.6. Both conditions led to similar spectroscopic events with an increase in donor A488 intensity at 518 nm and the ablation of the acceptor mCherry band at 605 nm. The equivalency of these results shows that Mg^{2+} not only leads to the membrane insertion of Bcl-xL at pH 7.5, but also to the release of its N-terminal BH4 helix.

These results were quantified by measuring the loss of FRET observed at increasing concentrations of Mg^{2+} or Ca^{2+} in LUV with increasing cardiolipin content. As in the case of Bcl-xL membrane insertion, the relative percentage of BH4 release was larger in membranes with hither cardiolipin concentrations (Fig. 5.8b). No FRET changes were detected in the absence of LUV (Fig. D1c, d), indicating that the Mg^{2+}-dependent BH4 release requires the interaction of Bcl-xL with membranes. Single molecule FCS measurements revealed that the Mg^{2+}-induced loss of FRET due to the release of BH4 is characterized by different smFRET distributions at each [Mg^{2+}] (Fig. 5.8c). This points to different Bcl-xL intermediate conformations of various compactness, consistent with the protonation-dependent multi-conformation refolding of Bcl-xL (Fig. 5.6). The calculated FRET efficiencies for both the ensemble and FCS measurements are in agreement (Fig. 5.8d). They start at ~ 0.4 for the folded form of Bcl-xL in solution and decrease to ~0.05 at 2.0 mM Mg^{2+} for its membrane inserted and refolded conformation. The starting FRET efficiency is characteristic of the FRET construct used (Fig. 5.2 and 5.6). Similarly, the saturating FRET

efficiency is consistent with the one observed for the protonation-dependent refolded form of Bcl-xL (Fig. 5.6e). This points again to the equivalency between the protonation-induced state of Bcl-xL and the one induced by cytosolic [Mg^{2+}] at pH 7.5.

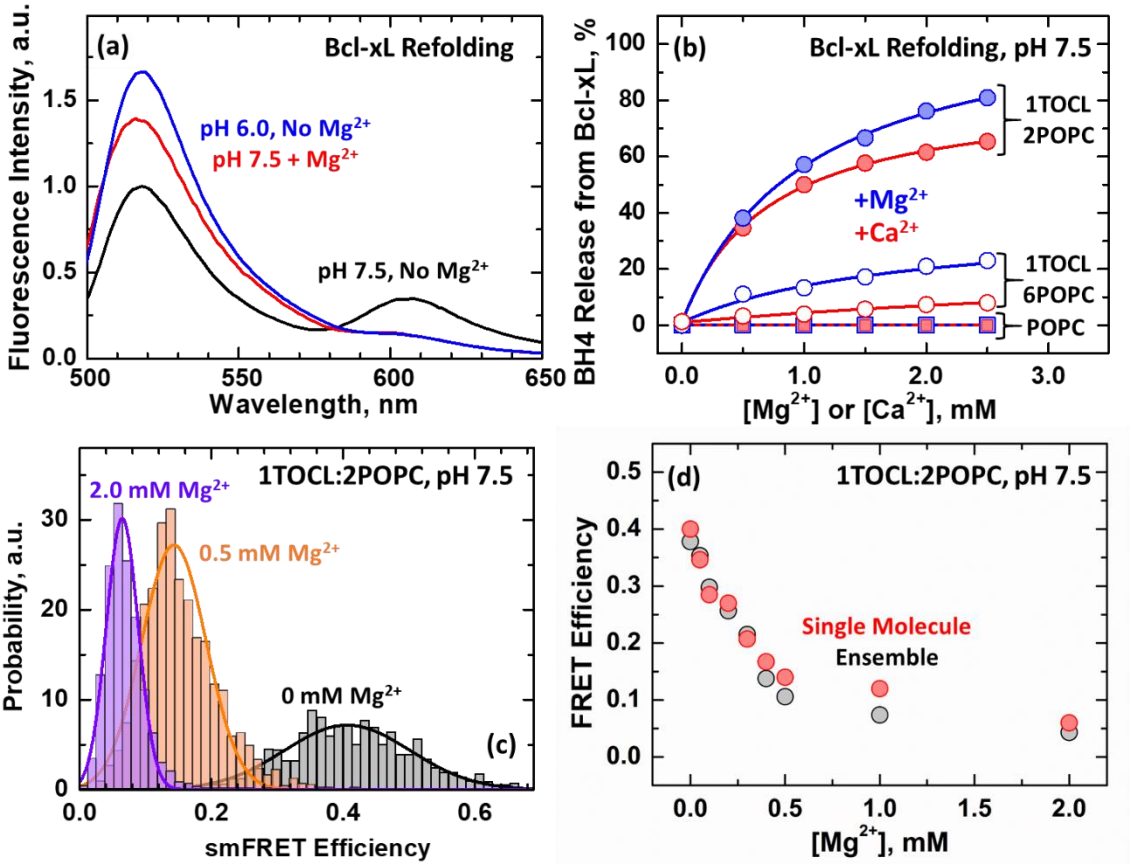

FIGURE 5.8. BH4 release in the presence of Mg^{2+} and Ca^{2+}.

The release of the N-terminal BH4 domain was measured as described in Fig. 5.6 using the mCherry-Bcl-xL D189C-A488 construct described in Fig. 5.2. (a) The addition of 2.0 mM Mg^{2+} at pH 7.5 (red) reproduces the loss off FRET induced by the acidification of the sample (blue). Both conditions therefore lead to the release of the BH4 domain. (b) Consistent with the lipid-dependent Mg^{2+}-induced membrane insertion of Bcl-xL (Fig. 5.7b), the release of the BH4 domain is more favorable in membranes with larger cardiolipin content. (c) Single molecule FCS measurements show distinct FRET efficiency distributions at each [Mg^{2+}]. This is consistent with our protonation-dependent measurements (Fig. 5.6) and points to a refolding event with multiple intermediate conformations, each with different compactness. (d) The calculated FRET efficiencies of Bcl-xL BH4 release determined by ensemble or single molecule (FCS) measurements are in agreement. They show a concentration dependent decrease from ~ 0.4 to ~ 0.05, consistent with our protonation-dependent FRET efficiency measurements (Fig. 5.6e).

5.4.6. Membrane binding and refolding of the α1-2 loop is induced by Mg^{2+}/Ca^{2+}

The last known feature of the membrane inserted conformation of Bcl-xL is the membrane binding and refolding of the α1-2 loop (Fig. 5.3 and 5.4). The addition of Mg^{2+} at pH 7.5 to samples containing the Bcl-xL G70C-NBD variant described for Fig. 5.3 in the presence of 1TOCL:2POPC leads to increases in NBD intensity and fluorescence blue-shifts (Fig. 5.9a). These spectral changes are consistent with our results in Fig. 5.3 and indicate the membrane interaction of the α1-2 loop. The extent of this interaction was similar for both Mg^{2+} and Ca^{2+} (Fig. 5.9b), similar to our results with Bcl-xL membrane insertion (Fig. 5.7) and BH4 release (Fig. 5.8).

Circular dichroism measurements showed that the Mg2+-induced membrane interaction of Bcl-xL leads to an increase in ellipticity (Fig. D3), consistent with our protonation-dependent measurements (Fig. 5.4). This leads to a gain in ellipticity at 222 nm, an indicator of α-helical content (Fig. 5.9c). Together with the membrane partitioning of the α1-2 loop, the Mg^{2+}-induced gain in ellipticity is consistent with the folding of the partitioning-coupled folding of the α1-2 loop (as previously described in Fig. 5.4).

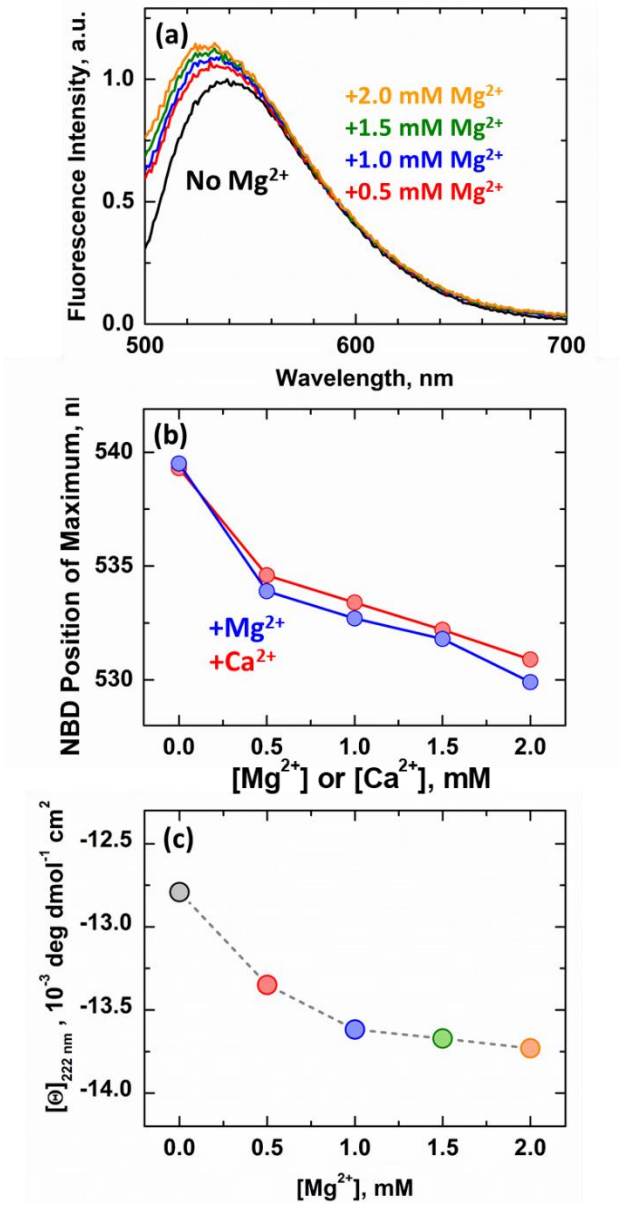

FIGURE 5.9. Mg^{2+} and Ca^{2+} induce the partitioning-coupled folding of the α1-2 loop in 1TOCL:2POPC LUV at pH 7.5.

The membrane binding and refolding of the α1-2 loop was measured with using the Bcl-xL G70C-NBD variant described for Fig. 5.3. (a) The addition of Mg^{2+} at pH 7.5 in the presence of 1TOCL:2POPC leads to intensity increases and blue shifts of the NBD spectrum, indicative of solution to membrane transitions. (b) The presence of Mg2+ and Ca2+ produced equivalent NBD blue shifts at all divalent cation concentrations tested. (c) Color coded ellipticities measured at 222 nm by circular dichroism (original spectra are presented in Fig. D3).

5.5 DISCUSSION

Apoptosis is crucial for the proper development and function of cell populations in tissues, and its dysregulation impacts many diseases [203-205]. Hyperactive apoptosis contributes to neurodegeneration and immunodeficiency, while insufficient apoptosis leads to autoimmunity and cancer, and the ability of cancer cells to avoid apoptosis significantly complicates treatment [206]. The critical step in triggering apoptosis is the permeabilization of the mitochondrial outer membrane (MOMP), which releases apoptotic factors into the cytosol that lead to cell death [24, 127]. MOMP is controlled and executed by the numerous proteins of the Bcl-2 family, which include three types: pro-apoptotic pore formers (*e.g.,* BAX, Bak), anti-apoptotic pore inhibitors (*e.g.,* Bcl-xL, BCL-2), and BH3-only regulators (*e.g.,* Bid) [13, 128]. These proteins directly interact within the mitochondrial outer membrane (MOM) either to promote or prevent protein conformational changes that lead to the formation of an oligomeric pore [11, 13, 14, 194, 195]. Alterations to the lipid composition are also involved in the regulation of apoptosis [23, 207-210].

In spite of the recent advances in solving the structures of the soluble conformations, the exact mechanism of Bcl-2 proteins remains unresolved, primarily because the functionally-important conformations are induced by interactions with the membrane [12-14]. A major knowledge gap is the lack of accurate molecular pictures of "protein-protein and protein-lipid interactions that mediate MOMP" [49, 194, 195]. In this publication, we continued the line of studies [126, 137], aiming at bridging this knowledge gap for Bcl-xL.

The apoptotic inhibitor Bcl-xL prevents BAX from forming high-order oligomers on the membrane [193], presumably by making a heterodimeric complex. Two non-exclusive models of inhibition have been developed from co-crystallization of regulatory domains with soluble conformations of partner proteins: (1) a canonical mode in which the anti-apoptotic protein

captures the BH3 domain of BAX to prevent its homodimerization [172] and (2) a novel, non-canonical mode, in which the BH4 domain of anti-apoptotic protein engages BAX to prevent its activation [140]. The only structural features known of the membrane inserted form of Bcl-xL are the deep interfacial topology of the central hydrophobic α6 helix and the release of the N-terminal BH4 helix [126]. Our results, summarized in Fig. 5.7, show that these processes were accompanied by a gain in helical content (Fig. 5.4), presumably due to the folding of the loop between helixes α1 and α2 (Fig. 5.3).

From our CD measurements (Fig.5.4), we estimated that upon membrane insertion, the helical content of Bcl-xL increased by the equivalent of a 10-residue segment, which we referred to as helix αX. The most likely place in the sequence where this could occur was in the extended loop, which we also demonstrated to interact with the membrane (Fig. 5.3). This was consistent with the general thermodynamic principles of partitioning-folding coupling that govern interfacial membrane interactions of proteins and peptides [72]. Notably, upon acidification, the gain in helicity appeared to be happening earlier (*i.e.*, at more neutral pH) than the insertion (Fig. 5.4b). This difference between pH dependencies of the folding and insertion events provided the initial evidence that the insertion process was not a simple two-state transition.

Our single-molecule FRET data on the release of the BH4 domain clearly demonstrated the existence of intermediates of various compactness (Fig. 5.6). The FRET efficiency histogram at pH 8 was centered at 0.3, which was consistent with the structural model presented in Fig. 5.2. In the case of a two-state transition between a folded and completely unfolded state, the histogram for the partial transition would contain a strong component of the folded state, which was not observed at pH 7 or 6. Instead, the entire profile gradually shifted towards low efficiencies, indicating the presence of intermediate states along the insertion/unfolding pathway of Bcl-xL.

Note that acidification in the absence of membranes did not lead to changes in FRET and that lipid composition was a factor in this membrane-controlled refolding.

Our results show that under physiological conditions (pH 7.5 and 1.0 mM Mg^{2+}) Bcl-xL interacts favorably with membranes in the absence of any activator proteins. This interaction leads to the lipid-dependent membrane insertion (Fig. 5.7), multi-step release of BH4 (Fig. 5.8), and partitioning-coupled folding of the α1-2 loop (Fig. 5.9). These results are consistent with the previously described protonation-induced features of Bcl-xL presented here and, in the literature, [126, 137], suggesting that the effects of Mg^{2+}/Ca^{2+} are mediated through changes in the protonation of anionic residues in Bcl-xL. We have described similar effects for the model peptide pHLIP (pH-Low Insertion Peptide), which also presents a much higher protonation-dependent insertion in the presence of divalent cations [202].

We summarized the results reported here and those from the literature in Fig. 5.10, depicting the conformational changes along the pathway between the anchored (top panel) and inserted conformations of Bcl-xL (bottom panel). We proposed that lipids played a central role in the conformational switching of Bcl-xL, which, in turn, was related to changes in the mode of apoptotic inhibition (Fig. 5.1b). The physiological advantages of the switching between canonic and non-canonic BH4-dependent inhibition of MOMP were not immediately obvious. One could speculate, however, that the reason might be related to the need to counter the cardiolipin-dependent recruitment of BAX to MOM. The release of the BH4 helix would increase the radius of action of Bcl-xL inhibition, while membrane targeting of the loop might direct this action toward membrane-bound BAX. Thus, further studies are needed to establish the structural,

thermodynamic, and functional aspects of membrane-modulated conformational switching in Bcl-xL and its role in apoptotic regulation.

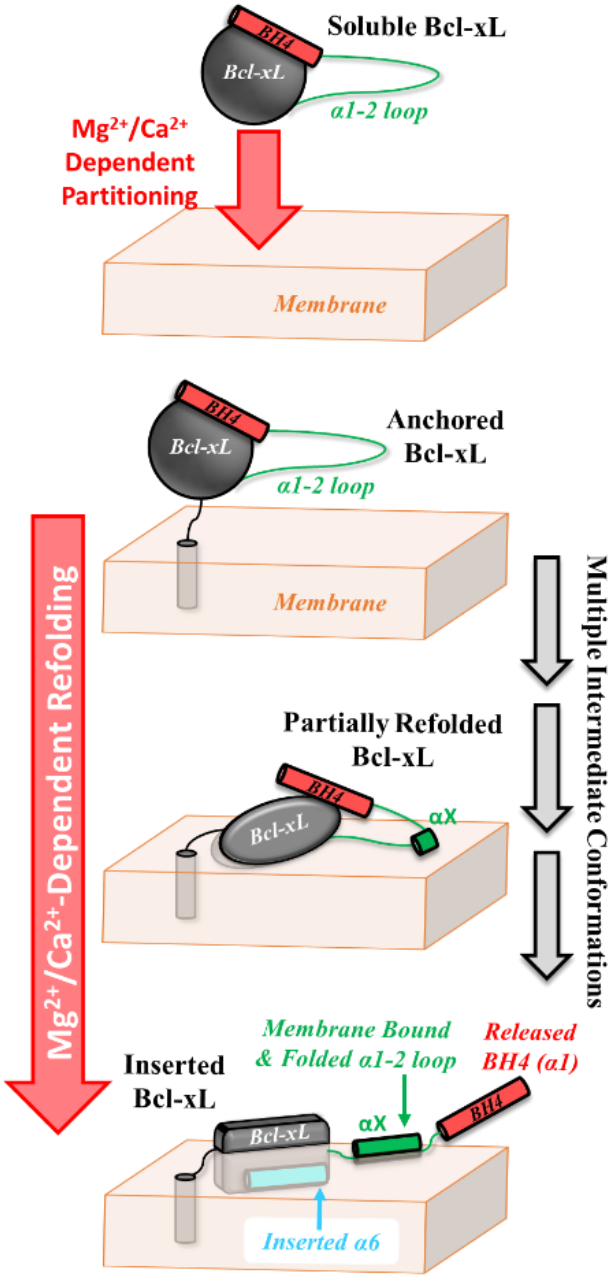

FIGURE 5.10. Schematic representation of the conformational switching pathway between membrane-anchored and inserted Bcl-xL.

After the initial targeting to the MOM *via* a yet to be fully understood mechanism, Bcl-xL resides in the conformation closely resembling its solution fold, anchored by a single transmembrane helix α8 [133] (top panel). This anchored conformation is distinctly different from the membrane-inserted one (lower panel), characterized by the refolded secondary and tertiary structure, bilayer penetration of various segments (*e.g.*, α6 helix resides about 15 Å from bilayer center [126], and the release of the regulatory BH4 domain (α1 helix) [126]. In this study, we demonstrated that the

originally disordered loop between helices α1 and α2 gained helical structure (helix αX) and interacted with the membrane (Fig. 5.3 and 5.4). Our single-molecule FRET measurements indicated that the insertion transition contained several intermediate states of different compactness (Fig. 5.6). Lipid composition (notably the presence of cardiolipin and other anionic lipids) modulates the propensity of Bcl-xL to undergo protonation-dependent insertion. We hypothesized that conformational switching between the anchored and the inserted conformations of Bcl-xL results in functional switching between canonical and non-canonical (BH4-dependent) modes of apoptotic inhibition (Fig. 5.1b).

5.5 CONTRIBUTIONS

Vasquez Montes V. designed, performed and analyzed most biophysical assays and wrote the manuscript. A. Kyrychenko (Ladokhin Lab at the University of Kansas Medical Center) and Vasquez Montes V. collected single molecule FRET measurements in Fig. 5.6 and Fig. 5.8. Vargas-Uribe M. (Ladokhin Lab at the University of Kansas Medical Center) collected data in Fig. 5.3. M. V. Rodnin (Ladokhin Lab at the University of Kansas Medical Center) designed and purified the Bcl-xL constructs used.

Chapter 6: Discussion

The activity of membrane-active proteins in the cell requires their partitioning and proper refolding in cellular membranes. These complex events are modulated by the intricate environment in the cell. However, many biophysical studies have ignored the cellular context in which these interactions occur. For example, measurements are often performed on simple membranes containing a single lipid species and in the absence of physiological divalent cations. This dissertation explores the modulation of protein membrane interactions by Ca^{2+}/Mg^{2+} and its coupling to membrane lipid composition. These effects were characterized using the tumor targeting peptide pHLIP (pH-Low Insertion Peptide) as a model system for the transmembrane insertion of proteins. The results obtained were then extrapolated to the much larger apoptotic inhibitor Bcl-xL.

The peptide pHLIP is an intriguing system, characterized by a spontaneous transmembrane insertion from a soluble state. Prior to this dissertation, the only mechanism known to cause its membrane insertion was environmental acidity. The results presented here, however, show that extracellular divalent cations also lead to the transmembrane insertion of pHLIP without the need of changes in pH (Chapter 3). This protonation-independent insertion in the presence of Ca^{2+}/Mg^{2+} accompanied the modulation of pHLIP protonation-dependent insertion, leading to a favorable pK_a for insertion (Chapter 3). The presence of divalent cations is therefore crucial for the insertion mechanism of pHLIP under cellular conditions and its selective targeting of tumors. Adding to this complexity, the membrane insertion of pHLIP was also modulated by membrane lipid composition (Chapters 2 and 3), which is also affected during tumor development [27-30]. Physiological conditions (lipid composition and Ca^{2+}/Mg^{2+} concentrations) must, therefore, be considered in the study and optimization of pHLIP-like cancer targeting systems.

Divalent cations and lipid composition were also found to be crucial for the modulation of the membrane interactions of the apoptotic inhibitor Bcl-xL (Chapter 4 and 5). This crucial cellular component is expressed in the cytosol and transitions to the mitochondrial outer membrane (MOM) to inhibit apoptosis. The transition of Bcl-xL to the MOM in cells was believed to only be induced by the protein Bid. The results presented in this dissertation, however, show that cytosolic [Mg^{2+}] is sufficient to allow the interaction of Bcl-xL with MOM-like membranes (Chapter 5). This Mg^{2+}-dependent process leads to the insertion and refolding of membrane associated Bcl-xL. Both events were also modulated by membrane lipid composition (Chapter 4 and 5) and promoted by the mitochondrial specific lipid cardiolipin, which is enriched in the MOM during apoptosis [23-26].

The results presented in this dissertation highlight the crucial role of Ca^{2+} and Mg^{2+} on the membrane binding, refolding and insertion of proteins and show their omission can lead to false negative results. It is therefore likely that we currently underestimate the number of membrane active peptides and proteins in the cell. The interpretation of these effects does not imply that an increase in cellular divalent concentration is required for the levels of interaction seen in this dissertation. Ca^{2+} and Mg^{2+} levels are highly regulated and an increase in cytosolic [Mg^{2+}] for example, is not expected. Similarly, the changes in [Ca^{2+}] that occur during apoptosis or in synapses take place in a background of 1 mM Mg^{2+} compared to nM levels of Ca^{2+}. Changes in membrane lipid composition coupled to pre-existing concentrations of Ca^{2+} and Mg^{2+} are instead hypothesized to modulate protein-membrane interactions.

The study of divalent cations has expanded our understanding of protein-membrane interactions and so far, revealed a new pathway in each of the systems where they have been applied. Further

studies, however, have to be performed to determine the mechanism behind the divalent cation-dependent effects and determine why in some cases they oppose the effects of monovalent cations.

References

1. Hoch, D.H., et al., *Channels formed by botulinum, tetanus, and diphtheria toxins in planar lipid bilayers: Relevance to translocation of proteins.* Proc.Natl.Acad.Sci.USA, 1985. **82**: p. 1692-1696.
2. Neale, E.A., *Moving across membranes.* Nature Struct.Biol., 2003. **10**(1): p. 2-3.
3. Koriazova, L.K. and M. Montal, *Translocation of botulinum neurotoxin light chain protease through the heavy chain channel.* Nature Struct.Biol., 2003. **10**(1): p. 13-18.
4. Collier, R.J. and J.A. Young, *Anthrax toxin.* Annu Rev Cell Dev Biol, 2003. **19**: p. 45-70.
5. Murphy, J.R., *Mechanism of diphtheria toxin catalytic domain delivery to the eukaryotic cell cytosol and the cellular factors that directly participate in the process.* Toxins (Basel), 2011. **3**(3): p. 294-308.
6. Ladokhin, A.S., *pH-triggered conformational switching along the membrane insertion pathway of the diphtheria toxin T-domain.* Toxins (Basel), 2013. **5**(8): p. 1362-1380.
7. Kielian, M. and F.A. Rey, *Virus membrane-fusion proteins: more than one way to make a hairpin.* Nat Rev Microbiol, 2006. **4**(1): p. 67-76.
8. Neuman, B.W., et al., *Direct observation of membrane insertion by enveloped virus matrix proteins by phosphate displacement.* PLoS One, 2013. **8**(2): p. e57916.
9. Hsu, Y.T., K.G. Wolter, and R.J. Youle, *Cytosol-to-membrane redistribution of Bax and Bcl-X(L) during apoptosis.* Proc Natl Acad Sci U S A, 1997. **94**(8): p. 3668-3672.
10. Antignani, A. and R.J. Youle, *How do Bax and Bak lead to permeabilization of the outer mitochondrial membrane?* Curr Opin Cell Biol, 2006. **18**(6): p. 685-689.
11. Youle, R.J. and A. Strasser, *The BCL-2 protein family: opposing activities that mediate cell death.* Nat Rev Mol Cell Biol, 2008. **9**(1): p. 47-59.
12. Leber, B., J. Lin, and D.W. Andrews, *Embedded together: the life and death consequences of interaction of the Bcl-2 family with membranes.* Apoptosis, 2007. **12**(5): p. 897-911.
13. Bogner, C., B. Leber, and D.W. Andrews, *Apoptosis: embedded in membranes.* Curr Opin Cell Biol, 2010. **22**(6): p. 845-51.
14. Chi, X., et al., *Regulating cell death at, on, and in membranes.* Biochim Biophys Acta, 2014. **1843**(9): p. 2100-13.
15. Kyrychenko, A., et al., *Fluorescence Applications for Structural and Thermodynamic Studies of Membrane Protein Insertion*, in *Reviews in Fluorescence 2016*, C.D. Geddes, Editor. 2017, Springer. p. 243-274.
16. Wiener, M.C., G.I. King, and S.H. White, *Structure of a fluid dioleoylphosphatidylcholine bilayer determined by joint refinement of x-ray and neutron diffraction data. I. Scaling of neutron data and the distribution of double-bonds and water.* Biophys.J., 1991. **60**: p. 568-576.
17. White, S.H. and W.C. Wimley, *Hydrophobic interactions of peptides with membrane interfaces.* Biochim.Biophys.Acta, 1998. **1376**: p. 339-352.
18. White, S.H. and W.C. Wimley, *Peptides in lipid bilayers: Structural and thermodynamic basis for partitioning and folding.* Curr.Opin.Struct.Biol., 1994. **4**: p. 79-86.
19. White, S.H., et al., *How membranes shape protein structure.* J.Biol.Chem., 2001. **276**(35): p. 32395-32398.
20. Yang, Y., M. Lee, and G.D. Fairn, *Phospholipid subcellular localization and dynamics.* J Biol Chem, 2018. **293**(17): p. 6230-6240.
21. Echard, A. and D. Burgess, *The changing lipidome during cell division.* Cell, 2014. **156**(3): p. 394-5.

22. Atilla-Gokcumen, G.E., et al., *Dividing cells regulate their lipid composition and localization.* Cell, 2014. **156**(3): p. 428-39.
23. Crimi, M. and M.D. Esposti, *Apoptosis-induced changes in mitochondrial lipids.* Biochim Biophys Acta, 2011. **1813**(4): p. 551-7.
24. Cosentino, K. and A.J. García-Sáez, *Mitochondrial alterations in apoptosis.* Chemistry and physics of lipids, 2014.
25. McMillin, J.B. and W. Dowhan, *Cardiolipin and apoptosis.* Biochim Biophys Acta, 2002. **1585**(2-3): p. 97-107.
26. Cristea, I.M. and M. Degli Esposti, *Membrane lipids and cell death: an overview.* Chem Phys Lipids, 2004. **129**(2): p. 133-60.
27. Utsugi, T., et al., *Elevated expression of phosphatidylserine in the outer membrane leaflet of human tumor cells and recognition by activated human blood monocytes.* Cancer Research, 1991. **51**: p. 3061-3066.
28. Zwaal, R.F., P. Comfurius, and E.M. Bevers, *Surface exposure of phosphatidylserine in pathological cells.* Cell Mol Life Sci, 2005. **62**(9): p. 971-88.
29. Riedl, S., et al., *In search of a novel target - phosphatidylserine exposed by non-apoptotic tumor cells and metastases of malignancies with poor treatment efficacy.* Biochim Biophys Acta, 2011. **1808**(11): p. 2638-45.
30. Stafford, J.H. and P.E. Thorpe, *Increased exposure of phosphatidylethanolamine on the surface of tumor vascular endothelium.* Neoplasia, 2011. **13**(4): p. 299-308.
31. Wiggins, P. and R. Phillips, *Membrane-protein interactions in mechanosensitive channels.* Biophys.J., 2005. **88**: p. 880-902.
32. Ladokhin, A.S. and S.H. White, *Protein chemistry at membrane interfaces: Non-additivity of electrostatic and hydrophobic interactions.* J.Mol.Biol., 2001. **309**: p. 543-552.
33. Wimley, W.C. and S.H. White, *Experimentally determined hydrophobicity scale for proteins at membrane interfaces.* Nature Struct.Biol., 1996. **3**(10): p. 842-848.
34. Wimley, W.C., T.P. Creamer, and S.H. White, *Solvation energies of amino acid sidechains and backbone in a family of host-guest pentapeptides.* Biochemistry, 1996. **35**: p. 5109-5124.
35. Moon, C.P. and K.G. Fleming, *Side-chain hydrophobicity scale derived from transmembrane protein folding into lipid bilayers.* Proc Natl Acad Sci U S A, 2011. **108**(25): p. 10174-7.
36. Hessa, T., et al., *Recognition of transmembrane helices by the endoplasmic reticulum translocon.* Nature, 2005. **433**: p. 377-381.
37. Kyte, J. and R.F. Doolittle, *A simple method for displaying the hydropathic character of a protein.* J.Mol.Biol., 1982. **157**: p. 105-132.
38. Andreev, O.A., D.M. Engelman, and Y.K. Reshetnyak, *Targeting diseased tissues by pHLIP insertion at low cell surface pH.* Front Physiol, 2014. **5**: p. 97.
39. Reshetnyak, Y.K., et al., *Measuring Tumor Aggressiveness and Targeting Metastatic Lesions with Fluorescent pHLIP.* Mol Imaging Biol, 2010.
40. Andreev, O.A., D.M. Engelman, and Y.K. Reshetnyak, *pH-sensitive membrane peptides (pHLIPs) as a novel class of delivery agents.* Mol Membr Biol, 2010. **27**(7): p. 341-352.
41. Wyatt, L.C., et al., *Applications of pHLIP Technology for Cancer Imaging and Therapy: (Trends in Biotechnology 35, 653-664, 2017).* Trends Biotechnol, 2018. **36**(12): p. 1300.
42. Cheng, C.J., et al., *MicroRNA silencing for cancer therapy targeted to the tumour microenvironment.* Nature, 2015. **518**(7537): p. 107-10.

43. Otieno, S.A., et al., *pH-dependent thermodynamic intermediates of pHLIP membrane insertion determined by solid-state NMR spectroscopy.* Proc Natl Acad Sci U S A, 2018. **115**(48): p. 12194-12199.
44. Hunt, J.F., et al., *Spontaneous, pH-dependent membrane insertion of a transbilayer α-helix.* Biochemistry, 1997. **36**(49): p. 15177-15192.
45. Hashim, A.I., et al., *Imaging pH and metastasis.* NMR Biomed, 2011. **24**(6): p. 582-91.
46. Damaghi, M., J.W. Wojtkowiak, and R.J. Gillies, *pH sensing and regulation in cancer.* Front Physiol, 2013. **4**: p. 370.
47. Kyrychenko, A., et al., *Lipid headgroups modulate membrane insertion of pHLIP peptide.* Biophys J, 2015. **108**(4): p. 791-794.
48. Leber, B., J. Lin, and D.W. Andrews, *Still embedded together binding to membranes regulates Bcl-2 protein interactions.* Oncogene, 2010. **29**(38): p. 5221-30.
49. Moldoveanu, T., et al., *Many players in BCL-2 family affairs.* Trends Biochem Sci, 2014. **39**(3): p. 101-11.
50. Wei, M.C., et al., *Proapoptotic BAX and BAK: a requisite gateway to mitochondrial dysfunction and death.* Science, 2001. **292**(5517): p. 727-30.
51. Walensky, L.D. and E. Gavathiotis, *BAX unleashed: the biochemical transformation of an inactive cytosolic monomer into a toxic mitochondrial pore.* Trends Biochem Sci, 2011. **36**(12): p. 642-52.
52. Todt, F., et al., *The C-terminal helix of Bcl-x(L) mediates Bax retrotranslocation from the mitochondria.* Cell Death Differ, 2013. **20**(2): p. 333-42.
53. Edlich, F., et al., *Bcl-x(L) retrotranslocates Bax from the mitochondria into the cytosol.* Cell, 2011. **145**(1): p. 104-16.
54. Wolter, K.G., et al., *Movement of Bax from the cytosol to mitochondria during apoptosis.* J Cell Biol, 1997. **139**(5): p. 1281-92.
55. Kale, J., E.J. Osterlund, and D.W. Andrews, *BCL-2 family proteins: changing partners in the dance towards death.* Cell Death Differ, 2018. **25**(1): p. 65-80.
56. Billen, L.P., et al., *Bcl-XL inhibits membrane permeabilization by competing with Bax.* PLoS Biol, 2008. **6**(6): p. e147.
57. Kyrychenko, A., et al., *Refining Protein Penetration into the Lipid Bilayer Using Fluorescence Quenching and Molecular Dynamics Simulations: The Case of Diphtheria Toxin Translocation Domain.* J Membr Biol, 2018. **251**(3): p. 379-391.
58. Andreev, O.A., D.M. Engelman, and Y.K. Reshetnyak, *Targeting acidic diseased tissue: New technology based on use of the pH (Low) Insertion Peptide (pHLIP).* Chim Oggi, 2009. **27**(2): p. 34-37.
59. Segala, J., et al., *Accurate analysis of tumor margins using a fluorescent pH Low Insertion Peptide (pHLIP).* Int J Mol Sci, 2009. **10**(8): p. 3478-87.
60. Vavere, A.L., et al., *A novel technology for the imaging of acidic prostate tumors by positron emission tomography.* Cancer Res, 2009. **69**(10): p. 4510-6.
61. Sosunov, E.A., et al., *pH (low) insertion peptide (pHLIP) targets ischemic myocardium.* Proc Natl Acad Sci U S A, 2013. **110**(1): p. 82-6.
62. Weerakkody, D., et al., *Family of pH (low) insertion peptides for tumor targeting.* Proc Natl Acad Sci U S A, 2013. **110**(15): p. 5834-9.
63. Burns, K.E., et al., *Therapeutic Efficacy of a Family of pHLIP-MMAF Conjugates in Cancer Cells and Mouse Models.* Mol Pharm, 2017. **14**(2): p. 415-422.

64. Burns, K.E., T.P. McCleerey, and D. Thevenin, *pH-Selective Cytotoxicity of pHLIP-Antimicrobial Peptide Conjugates.* Sci Rep, 2016. **6**: p. 28465.
65. Burns, K.E. and D. Thevenin, *Down-regulation of PAR1 activity with a pHLIP-based allosteric antagonist induces cancer cell death.* Biochem J, 2015. **472**(3): p. 287-95.
66. Burns, K.E., M.K. Robinson, and D. Thevenin, *Inhibition of cancer cell proliferation and breast tumor targeting of pHLIP-monomethyl auristatin E conjugates.* Mol Pharm, 2015. **12**(4): p. 1250-8.
67. Musial-Siwek, M., et al., *Tuning the insertion properties of pHLIP*. Biochim Biophys Acta, 2010. **1798**(6): p. 1041-6.
68. Barrera, F.N., J. Fendos, and D.M. Engelman, *Membrane physical properties influence transmembrane helix formation.* Proc Natl Acad Sci U S A, 2012. **109**(36): p. 14422-7.
69. Fendos, J., F.N. Barrera, and D.M. Engelman, *Aspartate Embedding Depth Affects pHLIP's Insertion pK.* Biochemistry, 2013.
70. Reshetnyak, Y.K., et al., *A monomeric membrane peptide that lives in three worlds: in solution, attached to, and inserted across lipid bilayers.* Biophys J, 2007. **93**(7): p. 2363-2372.
71. Kyrychenko, A., et al., *Lipid Headgroups Modulate Membrane Insertion of pHLIP Peptide.* Biophysical journal, 2015. **108**(4): p. 791-794.
72. Ladokhin, A.S. and S.H. White, *Folding of amphipathic α-helices on membranes: Energetics of helix formation by melittin.* J.Mol.Biol., 1999. **285**: p. 1363-1369.
73. Fernandez-Vidal, M., et al., *Folding amphipathic helices into membranes: amphiphilicity trumps hydrophobicity.* J Mol Biol, 2007. **370**(3): p. 459-470.
74. Almeida, P.F., A.S. Ladokhin, and S.H. White, *Hydrogen-bond energetics drive helix formation in membrane interfaces.* Biochim Biophys Acta, 2011.
75. Hope, M.J., et al., *Generation of multilamellar and unilamellar phospholipid vesicles.* Chem.Phys.Lipids, 1986. **40**: p. 89-107.
76. Mayer, L.D., M.J. Hope, and P.R. Cullis, *Vesicles of variable sizes produced by a rapid extrusion procedure.* Biochim.Biophys.Acta, 1986. **858**: p. 161-168.
77. Ladokhin, A.S., S. Jayasinghe, and S.H. White, *How to measure and analyze tryptophan fluorescence in membranes properly, and why bother?* Anal.Biochem., 2000. **285**: p. 235-245.
78. White, S.H., et al., *Protein folding in membranes: Determining the energetics of peptide-bilayer interactions.* Methods Enzymol., 1998. **295**: p. 62-87.
79. Montgomery, D.C. and E.A. Peck, *Introduction to linear regression analysis*. Wiley series in probability and mathematical statistics Applied probability and statistics,. 1982, New York: Wiley. xiii, 504 p.
80. Scott, H.L., J.M. Westerfield, and F.N. Barrera, *Determination of the Membrane Translocation pK of the pH-Low Insertion Peptide.* Biophys J, 2017. **113**(4): p. 869-879.
81. Chen, Y.H., J.T. Yang, and K.H. Chau, *Determination of the helix and beta form of proteins in aqueous solution by circular dichroism.* Biochemistry, 1974. **13**(16): p. 3350-9.
82. Luo, P.Z. and R.L. Baldwin, *Mechanism of helix induction by trifluoroethanol: A framework for extrapolating the helix-forming properties of peptides from trifluoroethanol/water mixtures back to water.* Biochemistry, 1997. **36**(27): p. 8413-8421.
83. Luo, P.Z. and R.L. Baldwin, *Interaction between water and polar groups of the helix backbone: An important determinant of helix propensities.* Proc.Natl.Acad.Sci.USA, 1999. **96**(9): p. 4930-4935.

84. Roccatano, D., et al., *Mechanism by which 2,2,2-trifluoroethanol/water mixtures stabilize secondary-structure formation in peptides: a molecular dynamics study.* Proc Natl Acad Sci U S A, 2002. **99**(19): p. 12179-84.
85. Kyrychenko, A., et al., *Thermodynamic measurements of bilayer insertion of a single transmembrane helix chaperoned by fluorinated surfactants.* J Mol Biol, 2012. **416**(3): p. 328-34.
86. Reshetnyak, Y.K., et al., *Energetics of peptide (pHLIP) binding to and folding across a lipid bilayer membrane.* Proc Natl Acad Sci U S A, 2008. **105**(40): p. 15340-15345.
87. Ladokhin, A.S. and S.H. White, *Interfacial folding and membrane insertion of a designed helical peptide.* Biochemistry, 2004. **43**(19): p. 5782-5791.
88. Wimley, W.C., et al., *A direct measurement of salt-bridge solvation energies using a peptide model system: Implications for protein stability.* Proc.Natl.Acad.Sci.USA, 1996. **93**: p. 2985-2990.
89. Pink, D.A., et al., *A model of hydrogen bond formation in phosphatidylethanolamine bilayers.* Biochim.Biophys.Acta, 1998. **1368**(2): p. 289-305.
90. Soubias, O., et al., *Contribution of membrane elastic energy to rhodopsin function.* Biophys J, 2010. **99**(3): p. 817-24.
91. Boggs, J.M., *Lipid intermolecular hydrogen bonding: Influence on structural organization and membrane function (BBA 85315).* Biochim.Biophys.Acta, 1987. **906**: p. 383-404.
92. Slater, S.J., et al., *Contribution of hydrogen bonding to lipid-lipid interactions in membranes and the role of lipid order: Effects of cholesterol, increased phospholipid unsaturation, and ethanol.* Biochemistry, 1993. **32**(14): p. 3714-3721.
93. Zakharov, S.D. and W.A. Cramer, *On the mechanism and pathway of colicin import across the E. Coli outer membrane.* Front Biosci, 2004. **9**: p. 1311-7.
94. Jakes, K.S. and W.A. Cramer, *Border crossings: colicins and transporters.* Annu Rev Genet, 2012. **46**: p. 209-31.
95. Reshetnyak, Y.K., et al., *Translocation of molecules into cells by pH-dependent insertion of a transmembrane helix.* Proc Natl Acad Sci U S A, 2006. **103**(17): p. 6460-6465.
96. Thevenin, D., M. An, and D.M. Engelman, *pHLIP-mediated translocation of membrane-impermeable molecules into cells.* Chem Biol, 2009. **16**(7): p. 754-62.
97. Karabadzhak, A.G., et al., *pHLIP-FIRE, a cell insertion-triggered fluorescent probe for imaging tumors demonstrates targeted cargo delivery in vivo.* ACS Chem Biol, 2014. **9**(11): p. 2545-53.
98. Nguyen, V.P., et al., *A Novel Soluble Peptide with pH-Responsive Membrane Insertion.* Biochemistry, 2015. **54**(43): p. 6567-75.
99. Alves, D.S., et al., *A novel pH-dependent membrane peptide that binds to EphA2 and inhibits cell migration.* Elife, 2018. **7**.
100. An, M., et al., *pH-(low)-insertion-peptide (pHLIP) translocation of membrane impermeable phalloidin toxin inhibits cancer cell proliferation.* Proc Natl Acad Sci U S A, 2010. **107**(47): p. 20246-20250.
101. Ding, G.B., et al., *Robust Anticancer Efficacy of a Biologically Synthesized Tumor Acidity-Responsive and Autophagy-Inducing Functional Beclin 1.* ACS Appl Mater Interfaces, 2018. **10**(6): p. 5227-5239.
102. Scott, H.L., et al., *Phosphatidylserine Asymmetry Promotes the Membrane Insertion of a Transmembrane Helix.* Biophys J, 2019. **116**(8): p. 1495-1506.

103. Vasquez-Montes, V., et al., *Comparison of lipid-dependent bilayer insertion of pHLIP and its P20G variant.* Biochim Biophys Acta Biomembr, 2018. **1860**(2): p. 534-543.
104. Fendos, J., F.N. Barrera, and D.M. Engelman, *Aspartate embedding depth affects pHLIP's insertion pKa.* Biochemistry, 2013. **52**(27): p. 4595-604.
105. Ulmschneider, M.B., J.C. Smith, and J.P. Ulmschneider, *Peptide partitioning properties from direct insertion studies.* Biophys J, 2010. **98**(12): p. L60-2.
106. Wimley, W.C. and S.H. White, *Designing transmembrane alpha-helices that insert spontaneously.* Biochemistry, 2000. **39**(15): p. 4432-42.
107. Ladokhin, A.S. and S.H. White, *'Detergent-like' permeabilization of anionic lipid vesicles by melittin.* Biochim Biophys Acta, 2001. **1514**(2): p. 253-60.
108. Martin-Molina, A., C. Rodriguez-Beas, and J. Faraudo, *Effect of calcium and magnesium on phosphatidylserine membranes: experiments and all-atomic simulations.* Biophys J, 2012. **102**(9): p. 2095-103.
109. Ohki, S., *A mechanism of divalent ion-induced phosphatidylserine membrane fusion.* Biochim Biophys Acta, 1982. **689**(1): p. 1-11.
110. Wu, Y., H.W. Huang, and G.A. Olah, *Method of oriented circular dichroism.* Biophys J, 1990. **57**(4): p. 797-806.
111. Andreev, O.A., et al., *pH (low) insertion peptide (pHLIP) inserts across a lipid bilayer as a helix and exits by a different path.* Proc Natl Acad Sci U S A, 2010. **107**(9): p. 4081-6.
112. Karabadzhak, A.G., et al., *Bilayer Thickness and Curvature Influence Binding and Insertion of a pHLIP Peptide.* Biophys J, 2018. **114**(9): p. 2107-2115.
113. Utsugi, T., et al., *Elevated expression of phosphatidylserine in the outer membrane leaflet of human tumor cells and recognition by activated human blood monocytes.* Cancer Res, 1991. **51**(11): p. 3062-6.
114. Tan, L.T., et al., *Targeting Membrane Lipid a Potential Cancer Cure?* Front Pharmacol, 2017. **8**: p. 12.
115. Lautenschlager, J., et al., *C-terminal calcium binding of alpha-synuclein modulates synaptic vesicle interaction.* Nat Commun, 2018. **9**(1): p. 712.
116. Andreev, O.A., et al., *Mechanism and uses of a membrane peptide that targets tumors and other acidic tissues in vivo.* Proc Natl Acad Sci U S A, 2007. **104**(19): p. 7893-8.
117. Melcrova, A., et al., *The complex nature of calcium cation interactions with phospholipid bilayers.* Sci Rep, 2016. **6**: p. 38035.
118. Valentine, M.L., et al., *Physiological Calcium Concentrations Slow Dynamics at the Lipid-Water Interface.* Biophys J, 2018. **115**(8): p. 1541-1551.
119. Vernier, P.T., M.J. Ziegler, and R. Dimova, *Calcium binding and head group dipole angle in phosphatidylserine-phosphatidylcholine bilayers.* Langmuir, 2009. **25**(2): p. 1020-7.
120. Lau, A., A. McLaughlin, and S. McLaughlin, *The adsorption of divalent cations to phosphatidylglycerol bilayer membranes.* Biochim.Biophys.Acta, 1981. **645**: p. 279-292.
121. Westerfield, J., et al., *Ions Modulate Key Interactions between pHLIP and Lipid Membranes.* Biophys J, 2019. **117**(5): p. 920-929.
122. Luecke, H., et al., *Crystal structure of the annexin XII hexamer and implications for bilayer insertion.* Nature, 1995. **378**(6556): p. 512-515.
123. Kuo, W., et al., *The calcium-dependent and calcium-independent membrane binding of synaptotagmin 1: two modes of C2B binding.* J Mol Biol, 2009. **387**(2): p. 284-94.

124. van Genderen, H.O., et al., *Extracellular annexin A5: functions of phosphatidylserine-binding and two-dimensional crystallization.* Biochim Biophys Acta, 2008. **1783**(6): p. 953-63.
125. Minn, A.J., et al., *Bcl-x(L) forms an ion channel in synthetic lipid membranes.* Nature, 1997. **385**(6614): p. 353-7.
126. Vasquez-Montes, V., et al., *Lipid-modulation of membrane insertion and refolding of the apoptotic inhibitor Bcl-xL.* Biochim Biophys Acta Proteins Proteom, 2019. **1867**(7-8): p. 691-700.
127. Wang, C. and R.J. Youle, *The role of mitochondria in apoptosis*.* Annu Rev Genet, 2009. **43**: p. 95-118.
128. Hardwick, J.M. and R.J. Youle, *SnapShot: BCL-2 proteins.* Cell, 2009. **138**(2): p. 404, 404 e1.
129. Luna-Vargas, M.P. and J.E. Chipuk, *The deadly landscape of pro-apoptotic BCL-2 proteins in the outer mitochondrial membrane.* FEBS J, 2015.
130. Muchmore, S.W., et al., *X-ray and NMR structure of human Bcl-xL, an inhibitor of programmed cell death.* Nature, 1996. **381**(6580): p. 335-41.
131. Lessene, G., et al., *Structure-guided design of a selective BCL-X(L) inhibitor.* Nat Chem Biol, 2013. **9**(6): p. 390-7.
132. Lee, E.F., et al., *The functional differences between pro-survival and pro-apoptotic B cell lymphoma 2 (Bcl-2) proteins depend on structural differences in their Bcl-2 homology 3 (BH3) domains.* J Biol Chem, 2014. **289**(52): p. 36001-17.
133. Yao, Y., et al., *Conformation of BCL-XL upon membrane-integration.* Journal of Molecular Biology, 2015(0).
134. Thuduppathy, G.R., et al., *Evidence that membrane insertion of the cytosolic domain of Bcl-xL is governed by an electrostatic mechanism.* J Mol Biol, 2006. **359**(4): p. 1045-58.
135. Thuduppathy, G.R., et al., *The N-terminal domain of Bcl-xL reversibly binds membranes in a pH-dependent manner.* Biochemistry, 2006. **45**(48): p. 14533-42.
136. Garcia-Saez, A.J., et al., *Membrane promotes tBID interaction with BCL(XL).* Nat Struct Mol Biol, 2009. **16**(11): p. 1178-85.
137. Vargas-Uribe, M., M.V. Rodnin, and A.S. Ladokhin, *Comparison of membrane insertion pathways of the apoptotic regulator Bcl-xL and the diphtheria toxin translocation domain.* Biochemistry, 2013. **52**(45): p. 7901-7909.
138. Rodnin, M.V., et al., *Conformational switching of the diphtheria toxin T domain.* J Mol Biol, 2010. **402**(1): p. 1-7.
139. Kyrychenko, A., et al., *Kinetic intermediate reveals staggered pH-dependent transitions along the membrane insertion pathway of the diphtheria toxin T-domain.* Biochemistry, 2009. **48**(32): p. 7584-7594.
140. Barclay, L.A., et al., *Inhibition of Pro-apoptotic BAX by a noncanonical interaction mechanism.* Mol Cell, 2015. **57**(5): p. 873-86.
141. Haugland, R.P., *Handbook of Fluorescent Probes and Research Chemicals*. 6th ed. 1996, Eugene, OR: Molecular Probes, Inc.
142. Ladokhin, A.S., *Fluorescence spectroscopy in thermodynamic and kinetic analysis of pH-dependent membrane protein insertion.* Methods Enzymol., 2009. **466**: p. 19-42.
143. McLaughlin, S., *The electrostatic properties of membranes.* Annual review of biophysics and biophysical chemistry, 1989. **18**(1): p. 113-136.

144. Kučerka, N., M.-P. Nieh, and J. Katsaras, *Fluid phase lipid areas and bilayer thicknesses of commonly used phosphatidylcholines as a function of temperature.* Biochimica et Biophysica Acta (BBA)-Biomembranes, 2011. **1808**(11): p. 2761-2771.
145. Pan, J., et al., *Molecular structures of fluid phase phosphatidylglycerol bilayers as determined by small angle neutron and X-ray scattering.* Biochimica et Biophysica Acta (BBA)-Biomembranes, 2012. **1818**(9): p. 2135-2148.
146. Pan, J., et al., *The molecular structure of a phosphatidylserine bilayer determined by scattering and molecular dynamics simulations.* Soft matter, 2014. **10**(21): p. 3716-3725.
147. Cheng, M.H., et al., *Molecular dynamics simulations of ternary membrane mixture: phosphatidylcholine, phosphatidic acid, and cholesterol.* The Journal of Physical Chemistry B, 2007. **111**(51): p. 14186-14192.
148. Pan, J., et al., *Structural and mechanical properties of cardiolipin lipid bilayers determined using neutron spin echo, small angle neutron and X-ray scattering, and molecular dynamics simulations.* Soft matter, 2015. **11**(1): p. 130-138.
149. Posokhov, Y.O. and A.S. Ladokhin, *Lifetime fluorescence method for determining membrane topology of proteins.* Anal Biochem, 2006. **348**(1): p. 87-93.
150. Kyrychenko, A., et al., *Refining Protein Penetration into the Lipid Bilayer Using Fluorescence Quenching and Molecular Dynamics Simulations: The Case of Diphtheria Toxin Translocation Domain.* J Membr Biol, 2018.
151. Kyrychenko, A. and A.S. Ladokhin, *Refining membrane penetration by a combination of steady-state and time-resolved depth-dependent fluorescence quenching.* Anal Biochem, 2014. **446**: p. 19-21.
152. Kyrychenko, A., M.V. Rodnin, and A.S. Ladokhin, *Calibration of Distribution Analysis of the Depth of Membrane Penetration Using Simulations and Depth-Dependent Fluorescence Quenching.* J Membr Biol, 2014.
153. Ladokhin, A.S., *Distribution analysis of depth-dependent fluorescence quenching in membranes: A practical guide.* Methods Enzymol., 1997. **278**: p. 462-473.
154. Ladokhin, A.S., *Measuring membrane penetration with depth-dependent fluorescence quenching: distribution analysis is coming of age.* Biochim Biophys Acta, 2014. **1838**(9): p. 2289-95.
155. Ladokhin, A.S., *Analysis of protein and peptide penetration into membranes by depth-dependent fluorescence quenching: Theoretical considerations.* Biophys.J., 1999. **76**: p. 946-955.
156. Kyrychenko, A. and A.S. Ladokhin, *Molecular Dynamics Simulations of Depth Distribution of Spin-Labeled Phospholipids within Lipid Bilayer.* J Phys Chem B, 2013. **117**: p. 5875-5885.
157. Ambroso, M.R., B.G. Hegde, and R. Langen, *Endophilin A1 induces different membrane shapes using a conformational switch that is regulated by phosphorylation.* Proc Natl Acad Sci U S A, 2014. **111**(19): p. 6982-7.
158. Altenbach, C., et al., *A collision gradient method to determine the immersion depth of nitroxides in lipid bilayers: Application to spin-labeled mutants of bacteriorhodopsin.* Proc.Natl.Acad.Sci.USA, 1994. **91**: p. 1667-1671.
159. Ardail, D., et al., *Mitochondrial contact sites: Lipid composition and dynamics.* J.Biol.Chem., 1990. **265**(31): p. 18797-18802.
160. Daum, G., *Lipids of mitochondria.* Biochimica et Biophysica Acta (BBA)-Reviews on Biomembranes, 1985. **822**(1): p. 1-42.

161. Ofengeim, D., et al., *N-terminally cleaved Bcl-xL mediates ischemia-induced neuronal death.* Nat Neurosci, 2012. **15**(4): p. 574-80.
162. Huang, D.C., J.M. Adams, and S. Cory, *The conserved N-terminal BH4 domain of Bcl-2 homologues is essential for inhibition of apoptosis and interaction with CED-4.* EMBO J, 1998. **17**(4): p. 1029-39.
163. Clem, R.J., et al., *Modulation of cell death by Bcl-XL through caspase interaction.* Proc Natl Acad Sci U S A, 1998. **95**(2): p. 554-9.
164. Schug, Z.T. and E. Gottlieb, *Cardiolipin acts as a mitochondrial signalling platform to launch apoptosis.* Biochimica et Biophysica Acta (BBA)-Biomembranes, 2009. **1788**(10): p. 2022-2031.
165. Aisha, S.-D., et al., *Distinct lipid effects on tBid and Bim activation of membrane permeabilization by pro-apoptotic Bax.* Biochemical Journal, 2015.
166. Lucken-Ardjomande, S., S. Montessuit, and J.-C. Martinou, *Contributions to Bax insertion and oligomerization of lipids of the mitochondrial outer membrane.* Cell Death & Differentiation, 2008. **15**(5): p. 929-937.
167. Esposti, M.D., *Lipids, cardiolipin and apoptosis: a greasy licence to kill.* Cell death and differentiation, 2002. **9**(3): p. 234.
168. Kyrychenko, A., D.J. Tobias, and A.S. Ladokhin, *Validation of Depth-Dependent Fluorescence Quenching in Membranes by Molecular Dynamics Simulation of Tryptophan Octyl Ester in POPC Bilayer.* J Phys Chem B, 2013. **117**(17): p. 4770-4778.
169. Borgese, N., S. Brambillasca, and S. Colombo, *How tails guide tail-anchored proteins to their destinations.* Curr Opin Cell Biol, 2007. **19**(4): p. 368-75.
170. Borgese, N., S. Colombo, and E. Pedrazzini, *The tale of tail-anchored proteins: coming from the cytosol and looking for a membrane.* J Cell Biol, 2003. **161**(6): p. 1013-9.
171. Brambillasca, S., et al., *Transmembrane topogenesis of a tail-anchored protein is modulated by membrane lipid composition.* Embo J, 2005. **24**(14): p. 2533-42.
172. Czabotar, P.E., et al., *Bax crystal structures reveal how BH3 domains activate Bax and nucleate its oligomerization to induce apoptosis.* Cell, 2013. **152**(3): p. 519-31.
173. Oh, K.J., et al., *Organization of diphtheria toxin T domain in bilayers: A site-directed spin labeling study.* Science, 1996. **273**(5276): p. 810-812.
174. Oh, K.J., et al., *Conformation of the diphtheria toxin T domain in membranes: A site-directed spin-labeling study of the TH8 helix and TL5 loop.* Biochemistry, 1999. **38**(32): p. 10336-10343.
175. Rosconi, M.P., G. Zhao, and E. London, *Analyzing topography of membrane-inserted diphtheria toxin T domain using BODIPY-streptavidin: At low pH, helices 8 and 9 form a transmembrane hairpin but helices 5-7 form stable nonclassical inserted segments on the cis side of the bilayer.* Biochemistry, 2004. **43**(28): p. 9127-9139.
176. Kurnikov, I.V., et al., *pH-Triggered Conformational Switching of the Diphtheria Toxin T-Domain: The Roles of N-Terminal Histidines.* J Mol Biol, 2013. **425**: p. 2752-2764.
177. Martínez-Abundis, E., et al., *Changes in specific lipids regulate BAX-induced mitochondrial permeability transition.* Febs Journal, 2007. **274**(24): p. 6500-6510.
178. Zhao, K., et al., *Phosphatidic acid mediates the targeting of tBid to induce lysosomal membrane permeabilization and apoptosis.* Journal of lipid research, 2012. **53**(10): p. 2102-2114.
179. Cho, E.Y., C.-H. Yun, and T. Ahn, *Effects of phospholipids on the functional regulation of tBID in membranes.* Molecular and cellular biochemistry, 2012. **363**(1-2): p. 395-408.

180. Mignard, V., et al., *Bioactive lipids and the control of Bax pro-apoptotic activity*. Cell death & disease, 2013. **5**: p. e1266-e1266.
181. Zhang, T. and A. Saghatelian, *Emerging roles of lipids in BCL-2 family-regulated apoptosis.* Biochimica et Biophysica Acta (BBA)-Molecular and Cell Biology of Lipids, 2013. **1831**(10): p. 1542-1554.
182. van Meer, G., D.R. Voelker, and G.W. Feigenson, *Membrane lipids: where they are and how they behave.* Nat Rev Mol Cell Biol, 2008. **9**(2): p. 112-24.
183. Olofsson, G. and E. Sparr, *Ionization constants pKa of cardiolipin.* PLoS One, 2013. **8**(9): p. e73040.
184. Casey, J.R., S. Grinstein, and J. Orlowski, *Sensors and regulators of intracellular pH.* Nature reviews Molecular cell biology, 2010. **11**(1): p. 50-61.
185. Teixeira, V.H., et al., *pK(a) Values of Titrable Amino Acids at the Water/Membrane Interface.* J Chem Theory Comput, 2016. **12**(3): p. 930-4.
186. Posokhov, Y.O., et al., *Membrane insertion pathway of annexin B12: thermodynamic and kinetic characterization by fluorescence correlation spectroscopy and fluorescence quenching.* Biochemistry, 2008. **47**(18): p. 5078-5087.
187. Kyrychenko, A., et al., *Structural plasticity in the topology of the membrane-interacting domain of HIV-1 gp41.* Biophys J, 2014. **106**(3): p. 610-620.
188. Vasquez-Montes, V., et al., *Comparison of lipid-dependent bilayer insertion of pHLIP and its P20G variant.* Biochim Biophys Acta, 2018. **1860**(2): p. 534-543.
189. Kim, T.-H., et al., *Bid-cardiolipin interaction at mitochondrial contact site contributes to mitochondrial cristae reorganization and cytochrome C release.* Molecular biology of the cell, 2004. **15**(7): p. 3061-3072.
190. Lutter, M., G.A. Perkins, and X. Wang, *The pro-apoptotic Bcl-2 family member tBid localizes to mitochondrial contact sites.* BMC cell biology, 2001. **2**(1): p. 22.
191. Martinou, J.-C. and R.J. Youle, *Mitochondria in apoptosis: Bcl-2 family members and mitochondrial dynamics.* Developmental cell, 2011. **21**(1): p. 92-101.
192. Ding, J., et al., *After embedding in membranes antiapoptotic Bcl-XL protein binds both Bcl-2 homology region 3 and helix 1 of proapoptotic Bax protein to inhibit apoptotic mitochondrial permeabilization.* Journal of Biological Chemistry, 2014. **289**(17): p. 11873-11896.
193. Subburaj, Y., et al., *Bax monomers form dimer units in the membrane that further self-assemble into multiple oligomeric species.* Nat Commun, 2015. **6**: p. 8042.
194. Huang, K., et al., *BH3-only proteins target BCL-xL/MCL-1, not BAX/BAK, to initiate apoptosis.* Cell Res, 2019. **29**(11): p. 942-952.
195. Adams, J.M., *BAX and BAK become killers without a BH3 trigger.* Cell Res, 2019. **29**(12): p. 967-968.
196. Diaz, J.L., et al., *A common binding site mediates heterodimerization and homodimerization of Bcl-2 family members.* J Biol Chem, 1997. **272**(17): p. 11350-5.
197. Sattler, M., et al., *Structure of Bcl-xL-Bak peptide complex: recognition between regulators of apoptosis.* Science, 1997. **275**(5302): p. 983-6.
198. Snider, C., et al., *MPEx: a tool for exploring membrane proteins.* Protein Sci, 2009. **18**(12): p. 2624-8.
199. Lakowicz, J.R., *Principles of Fluorescence Spectroscopy*. 2nd ed. 1999, New York: Kluwer Academic/Plenum Publishers. 1-698.

200. Kyrychenko, A., et al., *Joint refinement of FRET measurements using spectroscopic and computational tools.* Anal Biochem, 2017. **522**: p. 1-9.
201. Rosenkranz, T., et al., *Native and unfolded states of phosphoglycerate kinase studied by single-molecule FRET.* Chemphyschem, 2011. **12**(3): p. 704-10.
202. Vasquez-Montes, V., et al., *Divalent Cations and Lipid Composition Modulate Membrane Insertion and Cancer-Targeting Action of pHLIP.* J Mol Biol, 2019. **431**(24): p. 5004-5018.
203. Kerr, J.F., A.H. Wyllie, and A.R. Currie, *Apoptosis: a basic biological phenomenon with wide-ranging implications in tissue kinetics.* British journal of cancer, 1972. **26**(4): p. 239.
204. Tsujimoto, Y., et al., *Involvement of the bcl-2 gene in human follicular lymphoma.* Science, 1985. **228**(4706): p. 1440-3.
205. Vaux, D.L., S. Cory, and J.M. Adams, *Bcl-2 gene promotes haemopoietic cell survival and cooperates with c-myc to immortalize pre-B cells.* Nature, 1988. **335**(6189): p. 440-2.
206. Strasser, A., S. Cory, and J.M. Adams, *Deciphering the rules of programmed cell death to improve therapy of cancer and other diseases.* EMBO J, 2011. **30**(18): p. 3667-83.
207. Chipuk, J.E., et al., *Sphingolipid metabolism cooperates with BAK and BAX to promote the mitochondrial pathway of apoptosis.* Cell, 2012. **148**(5): p. 988-1000.
208. Hollville, E. and S.J. Martin, *Greasing the path to BAX/BAK activation.* Cell, 2012. **148**(5): p. 845-6.
209. Renault, T.T. and J.E. Chipuk, *Death upon a kiss: mitochondrial outer membrane composition and organelle communication govern sensitivity to BAK/BAX-dependent apoptosis.* Chem Biol, 2014. **21**(1): p. 114-23.
210. Raemy, E. and J.C. Martinou, *Involvement of cardiolipin in tBID-induced activation of BAX during apoptosis.* Chem Phys Lipids, 2014. **179**: p. 70-4.
211. Horvath, S.E. and G. Daum, *Lipids of mitochondria.* Progress in lipid research, 2013. **52**(4): p. 590-614.

Appendices

Appendix A: Comparison of Membrane Insertion of pHLIP and its pHLIP-P20G Variant

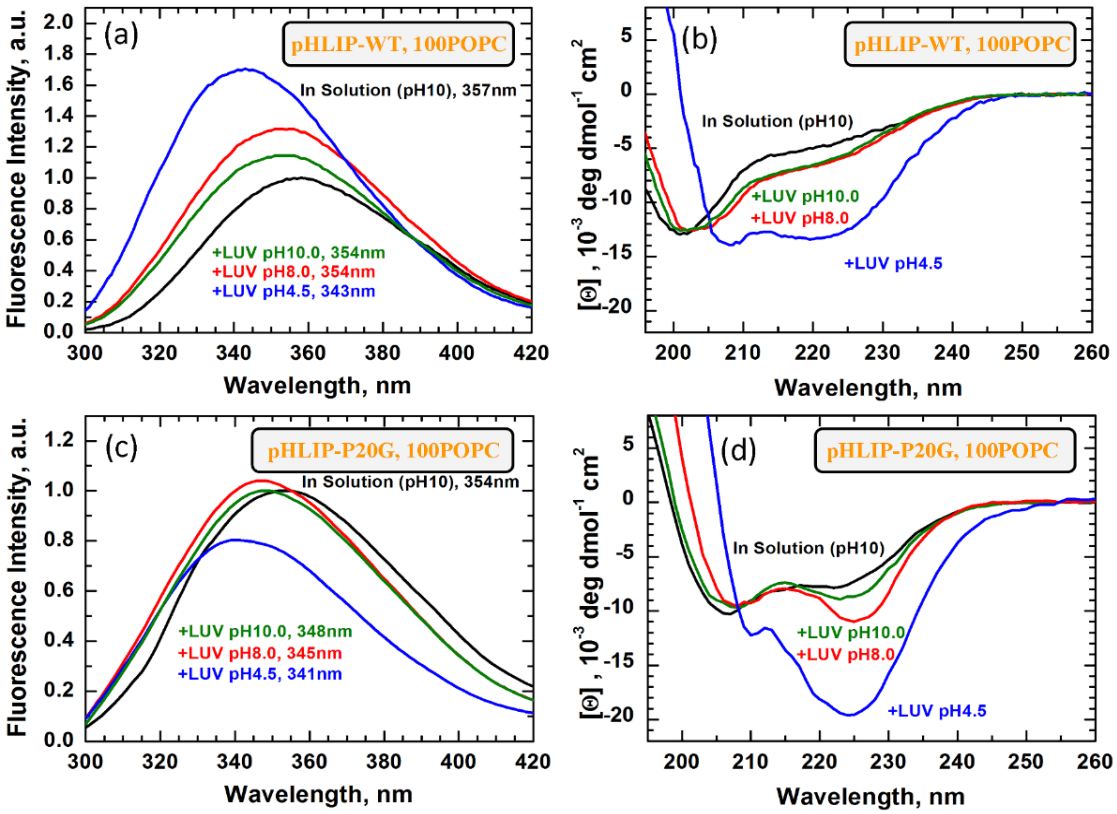

FIGURE A1. Trp emission and CD spectra of pHLIP-WT and P20G in pure POPC LUV.

Trp emission and CD spectra of both pHLIP variants were measured in solution at pH 10 (State I) and in the presence of membranes containing purely POPC as a function of pH. The blue shift and CD spectral change observed at pH 10 upon addition of membranes indicates the interfacial partitioning of pHLIP into its State II. Incremental blue shift and helical content (ellipticity at 222 nm) is a result of the peptide transitioning to its transmembrane α-helical State III. The larger contribution of the 222 nm band in the CD spectra of pHLIP-P20G in pure POPC at low pH is characteristic of this peptide in membranes. Similar spectral shape was observed across all membranes tested and previously observed by Barrera et al[68].

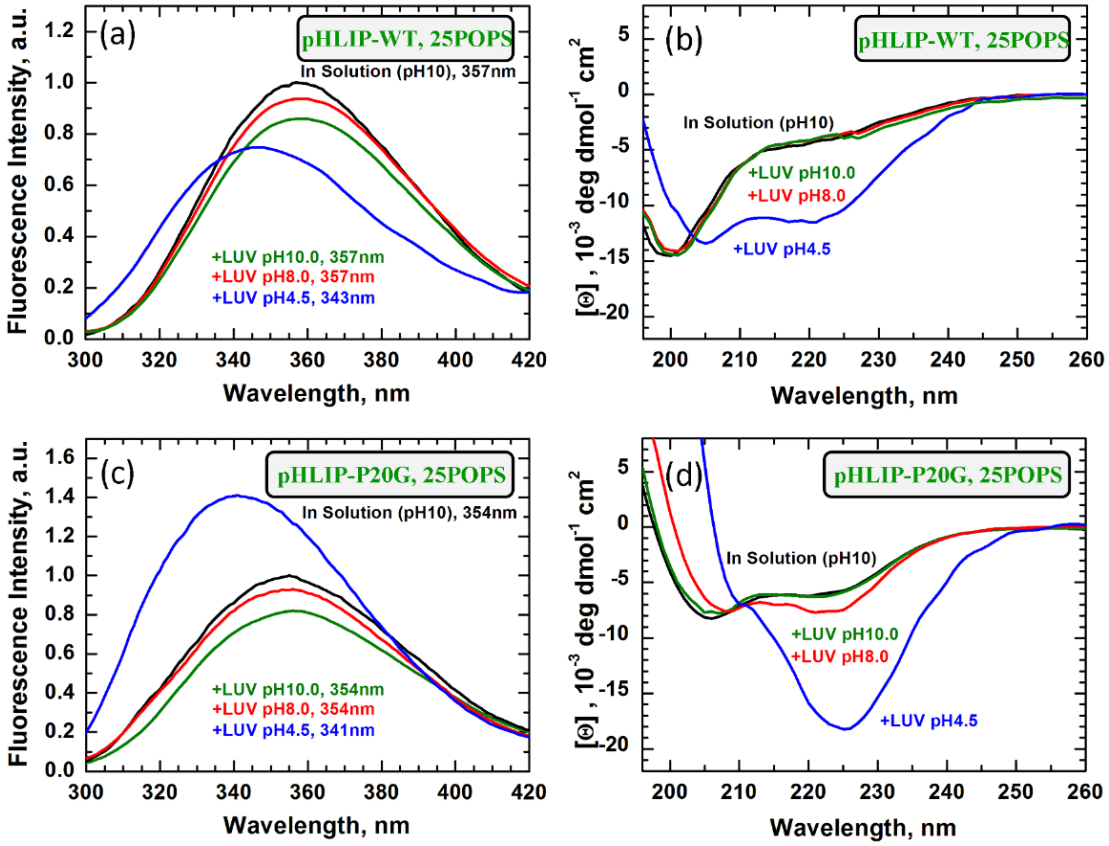

FIGURE A2. Trp emission and CD spectra of pHLIP-WT and P20G in 25POPS:75POPC LUV.

Similar to measurement performed in pure POPC membranes, Trp emission and CD spectra of both pHLIP variants were measured in solution at pH 10 and in the presence of 25POPS:75POPC at decreasing pH. No blue shift or CD spectral changes were observed after the addition of LUV at pH 10 indicating lack of State II formation. pHLIP-P20G showed a similar CD spectral shape in 25POPS:75POPC at low pH as in membranes containing only POPC and in the previous Barrera et al. publication[68].

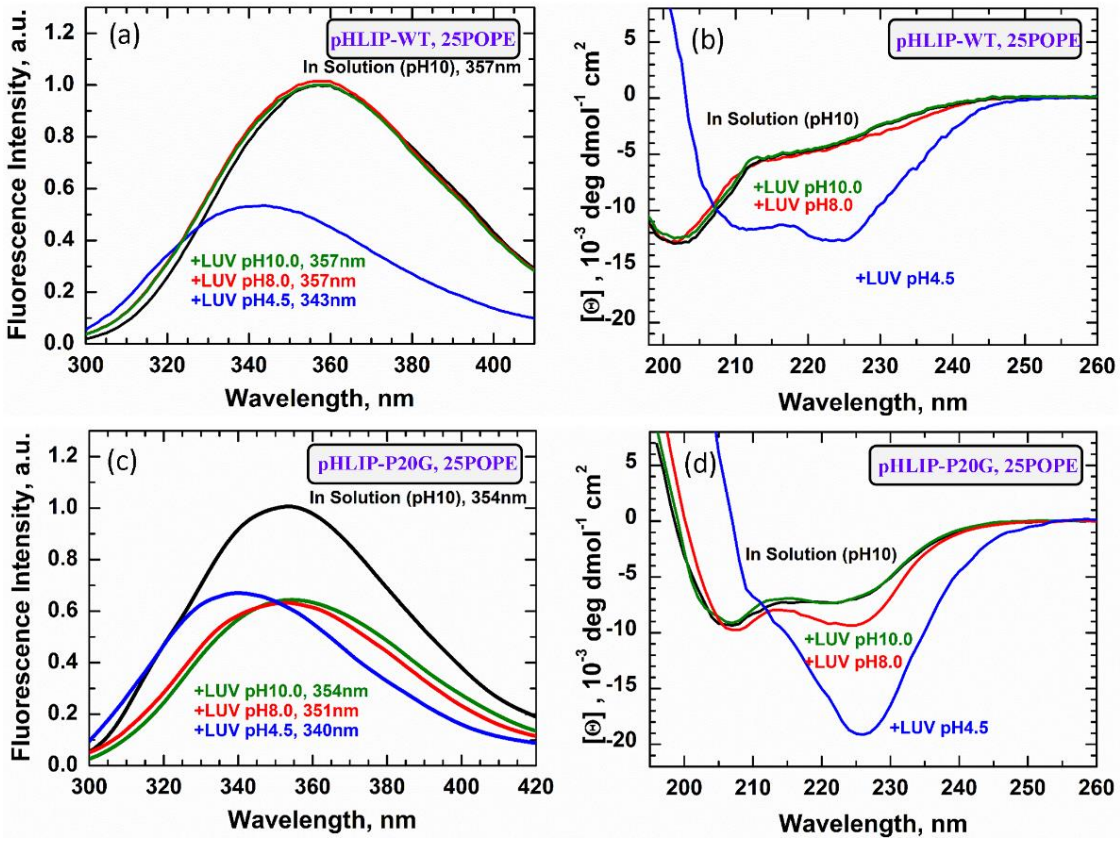

FIGURE A3. Trp emission and CD spectra of pHLIP WT and P20G in 25POPE:75POPC LUV.

Trp emission and CD spectra of both pHLIP variants were measured in solution at pH 10 and in the presence of 25POPE:75POPC at decreasing pH. No blue shift or CD spectral changes were observed at pH 10 after the addition of membranes indicating lack of State II formation. pHLIP-P20G showed a similar CD spectral shape in 25POPE:75POPC at low pH as in LUV containing purely POPC and in the previous Barrera et al. publication[68].

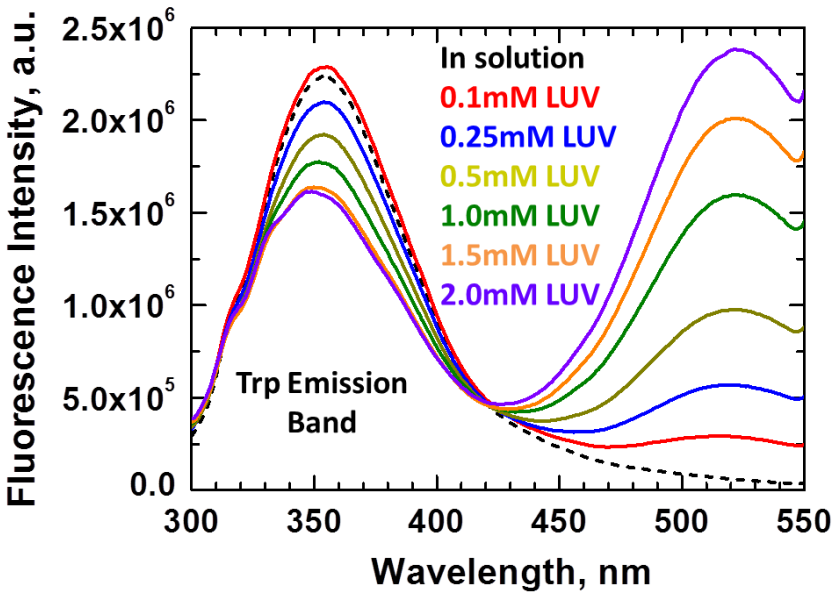

FIGURE A4. Representative data for pHLIP Trp-Dansyl FRET measurements.

FRET measurements were performed between Trp (donor) present in both pHLIP constructs and membranes containing 2% Dansyl-PE (acceptor) by gradually the increasing LUV concentration. The partitioning of pHLIP to membranes is indicated by the decrease in the intensity of the donor Trp peak as a function of Dansyl containing LUV. The plot shows the partitioning of pHLIP-P20G to pure POPC membranes containing 2% Dansyl-PE

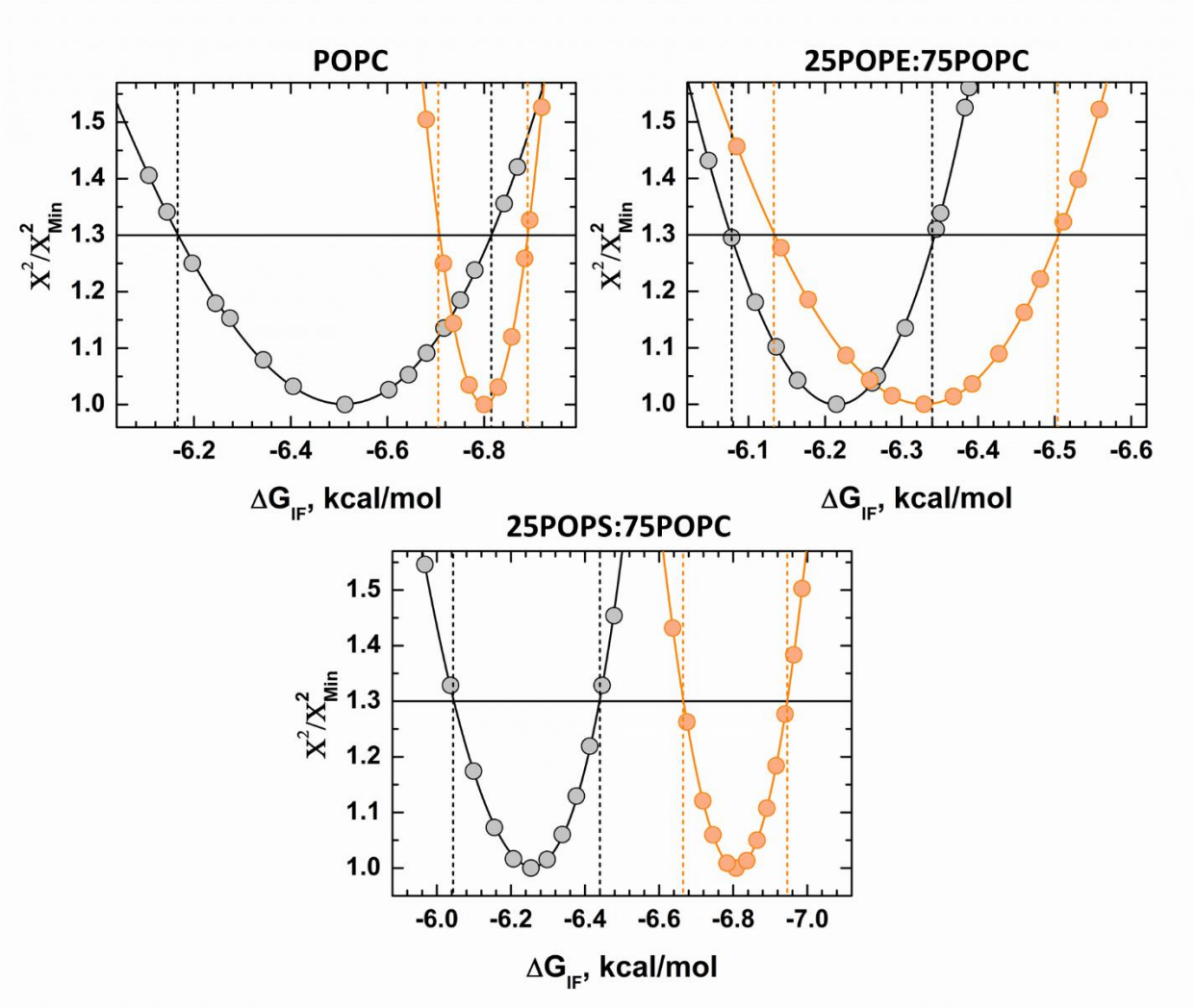

FIGURE A5. Support plane analysis of partitioning free energy (ΔG_{IF}) in FRET study between pHLIP and membranes.

Support plane analysis was performed on the fits obtained from the membrane partitioning FRET measurements described in Fig. 2.3 and A4. Error in the fits is indicated for both pHLIP-WT (black) and P20G (orange) in brackets and demarked in the plots by dashed lines for pure POPC, 25POPE:75POPC and 25POPS:75POPC LUV using 1 standard deviation as cutoff (horizontal line). For POPC: pHLIP WT ΔG_{IF} = -6.5 [-6.3;6.7], pHLIP P20G ΔG_{IF} = -6.8 [-6.7;6.9]. For 25POPE:75POPC: pHLIP WT ΔG_{IF} = -6.2 [-6.1;6.3], pHLIP P20G ΔG_{IF} = -6.3 [-6.2;6.4]. For 25POPS:75POPC: pHLIP WT ΔG_{IF} = -6.3 [-6.1;6.4], pHLIP P20G ΔG_{IF} = -6.8 [-6.7;6.9]

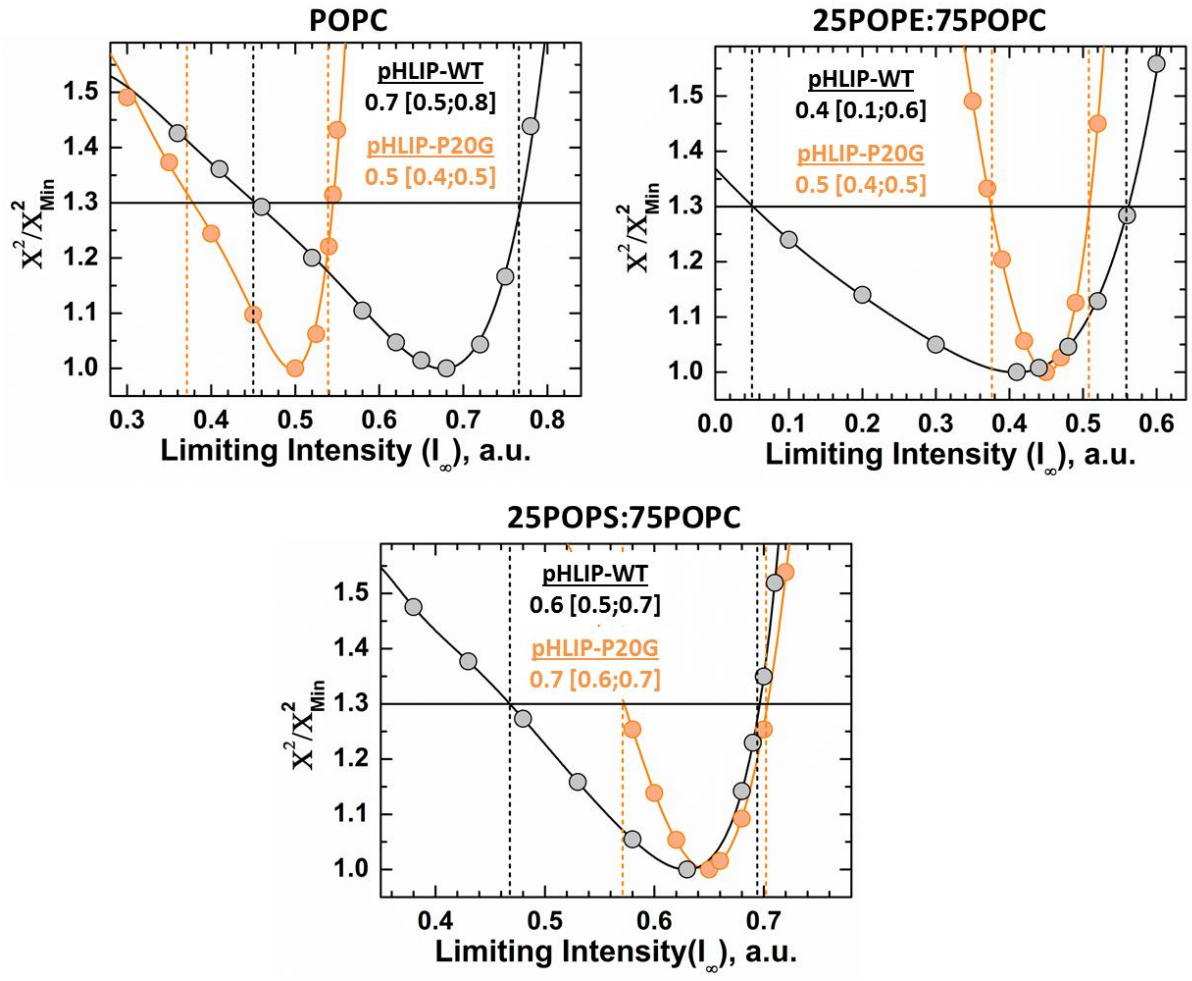

FIGURE A6. Support plane analysis of limiting intensity (I_∞) in FRET study between pHLIP and membranes.

Support plane analysis was performed on the fits obtained from the membrane partitioning FRET measurements described in Fig. 2.3 and A4. Error in limiting intensity (I_∞) is indicated for both pHLIP-WT (black) and P20G (orange) in brackets and demarked in the plots by dashed lines for pure POPC, 25POPE:75POPC and 25POPS:75POPC LUV using 1 standard deviation as cutoff (horizontal line).

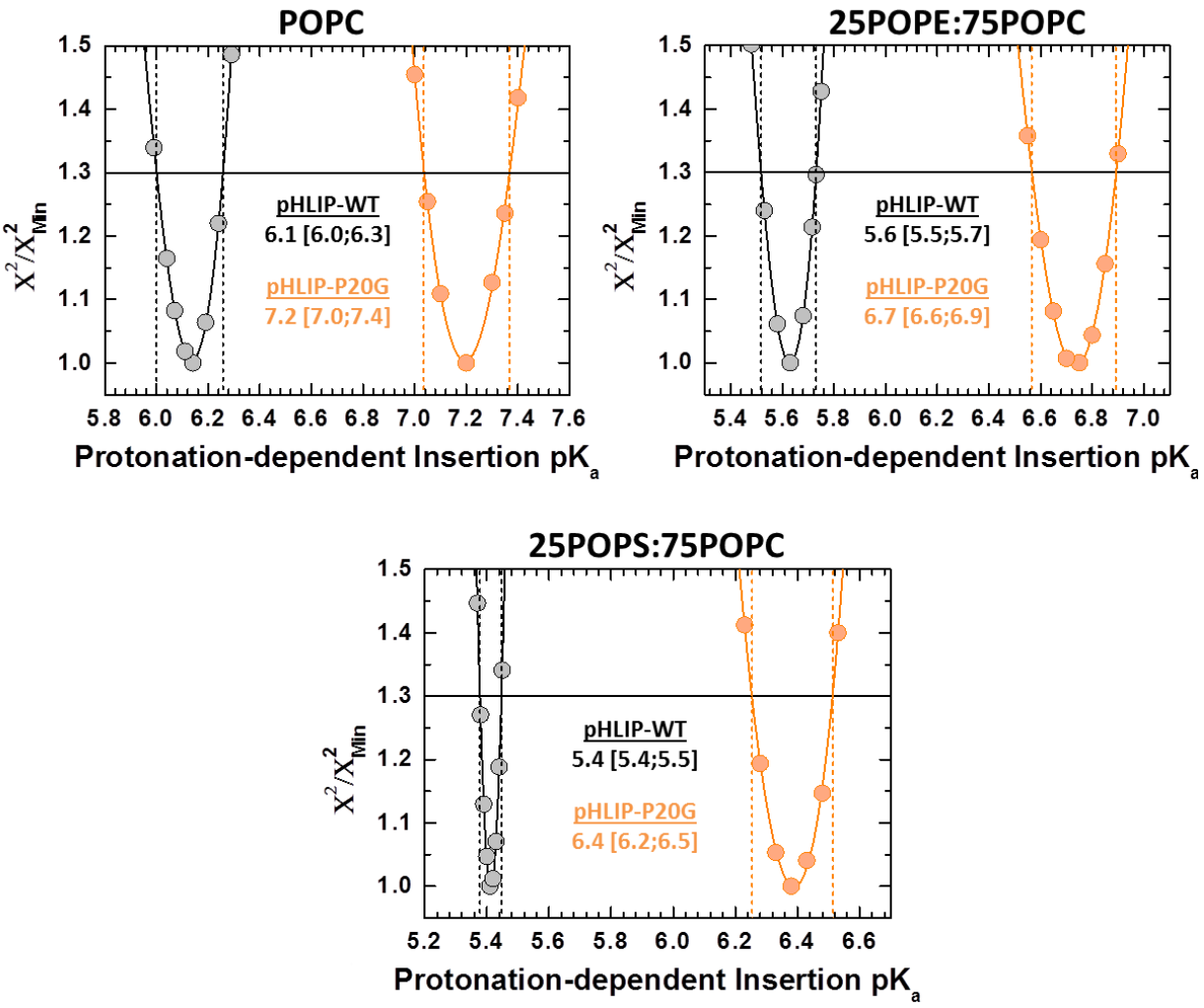

FIGURE A7. Protonation-dependent insertion pK_a support plane analysis.

Support plane analysis was performed on the fits obtained from the pH-titrations described in Fig. 2.4. Error in the fits is indicated for both pHLIP-WT (black) and P20G (orange) in brackets and demarked in the plots by dashed lines for pure POPC, 25POPE:75POPC and 25POPS:75POPC LUV using 1 standard deviation as cutoff (horizontal line).

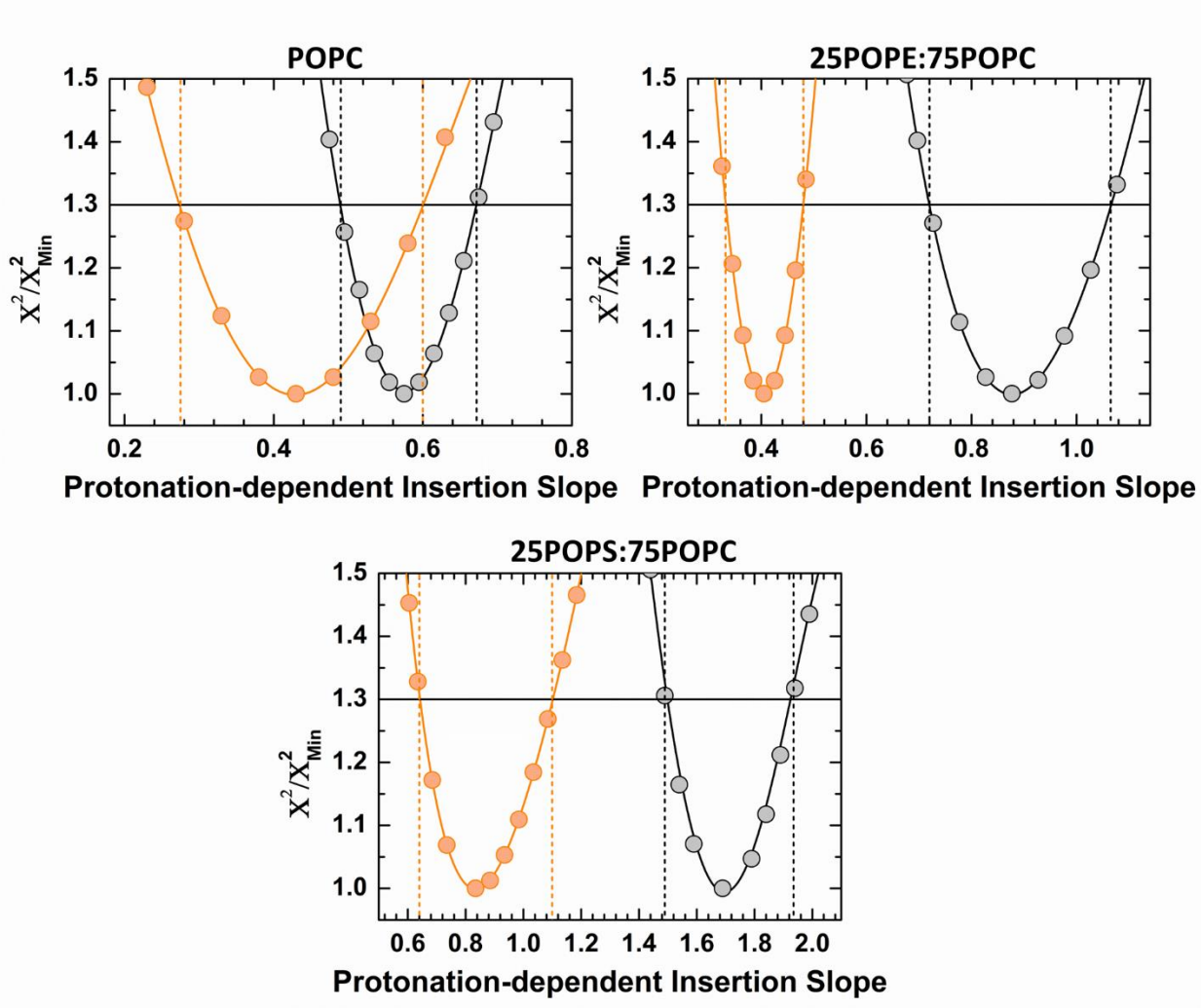

FIGURE A8. Support plane analysis for the slope (m) of the fit of pHLIP pH-dependent membrane insertion.

Support plane analysis was performed on the fits obtained from the pH-titrations described in Fig. 2.4. Error in the fits is indicated for both pHLIP-WT (black) and P20G (orange) in brackets and demarked in the plots by dashed lines for pure POPC, 25POPE:75POPC and 25POPS:75POPC LUV using 1 standard deviation as cutoff (horizontal line). For POPC: pHLIP WT slope = 0.6 [0.5;0.7], pHLIP P20G slope = 0.4 [0.3;0.6]. For 25POPE:75POPC: pHLIP WT slope = 0.9 [0.7;1.1], pHLIP P20G slope = 0.4 [0.3;0.5]. For 25POPS:75POPC: pHLIP WT slope = 1.7 [1.5;2.0], pHLIP P20G slope = 0.8 [0.6;1.1]

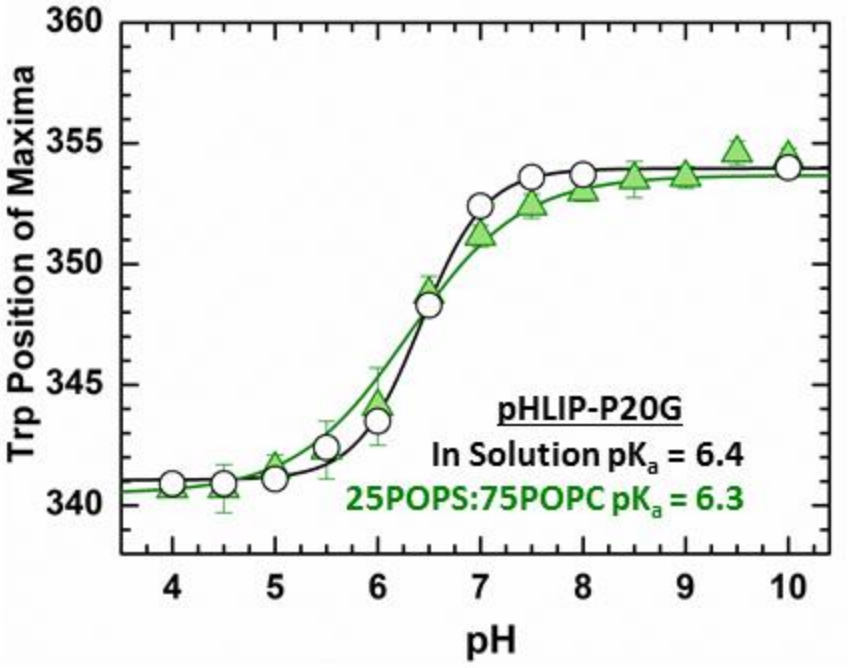

FIGURE A9. pH-dependent aggregation of pHLIP-P20G vs insertion into 25POPS LUV.

The pH-induced aggregation (pK_a = 6.4) of pHLIP-P20G was measured by plotting the changes in its Trp emission position of maxima as a function of pH and compared to its pH-dependent insertion into 25POPS:75POPC LUV (pK_a = 6.3). Unlike pHLIP-WT (Fig. 2.5), the difference between both titrations is too small and beyond resolution capabilities.

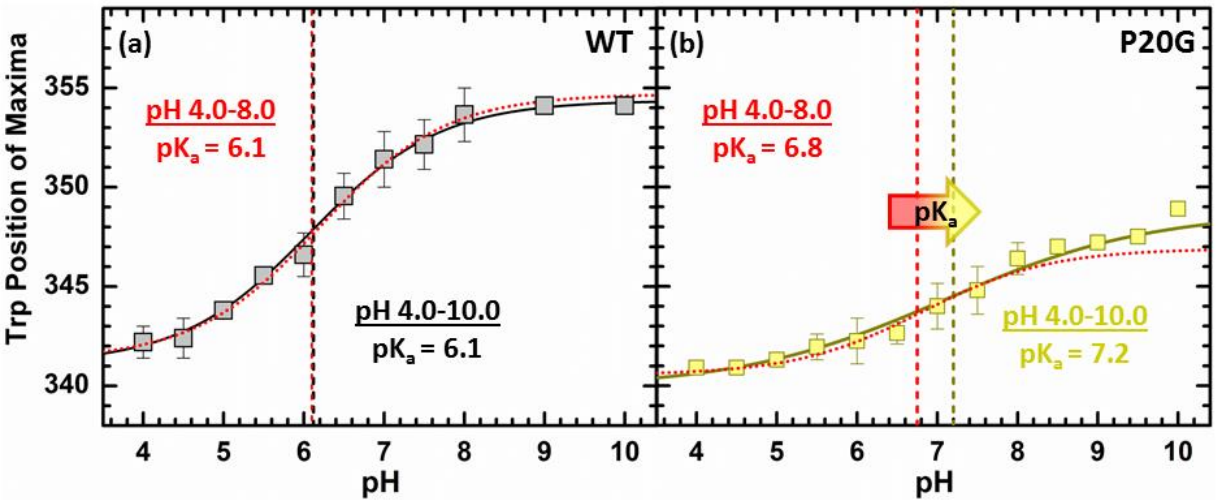

FIGURE A10. Effect of pH range on membrane insertion pK$_a$.

Comparison of pH-dependent membrane insertion pK$_a$ for pHLIP-WT (black) and pHLIP-P20G (yellow) calculated using different pH ranges in pure POPC membranes. Fits were analyzed as described in the method section using either pH 4-8 (red) or pH 4-10 (WT: black, P20G: yellow). (a) pHLIP-WT achieves a full titration at pH 8 therefore the calculated pK$_a$ (dashed lines) are unaffected by increased pH range. (b) Unlike pHLIP-WT, pHLIP-P20G is at the middle of a transition at pH 8 with a calculated pK$_a$ of 6.8 as described by Barrera et al. If the transition is completed by extending the titration to pH 10, the calculated pK$_a$ increases to 7.2. Similar results are obtained in other lipid compositions, data not shown.

Appendix B: Modulation of pHLIP Membrane Interactions by Divalent Cations

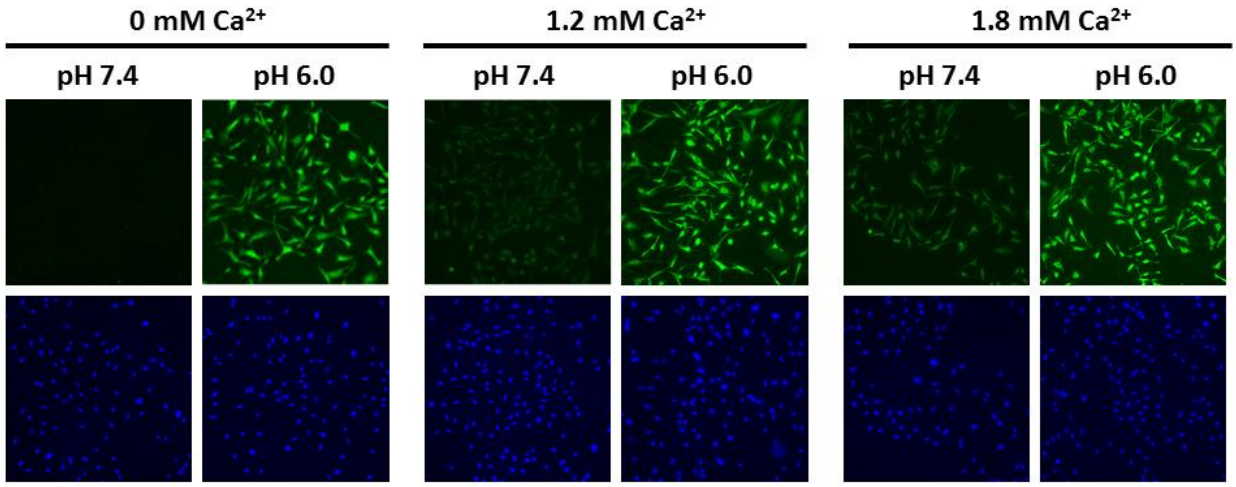

FIGURE B1. A488-pHLIP fluorescent microscopy.

Images of MDA-MB-231 cells incubated with pHLIP N-terminally conjugated to the fluorophore A488. Measurements performed in the absence of divalent cations show an increase in A488 intensity after acidification, consistent with previous reports [95], and the cellular interaction of pHLIP. The significant increase in fluorescence intensity in the presence of 1.8 mM Ca^{2+} shows that Ca^{2+} promotes the cellular interaction of pHLIP in the absence of acidic conditions. Bottom panels show the Hoechst stain of cellular samples. Cellular measurements were performed in collaboration with the Damien Thevenin Lab

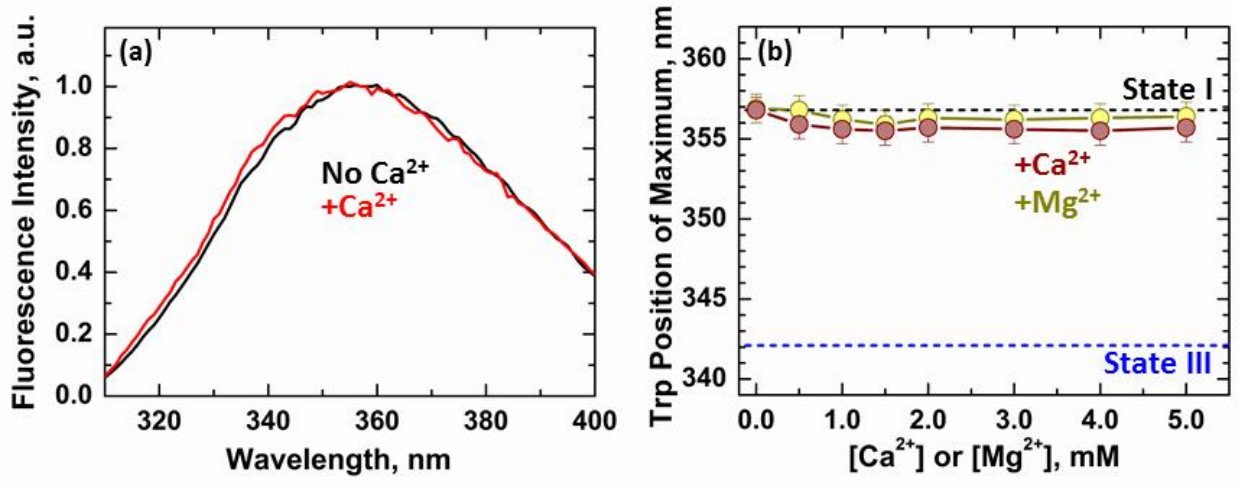

FIGURE B2. Ca^{2+} and Mg^{2+} induced spectroscopic effects in the absence of membranes.

Trp emission spectra were collected at increasing concentrations of Ca^{2+} and Mg^{2+} in the absence of LUV to establish whether divalent cations induced the aggregation of pHLIP. (a) Representative Trp emission spectra of pHLIP in a sample lacking LUV, before and after the addition of 2.0 mM Ca^{2+}. The presence of Ca^{2+} induced no significant changes on the Trp emission spectrum in the absence of membranes, with only a 1 nm decrease to 356 nm from 357 nm. (b) No further spectroscopic changes were observed at higher [Ca^{2+}] used, indicating that Ca^{2+} does not induce pHLIP aggregation under conditions used for this study. Dashed lines indicate the positions of maximum for the soluble (State I) and transmembrane (State III) forms of pHLIP [103].

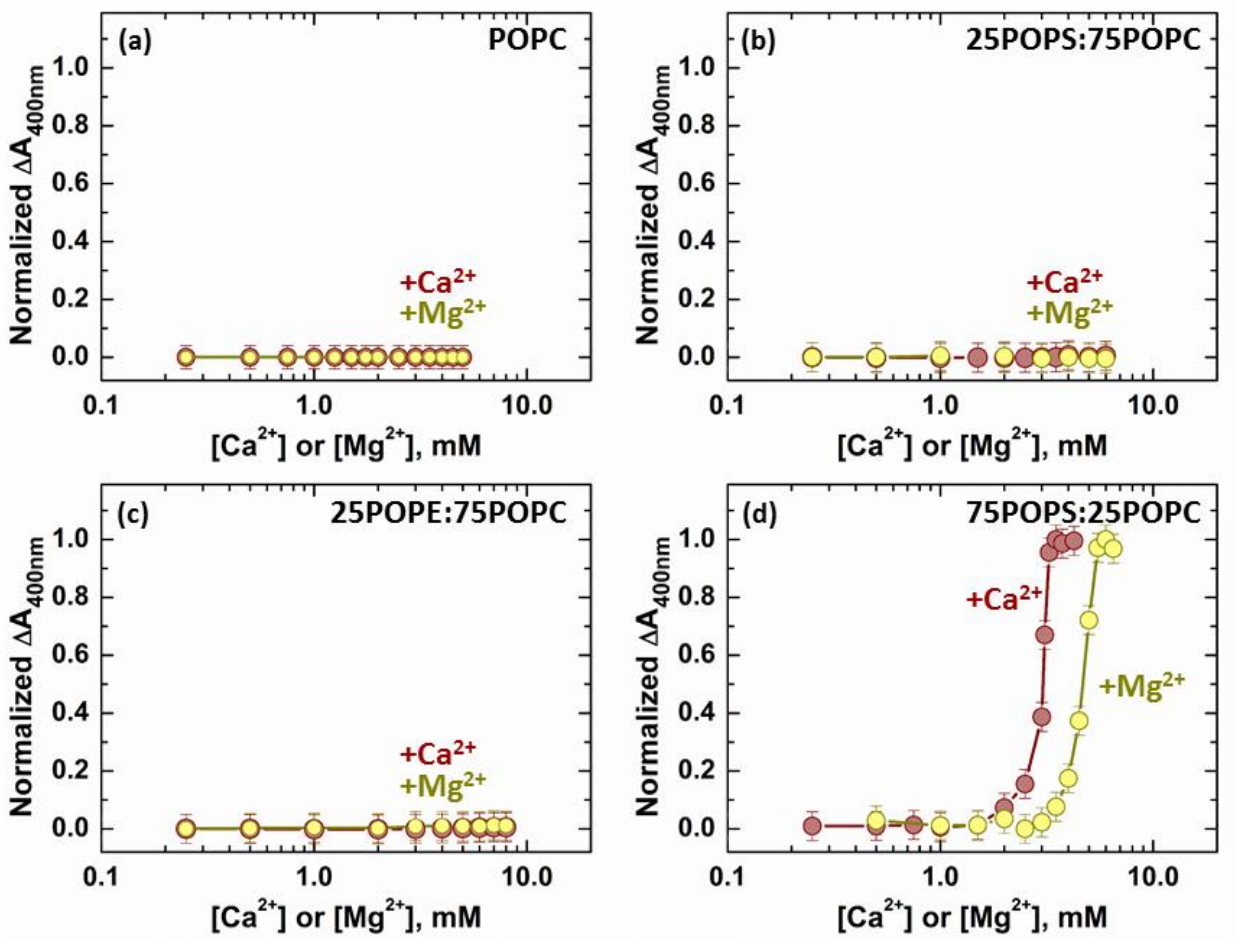

FIGURE B3. Light scattering of LUV in the presence of Ca^{2+} or Mg^{2+}.

The aggregation of LUV used in this study was determined by measuring the scattering of 0.1 % LUV solutions at 400 nm and increasing [Ca^{2+}] or [Mg^{2+}] as described in the methods section. (a) No significant increases in scattering were observed for POPC LUV under [Ca^{2+}] or [Mg^{2+}] < 10.0 mM. These results show that concentrations of divalent cations used in this study do not induce the aggregation of POPC LUV. (b, c) Similarly, no significant changes in scattering were detected for 25POPS:75POPC or 25POPE:75POPC LUV at the same concentration range. (d) The aggregation of 75POPS:25POPC LUV was used as a positive control of the technique, which showed large increases in scattering at [Ca^{2+}] > 2.0 mM or [Mg^{2+}] > 4.0 mM, indicative of LUV aggregation.

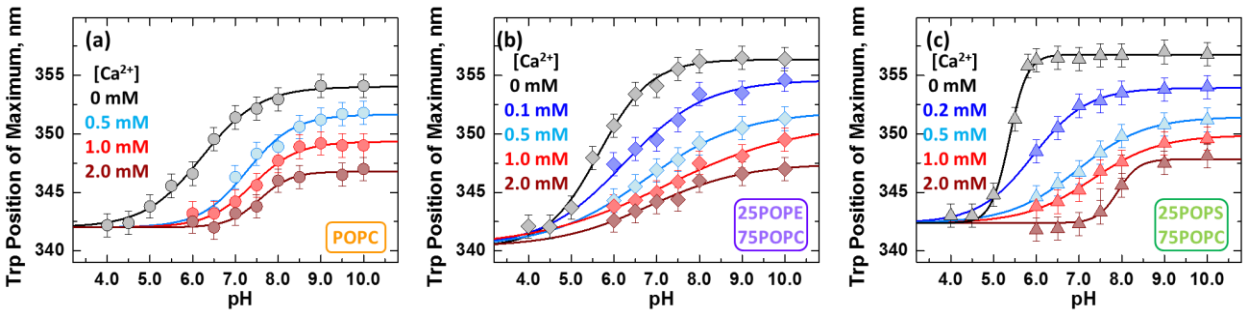

FIGURE B4. Lipid modulation of Ca2+-dependent membrane interactions of pHLIP.

The protonation-dependent membrane insertion of pHLIP was measured at increasing [Ca^{2+}] from 0-2.0 mM in membranes containing (a) POPC, (b) 25POPE:75POPC, or (c) 25POPS:75POPC. All fits were globally fitted due to the lack of experimental data below pH 6.0. (a) The following pK_a were obtained for membranes containing only POPC: 0 mM Ca^{2+}: 6.2 ± 0.1, 0.5 mM Ca^{2+}: 7.3 ± 0.1, 1.0 mM Ca^{2+}: 7.4 ± 0.1, 2.0 mM Ca^{2+}: 7.6 ± 0.1. (b) The following pK_a were obtained for membranes containing 25POPE:75POPC: 0 mM Ca^{2+}: 5.7 ± 0.1, 0.1 mM Ca^{2+}: 6.2 ± 0.1, 0.5 mM Ca^{2+}: 6.7 ± 0.1, 1.0 mM Ca^{2+}: 6.9 ± 0.1, 1.0 mM Ca^{2+}: 7.2 ± 0.1. (b) The following pK_a were obtained for membranes containing 25POPS:75POPC: 0 mM Ca^{2+}: 5.4 ± 0.1, 0.2 mM Ca^{2+}: 5.9 ± 0.1, 0.5 mM Ca^{2+}: 6.9 ± 0.1, 1.0 mM Ca^{2+}: 7.3 ± 0.1, 1.0 mM Ca^{2+}: 7.9 ± 0.1.

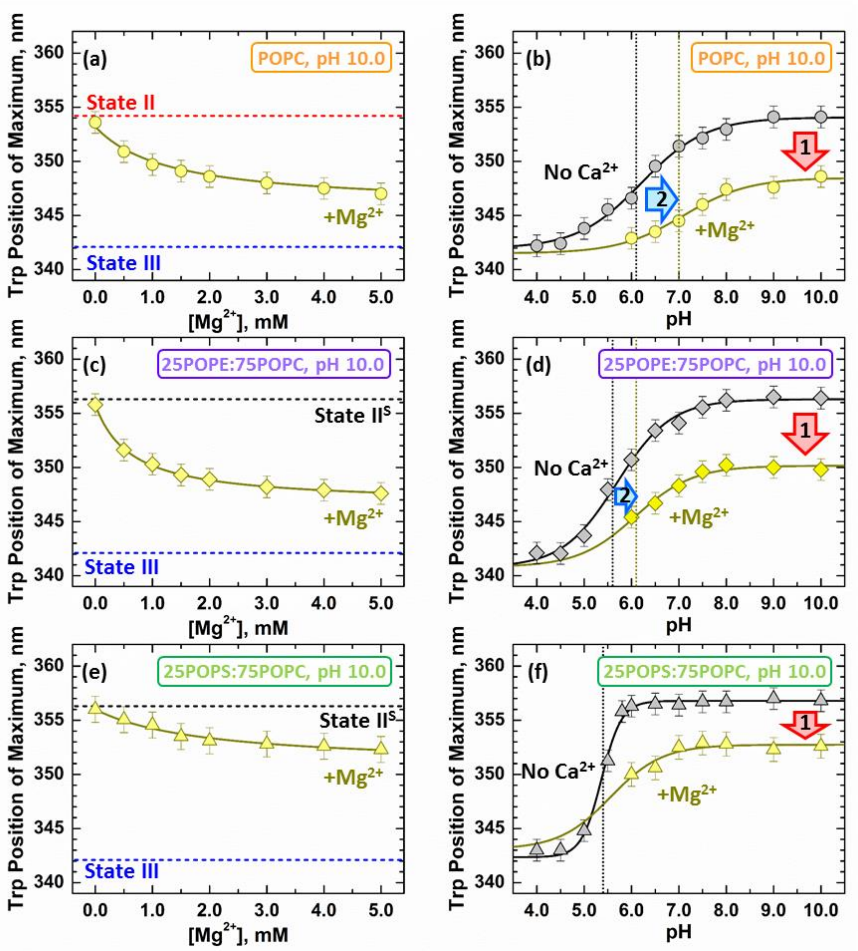

FIGURE B5. Mg^{2+}-mediated membrane insertion of pHLIP.

Mg^{2+}-titrations at constant pH 10.0 and pH-titrations in the presence of 2.0 mM Mg^{2+} were performed in POPC, 25POPE:75POPC, or 25POPS:75POPC LUV. (a, c, and e) In all LUV tested, incremental concentrations of Mg^{2+} at pH 10.0 induced a concentration-dependent decrease in Trp positions of maximum (red arrows). The observed changes, however, were weaker compared to the ones observed at equimolar concentrations of Ca^{2+} (Fig. 3.4). (b, d, and f) As in the case of Ca^{2+} the addition of 2.0 mM Mg^{2+} shifted the pH-titration curves of pHLIP towards alkali pH (blue arrows). A 1.0 pH unit increase was observed in the case of POPC from 6.1 ± 0.1 in the absence of Mg^{2+} to 7.1 ± 0.1 in the presence of 2.0 mM Mg^{2+}. In the presence of the zwitterionic 25POPE:75POPC LUV the addition of 2.0 mM Mg^{2+} led to a 0.3 pH unit increase in pK_a from 5.7 ± 0.1 to 6.0 ± 0.1. The change in pK_a could not be quantified for the 25POPS:75POPC LUV due to experimental limitations related to the short buffering range of the buffer used (see methods section for details). The horizontal dashed lines denote the positions of maximum for the two known interfacial forms of pHLIP (State II in POPC and II^S in non-POPC LUV) and the transmembrane (State III) [103]. The transition pK_a of each curve is graphically indicated by color-coded vertical dotted lines.

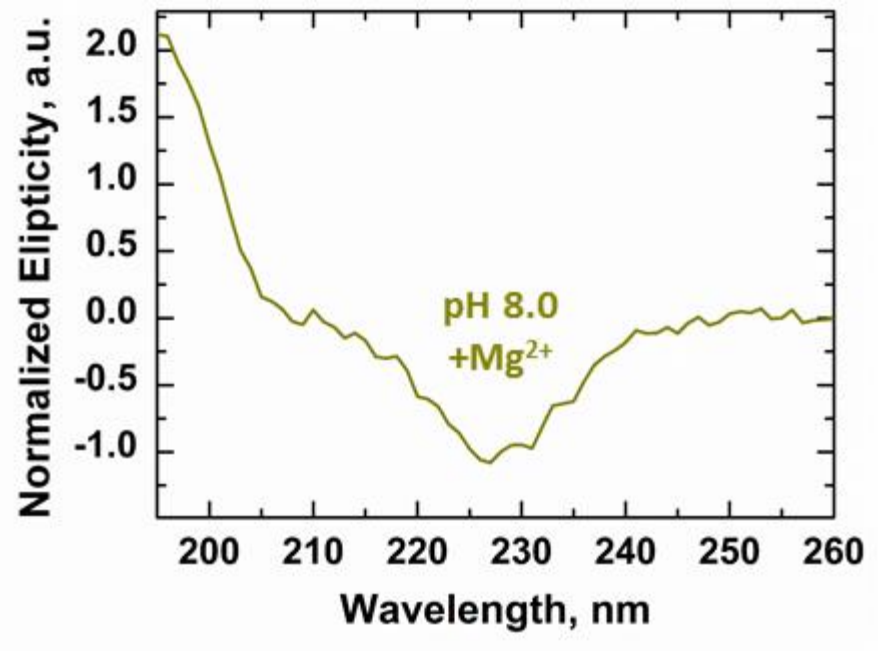

FIGURE B6. Oriented CD of pHLIP in POPC and in the presence of Mg^{2+}.

As in the case of Ca^{2+} (Fig. 3.3c, red) the OCD spectrum of pHLIP in the presence of Mg^{2+} at pH 8.0 presents with a single minimum at 228 nm. This spectrum is consistent with the State III OCD spectrum of pHLIP at pH 4.0 (Fig. 3.3c, blue) and shows that Mg^{2+} induces the transmembrane conformation of pHLIP in POPC membranes, absent acidic conditions.

Appendix C: Modulation of Bcl-xL Membrane Insertion and Refolding by Lipid Headgroups

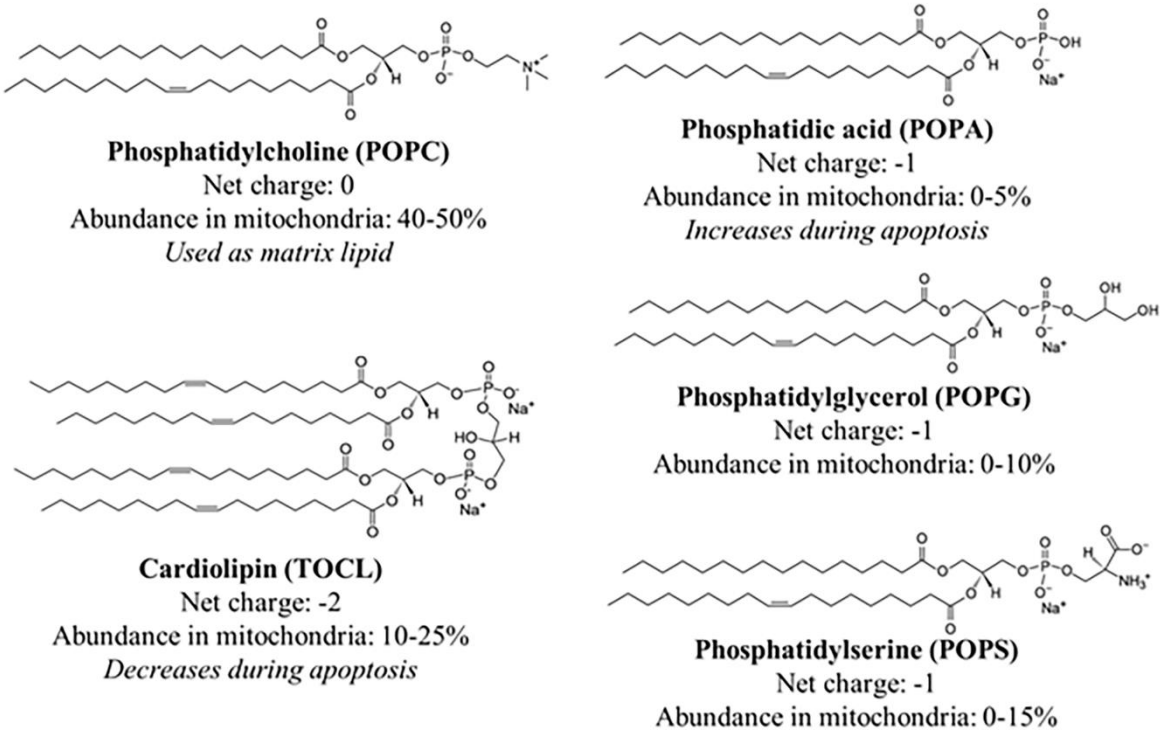

FIGURE C1. Structures and properties of lipids used in this study.

Information such as net charge, relative abundance in the mitochondria [160, 211], and changes during apoptosis are indicated below each structure [23].

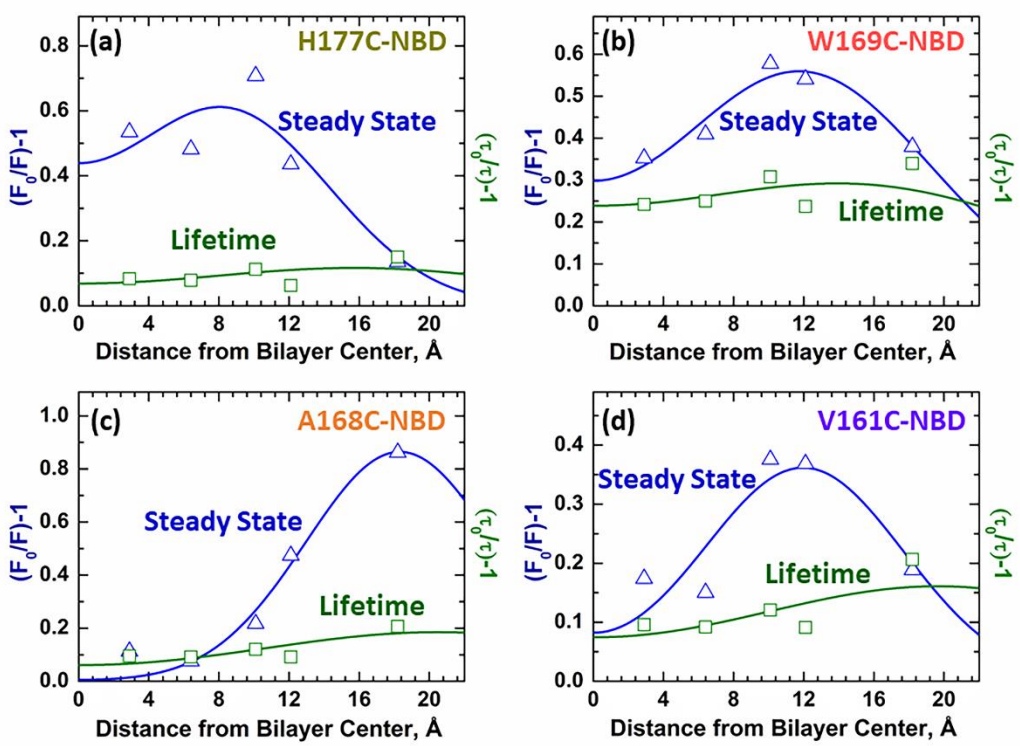

FIGURE C2. Primary data for depth-dependent quenching measurements in 3TOLC:2POPC LUV.

Steady-state (blue) and lifetime (green) depth-dependent quenching data used in calculations of the differential quenching profiles of Bcl-xL ΔTM NBD-labeled mutants in 3TOCL:2POPC LUV (Fig. 4.6). Results are presented as the ratio of emission intensity (left side scale) or lifetime (right side scale) in the presence or absence of five different spin-labeled lipids. Each data point is plotted against the known depth of a spin label in the membrane [168].

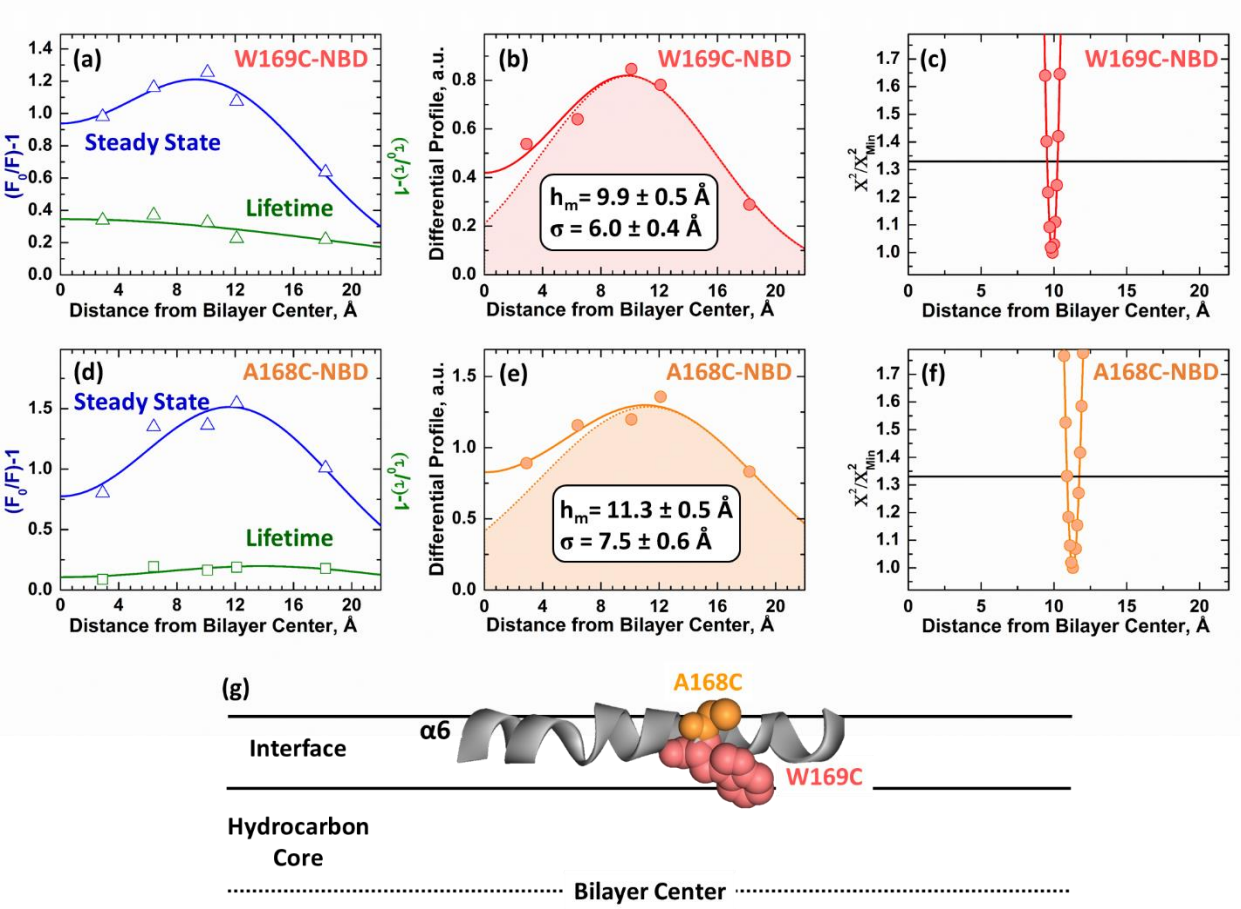

FIGURE C3. Depth-dependent quenching of α6 in membrane inserted Bcl-xL ΔTM using 75POPG:25POPC LUV.

Depth-dependent fluorescence quenching of NBD-labeled single-Cys mutants (A169C-NBD, top row; A168C-NBD, bottom row) of Bcl-xL ΔTM inserted into 75POPG:25POPC LUV at pH 4.5. Left panels show the primary steady-state (blue) and lifetime (green) depth-dependent quenching data used in the calculation of the differential quenching profiles (middle panels). The latter are analyzed using DA methodology to estimate the most likely depth of the fluorophore (h_m) and the width of the transverse distribution (σ). The robustness of the fits used to calculate the h_m parameter were evaluated by support plane analysis (right panels). For W169C: h_m = 9.9 [9.5;10.3] Å, for A168C: h_m = 11.2 [10.9;11.7] Å. The probes in both mutants, placed in the middle of α6, were located about 10 Å away from the center of the bilayer, which is not consistent with a transmembrane orientation. (g) Cartoon representation of Bcl-xL hydrophobic α6 helix and single-Cys mutants used. These measurements are consistent with the results in 3TOCL:2POPC LUV (Fig. 4.6) and EPR O_2/NiEDDA accessibility (Fig. 4.5).

Appendix D: Modulation of Bcl-xL Conformational Switching

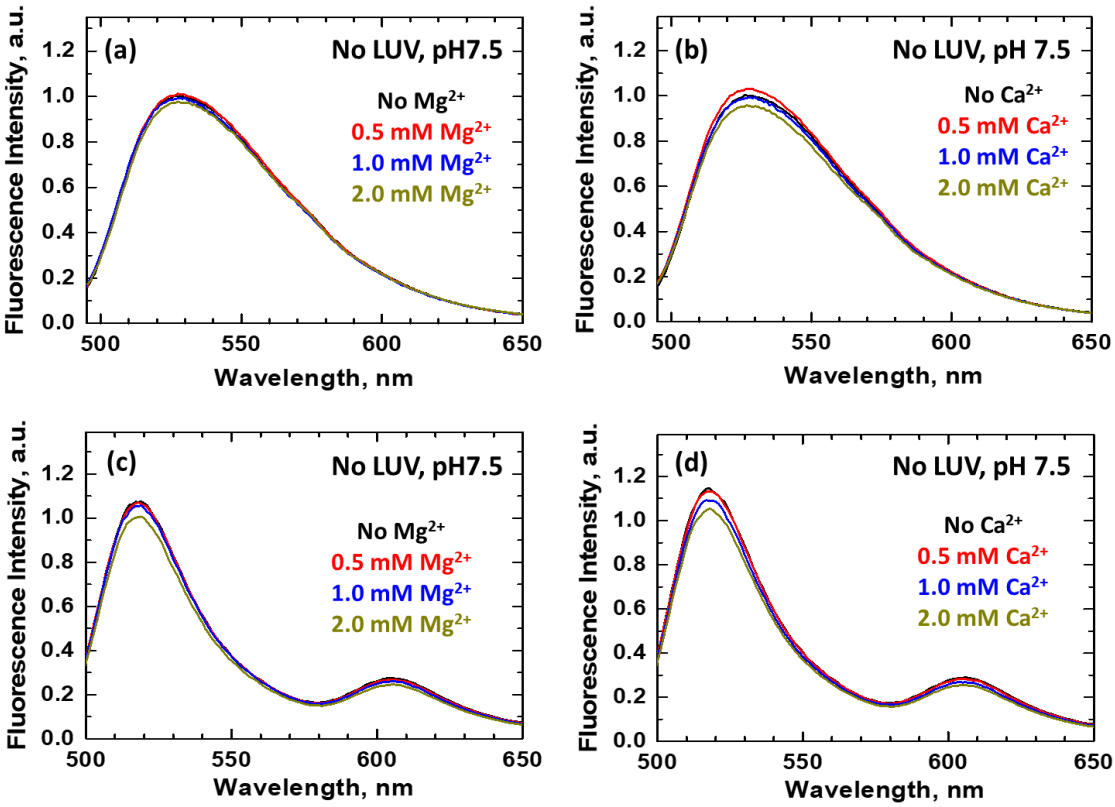

FIGURE D1. Control NBD and FRET measurements in the absence of LUV

(a, b) The addition of Mg^{2+} or Ca^{2+} produced no significant changes in the NBD emission spectrum of Bcl-xL W169C-NBD in the absence of LUV, rulling out aggregation in solution. (c, d) Simialrly, the presence of divalent cations did not affect the FRET of mCherry-Bcl-xL D189C-A488 in the absence of LUV, pointing to the requirement of LUV on the release of the BH4 domain.

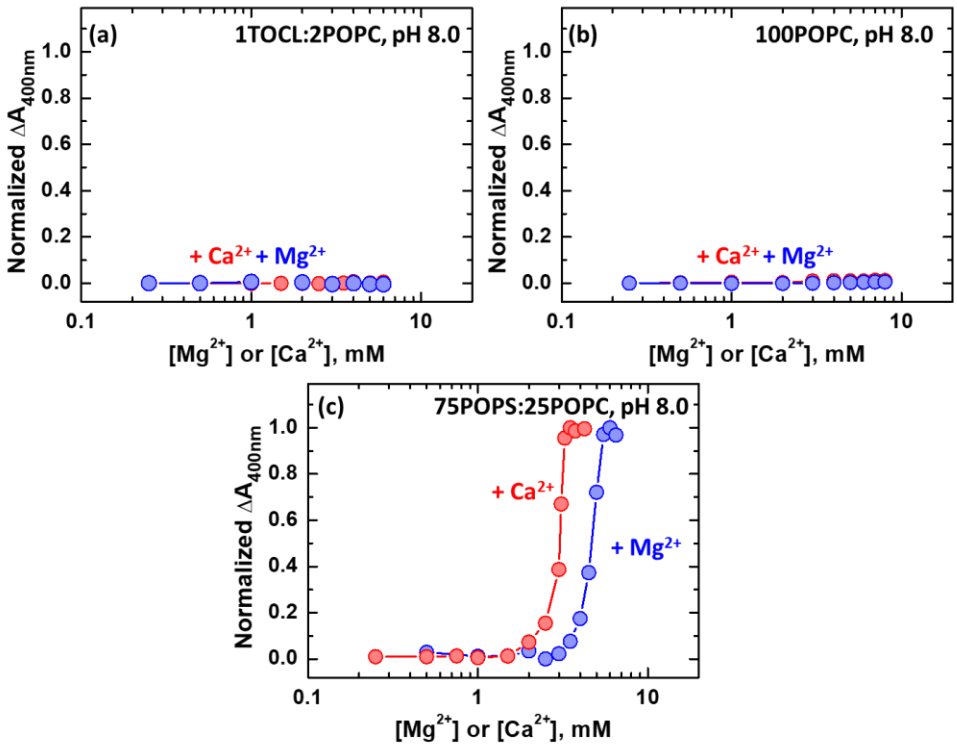

FIGURE D2. Light scattering of LUV in the presence of Ca^{2+} or Mg^{2+}.

The scattering of 0.1 % LUV solutions at 400 nm and increasing [Ca^{2+}] or [Mg^{2+}] was used to measure the aggregation of LUV used in this study. (a, b) No significant changes in scattering were observed for POPC or 1TOCL:2POPC LUV at [Ca^{2+}] or [Mg^{2+}] < 10.0 mM. This indicates that the LUV used in this study do not aggregate under experimental conditions. (d) The divalent cation-induced aggregation of anionic LUV composed of 75POPS:25POPC was used as a positive control.

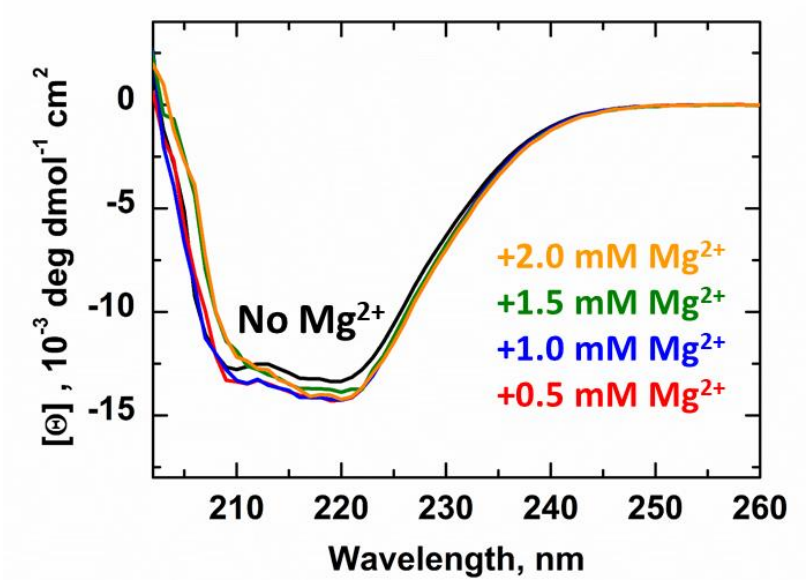

FIGURE D3. Bcl-xL refolding at increasing [Mg^{2+}] in the presence of 1TOCL:2POPC LUV.

The secondary structure of Bcl-xL was measured by circular dichroism (CD) in the presence of 1TOCL:2POPC at increasing [Mg^{2+}]. The double minimum at 209 and 222 nm is consistent with its NMR α-helical structure in solution (Fig. 5.2) and previous CD measurements (Fig. 5.4). The addition of Mg^{2+} leads to larger ellipticities at 222 nm, indicative of larger α-helical content.